MODELING, PROCESSING, FABRICATION AND CHARACTERIZATION OF CARBON NANOMATERIALS-REINFORCED POLYMER COMPOSITES

Mohammad Rafiee

Thesis submitted in partial fulfillment of the requirements for the

Doctorate in Philosophy degree in Mechanical Engineering

Ottawa-Carleton Institute for Mechanical and Aerospace Engineering
University of Ottawa
Ottawa, Canada

September 2018

Abstract

Fiber and matrix-dominant properties of fiber-reinforced polymer composites are important in many advanced technological fields, such as aviation, aerospace, transportation, energy industry, etc. Still, pre-mixing the polymer matrix with nanoparticles may enhance the through-thickness or matrix-dominant properties, and surface treatment of fiber reinforcements with nanoparticles, on the other hand, may improve the in-plane or fiber-dominated properties of laminated composites, as well as interfacial adhesion. A novel manufacturing method that combines a spraying process with nanoparticle/epoxy mixture technique was introduced to incorporate carbon nanoparticles for enhancement of thermal properties of multiscale laminates. Several graphene-based nanomaterials including graphene oxide (GO), reduced graphene oxide (rGO), graphene nanoplatelets (GNPs) and multi-walled carbon nanotubes (MWCNTs) were employed to modify the epoxy matrix and the surface of glass fibers. Multiscale glass fiber-reinforced composites were fabricated from unmodified and modified epoxy, as well as fibers, using the vacuum-assisted resin transfer molding (VARTM) process. The composites obtained combined improvements in both the fiber and matrix- dominant properties, resulting in superior composites. The morphological, rheological, thermal and mechanical properties of the glass fiber-reinforced multiscale composites were investigated. The thermal properties of the epoxy/nanoparticle composites were studied through differential scanning calorimetry (DSC), thermo-gravimetric analysis (TGA) and thermal conductivity measurements. The tensile, bending, vibration, interlaminar shear strength (ILSS) and thermal characterization results indicated that the introduction of GNPs, GO, rGO, and MWCNTs enhanced the themo-mechanical properties. The fracture surfaces of the fiber-reinforced composites were examined by scanning electron microscopy (SEM) and the micrographs were analyzed to comment on the mechanical results.

Acknowledgements

First, I thank my research supervisors, Dr. Michel Labrosse (University of Ottawa) and Dr. Fred Nitzsche (Carleton University) for supervising me, being available to discuss the results, giving me critical feedback on my papers, and teaching me and pointing me in the right direction toward what I needed to know in order to successfully conduct my research.

In addition to two supervisors, there have been over 40 people at the University of Ottawa and Carleton University whose assistance has been invaluable. I would like to express my appreciation to Drs. Francois Robitaille (UOttawa) and Jeremy Laliberte (CarletonU) for allowing me access to their labs for the composite manufacturing. I also thank Drs. Marianne Fenech and Mohammed Yandouzi (Department of Mechanical Engineering, University of Ottawa) for their technical supports on optical and SEM imaging. I am pleased to thank Dr. Xudong Cao (Department of Chemical and Biological Engineering, University of Ottawa) for his great support and help during the design of experiments. I am also grateful from Dr. Jules Thibault (Department of Chemical and Biological Engineering, University of Ottawa) for the access to his lab and valuable instructions and comments. Technical support from Drs. Christopher Lan and Mohammadali Baghbanzadeh (both from Department of Chemical and Biological Engineering, University of Ottawa) for the access to their lab, probe sonication and dispersion of nanoparticles, was also much appreciated. I would also like to acknowledge the help of Dr. Boguslaw Kruczek (Department of Chemical and Biological Engineering, University of Ottawa) for allowing me access to his lab. I am also grateful for the great help from Simon Hind from the National Research Council Institute for Aerospace for providing me with thermal conductivity measurement equipment and comments.

I had an excellent opportunity to work with professional individuals at the University of Ottawa and Carleton University during this research. I thank all of them for the valuable collaborations. Specifically, I would like to express my deep appreciation to Mr. Leo Denner, technical officer at the Faculty of Engineering of the University of Ottawa. The discussions with him were always fruitful and constructive over the testing of specimens. Special thanks are reserved for machine shop personnel at the University of Ottawa: John Perrins (Senior technical officer), and technical officers Jacques Audet, Stanley Weedmark, Paul Burberry, Mihaita Matei, and machine shop personnel at Carleton University: Alex Proctor (Mechanical Laboratory-Shop

Supervisor) and Ian Lloy (Machinist) who greatly helped me during the design and fabrication of the molds and fixtures for the manufacturing and testing of materials.

The expertise of Aaron Miller (Composites Canada, Mississauga, ON, Canada) on the epoxy resin was extremely valuable to this research, and I thank Dr. Yun Liu for allowing me access to the facilities for the transmission electron microscopy (TEM), TEM sample preparation, DSC and SEM tests. I also express my thanks to Drs. Carlos Cesnik and Fang Liang for their assistance and helpful discussions on the use of VABS. I would also like to thank Dr. Mathias Althoff for the great help over the mathematical coding of rotating beams. Many thanks are given to Dr. Daniel Fetzsy and Jeff Carret for their support. I would also like to acknowledge the help of M. Eng. students Amir Soleiman and Deepak Agarwal who helped me in the manufacturing and testing of nanocomposite materials. A big thanks to all of my friends: Dr. Erfan Niazi, Dr. Melissa Arras, Marcel Clementino, Dr. Wander Vieira and Jack Xu for their assistance and supports.

I also acknowledge the supply of nanoparticles: MWCNTs by Nanocyl S.A. (Belgium), Cheap Tubes Inc. (U.S.A.), GO and rGO by Abalonyx (Norway). In addition, I gratefully acknowledge the financial support from the Ontario Trillium Scholarship and the University of Ottawa, Canada.

Finally, I would like to especially thank my parents for their unconditional support and their endless love. I would like to express my deepest thanks to my wife, Soraya, for her sacrifice, support, encouragement, and sincere heart through my doctoral degree program. I dedicate my dissertation to my family, and thank them with all my heart.

Table of contents

List of figures

List of tables

Chapter 1

1. Introduction

Foreword

This dissertation is divided into three major sections: introductory material, results and analysis in the form of peer reviewed publications, and a general discussion and conclusions section. The introduction contains a brief motivation for this research as well as the material needed to understand the analysis: an introduction to carbon nanomaterials, multiscale composites and characterization. The subsequent chapters are each devoted to a single peer reviewed publication and contain their own introduction, discussion and conclusions, as well as a foreword to create a more continuous flow and to explain how the publication fits into the dissertation (several of these forewords contain references of their own, which are listed at the bottom of the foreword section). Relevant prior research is addressed on a chapter-by-chapter basis. The general discussion ties all of the chapters together and provides a unifying summary and conclusion to the dissertation.

1.1 Background and significance

Nanocomposite materials reinforced with low density carbon nanomaterials (such as carbon nanotubes and graphene) and microscale high strength fibers are a new generation of multifunctional, high-performance engineering composites that have attracted considerable attention in recent years due to their outstanding mechanical properties and excellent electrical and thermal conductivities [1–3]. While conventional polymer composite materials reinforced by continuous fibers are strong in in-plane directions, they are usually weak against matrix-dominated failures. Graphene nanomaterials such as single- and multi-walled carbon nanotubes (SWCNTs and MWCNTs), graphene nanoplatelets (GNPs), graphene oxide (GO) and reduced-graphene oxide (rGO) are light nano-sized allotropes of carbon with excellent thermo-electro-mechanical properties. When conventional fiber-reinforced laminates are modified with graphene nanomaterials, new materials with improved mechanical, thermal and electrical properties may be developed [1,4–8]. Carbon nanotubes are an allotrope of sp2 hybridized carbon with one or several tubes in concentric cylinders. GNPs are composed of several layers of graphene and are considered as smart reinforcing fillers [4,9]. GNPs' properties can be influenced by their manufacturing methods. GNPs were also noted as a probable substitute to carbon nanotube in terms of cost and better targeted properties [10]. Graphene oxide is a compound of carbon, oxygen, and hydrogen in variable ratios. It can be synthesized by exfoliating layered graphite oxide (graphite with strong oxidizers) [11,12]. Graphene oxide does not require functionalization as it consists of graphene sheets with hydroxyl, carboxyl, and epoxide groups. Reduced-graphene oxide can be obtained as a powder form by reducing GO using several methods such as microwave, laser, electrochemical, or hydrazine vapor treatment.

1.2 Mathematical modeling

The problem of effective material properties and mechanical behavior of laminated composite structural members such as beams and plates has drawn a significant amount of attention over the last decades. A review of composite beam theories can be found in the book by Hodges [13]. The advent of advanced composite materials has been a strong stimulus for such developments. Moreover, their incorporation is likely to expand the use and capabilities of beam structures. The new and stringent requirements imposed on aeronautical/aerospace, turbomachinery and shaft structural systems will be best met by such new types of material structures. An intrinsic formulation developed by Hodges and his co-workers [14–16] covers anisotropic beams with large deformations and small strains. The approach, extracted from a three-dimensional elasticity formulation, provides two streams of analyses: one stream is concerned with the cross section, providing elastic constants that might be used in a suitable set of beam equations, and the other stream being the beam equations themselves. Thin-walled composite beams have been extensively investigated by Librescu and Song [17,18] and their co-workers, e.g. [19–24]. These authors developed and refined thin-walled beam models for an arbitrary, closed or open cross-section. A number of non-classical effects such as the anisotropy and heterogeneity of constituent materials, transverse shear, primary and secondary warping phenomena (Vlasov effect) are considered in their works, with the assumption that the cross-section is rigid in its own plane. In the analysis performed on rotating systems [17], the effects of the centrifugal and Coriolis forces were taken into account as well. Furthermore, the importance of shear effects in composite material was emphasized. The nonlinear response of multiscale nanocomposites beams and beam-type structures has also been investigated in the literature. Examples are: large amplitude free vibration [25], buckling and post buckling [26] and energy harvesting [27] analyses in piezoelectric two-phase nanocomposite beams.

1.3 Processing, manufacturing and characterization

A literature review reveals that there are two approaches to fabricate fiber reinforced polymer multiscale composites: a) by dispersing nanotubes within a polymeric matrix and, subsequently, impregnating the conventional fibers with this nanodispersed resin system, and b) incorporating nanotubes within fibers, followed by their impregnation with a pure matrix. In this dissertation, a novel low cost manufacturing method, combining surface treatment of fibers with matrix modification techniques, was devised to incorporate nanoparticles for the simultaneous reinforcement of matrix and fibers. A schematic of this approach is shown in Fig. 1-1.

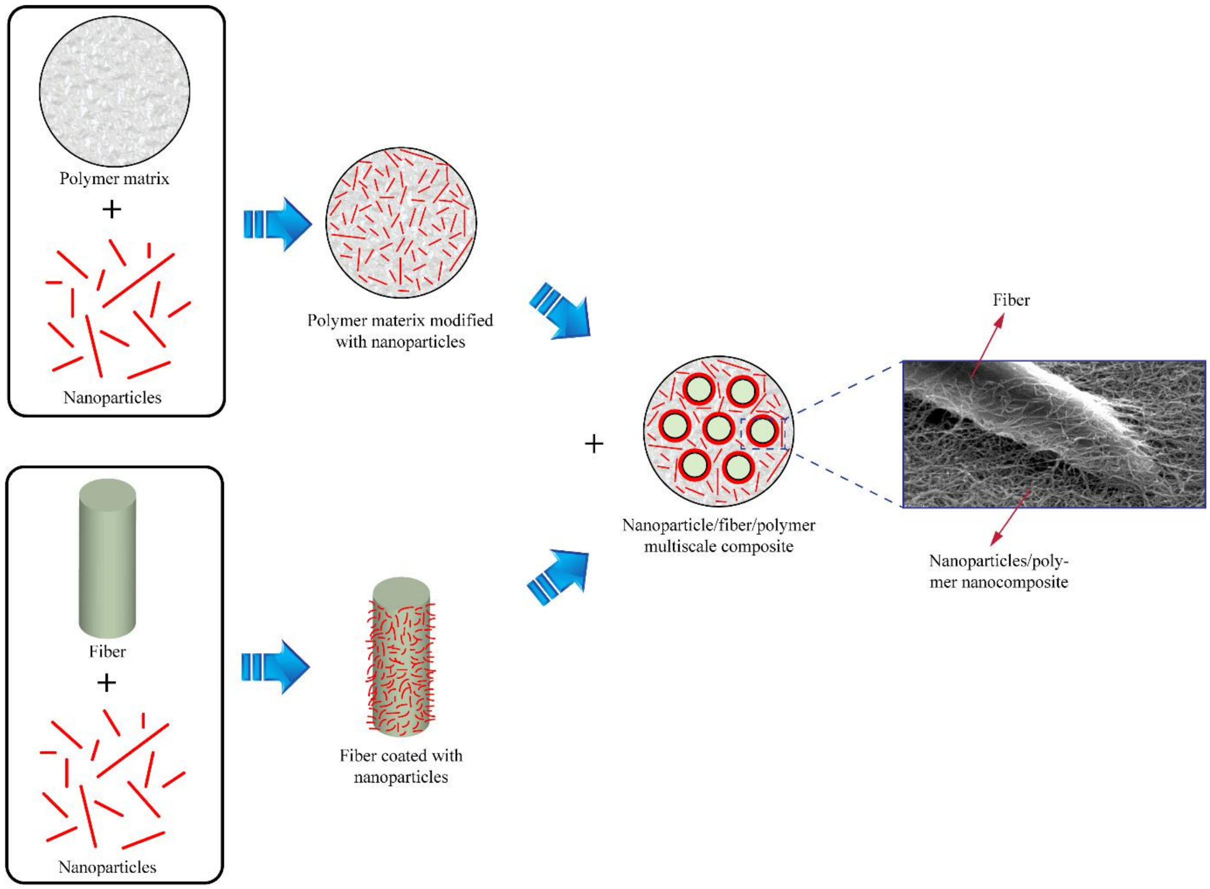

Fig. 1-1. New route to fabricate multiscale nanocomposites.

1.3.1 Processing and fabrication

Several graphene-based nanomaterials, including graphene oxide (GO) and its thermally reduced version (rGO), graphene nanoplatelets (GNPs), and multi-walled carbon nanotubes (MWCNTs) were employed to modify the epoxy matrix and the surface of glass fibers. Fig. 1-2 shows a general schematic of the method for the preparation of the multiscale nanocomposites.

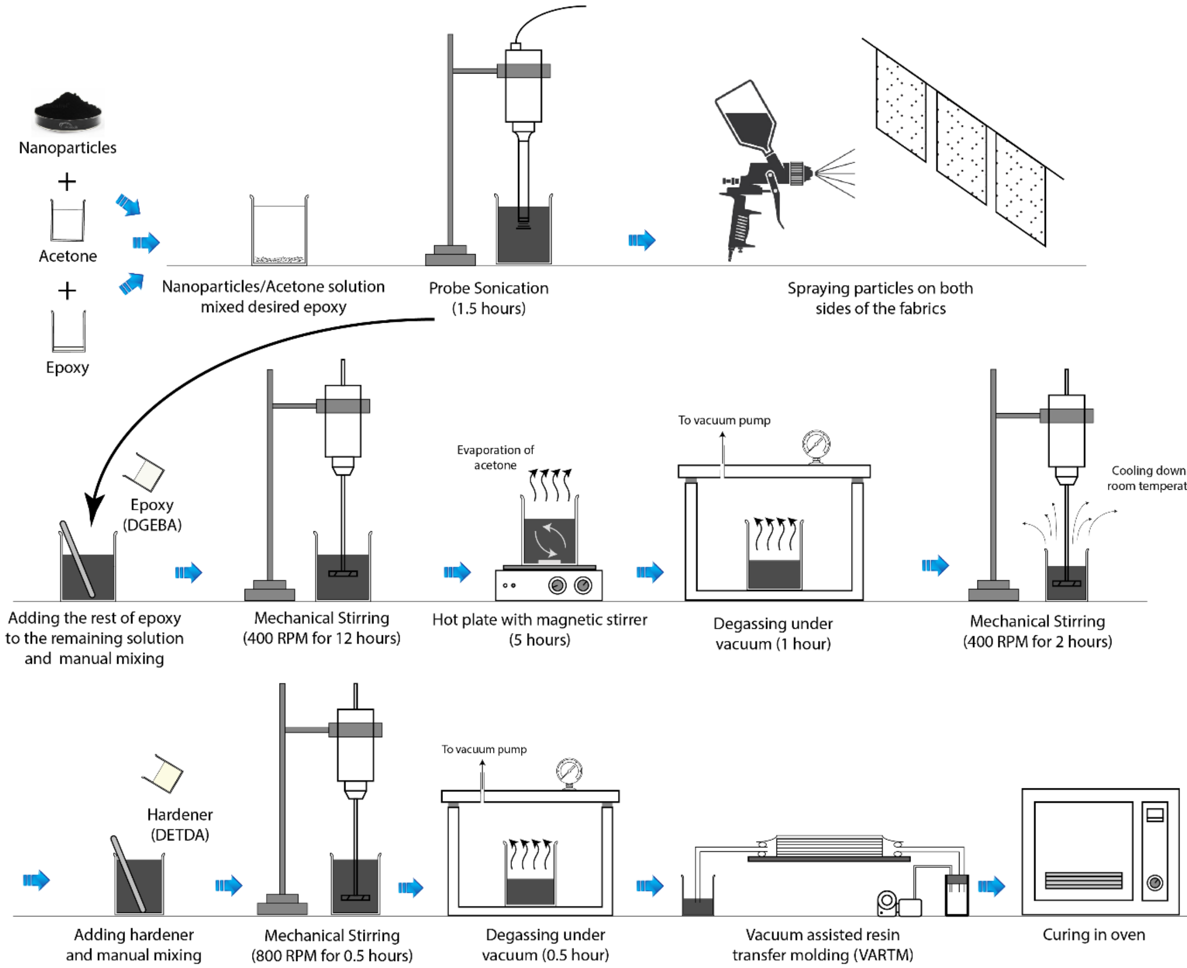

Fig. 1-2. Fabrication process of multiscale fiber glass/epoxy composites modified with graphene-based nanoparticles.

The vacuum assisted resin transfer molding (VARTM) method was used to manufacture multiscale composites (Fig. 1-3). VARTM is a composite manufacturing technique in which vacuum is used to draw a liquid resin through dry fibers that are laid on a flat surface. This technique was selected due to its flexibility and low tooling cost for large composite part manufacturing; it is successfully used for manufacturing nanocomposites. The mold tooling system typically consists of a solid open mold, flow distribution network (i.e., resin inflow gates, resin distribution medium layer, flow channels and vents (or vacuum ports)), a peel ply layer, and a vacuum bag. By utilizing the pressure difference between the environmental pressure and the vacuum pressure applied through the vent, the dry fabric encapsulated between the vacuum bag and the solid mold is compressed against the mold surface. Then, the resin is infused into the fabric due to the relatively higher pressure in the resin reservoir. A flow distribution medium layer is commonly applied on the top of the fabric to assist with the flow of resin across the flow distribution medium and simultaneously infusing into the preform in the thickness direction. Once the resin infusion is completed, one may close the resin inflow gate to allow the excess resin to be removed though the vent before the resin becomes too viscous to flow. The full cure cycle is then completed and the final part can be demolded.

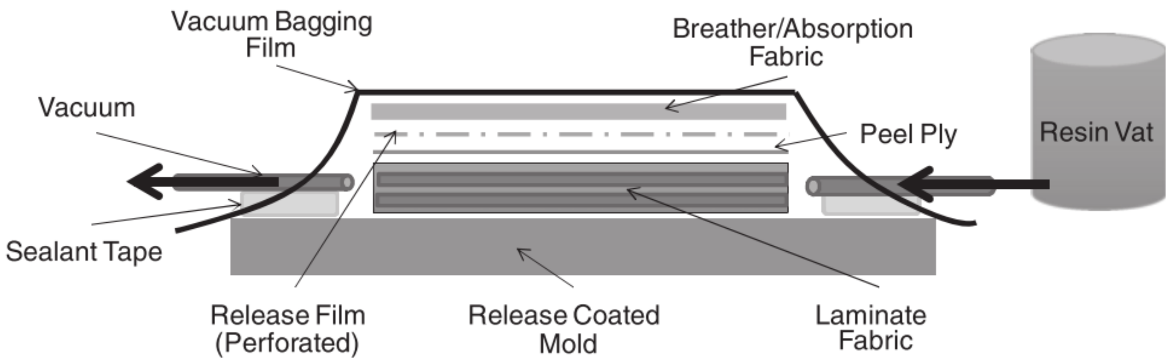

Fig. 1-3. Vacuum-assisted resin transfer molding (VARTM) lay-up illustration [6].

1.3.2 Characterization

The viscosity of the epoxy matrix containing carbon nanomaterials was measured using a rheometer. Additionally, the dispersion of carbon nanomaterials in the epoxy matrix before and after the curing reaction was analyzed by using an optical image analyzer, a scanning electron microscope (SEM) and a transmission electron microscopy (TEM). The mechanical and thermal properties of multiscale composites were studied in this dissertation. Mechanical characterization including tensile, bending, short beam shear, and vibration tests was carried out to investigate the effect of carbon nanomaterials on the mechanical properties of the multiscale composites.

1.4 Summary

The overall goal of this work was the modeling, processing, fabrication and characterization of carbon nanomaterials-reinforced polymer composites. Specifically, the dissertation is focused on the development of a multiscale material model that can predict the effective material properties of graphene-reinforced composites (Objective #1). The developed effective material properties were used to perform the analysis of the cross-section and then the global behaviors of nanocomposite beams and blades (Objective #2). Such nanocomposite materials were then manufactured using the low cost method of VARTM (Objective #3). Finally, extensive material characterizations were proposed to investigate the effect of carbon nanomaterials on the thermomechanical properties of multiscale nanocomposites.

This first chapter introduced the background information useful to understand the results that will be presented in the main body of this dissertation which includes seven chapters, each devoted to a single peer-reviewed publication.

A comprehensive review of previous studies on the subject of advanced composite materials and beam-type structures is presented in Chapter 2. The review addresses analytical, semi-analytical and numerical studies dealing with dynamical problems involving adaptive/smart/intelligent materials (e.g. piezoelectric materials, electrorheological fluids, shape memory alloys, etc.), damping and vibration control, advanced composite materials (e.g. functionally graded materials and nanocomposites), complicating effects and loadings (e.g. added mass, tapered beams, initial curve and twist, etc.), and experimental methods. In Chapter 3, a computational model is developed to study the nonlinear steady state static response and free vibrations of thin-walled carbon nanotubes/fiber/polymer laminated multiscale composite beams and blades. Chapter 4 addresses with the cross-sectional design and analysis of fiber-reinforced multiscale composite beams of general cross-sectional shape and arbitrary anisotropic material properties and investigates the effect of carbon nanotubes on their stiffness properties. In Chapter 5, a mathematical model is developed to predict the effective material properties of graphene nanoplatelets/fiber/polymer multiscale composites. The large deflection, post-buckling and free nonlinear vibration of graphene nanoplatelets-reinforced multiscale composite beams are studied through a theoretical analysis. The vibration and damping characteristics of epoxy composites reinforced by pristine and functionalized multi-walled carbon nanotubes are then investigated experimentally in Chapter 6 for potential use as integral passive damping elements in structural composite applications. In Chapter 7, a novel low cost manufacturing method, combining surface treatment of fibers with matrix modification techniques, is introduced to incorporate nanoparticles for the simultaneous reinforcement of matrix and fibers. The thermal conductivities of the epoxy/fiberglass/nanoparticle composites are studied through differential scanning calorimetry (DSC), thermo-gravimetric analysis (TGA) and thermal conductivity measurements.

References

[1] M. Rafiee, X.Q. He, S. Mareishi, K.M. Liew, Modeling and stress analysis of smart CNTs/fiber/polymer multiscale composite plates, Int. J. Appl. Mech. 6 (2014) 1450025. doi:10.1142/S1758825114500252.

[2] E.T. Thostenson, W.Z. Li, D.Z. Wang, Z.F. Ren, T.W. Chou, Carbon nanotube/carbon fiber hybrid multiscale composites, J. Appl. Phys. 91 (2002) 6034–6037. doi:10.1063/1.1466880.

[3] T.T. Ebbesen, T. W., Lezec H. J., Hiura H., Bennett J. W., Ghaemi H. F, Electrical conductivity of individual carbon nanotubes, Nature. 382 (1996) 54–56. doi:10.1038/382054a0.

[4] M. Rafiee, F. Nitzsche, M.R. Labrosse, Modeling and mechanical analysis of multiscale fiber-reinforced graphene composites : Nonlinear bending , thermal post-buckling and large amplitude vibration, Int. J. Non. Linear. Mech. 103 (2018) 104–111. doi:10.1016/j.ijnonlinmec.2018.05.004.

[5] G.V. Seretis, G. Kouzilos, D.E. Manolakos, C.G. Provatidis, On the graphene nanoplatelets reinforcement of hand lay-up glass fabric/epoxy laminated composites, Compos. Part B Eng. 118 (2017) 26–32. doi:10.1016/j.compositesb.2017.03.015.

[6] M.C.L. McCrary-Dennis, O.I. Okoli, A review of multiscale composite manufacturing and challenges, J. Reinf. Plast. Compos. 31 (2012) 1687–1711. doi:10.1177/0731684412456612.

[7] D. Verma, P.C. Gope, A. Shandilya, A. Gupta, Mechanical-Thermal-Electrical and Morphological Properties of Graphene Reinforced Polymer Composites: A Review, Trans. Indian Inst. Met. 67 (2014) 803–816. doi:10.1007/s12666-014-0408-5.

[8] M. Rafiee, F. Nitzsche, M.R. Labrosse, Effect of functionalization of carbon nanotubes on vibration and damping characteristics of epoxy nanocomposites, Polym. Test. 69 (2018) 385–395.

[9] I. Mutlay, L.B. Tudoran, Percolation behavior of electrically conductive graphene nanoplatelets/polymer nanocomposites: Theory and experiment, Fullerenes Nanotub. Carbon Nanostructures. 22 (2014) 413–433. doi:10.1080/1536383X.2012.684186.

[10] F. Wang, L.T. Drzal, Y. Qin, Z. Huang, Mechanical properties and thermal conductivity of graphene nanoplatelet/epoxy composites, J. Mater. Sci. 50 (2014) 1082–1093. doi:10.1007/s10853-014-8665-6.

[11] F. Perrozzi, S. Prezioso, L. Ottaviano, Graphene oxide: from fundamentals to applications, J. Phys. Condens. Matter. 27 (2015) 013002. doi:10.1088/0953-8984/27/1/013002.

[12] R.M. Larsen, E.A. Jensen, Epoxy-graphite oxide nanocomposites: Mechanical properties, J. Appl. Polym. Sci. 133 (2016) 4–11. doi:10.1002/app.43591.

[13] D.H. Hodges, Nonlinear Composite Beam Thery, AIAA, 2006. doi:10.1243/0954410041872861.

[14] D.H. Hodges, A mixed variational formulation based on exact intrinsic equations for dynamics of moving beams, Int. J. Solids Struct. 26 (1990) 1253–1273.

[15] W. Yu, V. Volovoi, D.H. Hodges, X. Hong, Validation of the variational asymptotic beam sectional analysis, AIAA J. 40 (2002) 2105–2112. doi:10.2514/3.15301.

[16] D.H. Hodges, Nonlinear Composite Beam Theory, 2006.

[17] O. Song, L. Librescu, Structural Modeling and Free Vibration Analysis of Rotating Composite Thin-Walled Beams, J. Am. Helicopter Soc. 42 (1997) 358. doi:10.4050/JAHS.42.358.

[18] L. Librescu, O. Song, Thin-walled composite beams: theory and application, Springer Science & Business Media, Netherlands, 2005. doi:10.1007/1-4020-4203-5.

[19] S.-Y. Oh, O. Song, L. Librescu, Effects of pretwist and presetting on coupled bending vibrations of rotating thin-walled composite beams, Int. J. Solids Struct. 40 (2003) 1203–1224. doi:10.1016/S0020-7683(02)00605-4.

[20] S.-Y. Oh, L. Librescu, O. Song, Thermoelastic Modeling and Vibration of Functionally Graded Thin-Walled Rotating Blades, AIAA J. 41 (2003) 2051–2061. doi:10.2514/2.1897.

[21] L. Librescu, S.Y. Oh, O. Song, H.S. Kang, Dynamics of advanced rotating blades made of functionally graded materials and operating in a high-temperature field, J. Eng. Math. 61 (2008) 1–16. doi:10.1007/s10665-007-9155-5.

[22] S. Na, G.-C. Yoon, B.-H. Lee, P. Marzocca, L. Librescu, Dynamic Response Control of

Rotating Composite Booms Under Solar Radiation, J. Therm. Stress. 32 (2008) 21–40. doi:10.1080/01495730802540205.

[23] O. Song, L. Librescu, S.-Y. Oh, Dynamics of pretwisted rotating thin-walled beams operating in a temperature environment, J. Therm. Stress. 24 (2001) 255–279. doi:10.1080/014957301300006407.

[24] S. Na, L. Librescu, H. Jung, Dynamics and active bending vibration control of turbomachinery rotating blades featuring temperature-dependent material properties, J. Therm. Stress. 27 (2004) 625–644. doi:10.1080/01495730490466219.

[25] M. Rafiee, J. Yang, S. Kitipornchai, Large amplitude vibration of carbon nanotube reinforced functionally graded composite beams with piezoelectric layers, Compos. Struct. 96 (2013) 716–725.

[26] M. Rafiee, J. Yang, S. Kitipornchai, Thermal bifurcation buckling of piezoelectric carbon nanotube reinforced composite beams, Comput. Math. with Appl. 66 (2013) 1147–1160. doi:10.1016/j.camwa.2013.04.031.

[27] X.Q. He, M. Rafiee, S. Mareishi, Nonlinear dynamics of piezoelectric nanocomposite energy harvesters under parametric resonance, Nonlinear Dyn. 79 (2014) 1863–1880. doi:10.1007/s11071-014-1780-8.

Chapter 2

2. Dynamics, vibration and control of rotating composite beams and blades: A critical review

as published* in Thin-Walled Structures 119 (2017) 795–819

https://doi.org/10.1016/j.tws.2017.06.018

*In accordance with University of Ottawa regulations, the contact email address has been removed from this article.

Foreword

This chapter provides a comprehensive review of scholarly published articles about rotating composite beams and blades. The review addresses analytical, semi-analytical and numerical studies dealing with dynamical problems involving adaptive/smart/intelligent materials (e.g. piezoelectric materials, electrorheological fluids, shape memory alloys, etc.), damping and vibration control, advanced composite materials (e.g. functionally graded materials and nanocomposites), complicating effects and loadings (e.g. added mass, tapered beams, initial curve and twist, etc.), and experimental methods. Moreover, the influence of Vlasov or restrained warping, out-of-plane warping, transverse shear, arbitrary cross-sectional geometry, trapeze phenomena, swept tip, size-dependent effect, as well as other areas that have been considered in research, were reviewed in depth. The chapter concludes with a presentation of the remaining challenges and future research needs.

Thin-Walled Structures 119 (2017) 795–819

Contents lists available at ScienceDirect

Thin-Walled Structures

journal homepage: www.elsevier.com/locate/tws

Review

Dynamics, vibration and control of rotating composite beams and blades: A critical review

M. Rafiee[a,*], F. Nitzsche[b], M. Labrosse[a]

[a] Department of Mechanical Engineering, University of Ottawa, 161 Louis Pasteur, Ottawa, ON, Canada K1N 6N5
[b] Department of Mechanical and Aerospace Engineering, Carleton University, 1125 Colonel By Drive, Ottawa, ON, Canada K1S 5B6

ARTICLE INFO

Keywords:
Rotating thin-walled beams
Composite rotor blades
Review
Dynamics
Vibration
Control

ABSTRACT

Rotating composite beams and blades have a wide range of applications in various engineering structures such as wind turbines, industrial fans, and steam turbines. Therefore, proper understanding of such structures is of a great importance. As a result, the behavior of rotating composite beam structures has received a lot of attention. This paper presents a comprehensive review of scholarly articles about rotating composite beams as published in the past decades. The review addresses analytical, semi-analytical and numerical studies dealing with dynamical problems involving adaptive/smart/intelligent materials (e.g. piezoelectric materials, electrorheological fluids, shape memory alloys, etc.), damping and vibration control, advanced composite materials (e.g. functionally graded materials and nanocomposites), complicating effects and loadings (e.g. added mass, tapered beams, initial curve and twist, etc.), and experimental methods. Moreover, the influence of Vlasov or restrained warping, out-of-plane warping, transverse shear, arbitrary cross-sectional geometry, trapeze phenomena, swept tip, size-dependent effect, as well as other areas that have been considered in research, are reviewed in depth. The review concludes with a presentation of the remaining challenges and future research needs.

1. Introduction

Over the last few decades, rotating beams and blades made of composite materials have been increasingly used in a variety of industrial areas due to their high stiffness and strength-to-weight ratios, long fatigue life, resistance to electrochemical corrosion, and other superior material properties of composites. The advantages of composite materials, coupled with the ability to tailor their designs to specific purposes, have given them a competitive edge when compared with normal engineering materials and led to their extensive use in rotary applications. Therefore, a thorough understanding of their structural dynamic behavior is required.

The number of research articles pertaining to various structural dynamics and vibration control aspects of rotating composite beams and blades, as published in English language Science Citation Index (SCI) journals, have steadily increased since 1990, as shown in Fig. 1. In response to the growing interest in this area, the present article aims to present a comprehensive review of the state-of-the-art. However, to limit the scope of the review, the emphasis has only been placed on the vibrations, dynamics and control aspects of rotating beams and blades. Publications directly related to other aspects of rotating composite beams and blades, such as damage mechanics and structural health monitoring, static bending, deflection and torsional analyses, cross-section design and optimization, have been excluded from this review.

Some surveys of structural dynamics and vibration suppression of rotating composite beams and blades can be found elsewhere. Review articles [1–3] covered much of the research done on the rotor blades dynamic characteristics and strategies for vibration reduction prior to the early 1990s. It should be mentioned that journal papers and books [4–9] treated some review aspects of composite rotor blades dynamics. However, to the best of the authors' knowledge, there has not been a comprehensive review of the structural dynamics and vibration control of rotating composite beams and blades in the literature.

In this review, the beam theories for rotating composite beams and blades that have emerged from prior research efforts are summarized first. Then, analytical, semi-analytical and numerical methods are comprehensively reviewed. Adaptive/smart/intelligent rotating composite beams, and damping and vibration control of such structures will be presented next. The application of advanced composite materials such as functionally graded materials and nanocomposites on the rotating beams will be discussed. Complicating effects, including the effect of tip mass, nonuniform

* Corresponding author.
E-mail addresses:

http://dx.doi.org/10.1016/j.tws.2017.06.018
Received 5 January 2017; Received in revised form 12 April 2017; Accepted 17 June 2017

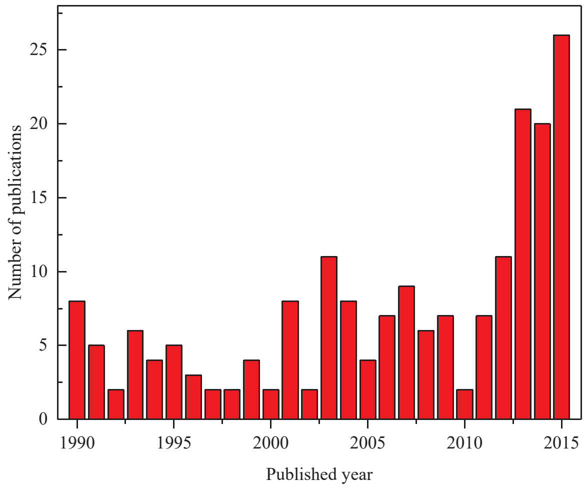

Fig. 1. Recent English language Science Citation Index journal papers directly related to structural dynamics and vibration control of rotating beams and blades made of composite materials.

cross-section, initial curvature/twist, swept tip, and size-dependent properties on the dynamics and vibration reduction of rotating composite beams will be addressed. Attention will also be given to experimental studies in the last section. The paper will conclude with recommendations for future research directions.

It should be noted that, in this review, multiple citations might be observed for a publication. For instance, a paper in which both a numerical model and an experimental study are presented will be cited in the "Numerical approaches" as well as the "Experimental investigations" sections.

2. Beam theories

Beams are three dimensional (3D) bodies in which one dimension is large compared to the other two. According to the current state-of-the-art, the theoretical framework around composite rotating beams and blades is quite advanced. The models based on 3D Finite Element Analysis (FEA) possess significant computational advantages. However, beam or one-dimensional (1D) models play an important role in structural analysis because they have smaller dimensionality and provide the designer with simple tools to analyze numerous problems. One-dimensional beam models can be investigated using classical or refined theories (See Fig. 2) in both

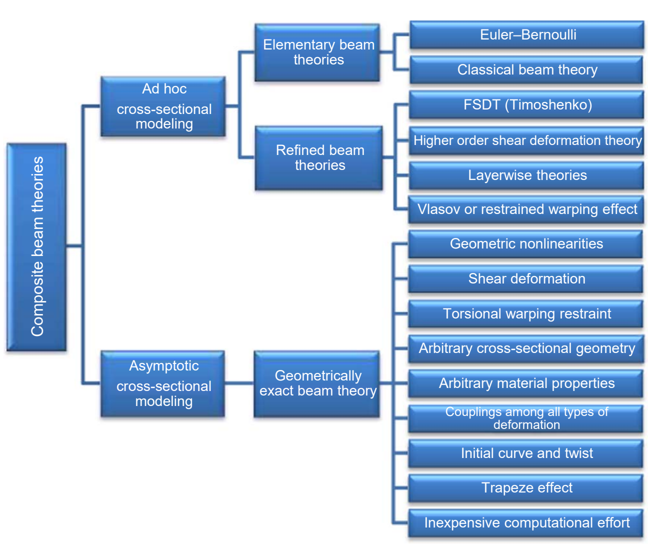

Fig. 2. Composite beam theories.

geometrically linear and nonlinear regimes that feature different levels of accuracy to evaluate the static and dynamic characteristics. An extensive discussion of various linear beam theories can be found in [10].

2.1. Elementary beam theories

2.1.1. Euler–Bernoulli beam theory (EBBT)

The Euler–Bernoulli beam theory (EBBT) is the most elementary one; it underestimates deflections and overestimates the natural frequencies because it disregards the transverse shear deformation and rotary inertia effects. The Euler-Bernoulli assumptions are: 1) The cross-section is infinitely rigid in its own plane; 2) the cross-section of a beam remains plane after deformation; 3) the cross-section remains normal to the deformed axis of the beam [11]. These assumptions are usually reasonably justified for isotropic homogeneous slender beams featuring simple cross-sections; however, they become questionable for beams of complex geometry made of general anisotropic, heterogeneous materials, such as composite rotor blades, especially at higher frequency. The shearing forces may be approximated as the derivatives of bending moments. Approximate bending and shear stresses may be recovered over a cross section.

Let us assume that u, v, and w are the elastic displacements of a point along x, y, and z-axes, respectively (right-hand axes system). The x-axis is aligned with the neutral axis of the beam (longitudinal direction), the y-axis is along the width of the beam (lateral direction), and the z-axis is aligned along the thickness direction (transverse direction). For such a beam, the Euler-Bernoulli approximation of axial displacement and strain can be defined as

$$u(x, z) = u_0(x) + z\phi_x(x), \quad w(x, z) = w_0(x), \tag{1a}$$

$$\varepsilon_x(x, z) = \varepsilon_0(x) - z\left(-\frac{\partial \phi_x(x)}{\partial x}\right), \tag{1b}$$

where $u_0(x)$ and $w_0(x)$ are longitudinal and vertical displacements at the neutral axis and $\phi_x(x)$ is the rotation of the transverse normal about the y-axis cane defined as $-\partial w(x)/\partial x$ and $\partial \phi_x(x)/\partial x$ is the bending curvature. The axial strain at the neutral axis can be defined as $\varepsilon_{x0}(x) = \partial u_0(x)/\partial x$ and $\varepsilon_{x0}(x) = \partial u_0(x)/\partial x + 1/2(\partial w_0(x)/\partial x)^2$ in geometrically linear and nonlinear (von-Kármán hypothesis) regimes, respectively.

2.1.2. Classical beam theory (CBT)

If the beam is twisted, the cross section will be warped and cannot remain plane after deformation in general. For this reason, Saint Venant relaxed the second Euler-Bernoulli assumption and derived the classical beam theory to recover the shear stresses that contribute to the torsional moment. Fig. 3 depicts the concept of different types of warpings associated with the Saint Venant theory of torsion (free warpings). Fig. 4 shows the influence of warping on the tip twist of bending-torsion coupled symmetric lay-up cantilever box-beams subjected to a unit tip torque. For composite beams, because of anisotropy, asymmetry of the cross-section, and non-uniform distribution of Poisson's ratio over the cross-section, all stresses and strains other than the ones along the span of the beam are non-zero. Hence, in-plane and out-of-plane warpings need to be known in order to obtain accurate structural stiffness values and account for 3D stress effects [12,13].

2.2. Refined beam theories

The most significant difference between the classical and refined beam theories is the inclusion of transverse shear deformation on the predicted bending deflections and natural frequencies. Fig. 5 shows a typical result for the effect of shear deformation on modeling of a composite box beam. These results clearly demonstrate

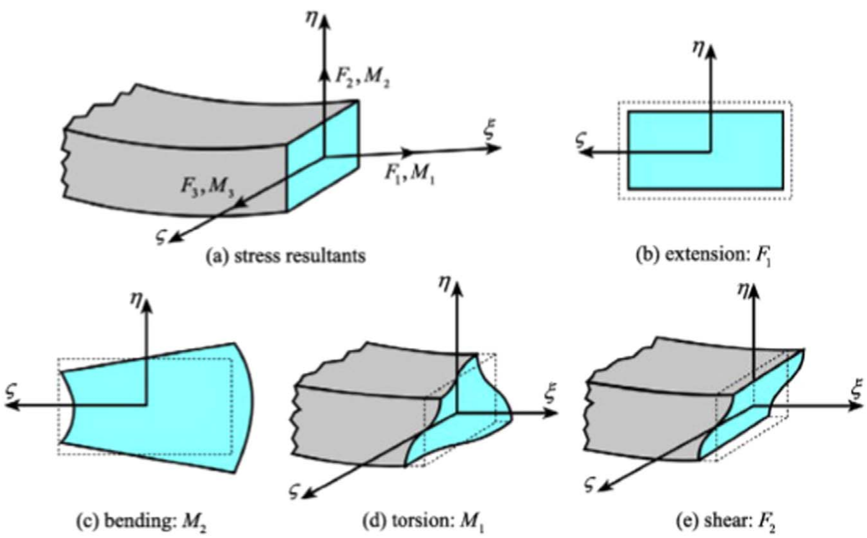

Fig. 3. Major types of cross-sectional warpings of a beam: (a) six stress resultants, (b) extension-induced in-plane warping, (c) bending-induced warping, (d) torsion-induced out-of-plane warping, and (e) shear-induced out-of-plane warping [230].

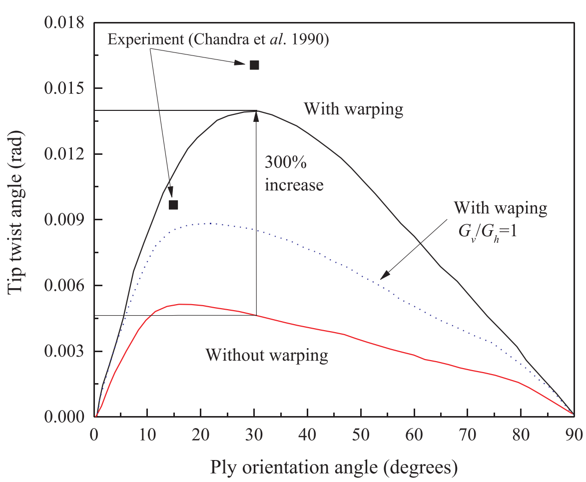

Fig. 4. Influence of warping on the tip twist of bending-torsion coupled symmetric lay-up (top and bottom $(\theta)_6$, sides $(\theta/\text{-}\theta)_3$) cantilever box-beams subjected to a unit tip torque (G_h and G_v are the effective inplane shear stiffnesses for horizontal and vertical walls of the box section, respectively) [53].

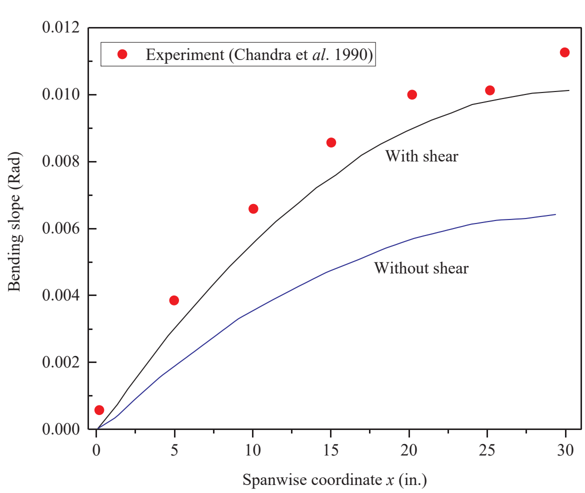

Fig. 5. Experimentally measured and analytically predicted spanwise bending slopes of $(13)_6$ anti-symmetric layup box-beams with aspect ratio of $L/d=56$ [53].

how elementary theories underpredict the bending of a typical composite box beam.

2.2.1. First order shear deformation theory (FSDT)

The next theory in the hierarchy of beam theories is the Timoshenko beam theory, or first order shear deformation theory, that includes refined effects such as rotary inertia and shear deformation [14]. The Timoshenko model is a major improvement for non-slender beams and for high-frequency responses where shear or rotary effects are not negligible. Since the FSDT violates the zero shear stress conditions on the top and bottom surfaces of the beam, a shear correction factor is required to account for the discrepancy between the actual stress state and the assumed constant stress state. This shear correction factor depends not only on the material and geometric parameters, but also on the loading and boundary conditions [15].

For the Timoshenko theory, the general form of axial and bending displacements are same as Eq. (1) with $\phi_x = \partial u(x)/\partial z$ as an independent variable. Thus, we require three variables (u_0,w, φ_x) to determine the strain at any point, where

$$\begin{Bmatrix} \varepsilon_x(x,z) \\ \gamma_{zx}(x,z) \end{Bmatrix} = \begin{Bmatrix} \varepsilon_{x0}(x) \\ \gamma_{zx0}(x,z) \end{Bmatrix} - z\begin{Bmatrix} -\frac{\partial \phi_x(x)}{\partial x} \\ 0 \end{Bmatrix}, \tag{2}$$

The shear strain at the neutral axis can be defined as $\gamma_{zx0}(x) = \partial w(x)/\partial x + \phi_x$ for both geometrically linear and nonlinear regimes.

2.2.2. Higher-order shear deformation theory (HSDT)

Timoshenko's theory fails to account for changes in shear strains due to the variation of material properties of each layer and has limitations when applied to composite beams. A number of theories have been proposed where a non-uniform shear stress distribution is taken into account. These limitations of CBT and FSDT, and the need for better predictions of the response of composite beams, led to the development of higher order shear deformation theories. Notable among them are the third-order theory [15,16], the sinusoidal theory [17], the hyperbolic theory [18], the exponential theory [19], and the unified formulation of Carrera [20]. These higher order shear deformation theories do not need the use of a shear correction factor.

The displacement field equations for the beam using higher order shear deformation theory ([16,21]) at any point through the thickness are presented by:

$$u(x, z) = u_0(x) + z\phi_x(x) - \frac{4}{3h^2}z^3\left[\phi_x + \frac{\partial w}{\partial x}\right], \quad w(x, z) = w_0(x), \tag{3a}$$

$$\begin{Bmatrix} \varepsilon_x(x, z) \\ \gamma_{zx}(x, z) \end{Bmatrix} = \begin{Bmatrix} \varepsilon_{x0}(x) \\ \gamma_{zx0}(x, z) \end{Bmatrix} - z\begin{Bmatrix} -\frac{\partial \phi_x(x)}{\partial x} \\ 0 \end{Bmatrix} - z^2\frac{4}{h^2}\begin{Bmatrix} \frac{z}{3}\left(\frac{\partial \phi_x(x)}{\partial x} + \frac{\partial^2 w(x)}{\partial x^2}\right) \\ \phi_x(x) + \frac{\partial w(x)}{\partial x} \end{Bmatrix}, \tag{3b}$$

2.2.3. Layerwise theories

Previously discussed classical and refined beam theories amount to replacing the heterogeneous laminate with a statically equivalent (in the integral sense), single, homogeneous layer namely called equivalent single layer (ESL) theories. To study the behavior of laminates at the global or laminate level, ESL theories provide simple and computationally inexpensive solutions. However, these theories suffer from a lack of accuracy when the behavior of laminates at the ply level or fiber/matrix level is intended, and they do not satisfy interlaminar equilibria for transverse shear. For an accurate calculation of local stresses at the level of individual laminae, and for thick laminated beams, more refined theories are necessary. Layer wise shear–deformable theory (LWSDT) [22,23], for instance, can capture these effects but increases the number of degrees of freedom. In this theory, the laminate is divided into a number of sublayers that are perfectly bonded. In each layer, the in-plane displacement is assumed to be piece-wise linear along the z direction. The beam displacements for the k^{th} ply are given by

$$u^{(k)}(x, z) = u_0^{(k)}(x) + z\phi_x^{(k)}(x), \quad w^{(k)}(x, z) = w_0(x), \tag{4}$$

where $\phi_x^{(k)}$ represents the rotations of the cross section of the kth layer. Note that for the case of a single-layer laminate, this layer-wise formulation reduces to FSDT. Even though the strains are assumed uniform in each layer, there is a variation from layer to layer.

$$\begin{Bmatrix} \varepsilon_x^{(k)}(x, z) \\ \gamma_{zx}^{(k)}(x, z) \end{Bmatrix} = \begin{Bmatrix} \varepsilon_{x0}^{(k)}(x) \\ \gamma_{zx0}^{(k)}(x, z) \end{Bmatrix} - z\begin{Bmatrix} -\frac{\partial \phi_x^{(k)}(x)}{\partial x} \\ 0 \end{Bmatrix}, \tag{5}$$

2.2.4. Vlasov or restrained warping effect

Restrained warping was introduced by V.Z. Vlasov in the context of a torsion theory [24]. This theory is also called “warping torsion” or “non-uniform torsion” while the torsion theory of Saint Venant is called “circulatory torsion” or “uniform torsion”. In the theory of Vlasov, the specific torsion is not constant along the axis of the beam span. The effect of restrained warping is particularly important for beams with thin-walled, open cross sections [5]. Fig. 6 depicts the influence of restrained warping on the frequencies of composite I-beams. Fig. 6a shows the effect of restrained warping on the torsional frequencies of graphite-epoxy I-beams for different slenderness ratios. Fig. 6b demonstrates the effect of constrained warping on the natural frequencies of a bending-torsion coupled graphite-epoxy I-beam. It can be observed that constrained warping increases the natural frequencies of torsion-related modes via an increase in torsional stiffness; the increase is larger for higher modes.

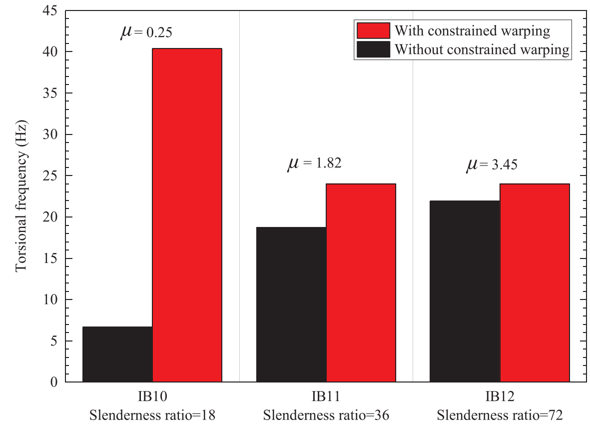

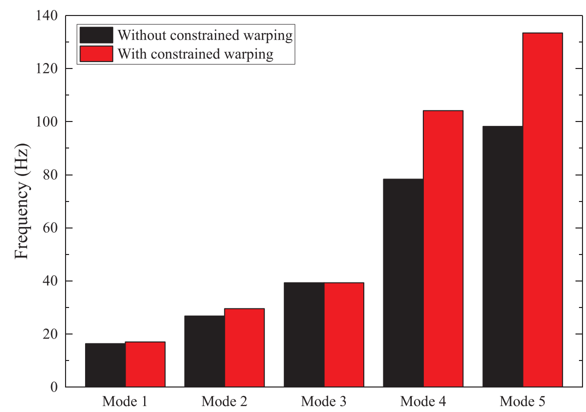

Fig. 6. Effect of restraint warping on a) Torsional frequencies of graphite-epoxy I-beams of different Slenderness ratios. b) natural frequencies of a bending-torsion coupled graphite- epoxy I-beam [221].

2.3. Adequate modeling of composite rotor blades

Composite rotor blades are generally complicated engineering structures and require adequate models for analysis. Such models should include at least the following characteristics: geometric and material nonlinearities, shear deformations, warping torsion, arbitrary cross-sectional geometry and material properties, initial curve and twist, trapeze effect and inexpensive computation. We describe each of these characteristics briefly in Table 1.

3. Analytical and semi-analytical approaches

Since beams have one dimension that is much larger than the other two, the warping deformations are much smaller than the deflections of the elastic axis. This enables the separation of the 3D problem into two parts: a 2D local deformation field of the cross-section that is used to calculate the section properties and a 1D global deformation field that is used to calculate the response of the blade. The cross-sectional properties can be obtained using either ad hoc assumptions or asymptotic methods. As detailed next, while the ad hoc models rely on assumptions about the displacement or stress field, the asymptotic methods take into account a number of small parameters [5].

3.1. Ad hoc modeling of cross-section

Most of the classical and refined beam theories use ad hoc assumptions or additions to simpler theories about the displacement field, and usually ignore shear deformation or warping displacements, or their couplings. These models can lead to serious errors [25,26]. It is sometimes challenging to adjust assumptions for new

Table 1
Composite rotor blades characteristics, challenges and solutions.

Characteristic	Problem/challenge	Solution/required model
Geometric nonlinearity	Bending slopes and twist in rotating composite blades are not sufficiently small for linear analysis (even at small strain) due to large axial force generated by the rotation of the rotor and the size of transverse deflections.	A geometrically nonlinear model to account for large deformations is required.
Material nonlinearity	The material nonlinearity in terms of plastic deformations might also occur and change the mechanical behavior.	A nonlinear model addressing at least an elasto-plastic or preferably visco-elasto-plastic behavior is required.
Shear deformation	CBT is not adequate in providing accurate solutions when the thickness-to-length ratio of the beam is relatively large. This is because the effect of transverse shear strains and rotary inertia, neglected in the classical theory, becomes significant in deep beams.	Shear deformation theories provide more accurate solutions than the classical theory.
Torsional warping restraint	This effect is particularly important for beams with thin-walled, open cross sections.	nonuniform warping takes into account the Vlasov effect of torsional warping restraint.
Arbitrary cross-sectional geometry	Modeling of rotor blades involves beams with arbitrary cross-sectional geometries	Therefore, the ability of a chosen beam theory to handle arbitrary cross-sectional geometries is of a great importance
Arbitrary material properties (anisotropy)	Composites are nonhomogeneous materials and as a whole might exhibit anisotropic behavior.	The model should be capable of taking arbitrary material properties into account.
Couplings among all types of deformation	Anisotropy can also be used to introduce elastic couplings between extension, torsion, bending and shear.	Theories for composite beams must be able to exhibit couplings among all types of deformation.
Initial curve and twist	Many composite rotor blades are initially twisted in their undeformed state and may be initially curved as well.	the theory should be able to model initially curved and/or twist rotor blades.
Size dependent analysis	Composite rotor blades can be used in micro/nano-electro-mechanical system (MEMS/NEMS) and atomic force microscopes (AFMs). Since the classical and refined elasticity theories do not include a material length scale, they are unable to account for the size effect.	a size-dependent continuum theory that can capture size effect is essential in the composite rotor blade model.
Trapeze effect	The trapeze effect is a coupling in beams between tension and torsion, resulting in an increase in effective torsional stiffness from axial tensile force [5].	To be accounted for in the beam constitutive law.
Centrifugal stiffening effect	It is known that the first 2–3 vibration modes are effected by centrifugal stiffening and the higher modes are primarily governed by flexural bending [237]. In particular, the fundamental mode shows a very strong influence of the centrifugal force which becomes very important for high speed rotating beams such as those used in turbomachinary [238].	Centrifugal stiffening effect is essential for accurate prediction of the fundamental mode in rotating beams as it shows a strong influence of rotational speed on the predominant mode of natural movement for a structure.[238–241]
Coriolis effect	In rotating beams, the assumption that the beam deforms only in bending is restrictive, since the coupling between the axial deformation and the lagwise motion can be significant (especially at high rotational speed) due to the Coriolis effects [64,122,242]. However, most studies neglected the Coriolis effects in the literature.	In order to take into account this coupling the introduction of the Coriolis force becomes mandatory.
Inexpensive computational effort	3D finite element models are computationally expensive. Computational inefficiency is a concern in multidisciplinary design and optimization where sufficient accuracy is needed as quickly as possible.	A general purpose composite rotor blade theory should have relatively few degrees of freedom and little complexity.

configurations. Therefore, they might not be appropriate for problems with advanced cross-sectional geometry and/or non-homogeneous materials. Nevertheless, they are the most common theories used to model rotating composite beams in the literature.

Librescu and his coworkers [7,27–38] developed a refined beam theory [7,27] and studied several aspects of rotating composite beams. This refined beam theory [27] was first used to study the free vibration of thin-walled composite rotating beams with arbitrary closed cross-sections. A number of non-classical features, such as the anisotropy and heterogeneity of constituent materials, transverse shear, primary and secondary warpings and the effects of the centrifugal and Coriolis force fields, were included in their work. Main assumptions were as follow [7]:

(a) The displacements u and v in the x and y direction, respectively, are small and finite, while the twist φ of the cross-section can be arbitrarily large.
(b) The displacement w is much smaller than u or v so that products of the derivatives of w can be neglected in the strain-displacement relations.
(c) Strains are small so that a linear constitutive law can be used to relate the second Piola-Kirchhoff stress tensor to Green-Lagrange's strain tensor.
(d) The shape of the cross-section and all its geometrical dimensions remain invariant in its plane. This implies that the beam cross-sections are assumed rigid in their own planes (i.e. that $\varepsilon_{xx} = \varepsilon_{yy} = \varepsilon_{xy} = 0$), but are allowed to warp out of their original planes. For thin-walled beam structures (such as aircraft wings and fuselage and ship hulls), the original cross-sectional shape is maintained by a system of transverse stiffening members (ribs or bulkheads). These are considered rigid within their plane but perfectly flexible with regard to deformation normal to their own plane, so that the adoption of this assumption leads to a reasonable mathematical model for the actual physical behavior.
(e) The transverse shear strains are uniform over the beam cross-section, and
(f) The ratio of the wall thickness to the radius of curvature at any point of the beam wall is negligibly small compared to unity. It is evident that this assumption is actually exact for prismatic thin-walled beams composed of linear segments, and very accurate for shallow curved surfaces as well.

By using Hamilton's variational principle of the 3D elasticity theory, the equations of motion of rotating elastic blades can be expressed in terms of displacement quantities as [7]

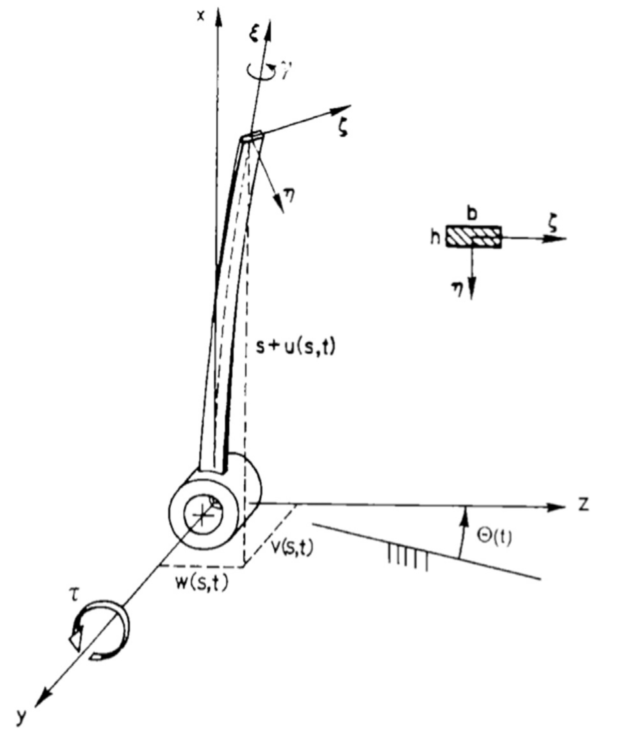

Fig. 7. Reference frame x-y-z and local coordinate system $\xi-\eta-\zeta$ which is a local frame fixed on the cross-section [49].

$$
\begin{aligned}
\delta u_P \; : \;\; & (T_z(u_P' + \phi'(y_P\cos\phi + x_P\sin\phi)))' \\
& + ((Q_x - M_x\phi')\cos\phi - (Q_y - M_y\phi')\sin\phi)' \\
& - B_1\ddot{u}_P + B_3(\ddot{\phi}\sin\phi + \phi^2\cos\phi) \\
& + B_2(\ddot{\phi}\cos\phi - \phi^2\sin\phi) + p_x + \delta_0\hat{p}_x = 0, \\
\delta v_P \; : \;\; & (T_z(v_P' + \phi'(y_P\sin\phi - x_P\cos\phi)))' \\
& + ((Q_y + M_y\phi')\cos\phi - (Q_x - M_x\phi')\sin\phi)' \\
& - B_1\ddot{v}_P - B_3(\ddot{\phi}\cos\phi - \phi^2\sin\phi) + B_2(\ddot{\phi}\sin\phi + \phi^2\cos\phi) \\
& + p_y + \delta_0\hat{p}_y = 0, \\
\delta w_0 \; : \;\; & T_z' - (B_1\ddot{w}_0 + B_{11}(\delta_t\ddot{\theta}_x + \delta_e T) + B_{12}(\delta_t\ddot{\theta}_y + \delta_e S) - B_7\ddot{\phi}') \\
& + p_z + \delta_0\hat{p}_z = 0, \\
\delta\theta_x \; : \;\; & M_x' - Q_y - (B_{11}\ddot{w}_0 + B_{13}(\delta_t\ddot{\theta}_x + \delta_e T) + B_{15}(\delta_t\ddot{\theta}_y + \delta_e S) - B_8\ddot{\phi}') \\
& + m_x + \delta_0\hat{m}_x = 0, \\
\delta\theta_y \; : \;\; & M_y' - Q_x - (B_{12}\ddot{w}_0 + B_{15}(\delta_t\ddot{\theta}_x + \delta_e T) + B_{14}(\delta_t\ddot{\theta}_y + \delta_e S) - B_9\ddot{\phi}') \\
& + m_y + \delta_0\hat{m}_y = 0, \\
\delta\phi \; : \;\; & (T_z((u_P'y_P - v_P'x_P)\cos\phi + (u_P'x_P + v_P'y_P)\sin\phi))' \\
& - T_z\phi'((u_P'x_P + v_P'y_P)\cos\phi + (-u_P'y_P + v_P'x_P)\sin\phi) \\
& - ((u_P'M_x - v_P'M_y)\cos\phi + (u_P'M_y + v_P'M_x)\sin\phi) \\
& + (\cos\phi(M_x v_P'\phi' + M_y u_P'\phi' + Q_y u_P' - Q_x v_P') \\
& + \cos\phi(M_x v_P'\phi' + M_y u_P'\phi' + Q_y u_P' - Q_x v_P') \\
& + \sin\phi(-M_x u_P'\phi' + M_y v_P'\phi' + Q_y v_P' - Q_x u_P')) + \delta_r B_\omega'' + (\Lambda_z\phi')' \\
& + M_z' - (B_3\ddot{v}_P - B_2\ddot{u}_P + (B_4 + B_5)(\ddot{\phi}\cos\phi - \phi^2\sin\phi))\cos\phi \\
& + (B_2\ddot{v}_P + B_3\ddot{u}_P - (B_4 + B_5)(\ddot{\phi}\sin\phi + \phi^2\cos\phi))\sin\phi \\
& - (B_7\ddot{w}_0 + B_8(\delta_t\ddot{\theta}_x + \delta_e T) + B_9(\delta_t\ddot{\theta}_y + \delta_e S) - B_{10}\ddot{\phi}')' \\
& + m_z\cos\phi + \lambda_T\sin\phi + m_\omega' + \delta_0(\hat{m}_z\cos\phi + \hat{\lambda}_T\sin\phi + \hat{m}_\omega') = 0.
\end{aligned} \tag{6}
$$

u_p, v_p and w_0 are displacement components of the beam axis in x, y and z directions, θ_p, θ_p and ϕ are rigid body rotations about the x, y axis and the twist about the z-axis, T_z, Q_x, and Q_y denote the axial and shear forces (in the x and y directions), M_x, M_y, and M_z, and B_ω denote the moments (about the x, y, and z-axes), and the bimoment global quantities, respectively. Here $p_x(z, t)$, $p_y(z, t)$, $p_z(z, t)$, $m_x(z, t)$, $m_y(z, t)$, $m_z(z, t)$, $\lambda_T(z, t)$, $m_\omega(z, t)$ and their counterparts identified by a circumflex represent equivalent line loads due to the effective external and body forces and couples, measured per unit span of the undeformed beam, and due to the tractions on the longitudinal edges of an open cross-section beam, respectively. The tracer δ_i takes the values 0 or 1 depending on whether the beam has closed or open cross-section, respectively. Boundary conditions, and all other terms appearing in Eq. (6) were defined in Ref. [7].

This refined beam theory [22] was a basis for much of Librescu's later research. For instance, it was extended to account for carrying a tip mass and incorporating adaptive capabilities using a system of piezoactuators with further application to vibration control [28]. In another study, the effects of a steady temperature gradient on a rotating pre-twisted composite beam were investigated [31]. Validations of these works against experimental, analytical, or numerical predictions, obtained within other thin-walled beam models, were provided in a publication co-authored by Qin and Librescu [30]. The effect of active feedback control [29], was also taken into account by Librescu and his coworkers using higher-order shear formulation [32], flapping-lagging-transverse shear coupling, ply-angle, pre-twist and presetting [35], forced vibration [33], functionally graded materials for tapered beams [34,39], blast loading [37] and solar radiation thermal loading [38]. This line of research served as a basis for many other works [38,40–48].

Pai and Nayfeh [49–51] generalized the set of 3D nonlinear equations derived by Crespo da Silva and Glynn [52] to study the free and forced extensional-flexural-flexural-torsional vibration of rotating nonuniform composite beams. By using the Newton's second law, they developed the nonlinear equations describing the extensional-flexural-flexural-torsional vibrations of slewing or rotating metallic and composite beams as follows:

$$
\begin{aligned}
m\ddot{u} + \mu_0\dot{u} &= G_u' + m(-\ddot{\Theta}w + \dot{\Theta}^2(s+u) - 2\dot{\Theta}\dot{w}) + (j_\eta\ddot{\Theta}w')', \\
m\ddot{v} + \mu_1\dot{v} &= G_v' + ((j_\eta - j_\xi)(\dot{\Theta}\dot{\gamma} + \dot{\Theta}^2 v') + j_\eta\ddot{\Theta}\gamma - j_\zeta(\dot{\Theta}\gamma)^{\cdot})', \\
m\ddot{w} + \mu_2\dot{w} &= G_w' + m(\ddot{\Theta}(s+u) + \dot{\Theta}^2 w + 2\dot{\Theta}\dot{u}) + \ddot{\Theta}(j_\eta u' - j_\eta)', \\
j_\xi\ddot{\gamma} + \mu_3\dot{\gamma} &= G_\gamma' - j_\xi(\ddot{\Theta}\left(v' - u'v' - u'^2v' - \frac{1}{2}v'^3 - \frac{1}{2}v'w'^2\right) \\
&\quad + \dot{\Theta}\left(\dot{v}' - u'\dot{v}' - \dot{u}'v' + u'^2\dot{v}' + 2\dot{u}'u'v' - \frac{3}{2}\dot{v}'v'^2\right. \\
&\quad \left.\left. - \frac{1}{2}\dot{v}'w'^2 - v'w'\dot{w}'\right)\right) + (j_\eta - j_\zeta)(\dot{\Theta}^2(-\gamma \\
&\quad + \int_0^s (v''w' + 2u'v'w'' \\
&\quad \left. + u''v'w'\right)\mathrm{d}s + \gamma v'^2 + \frac{2}{3}\gamma^3 - v'w'\Big) \\
&\quad + \dot{\Theta}(\dot{v}' - u'\dot{v}' - \dot{u}'v' + u'^2\dot{v}' + 2\dot{u}'u'v' - \frac{3}{2}\dot{v}'v'^2 \\
&\quad \frac{1}{2}\dot{v}'w'^2 - 2\gamma^2\dot{v}' + 2\gamma\dot{w}' - 2\gamma u'\dot{w}' - 2\gamma\dot{u}'w' + v'w'\dot{w}'\Big)\Big).
\end{aligned} \tag{7}
$$

where $\xi-\eta-\zeta$ is the local coordinate system (See Fig. 7), m mass per unit length, $u(s, t)$, $v(s, t)$, and $w(s, t)$ are the components of the elastic displacement vector of the centroid at an arbitrary location s, along the inertial axes x, y, and z, and j_ξ, j_η, and j_ζ are the rotary intertias per unit length of the beam, and all other terms are defined in Pai and Nayfeh [49].

The equations derived by Pai and Nayfeh [49] contain structural coupling terms and quadratic and cubic nonlinearities due to curvature and inertia. Pai and Nayfeh [49] investigate the response of an inextensional, symmetric angle-ply graphite-epoxy beam exhibiting bending-twisting coupling and a two-to-one internal resonance subjected to a harmonic base-excitation along the flapwise direction. In their second paper, Pai and Nayfeh [50] used a combination of the fundamental-matrix method and the method of multiple scales to derive four first-order ordinary-differential equations to describe the time variation of the amplitudes and phases of the interacting modes with damping, nonlinearity, and resonances. Hopf bifurcations, symmetry-breaking bifurcations, period-multiplying sequences, and chaotic solutions of the modulation equations were studied. The results showed that the motion could be nonplanar although the input force was planar. Their third paper [51] focused on the chordwise excitations of a symmetrically laminated graphite-epoxy composite beam.

Smith and Chopra [53] developed a direct analytical beam formulation for predicting the effective elastic stiffnesses and corresponding load deformation behavior of tailored composite box-beams. Using the displacement formulation, also called the stiffness formulation, Chandra and Chopra [54] studied the linear free vibration of rotating composite box beams theoretically and experimentally. The theoretical results were obtained using Galerkin's method. The stiffness formulation was based on suitable approximations to the displacement field of the shell wall. Since the displacement modes do not satisfy the equations of equilibrium of the shell wall, this approach leads to an overestimation of the beam stiffnesses. Chopra and his coworkers later developed a refined beam formulation for rotating composite beams with open- or closed-section. Their theory uses a mixed variational approach and accounts for the effects of elastic coupling, shell-wall thickness, warping, warping restraint, and transverse shear deformations. Their analysis was validated against experimental data and other analytical results [55,56].

Kim and Dugundji [57,58] studied the large amplitude free vibration and aeroelastic behavior of composite helicopter blades for rotating [58] and nonrotating [57] cases. Their model includes transverse shear and warping deformation; it is based on the Euler angle formulation of the basic large deflection equations together with the harmonic balance, finite difference, and Newton- Raphson technique. They indicated that the nonlinear stall is dominant at moderate amplitudes, but that nonlinear static-dynamic couplings in the structure, which bring a softening effect into the general aeroelastic behavior, could be equally important at large amplitudes.

The Euler-Bernoulli beam theory was used in a number of studies including free vibration of rotating FGM beams for linear [59,60] and nonlinear [61] analyses, nonlinear free vibration of laminated composite beams [62], vibration damping using embedded carbon nanotubes (CNTs) [63], transient response of a multilayered composite rotating airfoil [64] and free vibration of the rotating composite beams with a delamination [65].

In the past few years, the Timoshenko beam theory was also extensively used to study rotating composite beams, especially in the context of linear [65–77] and nonlinear [78,79] free vibration of rotating composite beams of made of either laminated composites [65–68,71,72,74,78,79] or FGMs [69,70,73,75–77].

The ad hoc cross-sectional analyses are not generally applicable to all types of rotating composite blades. They generally invoke assumptions that do not hold in the general case. Some of these assumptions are: ignoring the hoop stress or hoop moment, or ignoring shell bending measures.

3.2. Asymptotic modeling of cross-section

As reported by Atilgan and Hodges [80], Berdichevskii [81] appears to be the first to split a 3D geometrically nonlinear elasticity analysis for beam-like structures into a nonlinear 1D analysis and a (usually) linear 2D analysis, leading to the determination of the cross-sectional stiffness constants. Analytical analyses are available for simple geometries, however, arbitrary cross-sections require numerical analysis such as FEA. One of the most common FEA-based tools is the Variational Asymptotic Beam Section (VABS)[82–84].

In response to the quest for a theory adequate for rotor blade analysis, Hodges and his coworkers developed theoretical foundations for the analysis of rotating anisotropic composite beams based on the variational asymptotic method (VAM) [5,8,12,80,82,83,85–92]. The methodology presented by Hodges and his coworkers includes most of the characteristics explained in Table 1 for composite rotor blades, except the material nonlinearity and small scale size-dependent modeling. Providing an accurate cross-sectional analysis, strain and stress recovery [91], this approach yields geometrically exact canonical equations of motion for beams [5].

The nonlinear, intrinsic, mixed equations for the dynamics of a general (nonuniform, twisted, curved, anisotropic) beam undergoing small strains and large deformations can be written as follows based on the generalized Timoshenko beam model [5]:

$$\mathbf{F}' + (\widetilde{\mathbf{k}} + \widetilde{\kappa})\mathbf{F} + \mathbf{f} = \dot{\mathbf{P}} + \widetilde{\mathbf{\Omega}}\mathbf{P} \tag{8a}$$

$$\mathbf{M}' + (\widetilde{\mathbf{k}} + \widetilde{\kappa})\mathbf{M} + (\widetilde{\mathbf{e}}_1 + \widetilde{\gamma})\mathbf{F} + \mathbf{m} = \dot{\mathbf{H}} + \widetilde{\mathbf{\Omega}}\mathbf{H} + \widetilde{\mathbf{V}}\mathbf{P} \tag{8b}$$

$$\mathbf{V}' + (\widetilde{\mathbf{k}} + \widetilde{\kappa})\mathbf{V} + (\widetilde{\mathbf{e}}_1 + \widetilde{\gamma})\mathbf{\Omega} = \dot{\gamma} \tag{8c}$$

$$\mathbf{\Omega}' + (\widetilde{\mathbf{k}} + \widetilde{\kappa})\mathbf{\Omega} = \dot{\kappa} \tag{8d}$$

where the prime denotes the partial derivative with respect to the undeformed beam reference line defined by curvilinear coordinate x, the over dot denotes the partial derivative with respect to time t; and internal forces $\mathbf{F} = [F_1\ F_2\ F_3]^{\mathrm{T}}$, internal moments $\mathbf{M} = [M_1\ M_2\ M_3]^{\mathrm{T}}$, generalized force strains $\gamma = [\gamma_{11}\ 2\gamma_{12}\ 2\gamma_{13}]^{\mathrm{T}}$, generalized moment strains $\boldsymbol{\kappa} = [\kappa_1\ \kappa_2\ \kappa_3]^{\mathrm{T}}$, generalized curvatures $\mathbf{K} = [K_1\ K_2\ K_3]^{\mathrm{T}}$, linear momentums $\mathbf{P} = [P_1\ P_2\ P_3]^{\mathrm{T}}$, angular momentums $\mathbf{H} = [H_1\ H_2\ H_3]^{\mathrm{T}}$, linear velocities $\mathbf{V} = [V_1\ V_2\ V_3]^{\mathrm{T}}$, angular velocities $\Omega = [\ \Omega_1\ \Omega_2\ \Omega_3]^{\mathrm{T}}$, and external forces $\mathbf{f} = [f_1\ f_2\ f_3]^{\mathrm{T}}$; and external moments $\mathbf{m} = [m_1\ m_2\ m_3]^{\mathrm{T}}$; γ_{11} is the extensional strain measure, and $2\gamma_{12}$ and $2\gamma_{13}$ are the transverse shear measures; and, finally, the tilde over certain terms denotes a skew-symmetric matrix (pseudovector) of the components of the column matrix of the same name, namely,

$$\widetilde{\mathbf{K}} = \widetilde{\mathbf{k}} + \widetilde{\kappa} = \begin{bmatrix} 0 & -K_3 & K_2 \\ K_3 & 0 & -K_1 \\ -K_2 & K_1 & 0 \end{bmatrix}. \tag{9}$$

All measure numbers are calculated in the deformed cross-sectional frame. $\mathbf{k} = [k_1\ k_2\ k_3]^{\mathrm{T}}$; k_1 is the initial twist, k_2 and k_3 are the initial curvatures of the beam, and $\mathbf{e}_1 = [1\ 0\ 0]^{\mathrm{T}}$. For given boundary conditions, Eqs. (8) may be solved using semi-analytical methods such as the Galerkin method [93–96] or numerical methods such as the finite difference method [9,97,98] or the generalized differential quadrature method [99].

To ensure that the prediction of elastic constants from a cross-sectional analysis based on ad hoc assumptions is correct, it has to be asymptotically correct in terms of a small parameter [5]. Berdichevsky et al. [100] developed a variationally and asymptotically consistent theory to derive the governing equations for anisotropic thin-walled beams with closed sections. Their theory is aymptotically correct to the first order. This theory was further extended by Armanios and Badir [101] to the free vibration analysis of anisotropic thin-walled closed-section beams using Hamilton's principle. These derivations have become the underlying basis for the work of some researchers [102–105]. The applicability of these analytical models is limited to simple geometries and conceptual models such as those used in preliminary design.

Many researchers extended the research done by Hodges [12,86] to study the dynamics and vibration control of rotating composite beams. For instance, Traugott et al. [106] developed a set of nonlinear, intrinsic equations describing the dynamics of beam structures undergoing large deformations of active helicopters blade. Their active structural model could be coupled with a suitable aerodynamic model for aeroelastic simulation and aeroelastic control design. Ghorashi and Nitzsche [97] studied the nonlinear dynamic response of an accelerating composite rotor blade using perturbations. In another study, Ghorashi [98] also investigated the elasto-dynamic response of a rotating articulated blade. He used the linear VAM cross-sectional analysis, together with an improved damped nonlinear model for the rigid-body motion analysis of helicopter blades in coupled flap and lead-lag motions.

Patil and Althoff [93] presented an energy-consistent, Galerkin approach for the nonlinear dynamics of beams using intrinsic equations. The Galerkin approach gives accurate results with fewer degrees of freedom as compared to low-order finite-element formulation. Their reduced-order model is able to capture the dominant nonlinearities in the system and would be ideal for aeroelasticity, preliminary design, and control synthesis. Some researchers used this approach to study the control design [94], forced vibration [96], bifurcation analysis [107] and the steady state response and free vibration [95] of rotating composite beams. The later work focused on the application of CNTs-reinforced composites in rotating composite beams and blades.

4. Numerical approaches

The most extensively used numerical technique for modeling the dynamics and vibration control of rotating composite beams is the finite element method (FEM). The continuum in FEM is divided into a finite number of non-over-lapping regions called elements. The equilibrium requirements of each element are specified in terms of a finite number of state variables. The final solution of the entire system is obtained by assembling the results of the individual elements. To date, the most comprehensive and accurate finite element modeling of composite rotor blades seems to be the work of Hodges et al. [92] known as RCAS (Rotorcraft Comprehensive Analysis System), Yu and Blair [108] known as GEBT (Geometrically Exact Beam Theory), Bauchau [109] known as DYMORE and Johnson [110] known as CAMRAD II. Their formulations are based on a rigorous, asymptotic approximation of three-dimensional, geometrically nonlinear, anisotropic elasticity. The concept of VAM of splitting the original 3D analysis into a 2D cross-sectional analysis and 1D beam analysis was employed in RCAS, GEBT and DYMORE for nonlinear analysis. The computer program VABS was used for determining the cross-sectional elastic constants. General beam analysis procedure of RCAS and GEBT are shown in Figs. 8 and 9.

Many finite elements for the analysis of rotating composite beams have been proposed. For convenience in this review, we grouped the main developments in FE for rotating composite beams into the three following categories.

4.1. Line elements

Most of the FE research lies in this category. The number of works based on the classical beam theories is limited in the literature [65,111–116]. Linear free vibrations of rotating electrorheological (ER) composite beams composed of three layers with ER fluids sandwiched between two elastic layers were studied by Wei et al. [111]. They used a two-node element and each node has four degrees of freedom. Their results indicated that the ER materials layer have a significant effect on

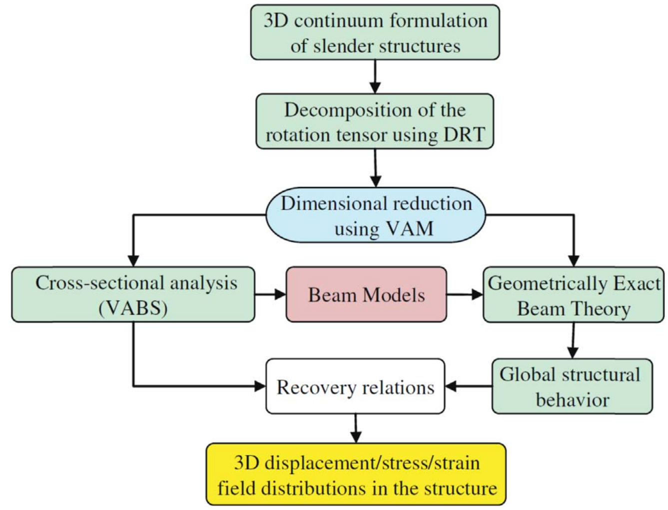

Fig. 9. Beam analysis procedure using GEBT [108].

the vibration suppression of rotating composite beam when subjected to an electric field. Their work was an underlying basis for some other researchers. For instance, it led to the analysis of variable speed and acceleration [112], the application of functionally graded materials [115] and the optimal parameters estimation [116] in composite beams. A two-noded element was used by Zarrinzadeh et al. [113] to study the free vibration of rotating, axially functionally graded tapered beams. Deepak et al. [114] developed a comparative study between carbon nanotubes-reinforced polymer composite beams and laminated composite beams using spectral finite elements.

While the number of investigations of the vibration behavior of rotating composite beams using classical theories has been limited, the majority of FEA research paid more attention to shear deformable line elements. Most investigated linear free vibrations [117–123]; however, forced vibrations [124,125] were also considered. Nonlinear vibrations [92,108,126–128], vibration attenuation [119,128–130], and dynamic stability [121,131–133] were also reported on in the literature. Epps and Chandra [134] developed a finite element model to correlate the results with their experimental model for vibration of rotating composite helicopter blades with swept tips.

Lee and Kim [135] developed a FE formulation that allows arbitrary warping for isotropic beams of complicated cross section, taper, and twist. In their formulation, a shear-flexible beam was used with a small warping displacement superimposed over the cross-sections in the deformed configuration. This work was further extended to the FE modeling of thin-walled composite beams [136], large deflections or finite rotations using the fixed or total Lagrangian descriptions [137], and vibrations of rotating and non-rotating composite beams [138]. Jeon and Lee [139] presented an FE approach using a large-deflection-type beam theory for the aeroelastic analysis of composite rotor blades in

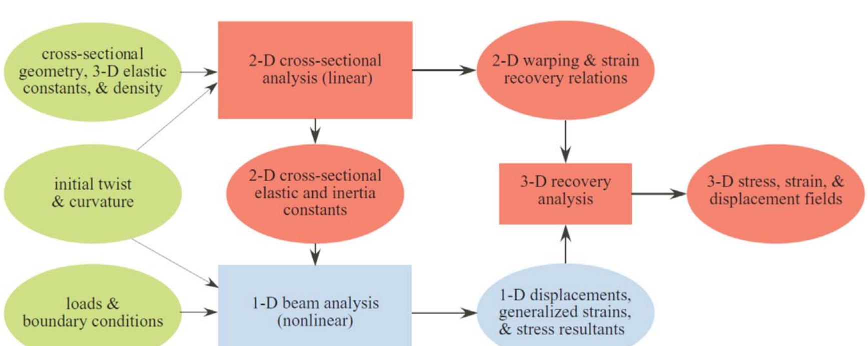

Fig. 8. Beam analysis procedure using RCAS [92].

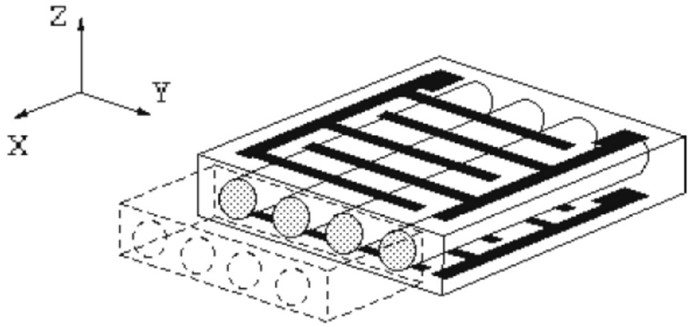

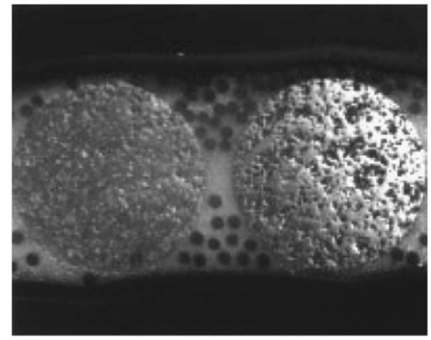

Fig. 10. Left: General configuration of Active Fiber Composite, Right: SEM photo of the cross section of AFC [103].

forward flight. Their composite rotor blade was idealized as a laminated thin-walled box beam and effective 6×6 elastic constants were obtained from the refined cross-sectional FE method.

4.2. Surface elements

Another approach to the modeling of rotating composite beams and blades consists in using surface elements such as plane or shell [140–142] elements. Kee and Kim [140] investigated the vibration characteristics of initially twisted rotating shell type composite blades. The blade was assumed to be a moderately thick open cylindrical shell that included the transverse shear deformation and rotary inertia, and was oriented arbitrarily with respect to the axis of rotation to consider the effects of disc radius and setting angle. Using an isoparametric nine-node of a degenerated shell element with the Reissner–Mindlin's assumptions, the FE method was used for solving the governing equations. Lin and Tsai [141] used a geometrically nonlinear degenerate shell element [143] to study the free vibration characteristics of a composite marine propeller blade. In their research, rotational effects and added mass were considered and composites with symmetric, balanced and unbalanced stacking sequences were analyzed. Their analysis indicated that the natural frequency of the blade in water was much lower than in air, and the mode shapes of the blade were almost the same in air as in water. They also concluded that the rotational effects can be ignored because the marine propeller rotates slowly. Very recently, Qiu and Xu [142] investigated the vibration control of a rotating two-connected flexible beam using chattering-free sliding mode controllers. Four-node rectangular plate elements were adopted to analyze the model of the rotating two-connected flexible beam by using the FEM.

4.3. Solid elements

The 3D solid-based finite element formulations may be chosen for their accuracy and robustness in large deformation nonlinear analyses of rotating composite beams. However, the number of studies using 3D solid elements is very limited. Three-dimensional finite elements were applied by Chattopadhyay et al. [144] to study the vibration reduction in rotor blades using active composite box beam including both in-plane and out-of-plane warpings. Kee and Shin [145] developed an eighteen-node solid-shell finite element to model the geometrically nonlinear blade structures. The incremental total Lagrangian approach was adopted to allow estimations on arbitrarily large rotations and displacements. The resulting nonlinear equilibrium equations were solved by applying the Newton-Raphson method combined with load control. The obtained numerical results were compared to several benchmark problems, and the results showed a good correlation with the experimental data and other FE analysis results.

5. Adaptive/smart/intelligent structures

Intelligent or smart or adaptive structures are a subset of active structures that have highly distributed actuator and sensor systems with structural functionality; in addition, they feature a distributed control function and computing architecture [146,147]. Some authors defined each of these terms distinctly [147,148]. A review of the state of the art about smart actuators, sensors, and integrated systems has been presented by Chopra [149]. Ganguli et al. [150] investigated the concepts of active trailing edge flap and active twist rotor blade for the helicopter vibration reduction problem.

Different types of adaptive materials for composite rotor blades have been described in the literature, such as piezoelectric materials, electrorheological fluids, and shape memory alloys. These materials are discussed and reviewed in below.

5.1. Piezoelectric materials

One of the most well-known type of adaptive materials is piezoceramics. Many actuators, accelerometers and other sensors are made of piezoceramics. However, monolithic piezoelectric materials (such as lead zirconate titanate: PZT) are brittle in nature, which makes them vulnerable to damage. Besides, their conformation to curved surfaces can be problematic. To overcome these drawbacks, piezoelectric fiber based sensors and actuators such as active fiber composites (AFC) [151], macro fiber composites (MFC) [152] and piezoelectric fiber reinforced composite (PFRC) [153] have been introduced. AFCs utilize interdigitated electrode poling and piezoelectric fibers embedded in an epoxy matrix (See Fig. 10), resulting in a high-performance actuator laminate. The disadvantages of AFCs are cost, difficulty of processing and handling during fabrication, and high voltage requirement. MFCs are also composed of piezoelectric fibers organized together in an epoxy matrix and interfaced with polyimide electrodes [154] (See Fig. 11). The major benefits of MFCs are the orthotropic and anisotropic actuation capabilities,which allow more independent and direct control of twist, bending, and extension [148]. Some authors used piezoelectric materials and their composites as an additional layer or patch to the structure in absence of sensing or actuation [54,68,97,103,104,124,125,134,155].

5.2. Electrorheological (ER) fluids

ER fluids are smart materials whose rheological properties can be rapidly varied when subjected to an electrical field. Working principle of ER fluids is shown in Fig. 12. These unusual properties enable ER fluids to be used in numerous potential engineering applications. For the application of rotating composite beams, Wei and his coworkers investigated the dynamic response [111] and vibration control [111,112,120] of rotating ER sandwich beams. The results of numerical simulations showed that the model loss factor of rotating ER beam can be substantially increased when an electric field is applied. The ER

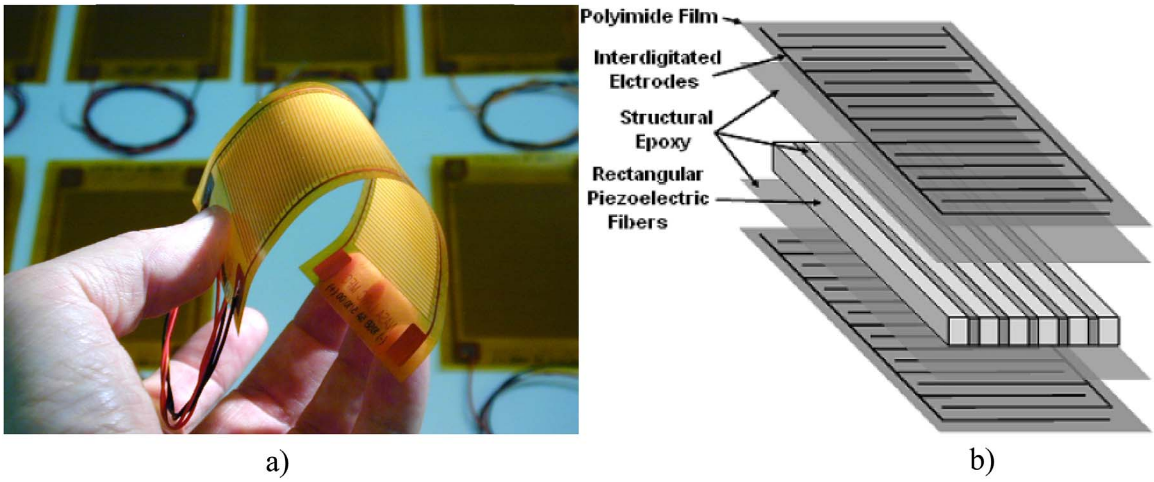

Fig. 11. MFC actuator: a) photo [231] and b) schematic [232].

materials had a significant effect on the vibration suppression of the rotating composite beam. Allahverdizadeh and his coworkers extended these investigations to the application of functionally graded [115] and optimal viscoelastic layer identification [116].

5.3. Shape memory alloys (SMAs)

Shape-memory alloys can remember their original shapes to the effect that they can return to their pre-deformed shapes when heated. Singh et al. [156] developed the design, analysis, and testing of an improved SMA-based tracking tab actuator. This actuator provided in-flight tracking capability for a helicopter rotor to attenuate the vibration due to rotor dissimilarities. Their theoretical model of the actuator was developed based on Brinson's thermomechanical model, and was used to predict the behavior of the actuator under external loading. It was further applied as a design tool to identify optimal actuator parameters. The modeling and free vibration behavior of rotating composite thin-walled closed-section beams with SMA fibers was also presented by Yongsheng et al. [102].

6. Damping and vibration control

Vibration in rotating beams and blades arises from a variety of sources and leads to damage of structural components and inefficiency of the systems. Consequently, vibration reduction strategies in rotating composite blades have received considerable attention. Commonly used methods to suppress vibrations are active, passive, semi-active and hybrid vibration control systems. However, for the application of rotating beams and blades, active and semi active methods seem to be the most common ones.

6.1. Active vibration control

Friedmann and Millot [3] presented a survey of the state of the art for the vibration reduction in rotorcraft using active controls. They described higher harmonic control, individual blade control, vibration reduction using an actively controlled flap located on the blade, and active control of structural response. Giurgiutiu [157] reviewed the smart-materials actuation solutions for the aeroelastic and vibration control. Alkhatib and Golnaraghi [158] provided a review of active vibration control techniques, with examples from mechanical to civil engineering applications. A concise review of the active control approaches for vibration reduction in rotorcraft was also presented by Friedmann [159]. The hierarchy of active control approaches for helicopter vibration suppression is illustrated in Fig. 13. It is worth noting that both Higher Harmonic Control (HHC) and pitch link actuated Individual Blade Control (IBC) are based upon the idea of oscillating the whole helicopter blade at its root with fairly high frequencies. For hingeless and bearingless rotor configurations, however, vibration reduction using smart materials such as Actively Controlled Flaps (ACF) and Active Twist Rotor (ATR) are logical.

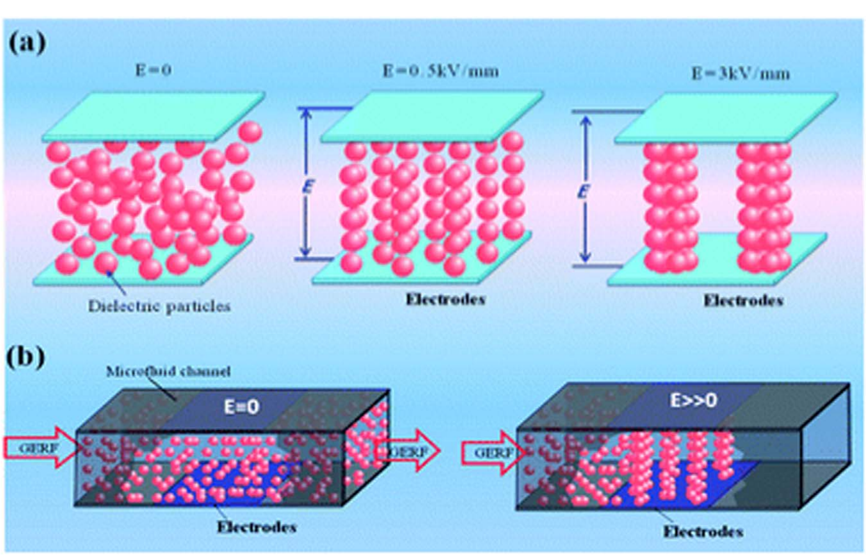

Fig. 12. Working principle of ER fluids. a) ER is fluid like when no electric field is applied and becomes solid like when an electric field is applied. b) in case of no electric field keeps flowing and solidifies when the electric field is applied on ER fluid by embedded parallel plate electrodes [233].

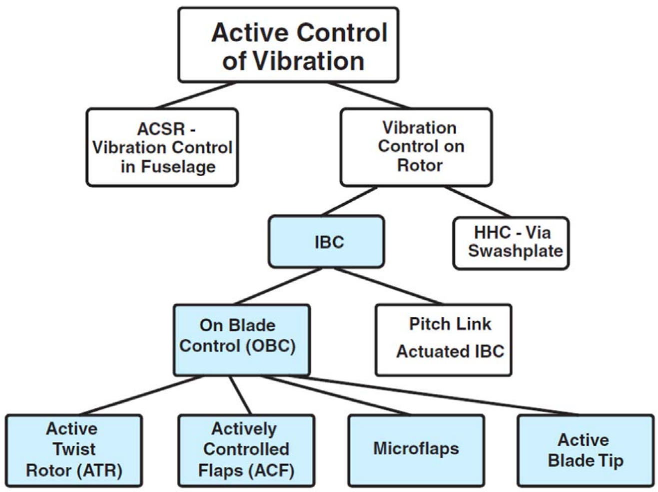

Fig. 13. Hierarchy of active control approaches in rotorcraft [159].

6.1.1. PID Control

Proportional-integral-derivative (PID) control has been widely used in rotating beam applications [28,29,37,41,119,128–130,144,160–162]. The PID controller attempts to minimize the error over time by adjustment of a control variable $u(t)$, such as the position or velocity of the midpoint of the cross section of the beam at a distance from the root of the beam, to a new value determined by a weighted sum:

$$u(t) = K_p e(t) + K_i \int_0^t e(\tau) d\tau + K_d \frac{de(t)}{dt}, . \tag{10}$$

where K_P, K_i and K_d, all non-negative, denote the coefficients for the proportional, integral, and derivative terms, respectively.

Song and Librescu [28] used a combined velocity and acceleration feedback control law relating the piezoelectrically induced bending moment at the beam tip with the kinematical response quantities to investigate its beneficial effects upon the closed-loop eigenvibration characteristics. Librescu and his coworkers [37] implemented the velocity feedback control to control the free and forced vibration of rotating beams of nonuniform cross section, operating in a temperature field and impacted by a blast. Vibration control methodology was based on the piezoelectric strain actuation. The results revealed, in both cases of existence and nonexistence of temperature field, that the control appeared very efficient. In another work, Song et al. [29] adopted two feedback control law strategies namely the proportional control law and the velocity control to reduce the vibration of pretwisted rotating anisotropic thin-walled beams. The results revealed that proportional feedback control strategy does not provide any substantial advantage compared to velocity feedback control. In addition, with that control methodology, there is no possibility to induce damping. Using a velocity feedback control law Shim and Na [163] developed a structural dynamic model of rotating composite beam of tapered cross-sections and assessed the effect of the taper ratio. The control was achieved through the piezoelectrically-induced flapwise bending moments at the tip of the beam. The obtained results revealed that, via this control capability, it was possible to conveniently tune the eigenfrequencies of the system, and consequently, to modify in a beneficial and predictable way the dynamic response characteristics of the structure.

Chattopadhyay et al. [144] studied the vibration reduction in rotor blades using active composite box beams. Their model was used to investigate the reductions in hub dynamic loads using closed-loop control. In the closed loop analysis, feedback actuator voltage was defined with the help of the current developed from the electric charge. A finite element formulation was used to implement the coupled theory. Vibration reduction up to 50% was achieved in vertical shear force for a typical case. The control results were also compared with and without the application of closed-loop control. It was observed that the convergence of collective flap fundamental response with time was faster with closed-loop damping.

As discussed earlier, to overcome the drawbacks of monolithic piezoelectric materials, piezoelectric fiber based sensors and actuators are attracting the attention of researchers. Numerous advantages of MFC sensors and actuators having over monolithic piezoelectric materials are discussed in the work of Park and Kim [164]. Using MFC actuators and monolithic piezoelectric sensors, Choi et al. [41,161] modeled a first-order shear deformation theory of rotating thin-walled beams. In their study, the negative velocity feedback control algorithm was used to suppress vibrations. Experimental study of vibration control of a rotating cantilevered beam using piezoactuators was also carried out by Choi and Han [160]. A constant amplitude controller was used in their study.

Thakkar and Ganguli [129] developed an active twist model by using induced-shear-based piezoceramic actuation to analyze the effect of piezoelectric material PZT-5H on vibration reduction of helicopter blades. An isotropic two-cell box beam with surface-bonded piezoelectric actuators was used to represent the cross-section of the blade. Such a blade was then studied in a forward flight condition and the reductions in vibration of the hub loads and moments due to induced shear actuation were investigated. A reduction of 51.4% in vibration was obtained by using the nonlinear law in the open loop case at an amplitude of 300 V mm^{-1} for the applied sinusoidal field. A closed loop algorithm was also developed based on the feedback of time rate of change of strain and hence calculating sensed voltage from the fed value, enabling actuation to the rotor blade. A reduction in overall vibration at the hub of approximately 43% was obtained for an advance ratio of 0.3.

Using a PID control law, Baz and Ro [119] demonstrated the vibration attenuation capabilities of actively controlled constrained layer damping (ACLD), an approach that will be detailed further in Section 6.3.1. The resonant vibration control of rotating beams was presented by Svendsen and Høgsberg [162]. Vibrations in their study were reduced by using a collocated sensor–actuator system governed by a resonant controller. The objective of the controller was to extract energy from the selected mode by imposing a specifically tuned resonant force to the structure. They showed that a collocated resonant controller, used for an active strut with acceleration feedback, was effective and robust in providing a specified level of modal damping for a selected mode. Furthermore, they showed that it is possible to position and tune multiple controllers with associated sensor/actuator pairs for effective, simultaneous damping of multiple modes. Using PID feedback controllers, the complex closed loop eigenvalue problem of rotating beams with combined active constrained layer damping and stressed layer damping treatment was developed and solved numerically. Experimental investigations have also been carried out to prove the effectiveness of their technique. Velocity feedback control law was also used in the work of Ray and Biswas [128]. The authors addressed the ACLD of geometrically nonlinear vibrations of rotating composite beams using 1–3 piezoceramics. The results showed that the damping characteristics of the overall rotating beam-ACLD system increased with the increase in the thickness of the viscoelastic layer while it decreased with the increase in the thickness of the 1–3 piezoceramic constraining layer. The effect of control gain on the nonlinear transient response of a clamped-free non-rotating ACLD-beam system is shown in Fig. 14.

6.1.2. Optimal control

An optimal control is a set of differential equations describing the paths of the control variables that minimize the cost function while maintaining a desired system state and minimizing the control effort. The most basic and commonly used optimal controller is the linear quadratic regulator (LQR). For structural control applications, the acceptable range of structure displacement and acceleration is considered as the cost function that is to be minimized.

Chandiramani et al. [36] studied the optimal control problem via

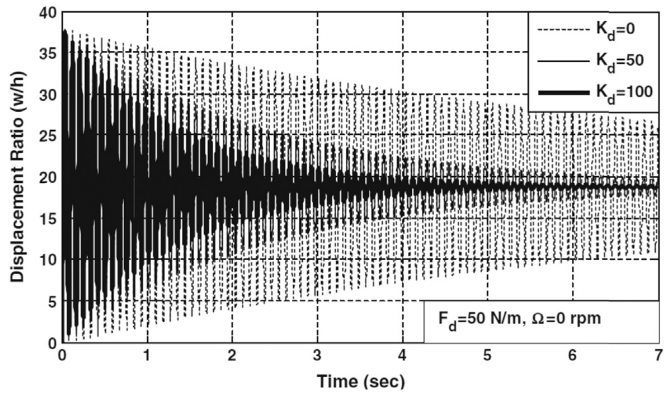

Fig. 14. Influence of control gain on the nonlinear transient response of a clamped-free non-rotating ACLD-beam system (symmetric cross ply—0°/90°/0°) [128].

the classical and instantaneous LQR methods. Their results revealed that structural tailoring can yield a lower steady-state response at the expense of increased settling time. Increasing the patch length beyond a limit proved ineffective. The instantaneous LQR control algorithm provided a reduced response, involving through-thickness shear strain variation. The optimal vibration control of a rotating composite pre-twisted single-celled box beam, exhibiting transverse shear flexibility and restrained warping, was analyzed by Shete and Chandiramani [165]. In another study, Chandiramani [43] carried out the optimal control of a thin-walled rotating composite beam using HSDTs. The optimal LQR control with state feedback was used to obtain the control input. Chattopadhyay et al. [166] developed a finite element model for the analysis of the smart box beam using the hybrid displacement field theory. The addition of a Kalman filter to a LQR control strategy leads to what is termed as Linear Quadratic Gaussian (LQG). They designed a LQG controller based on the transformation matrix and compared its performance with results of the open loop and the passive control systems. Their numerical results showed that the use of LQG control was efficient in stabilizing the unstable aeromechanical rotor response.

The vibration analysis and optimal control of rotating pre-twisted thin-walled beams using MFC actuators and sensors were studied by Vadiraja and Sahasrabudhe [167]. The optimal control problem was solved using LQG control algorithm. The controlled and uncontrolled tip displacement response of bending vibration using LQG control algorithm with four MFC sensors and actuators are shown in Fig. 15. A very good performance of MFC actuators for vibration suppression can be seen from the graph.

Traugott et al. [106] designed a multiple-input and multiple-output (MIMO) controller based on full-state optimal control (LQR approach) and optimal state estimation (Kalman filter) to add vibrational damping

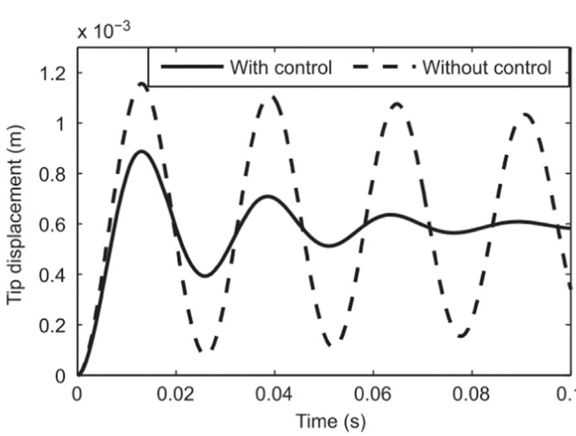

Fig. 15. Controlled and uncontrolled tip displacement of a rotating composite beam [167].

to the weakly damped system. Using analytical analysis and simulation runs of the closed loop, they showed that significant vibrational damping can be provided to the structure.

6.1.3. HHC and pitch link control

A study of the combined helicopter blade–vortex interaction noise and vibration reduction problem was conducted by Patt et al. [168]. Their simulation tool fully coupled aeroelastic and aeroacoustic phenomena. Their HHC control algorithm appeared to be an excellent algorithm for vibration and noise reduction, after some modifications to improve robustness and compensate for the highly nonlinear flight regime. In another study, Liu et al. [169] conducted a computational study of helicopter vibration and rotor shaft power reduction using actively controlled trailing-edge flaps (ACFs), implemented in both single and dual flap configurations. Their results indicated that the ACF system implemented either in a single or dual flap configurations was capable of simultaneously reducing vibration and enhancing rotor performance.

Using smart springs, Nitzsche et al. [170–174] studied the vibration control of rotor blades. They showed that smart springs are capable of significant reduction in the vibratory loads transmitted to the fuselage through the pitch link.

6.1.4. . Other active control methods

A nonlinear fuzzy logic system based control structure and adaptive algorithm (See Fig. 16) suitable for driving non-linear feedforward active vibration control systems was presented by Wenzhong et al. [243]. Numerical simulation results showed that the feedforward fuzzy active control method achieves better results than the conventional filtered-X LMS (Least Mean Square) algorithm for the composite beam. Using optimal tracking control method, Cai and Lim [244] investigated the control model of a flexible hub-beam system based on the assumed mode discretization approach. Their simulation results indicated that their model is valid for describing the dynamics of flexible hub-beam system and the vibration of beam may be suppressed effectively by this controller. The application of the nonlinear saturation control strategy for vibration suppression of the rotating hub-beam structure was proposed by Warminski and Latalski [245]. It has been shown that the proposed control strategy is effective if the frequency of the controller is precisely tuned to the half of the full structure natural frequency. In addition, properly chosen gains of the control signal are required.

6.2. Semi-active vibration control

Semi-active control devices often possess the advantages of active control and passive control devices and have been proposed for vibration control of rotating composite beams applications. These devices may include controllable fluids, electro-rheological fluid and magneto-rheological fluids.

Wei et al. [112] proposed the electrorheological sandwich structure for the vibration control of rotating flexible beams with variable speed/acceleration. In another study [111], they studied the vibration reduction of rotating sandwich beams filled with electrorheological fluids. They showed that the damping loss factors and natural frequencies of the rotating beam increased as the applied electric field strength was raised. However, the gain in the damping loss factor was much more than that in natural frequency. Allahverdizadeh et al. [116] optimally estimated the complex shear modulus of an ER adaptive sandwich beam to model the system for vibration control.

The design, analysis, and testing of an improved SMA-based tracking tab actuator was presented by Singh et al. [156]. The advantage of using a SMA actuator is the relatively large output force and deflection angle capability that ensures a simple actuator design with a minimum number of moving parts. Their test results revealed that although the system was highly nonlinear, it could be accurately controlled using only a simple single input, single output (SISO) PID controller with constant gains.

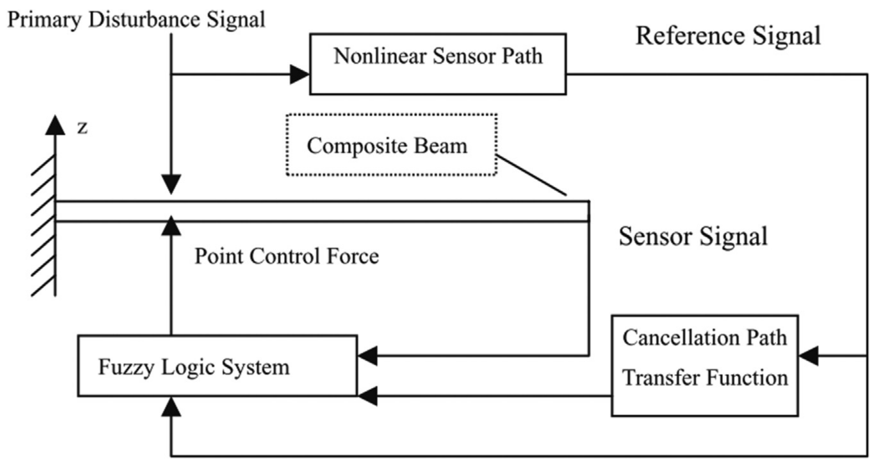

Fig. 16. Fuzzy control flow diagram for a composite beam [243].

6.3 Passive vibration control

In active vibration control, some sort of sensor is required to measure the displacement or force or acceleration etc. of the structure that is vibrating and an actuator is powered to generate a force to resist the unwanted motion. Passive vibration control, however, does not need any sensors or actuators and does not consume any power. Instead, it relies on the damping properties of materials used in its design. Passive control approaches such as the use of vibration absorbers have conventionally been pursued and widely implemented in rotating beams. However, the passive approach suffers from the major drawback of being ineffective at low frequencies [112]. While they cannot match active vibration reduction system in terms of versatility, adaptability, and optimum performance at diverse conditions, it is difficult to argue against their simplicity [175].

Austruy et al. [175] examined the effectiveness of a rotor-blade-embedded spanwise Coriolis absorber in reducing the in-plane vibratory hub loads. Their simulations showed that in high-speed flight, over 85% reductions in both 4/rev longitudinal and lateral hub shears could nominally be achieved using an absorber mass 3% of the blade mass situated at 60% span, oscillating at 3/rev with an amplitude of about 0.03 ft.

DeValve and Pitchumani [63] presented a numerical model to describe the effects of carbon nanotubes-based damping in a rotating fiber-reinforced composite beam. The simulations revealed that a dimensionless Coulomb damping factor on the order of 10^{-3}, which can be achieved with 1–2% by weight of CNT, can reduce the vibration settling time of a rotating composite beam by an average of 40–60%. A passive twist control was proposed by Peng et al. [176] as an adaptive way to maximize the overall efficiency of the small-scale rotor blade for multifunctional aircrafts.

6.3.1. Active constrained layer damping

The concept of active constrained layer damping (ACLD) treatment has been investigated by many researchers in the context of vibration control [177]. In constrained layer damping technique, a viscoelastic layer is sandwiched between the host and the constraining layer and vibration damping is attributed to the shear deformation of the viscoelastic layer. With ACLD treatment, an active piezoelectric material layer controls the shear deformations of the viscoelastic layer and thereby actively controls the damping of the structure. As the control effort required to cause transverse shear deformations in the viscoelastic constrained layer is compatible with the low control capability of the piezoelectric material, it has been found that the piezoelectric materials perform much better to attenuate the vibrations of smart structures when used as the constraining layer of the ACLD treatment rather than when they are used as standalones [177]. Vibration control of rotating beams with active constrained layer damping has been studied by Baz and Ro [119]. Chattopadhyay et al. [166] investigated the use of segmented constrained layer damping treatment and closed-loop control for improved rotor aeromechanical stability. Theoretical and experimental vibration analyses of rotating beams with combined ACLD and stressed layer damping treatment were presented by Kumar and Kumar [130]. Biswas and Ray [128] carried out an analysis for ACLD of rotating composite beams undergoing geometrically nonlinear vibrations. The Golla–Hughes–McTavish method was employed to model the constrained viscoelastic layer of the ACLD treatment in the time domain. The numerical responses revealed that the ACLD treatment with 1–3 piezoelectric composite constraining layers efficiently enforced active damping of geometrically nonlinear vibrations of the rotating composite beams.

7. Advanced composite materials

7.1. Functionally graded materials (FGMs)

Traditional laminated composites are being extensively used in various industries because of their flexibility in design and capacity to achieve desired strength and stiffness. However, since the laminates may tend to de-bond, cracks are likely to initiate at interfaces and propagate into the weaker material section. Furthermore, the difference in thermal coefficients of the materials may result in residual stresses. These problems can be mitigated by replacing conventional laminated composites with functionally graded materials where the material properties are gradually varied at the microscopic scale in the thickness direction (See Fig. 17). The present section concentrates on the application of FGM materials within rotating beams.

One of the early application of FGMs in rotating beams was implemented by Oh et al. [34]. Ceramic-metal based FGMs were used in the context of the vibrations and thermoelastic analysis of turbomachinery thin-walled rotating blades. In the work of Fazelzadeh et al. [42], the vibrations of rotating thin walled-blade made of FGMs operating under high temperature supersonic gas flow were studied. FGMs were also used by several other researchers [39,59,70,75,126,178–180]. Tapered rotating FGM beams were reported in the literature as well [60,61,69,73,77,113,181]. Among these refrences, Zarrinzadeh et al. [113], Kumar and Mitra [61] and Fang and Zhou [77] used functionally graded materials graded along the spanwise direction.

7.2. Nanocomposites

Rotating composite blades have become critical structural elements. Therefore, there is a strong need for the development of stronger and

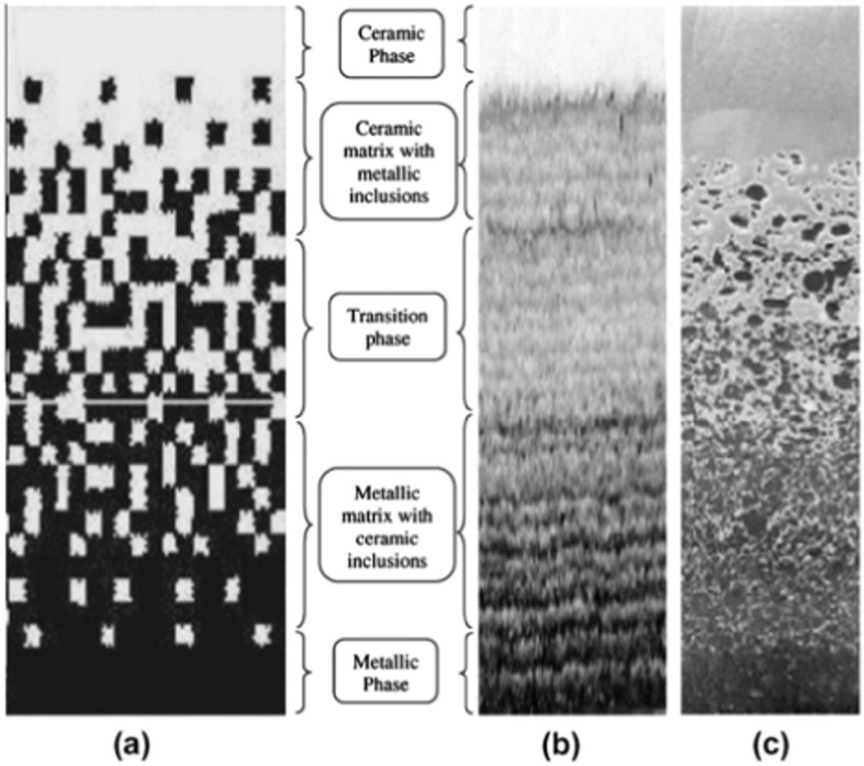

Fig. 17. Schematic of continuously graded microstructure with metal–ceramic constituents. (a) Smoothly graded microstructure, (b) enlarged view, and (c) ceramic–metal FGM [234].

lighter materials to enable the manufacture of rotating blades into more efficient rotors. In addition, manufacturers of rotating blades generally seek longer lifetimes for these products. To extend the working lifetime of blades, it is necessary to design and optimize blade materials to be much stiffer, stronger, and exhibit better fatigue resistance than the currently used ones. Nanocomposite materials can be an interesting choice in this regard. They are multifunctional, high-performance engineering composites that have attracted considerable attention in recent years due to their unique properties [95,182–184]. Thostenson and Chou [183] researched multi-walled carbon nanotube (MWCNT)-reinforced composites, which are based on a polystyrene matrix. They observed that with embedded nanotubes, the tensile modulus, yield strength and ultimate strengths of the composites are improved. Additionally, an improvement in elastic modulus with the aligned nanotube composite, which was five times greater than the improvement of the randomly oriented composite, was observed as shown in Fig. 18.

Deepak et al. [114] conducted a comparative study between CNT reinforced polymer and laminated rotating composite beams using spectral finite elements. A micromechanics model was used for calculating the properties of CNT based polymer composites in which the CNTs could be either uniformly or randomly aligned with the tensile loading direction. It was observed that CNT reinforced rotating beams were superior in performance compared to laminated composite rotating beams. DeValve and Pitchumani [63] studied the vibration damping effects of CNTs embedded in the matrix of fiber-reinforced composite materials used in rotating beams. The authors showed that a dimensionless Coulomb damping factor on the order of 10^{-3} could be achieved with 1–2% by weight of CNT. A micromechanics and structural dynamics analysis of the inherent damping exhibited by representative hybrid nanocomposite beams under axial strains was presented by Glaz et al. [185]. The results indicated that hybrid nanocomposites with nanoinclusions show significant potential for contributing to vertical lift capabilities by augmenting rotorcraft aeromechanical stability margins of hingeless/bearingless rotors. Very recently, Rafiee et al. [95] used the concept of CNTs/fiber/polymer laminated multiscale composite materials (See Fig. 19) to predict the

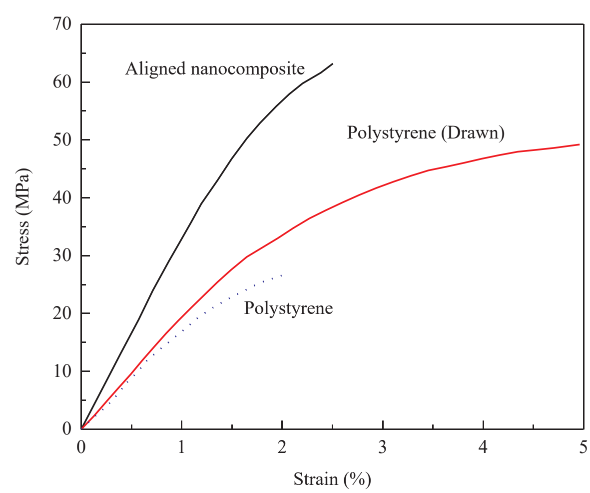

Fig. 18. Static stress–strain of polymer films under constant loading rate [183].

vibration behavior of rotating and nonrotating beams. Halpin–Tsai equations and fiber micromechanics were used to predict the bulk material properties of the multiscale nanocomposite. The carbon nanotubes were assumed to be uniformly distributed and randomly oriented through the epoxy resin matrix. The natural frequencies were found to be significantly influenced by a small percentage of CNTs. It was also found that the SWCNTs reinforcement produced more pronounced effects than MWCNTs on the nonlinear steady-state static response, and the natural frequencies of the composite beams.

8. Complicating effects & loadings

In this section, various complicating effects and loadings are discussed separately. These complicating effects include, but are not limited to: added mass, initially curved and twisted beams, swept tip, nonuniform beams and size-dependent analysis.

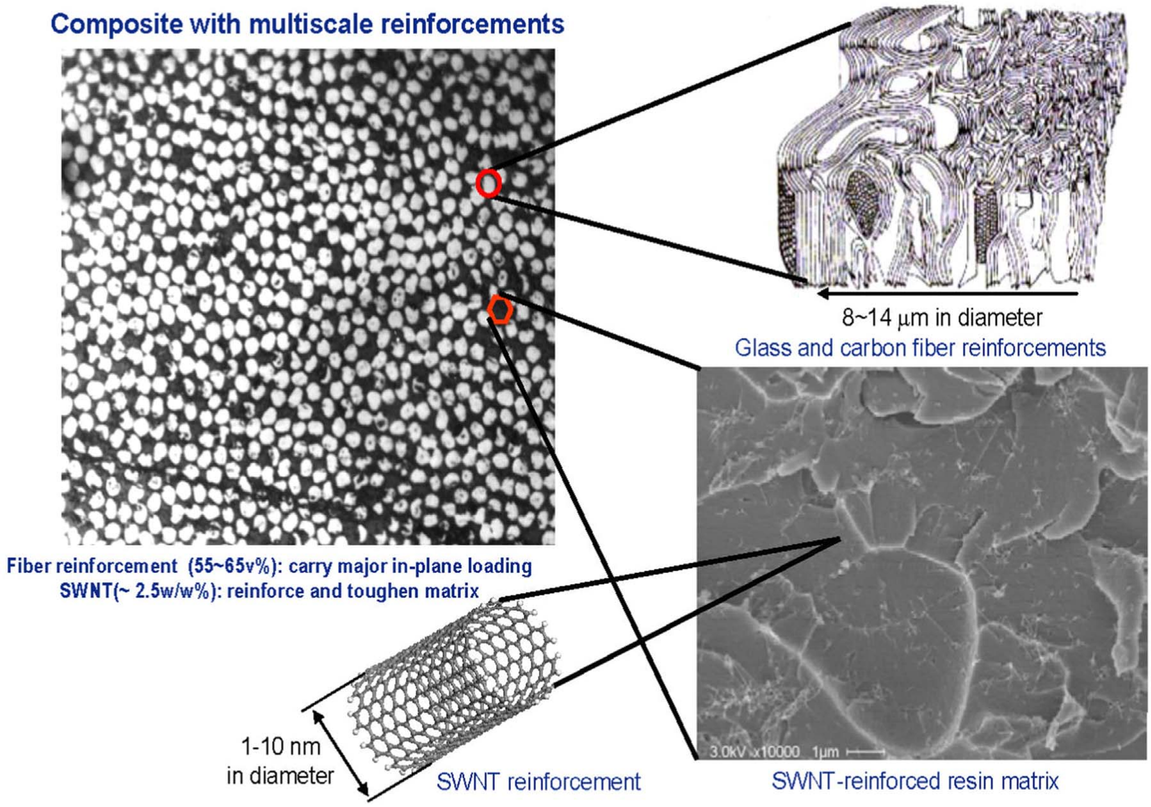

Fig. 19. Concept of multiscale reinforcement composites [235].

8.1. Added mass

Tip masses can be utilized in many rotary beam applications. They can modify the vibration frequency of components such as helicopter rotors; they can also increase the airflow, as in the case of a dynamic inducer in a wind turbine, or increase the flexing motion of the blades in flexible-blade auto cooling fans [186,187].

Lai [188] considered the geometrically nonlinear transient analysis of a rotating beam structure carrying a static payload. The influence of the payload on the system nonlinearity was significant in his study. The contribution was more than one hundred percent for a payload equivalent to 10% of the beam mass. Song and Librescu [28] investigated the dynamical behavior of rotating composite thin-walled blades carrying a tip mass. The tip mass in their study exerted a great influence on the mode shapes. The problem of determining the influence of a tip mass on the dynamic analysis of a flexible hub-beam system was studied by Cai et al. [189]. Their simulation and comparison studies using both the traditional zeroth-order model and the proposed first-order model showed that even a small tip mass may significantly affect the dynamic characteristics of the system, which may result in increasing the vibrating amplitude and decreasing the vibrating frequency of the beam, and may affect the end position of the hub-beam system as well. Chandiramani [43] studied the active control of a pre-twisted, doubly-tapered, piezo-composite rotating beam with a tip rotor. Their results showed that as the tip rotor mass was increased, centrifugal stiffening dominated the gyroscopic softening behavior.

8.2. Tapered beams

Rotating composite beams, such as wind turbine blades, may be made of tapered cross-sections. Consequently, the determination of their dynamics and vibration control are of prime interest to analysts and designers. Unlike the case of rotating composite uniform beams, the number of published results for rotating composite tapered beams is quite limited. A schematic of a rotating tapered beam can be seen in Fig. 20. Both single-tapered beams and double-tapered beams have been investigated in the literature.

As shown in Fig. 20b, for a double-tapered cantilever rotating beam of length L, the cross-sectional area reduces from A_0 at the root of beam to A at the free end according to equation (11c), due to the decrease in the height and breadth of beam according to Eqs. (11a) and (11b). The general equations for cross-sectional area $A(x)$, height $h(x)$, breadth $b(x)$, and moment of inertia $I_y(x)$ of the beam are given by [60]

$$b(x) = b_0\left(1 - c_b\frac{x}{L}\right)^m \tag{11a}$$

$$h(x) = h_0\left(1 - c_h\frac{x}{L}\right)^S \tag{11b}$$

$$A(x) = A_0\left(1 - c_b\frac{x}{L}\right)^m\left(1 - c_h\frac{x}{L}\right)^S \tag{11c}$$

$$I_y(x) = I_{y\,0}\left(1 - c_b\frac{x}{L}\right)^m\left(1 - c_h\frac{x}{L}\right)^{3S} \tag{11d}$$

8.2.1. Single-tapered beams

The single-tapered configuration is a simpler version of double-tapered beams. Das et al. [190] studied the free vibration dynamic behavior of rotating single-tapered beams in elastic and post-elastic regimes. They showed that the taper parameter can significantly affect the axial distribution of centrifugal force and the distribution of beam mass with respect to the root. The large amplitude, free vibration of axially functionally graded non-uniform rotating beams was presented by Kumar and Mitra [61]. Three different types of taper profiles were considered in their analysis. They concluded that there is almost no effect of taper on the first natural frequencies for all the cases, but the natural frequencies for other higher modes tend to decrease with increasing taper. Moreover, the extent of decrease in the natural frequencies were greater for higher modes.

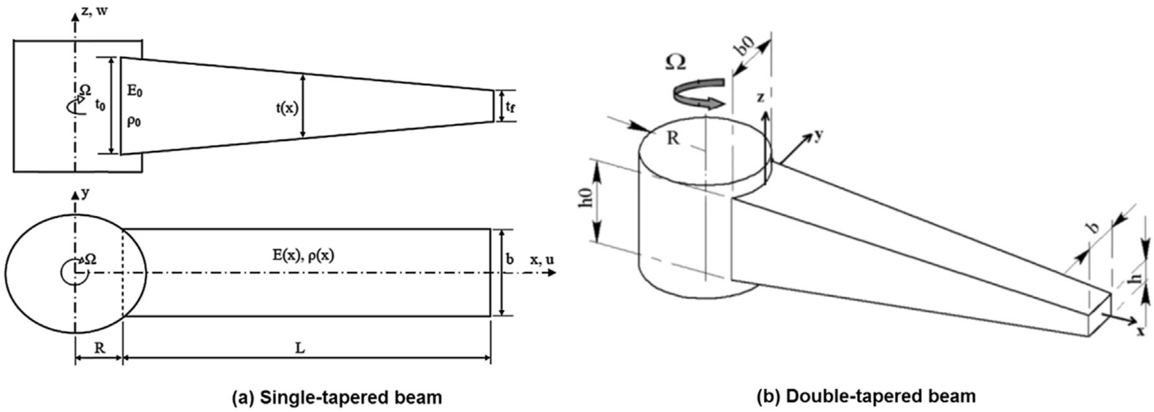

Fig. 20. Schematic of a rotating beam with (a) single tapered [61] and (b) double tapered [60] configurations.

8.2.2. Double-tapered beams

Shim and Na [163] developed a model to study the vibration control of rotating thin-walled composite beams of double-tapered cross-sections. The blade was considered to be tapered both in width and depth. Geometric configuration of a similar rotating blade is shown in. Fig. 21. The linear distribution of chord $c(\eta)$ and height $b(\eta)$ of the mid-line cross-section profiles along the beam span was considered as

$$\begin{pmatrix} c(\eta) \\ b(\eta) \end{pmatrix} = (1 - \eta(1 - \sigma))\begin{pmatrix} c_R \\ b_R \end{pmatrix} \tag{12}$$

They showed that the effects of taper ratio σ is much stronger for the lagging frequencies (second and third), than for their flapping frequencies counterparts. A similar beam configuration was also considered in the work of Na et al. [37]. The authors presented a model of rotating tapered beams characterized by decoupled flapping and lagging motions, exposed to a temperature field of a given spanwise distribution and to a time-dependent pressure field. The infuence of the taper ratio on the open/closed-loop dynamic response has been highlighted. The results revealed that the uncontrolled tapered beam featured smaller oscillation amplitudes than the uniform beam counterpart. However, for the controlled beam, an opposite effect was experienced. This trend was attributed to the fact that the tapered beam featuring a larger bending stiffness is more difficult to control than the uniform one, which experienced a lower bending stiffness. Thermally induced dynamic response of rotating composite double-tapered beams under solar radiation was presented by Na et al. [38]. The effect of taper ratio on the first coupled flap-lag bending frequency for different rotating speed and ply angles was investigated and is shown in Fig. 22. It can be seen that the taper ratio and ply angle can be chosen to structurally tailor helicopter and tilt rotor aircraft blades for improved dynamic responses.

Chandiramani [43] developed a model for a rotating, doubly tapered, pretwisted, composite blade, with piezoelectric sensors–actuator pairs, and a tip rotor. The time response amplitude increased with taper, i.e., a uniform cross-section beam had the lowest response, due to its bending rigidity being uniformly higher over the span. However, the attenuation rate also increased with taper, resulting in comparable settling times for all taper values. The free vibration of a rotating tapered composite thin-walled beam with closed cross-section featuring flap–twist coupling was presented by Sina et al. [44]. It was shown that taper profile and taper ratios have significant effects on the natural frequencies and eigenmodes.

Several researchers used the doubly-tapered configuration to study the dynamics and vibration control of rotating FG beams [60,69,73,77,191,192]. The effect of taper ratios on the chordwise bending natural frequency of FG double-tapered rotating beams was examined by Maganti and Nalluri [69]. The results showed that, in the case of single-tapered beams, the fundamental frequencies increased with increasing width taper ratio while the higher-order frequencies decrease. Height taper ratio had an increasing effect on all of the frequencies. The uniform rotating beam, as compared to the tapered beam, exhibited lower magnitude in respect to fundamental frequency, while the opposite was observed for higher-order frequencies. The beam with higher width ratio exhibited predominant influence on frequencies. Ebrahimi and Hashemi [60] studied the vibrations of a rotating FG double-tapered beam with the effect of porosities. The geometry of the system under their consideration is shown in Fig. 20b and the equation describing cross-sectional area $A(x)$, height $h(x)$, breadth $b(x)$, and moment of inertia $I_y(x)$ of the beam are given in (11). It was concluded that the fundamental frequency of tapered FG beams increases as the

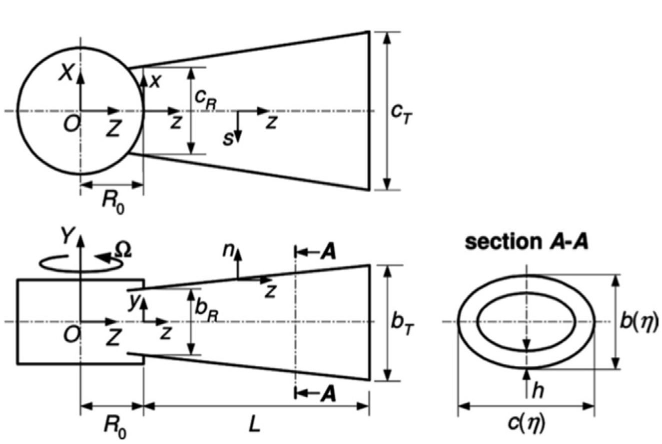

Fig. 21. Geometric configuration of a tapered rotating blade ($\sigma > 1$) [38].

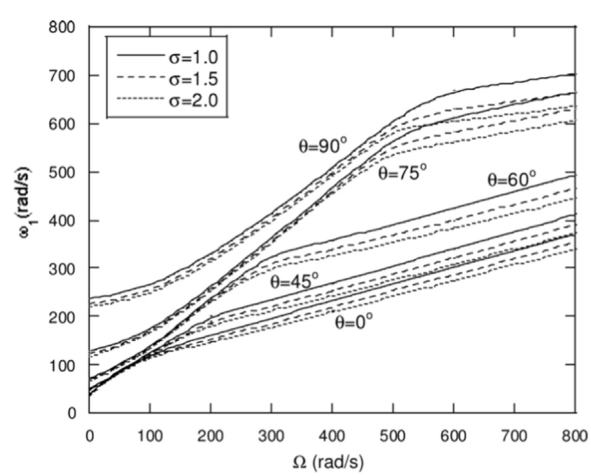

Fig. 22. Effect of taper ratio on the first coupled flap-lag bending frequency for different rotating speed and ply angles [38].

breadth and the height taper ratio increase, with the increase in the breadth taper ratio being the more significant effect.

8.3. Initially twisted/curved beams

In many applications, rotor blades are initially twisted in their undeformed state and may be initially curved as well. Song et al. [31] studied the dynamics of pre-twisted rotating thin-walled beams operating in a temperature environment. It was shown that the pre-twist effect induces supplementary couplings beneficial to the response behavior. Song et al. [29] extended this work to investigate the vibration of pre-twisted adaptive rotating blades modeled as anisotropic thin-walled beams. The vibrations of higher-order-shearable pre-twisted rotating composite blades were studied by Chandiramani et al. [33]. The increase in pretwist had a softening effect on the first two eigenfrequencies and a stiffening effect on the third one. The differences between results from the three models were significant and increased with increasing pretwist, in the case of the first and third coupled modes. For the second coupled modes, these differences diminished but remained significant throughout the range of pretwist considered. Kee and Kim [140] analyzed the vibration characteristics of initially twisted rotating shell type composite blades. For an initially twisted non-rotating blade, the bending frequencies tended to decrease, whereas the twisting frequencies increased with increasing initial twist. In the case of a rotating blade, when the initial twist of a blade increased the rate of increase in frequency parameters changed dramatically. The axial–torsional vibrations of rotating pre-twisted thin walled composite beams were investigated by Sina and Haddadpour [45]. The pretwist angle was assumed to vary linearly along the blade span $\beta=\beta_0(z/L)$. The results showed that the pretwist angle affect the torsional frequencies of the composite blade. The significance of this effect largely depended on the magnitude of pretwist, the rotational speed and fiber angle. For instance, Fig. 23 depicts the variation in fundamental torsional natural frequency of a rotating thin-walled beam versus the pretwist angle at different rotational speeds. As one can see, at higher rotational speeds, the fundamental natural frequency has a local minimum which can be treated as a tradeoff between centrifugal stiffening and softening terms. Arvin and Lacarbonara [79] developed a fully nonlinear dynamic formulation for pre-twisted rotating composite beams. The effect of pretwisting angle, however, was not investigated in the numerical results.

Some researchers studied the vibration control of initially twisted rotating composite beams [41,43,167]. Vibration control of pre-twisted rotating composite thin-walled beams with piezoelectric fiber composites was investigated by Choi et al. [41]. Vadiraja and Sahasrabudhe [167] presented the structural modeling of rotating pre-twisted thin-walled composite beams with embedded MFC actuators and sensors using HSDT. The optimal control of an initially twisted thin-walled rotating beam was researched by Chandiramani [43].

Pre-twisted composite beams made of FGMs have also been discussed in the literature. Oh et al. [34] investigated the vibration of pre-twisted and tapered thin-walled beams, rotating with a constant angular velocity and exposed to a steady temperature. Fazelzadeh et al. [42] presented the vibration analysis of a rotating thin-walled blade made of FGMs operating under high temperature supersonic gas flow. The dynamics of advanced rotating blades made of FGMs and operating in a high-temperature field were also studied Librescu et al. [39].

Unlike for pre-twisted rotating composite beams, published results for curved rotating beams are quite scarce. Based on a geometrically nonlinear finite element analysis, Hodges et al. [193] studied the nonlinear static deformation and linearized free vibration of initially curved and twisted composite beams.

8.4. Presetting angle (angle of attack)

The angle of attack (AOA) defined as the geometrical angle between the flow direction and the chord is a 2D concept used in aero-elastic engineering models for airfoil shaped cross-section blades. For non-airfoil shape cross-sections, however, the term “setting angle”, “pre-setting angle” or “pitch angle” is often used (See Fig. 24).

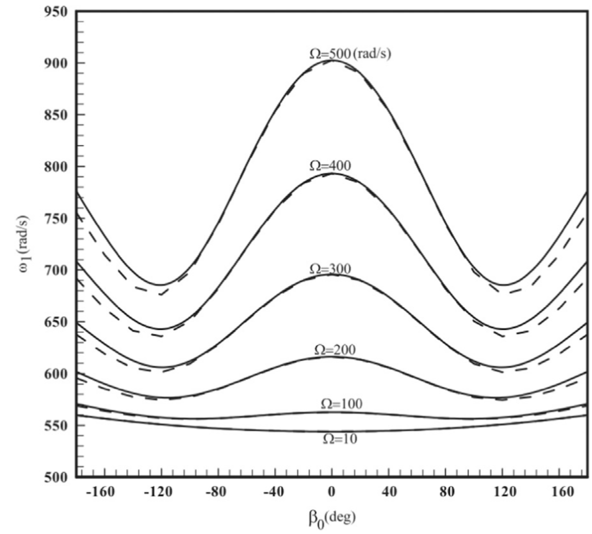

Fig. 23. Effect of pretwist angle and rotational speed on the first fundamental torsional natural frequency of a rotating thin-walled beam [236].

Lin [194] studied the effect of setting angle on the instability and vibration of rotating beams with arbitrary pretwist and an elastically restrained root. Baz and Ro [119] investigated the effect of presetting angle on the modal damping ratio of a rotating beam with active constrained layer damping closed-loop system. They concluded that decreasing the setting angle results in increasing the modal damping ratio. In a number of studies [131,132,195], the influence of the setting angle on the dynamic stability of rotating composite beams having a constrained damping layer [131,132] and a viscoelastic core [195] was studied by Lin and Chen. They showed that the resonant frequencies decrease and the modal system loss factor increase as the setting angle increases. But, it was observed that the changes in the second mode for the resonant frequency and in the modal system loss factor due to setting angle were very small [131]. Hosseini and Khadem [196] investigated the effect of the presetting angle on the vibration and reliability of a rotating beam with random properties under random excitation (See Fig. 25). The setting angles were $\Psi=0$, $\Psi=45°$ and $\Psi=90°$. The authors showed that the natural frequency decreases as the setting angle increases (Fig. 25b). Lin et al. [155] and Vadiraja and Sahasrabudhe [167] drew the same conclusion for rotating piezoelectric beams. The setting angle was also considered in the work of Na et *al*. [197], Yao et *al*. [46], and Georgiades [47]; however, no numerical results are given regarding its effect on the dynamical behavior of a rotating beam.

8.5. Swept tip

Tip sweeps are used in helicopters to improve their performance in terms of noise and vibration reduction, and to enhance aeromechanical stability [134]. Very few investigations of the effect of swept tip design on the dynamic characteristics of rotor blades exist in the literature. Yen [198] studied the effects of blade tip shape on dynamics, cost, weight, aerodynamic performance, and aeroelastic response of rotor blades. His results indicated that, in high-speed flight, the swept/ tapered tip reduced pitch-link loads, blade beam bending, and 4/rev hub moments, but had insignificant effect on blade chord bending and aerodynamic performance. Epps and Chandra [134] presented an experimental-theoretical investigation on the influence of tip sweep on the natural frequencies of rotating aluminum and composite

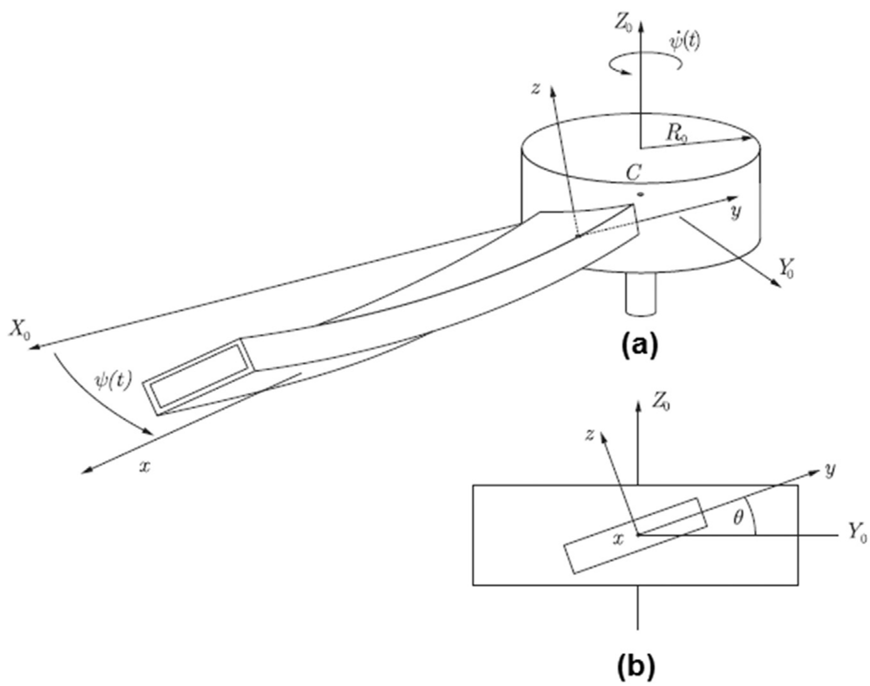

Fig. 24. Schematic of (a) a rotating thin-walled beam and (b) cross section of the blade with setting angle θ [207].

solid-section beams. The theoretical frequencies were calculated using a finite element structural model in which the beam had one elastic axis for the straight portion and another elastic axis for the swept portion.

8.6. Restrained/Elastic root

Rotating structures have inherent lateral flexibility as well as axial rigidity. The flexibility of the root was shown to have a significant effect on the stability of such structures and on their positioning control [199]. A soft base in combination with a high setting angle and high rotating speeds can make the fundamental frequency become imaginary, leading to a divergence instability [200,201]. Therefore, a model that accounts for the effect of inherent flexibility of the supporting base is in high demand. However, all the studies related to restrained and elastic roots are limited to isotropic rotating beams.

Abbas [199] investigated the effects of rotating speed and root flexibilities on the static buckling loads and on the unstable region of a Timoshenko beam by the finite element method. His study idealized the flexible root as translational and rotational elastic springs and introduced two flexibility parameters: translational and rotational where translational relates the total deflection to the shear force and rotational relates the bending slope to the bending moment. He showed that the increase in the rotational root flexibility makes the beam more sensitive to periodic excitation while the translational root flexibility has no effect on the static buckling load. The free vibration behavior of a rotating non-uniform pre-twisted beam having an elastically restrained root and

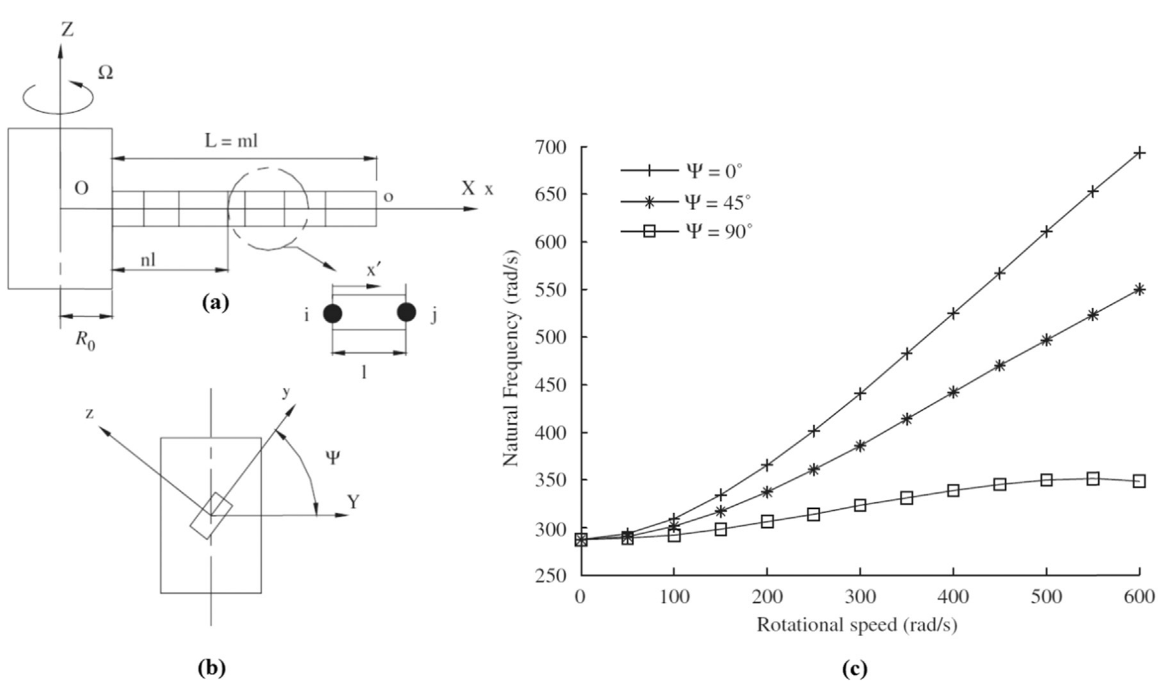

Fig. 25. (a) Schematic of a **r**otating composite beam, (b) influence of setting angle Ψ and rotating speed on the fundamental natural frequency a rotating composite beam [196].

a tip mass have been investigated by Lee et al. [202]. Lee et al. [203] studied the in-plane free vibration behavior of a rotating curved beam with an elastically restrained root. With a similar approach as Abbas [199], the elastically restrained root was mounted in a hub and represented by translational and rotational springs. They concluded that the natural frequencies of the curved beam increase as the values of the translational and rotational spring constants are increased. Of the two spring constants, the translational spring constant has a significantly greater effect on the natural frequency of the beam. Given a sufficiently low value of the translational spring constant, a divergent instability effect was induced in the rotating curved beam even at large values of the hub radius.

Yardimoglu et al. [204] studied the coupled bending-bending-torsion vibration of a rotating pre-twisted beam with airfoil cross-section and modeled the elastic root of the blade by using the continuum model approach (See Fig. 26). The authors employed the same finite element model formulation derived for a blade to determine the stiffness and mass matrices of elastic root. The influence of the root flexibility on the natural frequencies was studied in their work. Employing eight elements for the pre-twisted part and one element for the root part of the blade, the natural frequencies found for a non-rotating blade with rigid and elastic roots were in good agreement with the results reported by Montoya [205] in Table 2.

Table 2
Effect of root flexibility on the natural frequencies (Hz) of a nonrotating composite blade [204].

Source	Rigid root		Elastic root	
	Fundamental	First harmonic	Fundamental	First harmonic
Montoya (Experimental) [205]	83.4	184.8	82.25	174
Montoya (FEM) [205]	80.3	185.5	80.25	181.75
Yardimoglu and Inman (FEM) [204]	79.70	183.27	78.98	179.2

The hub inertia was also taken into account in the work of Latalski et al. [207]. They studied the coupled bending–shear–twist vibrations of a thin-walled rotating cantilever beam made of composite material. It has been shown that the hub–beam assembly has to be considered as a whole system since the hub mass moment of inertia has an essential impact on the natural frequencies of the structure. The first natural frequency of the system was located close to the natural frequency of the separated cantilever beam only in relatively large hubs.

8.7. Hub inertia

Rotating composite blades are often mounted onto a hub. The inertia of the hub can be large and might have significant effects on the natural frequency of the hub-beam system especially at relatively large angular speeds. Nevertheless, the effect of hub inertial has been ignored in many studies.

The dynamics of a slewing Euler–Bernoulli isotropic beam with a tip load was studied by Low [206]. The mass and inertia of the tip load as well as the total inertia of the hub and flexible beam assembly were taken into account. The author investigated the effect of the combined hub and beam inertia and concluded that the system frequencies decrease as the inertia of the combined hub–beam system increases. The author also showed that the combined inertia of the hub–beam assembly influenced the eigenvalues much more than the tip mass.

8.8. Nonconstant rotating speed

For composite rotor blades, a varying angular velocity rate would not only be more general but more physically realistic due to external perturbations such as aerodynamic excitation. However, research on rotating beams with time-dependent rotating speeds has been very limited. A nonconstant angular velocity seems to have been first considered by Kammer and Schlack [208] for an Euler-Bernoulli beam mounted parallel to the axis of rotation. Yang and Tsao [209] presented an analytical model to investigate the vibration and stability of a pretwisted blade under nonconstant rotating speed. The time-dependent rotating speed led to a system with six parametric instability regions in primary and combination resonances. Their analyses showed that the combination resonance at about twice the fundamental frequency was the most critical aspect and was sensitive to system parameter variation. An

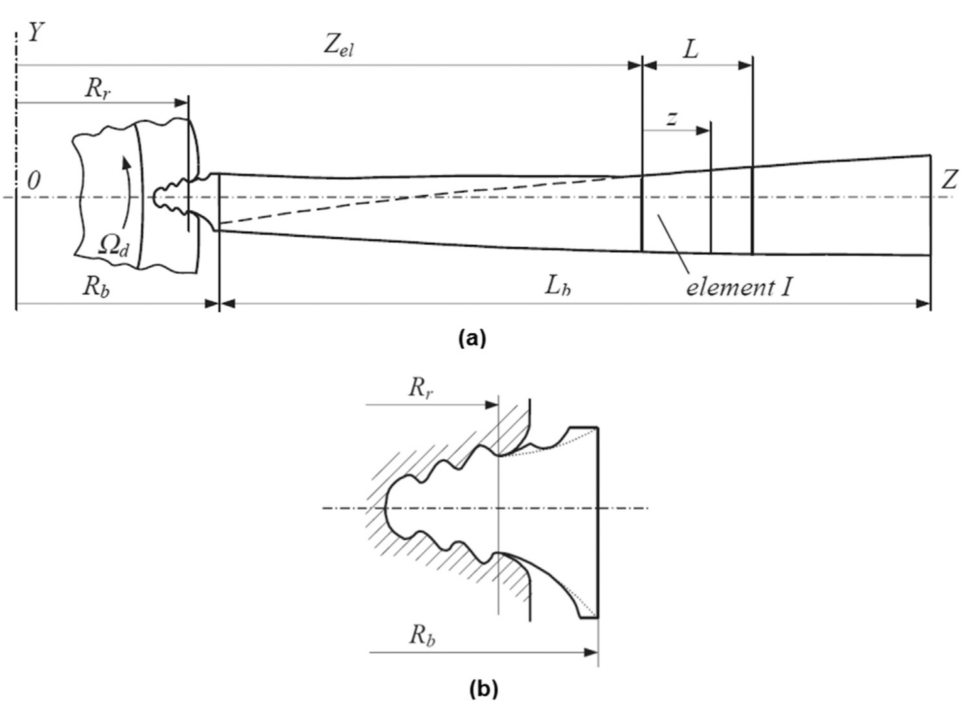

Fig. 26. Rotating blade under consideration from Yardimoglu and Inman [204], (a) geometry and finite element modeling and (b)Fir-tree root of the blade.

electrorheological sandwich structure was proposed in the work of Wei et al. [112] for vibration control of the rotating flexible beams with variable speed/acceleration. The experimental results of their study demonstrated that the vibrations of the beam caused by the rotating motion at different rotating speed and acceleration could be quickly suppressed by applying an electric field to the ER beam. Kallesøe [210] extended the blade model developed by Hodges and Dowell [211] to take pitch action, rotor speed variations and gravity into account. The non-linear coupled longitudinal and bending vibrations of a variable speed rotating beam were modeled and analyzed by Younesian and Esmailzadeh [212]. The multiple time scales method was used to obtain the exact first-order solution for both the stationary and non-stationary rotating speeds in two cases: a) damped beam with accelerating angular velocity in the form of $\Omega(\tau) = \alpha\tau$, and b) undamped beam with accelerating and decelerating angular velocities in the form of $\Omega(\tau) = \Omega_0 + \alpha\tau$ accelerating angular velocity where τ is time, α is a control parameter and Ω_0 is steady-state rotating speed. The method of multiple time scales was also used by Yao et al. [46,213] to study the nonlinear dynamic response of rotating blade with varying rotating speed under high-temperature supersonic gas flow. The blade was assumed to be rotated at a varying rotating speed $\Omega(t)$ about its polar axis. The time-dependent rotating speed $\Omega\ (t)$ was represented as a periodic perturbation $f\cos\Omega_1 t$ about steady-state rotating speed Ω_0, i.e., $\Omega(t) = \Omega_0 + f\cos\Omega_1 t$. The effects of the periodic perturbation speed on the frequency–response curves were investigated. It was found from numerical results that the frequency–response curves begin to bifurcate into two separated branches when the perturbation speed was larger than the critical value $f = 2.1$. Therefore, the system became more unstable when the amplitude f of the perturbation speed exceeded the critical value. Using a 3D geometrically nonlinear beam model, Stoykov and Ribeiro [214] investigated the moderately nonlinear vibrations of 3D beams with rectangular cross sections and that rotate about a fixed axis using the p-version finite element method. A linearly varying speed of rotation was considered and the transient responses were presented for different accelerations. It was verified that large vibration amplitudes can be caused by the acceleration that precedes a constant rotation speed. The equations of motion of composite Timoshenko beam experiencing variable angular velocity using a fully linear strain field were derived by Georgiades et *al.* [47]. Their work was further extended by Latalski et al. [207] considering higher-order terms in the strain field to study the coupled bending–shear–twist vibrations of a thin-walled rotating cantilever beam made of composite material. Cases of forced vibrations of the system were examined, where the driving torque was considered as the sum of a constant (mean value) and a periodic component. Their simulations showed that the rotation of the structure, as defined by the constant component of the forcing torque, shifted the resonance zones and entailed an involved pattern of beam oscillation amplitudes.

8.9. Size-dependent effect

With the development of material technology, composite rotor blades can be employed in micro/nano-electro-mechanical system (MEMS/NEMS). The size effect plays a significant role in mechanical response of small scaled structures [215]. On the other hand, the classical elasticity theory is unable to account for the size effect for lack of a material length scale. In this regard, Shafiei et al. [192] studied the size dependent vibration behavior of rotating tapered FG Timoshenko and Euler–Bernoulli microbeams based on the modified couple stress theory. Their results confirmed the significant role of small-scale parameters on the vibration response of composite microscale beams.

9. Experimental investigations

A vast literature is available on the mathematical modeling of rotating composite beams and blades; however, experimental investigations are quite scarce. Friedmann [159] reviewed the theoretical and experimental studies on the active vibration reduction in rotorcraft. Experiments and an analysis of dynamics of composite blades under large deflections were produced by Minguet and Dugundji [216]. Srinivasan et al. [217] performed an experimental and analytical study to investigate the structural dynamic behavior of a rotor system subjected to inertial and structural loads without any aerodynamic loads.

Rand [218] experimentally studied the structural dynamic characteristics of rotating thin-walled composite helicopter rotor blades undergoing periodical excitation. An experimental method for detecting the natural frequencies of helicopter-like thin-walled rotating composite blades was presented by Rand [219].

Chandra and Chopra [220] experimentally performed a structural analysis of two-cell composite rotor blades. Two-cell composite rotor blades with foam core were fabricated using a matched-die molding technique. Chandra and Chopra also studied the vibration characteristics of rotating composite box beams [54] and I-beams [221]. In another study, Epps and Chandra experimentally investigated the influence of tip sweep on the natural frequencies of rotating aluminum and composite solid-section beams.

Baz and Ro [119] studied the vibration control of rotating beams with active constrained layer damping. Choi and Han [160] presented the vibration control of a rotating cantilevered beam using piezoactuators. Using ER materials, Wei et al. [112] investigated the vibration control of the rotating flexible beams with variable speed/acceleration. The design and manufacturing of an active twist rotor blade for vibration reduction in helicopters were discussed by Shin et al. [222]. Kumar and Kumar [130] considered the theoretical and experimental vibration analysis of rotating beams with combined ACLD and stressed layer damping treatment. The numerical modeling and experimental study for piezoelectric vibration damping control of rotating composite fan blades were performed by Min et al. [223]. Qiu et al. [224] presented experiments on fuzzy sliding mode variable structure control for vibration suppression of a rotating flexible beam. Truong et al. [225] discussed the structural dynamics modeling of rectangular rotor blades with experimental validation. Allahverdizadeh et al. [116] mathematically and experimentally studied the vibration control of a viscoelastic adaptive sandwich beam incorporating an electrorheological fluid layer. Detection of cracks in aircraft engine fan blades using vibrothermography nondestructive evaluation was performed by Gao et al. [226]. Kumar and Cesnik [227] presented the development of a mixed-variable optimization framework for the design of composite rotor blades with active flaps in order to maximize the control authority for vibration reduction. Vibration control of a rotating two-connected flexible beam using chattering-free sliding mode controllers was studied by Qiu and Xu [142]. Their experimental results demonstrated that the designed fast terminal sliding mode (FTSM) and fuzzy fast terminal sliding mode (FFTSM) algorithms could significantly improve the vibration reduction performance and eliminate the chattering phenomenon effectively. The concept of deicing of a rotorcraft blade using a low-energy piezoelectric actuated system was presented by Villeneuve et al. [228]. Deicing was achieved using frequency sweeps of the actuator array to excite multiple resonant frequencies in the blade to weaken, crack, and debond the ice at multiple locations.

10. Discussion, evaluation and future directions

With the recent advances in the various theories of rotating composite beams and blades now reviewed with a focus on dynamics and vibration control, there are some areas which, in the authors' opinion, would benefit from further investigation

10.1. Large amplitude response

Rotating composite beams and blades often exhibit nonlinear behavior. However, only few studies exist that are related to the nonlinear free and forced vibration and dynamics response of rotor blades. A systematic approach should be followed to examine the effects of nonlinearity on vibration and dynamic responses of rotating composite beams and blades.

10.2. 3D FEA

The versatility and flexibility of FEA are quite considerable compared to analytical methods. Yet, more studies are warranted to identify the level of sophistication required in modeling composite rotor blades especially in the case of warping functions.

10.3. Material nonlinearity

The above literature review revealed that all studies of dynamics of rotating composite beams are based on an assumed elastic behavior. Specialized theoretical and experimental studies should be conducted in the post-elastic domain to generate detailed data when the external loading induces yielding in the rotating components.

10.4. Size-dependent analysis

The size effect plays a significant role in the mechanical response of small scaled structures. While theoretical studies of the phenomenon are scarce, no experimental data can be found in the literature. Research opportunities exist for theoretical and experimental investigations of the characterization, performance and designs of microscale and nanoscale rotating composite beams and blades.

10.5. Intelligent/smart/adaptive structures and vibration control

Both distributed and piecewise induced-strain actuators have been used to take advantage of smart materials in aeroelastic and vibration control. While the distributed induced-strain actuation has only had partial effectiveness [157], piecewise distribution seems to be more effective. Investigations of vibration control with multidisciplinary optimization of actuators location are expected to come to fruition in the coming years.

10.6. Damping

The material damping has a considerable influence on reduction of noise and vibration. This influence is more significant in the medium to high frequency range and is limited to an operating temperature range of 10–30 °C [229]. There is an explicit need for novel methodologies to increase damping characteristics of composite rotor blade materials to overcome these limitations.

10.7. Advanced composite materials

Even though significant progress has been made to develop CNT/polymer nanocomposites, their applications in composite rotor blades are still in the early stage of realization. CNT/polymer nanocomposites, which can be utilized either as a matrix or as a coating for fiber, have great potential to make blade materials much stiffer, stronger, and have better fatigue resistance.

Acknowledgements

The first author gratefully acknowledges the financial support from the Ontario Trillium Scholarship (OTS), Government of Ontario, Canada.

References

[1] D.H. Hodges, Review of composite rotor blade modeling, AIAA J. 28 (1990) 561–565.
[2] D.L. Kunz, Survey and comparison of engineering beam theories for helicopter rotor blades, J. Aircr. 31 (1994) 473–479, http://dx.doi.org/10.2514/3.46518.
[3] P.P. Friedmann, T.A. Millott, Vibration reduction in rotorcraft using active control - a comparison of various approaches, J. Guid. Control. Dyn. 18 (1995) 664–673, http://dx.doi.org/10.2514/3.21445.
[4] S.N. Jung, V.T. Nagaraj, I. Chopra, Assessment of composite rotor blade modeling techniques, J. Am. Helicopter Soc. 44 (1999) 188, http://dx.doi.org/10.4050/JAHS.44.188.
[5] D.H. Hodges, Nonlinear Composite Beam Theory, AIAA, United States of America, 2006, http://dx.doi.org/10.1243/0954410041872861.
[6] F. Jiang, W. Yu, D.H. Hodges, Analytical modeling of trapeze and poynting effects of initially twisted beams, J. Appl. Mech. 82 (2015) 61003, http://dx.doi.org/10.1115/1.4030362.
[7] L. Librescu, O. Song, Thin-Walled Composite Beams: Theory and Application, Springer Science & Business Media, Netherlands, 2005, http://dx.doi.org/10.1007/1-4020-4203-5.
[8] D.H. Hodges, Unified approach for accurate and efficient modeling of composite rotor blade dynamics The Alexander A. Nikolsky honorary lecture, J. Am. Helicopter Soc. 60 (2015) 1–28, http://dx.doi.org/10.4050/JAHS.60.011001.
[9] M. Ghorashi, Statics and Dynamics of Composite Beams, Springer, Switzerland, 2016.
[10] S.M. Han, H. Benaroya, T. Wei, Dynamics of transversely vibrating beams using four engineering theories, J. Sound Vib. 225 (1999) 935–988, http://dx.doi.org/10.1006/jsvi.1999.2257.
[11] O.A. Bauchau, J. Craig, Structural Analysis, Springer, New York, 2009, http://dx.doi.org/10.1007/978-90-481-2516-6.
[12] D.H. Hodges, A mixed variational formulation based on exact intrinsic equations for dynamics of moving beams, Int. J. Solids Struct. 26 (1990) 1253–1273.
[13] P.F. Pai, A.H. Nayfeh, A fully nonlinear theory of curved and twisted composite rotor blades accounting for warpings and three-dimensional stress effects, Int. J. Solids Strut. 31 (1994) 1309–1340.
[14] S.P. Timoshenko, LXVI. On the correction for shear of the differential equation for transverse vibrations of prismatic bars, Philos. Mag. Ser. 6 (41) (1921) 744–746, http://dx.doi.org/10.1080/14786442108636264.
[15] C.M. Wang, J.N. Reddy, K.H. Lee, Shear Deformable Beams and Plates, 2000. ⟨http://dx.doi.org/10.1016/B978-008043784-2/50000-9⟩.
[16] J.N. Reddy, A simple higher-order theory for laminated composite plates, J. Appl. Mech. 51 (1984) 745–752, http://dx.doi.org/10.1115/1.3167719.
[17] M. Touratier, An efficient standard plate theory, Int. J. Eng. Sci. 29 (1991) 901–916, http://dx.doi.org/10.1016/0020-7225(91)90165-Y.
[18] K.P. Soldatos, A transverse shear deformation theory for homogeneous monoclinic plates, Acta Mech. 94 (1992) 195–220, http://dx.doi.org/10.1007/BF01176650.
[19] M. Karama, K.S. Afaq, S. Mistou, Mechanical behaviour of laminated composite beam by the new multi-layered laminated composite structures model with transverse shear stress continuity, Int. J. Solids Struct. 40 (2003) 1525–1546, http://dx.doi.org/10.1016/S0020-7683(02)00647-9.
[20] E. Carrera, G. Giunta, M. Petrolo, Beam Structures: Classical and Advanced Theories (2011). doi: ⟨http://dx.doi.org/10.1002/9781119978565⟩.
[21] A.A. Khdeir, J.N. Reddy, An exact solution for the bending of thin and thick cross-ply laminated beams, Compos. Struct. 37 (1997) 195–203, http://dx.doi.org/10.1016/S0263-8223(97)80012-8.
[22] J.N. Reddy, A generalization of two-dimensional theories of laminated composite plates, Commun. Appl. Numer. Methods 3 (1987) 173–180, http://dx.doi.org/10.1002/cnm.1630030303.
[23] C. Sun, J.M. Whitney, Theories for the dynamic response of laminated plates, AIAA J. 11 (1972) 178–183.
[24] V. Vlasov, Thin-walled elastic beams, Natl. Tech. Inf. Serv. (1961), http://dx.doi.org/10.1007/s13398-014-0173-7.2.
[25] V.V. Volovoi, D.H. Hodges, C.E.S. Cesnik, B. Popescu, Assessment of beam modeling methods for rotor blade applications, Math. Comput. Model. 33 (2001) 1099–1112, http://dx.doi.org/10.1016/S0895-7177(00)00302-2.
[26] W. Yu, V. Volovoi, D.H. Hodges, X. Hong, Validation of the variational asymptotic beam sectional analysis, AIAA J. 40 (2002) 2105–2112, http://dx.doi.org/10.2514/3.15301.
[27] O. Song, L. Librescu, Structural modeling and free vibration analysis of rotating composite thin-walled beams, J. Am. Helicopter Soc. 42 (1997) 358, http://dx.doi.org/10.4050/JAHS.42.358.
[28] O. Song, L. Librescu, Modeling and dynamic behavior of rotating blades carrying a tip mass and incorporating adaptive capabilities, Acta Mech. 134 (1999) 169–197, http://dx.doi.org/10.1007/BF01312654.
[29] O. Song, L. Librescu, S.-Y. Oh, Vibration of pretwisted adaptive rotating blades modeled as anisotropic thin-walled beams, AIAA J. 39 (2001) 285–295, http://dx.doi.org/10.2514/2.1303.
[30] Z. Qin, L. Librescu, Static and dynamic validations of a refined thin-walled composite beam model, AIAA J. 39 (2001) 2422–2424, http://dx.doi.org/10.2514/2.1259.
[31] O. Song, L. Librescu, S.-Y. Oh, Dynamics of pretwisted rotating thin-walled beams operating in a temperature environment, J. Therm. Stress. 24 (2001) 255–279, http://dx.doi.org/10.1080/014957301300006407.
[32] N. Chandiramani, L. Librescu, C. Shete, On the free-vibration of rotating composite beams using a higher-order shear formulation, Aerosp. Sci. Technol. 6 (2002)

545–561, http://dx.doi.org/10.1016/S1270-9638(02)01195-1.
[33] N.K. Chandiramani, C.D. Shete, L.I. Librescu, Vibration of higher-order-shearable pretwisted rotating composite blades, Int. J. Mech. Sci. 45 (2003) 2017–2041, http://dx.doi.org/10.1016/j.ijmecsci.2004.02.001.
[34] S.-Y. Oh, L. Librescu, O. Song, Thermoelastic modeling and vibration of functionally graded thin-walled rotating blades, AIAA J. 41 (2003) 2051–2061, http://dx.doi.org/10.2514/2.1897.
[35] S.-Y. Oh, O. Song, L. Librescu, Effects of pretwist and presetting on coupled bending vibrations of rotating thin-walled composite beams, Int. J. Solids Struct. 40 (2003) 1203–1224, http://dx.doi.org/10.1016/S0020-7683(02)00605-4.
[36] N.K. Chandiramani, L.I. Librescu, V. Saxena, A. Kumar, Optimal vibration control of a rotating composite beam with distributed piezoelectric sensing and actuation, Smart Mater. Struct. 13 (2004) 433–442, http://dx.doi.org/10.1088/0964-1726/13/2/022.
[37] S. Na, L. Librescu, H. Jung, Dynamics and active bending vibration control of turbomachinery rotating blades featuring temperature-dependent material properties, J. Therm. Stress. 27 (2004) 625–644, http://dx.doi.org/10.1080/01495730490466219.
[38] S. Na, G.-C. Yoon, B.-H. Lee, P. Marzocca, L. Librescu, Dynamic response control of rotating composite booms under solar radiation, J. Therm. Stress. 32 (2008) 21–40, http://dx.doi.org/10.1080/01495730802540205.
[39] L. Librescu, S.Y. Oh, O. Song, H.S. Kang, Dynamics of advanced rotating blades made of functionally graded materials and operating in a high-temperature field, J. Eng. Math. 61 (2008) 1–16, http://dx.doi.org/10.1007/s10665-007-9155-5.
[40] F. Shadmehri, H. Haddadpour, M.A. Kouchakzadeh, Flexural-torsional behavior of thin-walled composite beams with closed cross-section, Thin-Walled Struct. 45 (2007) 699–705, http://dx.doi.org/10.1016/j.tws.2007.05.006.
[41] S.C. Choi, J.S. Park, J.H. Kim, Vibration control of pre-twisted rotating composite thin-walled beams with piezoelectric fiber composites, J. Sound Vib. 300 (2007) 176–196, http://dx.doi.org/10.1016/j.jsv.2006.07.051.
[42] S.A. Fazelzadeh, P. Malekzadeh, P. Zahedinejad, M. Hosseini, Vibration analysis of functionally graded thin-walled rotating blades under high temperature supersonic flow using the differential quadrature method, J. Sound Vib. 306 (2007) 333–348, http://dx.doi.org/10.1016/j.jsv.2007.05.011.
[43] N.K. Chandiramani, Active control of a piezo-composite rotating beam using coupled plant dynamics, J. Sound Vib. 329 (2010) 2716–2737, http://dx.doi.org/10.1016/j.jsv.2010.01.023.
[44] S.A. Sina, M.J. Ashrafi, H. Haddadpour, F. Shadmehri, Flexural–torsional vibrations of rotating tapered thin-walled composite beams, Proc. IMechE Part G J. Aerosp. Eng. 225 (2011) 387–402, http://dx.doi.org/10.1243/09544100JAERO828.
[45] S.A. Sina, H. Haddadpour, Axial–torsional vibrations of rotating pretwisted thin walled composite beams, Int. J. Mech. Sci. 80 (2014) 93–101, http://dx.doi.org/10.1016/j.ijmecsci.2013.12.018.
[46] M.H. Yao, W. Zhang, P. Chen, Analysis on nonlinear oscillations and resonant responses of a compressor blade, Acta Mech. 3510 (2014) 3483–3510, http://dx.doi.org/10.1007/s00707-014-1151-z.
[47] F. Georgiades, J. Latalski, J. Warminski, Equations of motion of rotating composite beam with a nonconstant rotation speed and an arbitrary preset angle, Meccanica 49 (2014) 1833–1858, http://dx.doi.org/10.1007/s11012-014-9926-9.
[48] J.K. Shim, S. Na, Modeling and vibration feedback control of rotating tapered composite thin-walled blade, KSME Int. J. 17 (2003) 380–390.
[49] P.F. Pai, A.H. Nayfeh, Three-dimensional nonlinear vibrations of composite beams - I. Equations of motion, Nonlinear Dyn. 1 (1990) 477–502.
[50] P.F. Pai, A.H. Nayfeh, Three-dimensional nonlinear vibrations of composite beams - II. flapwise excitations, Nonlinear Dyn. 2 (1991) 1–34, http://dx.doi.org/10.1007/BF00045053.
[51] P.F. Pai, A.H. Nayfeh, Three-dimensional nonlinear vibrations of composite beams - III. Chordwise excitations, Nonlinear Dyn. 2 (1991) 137–156, http://dx.doi.org/10.1007/BF00053833.
[52] M.R.M.C. Silva, C.C. Glynn, An international nonlinear flexural-flexural-torsional dynamics of inextensional beams. I. Equations of motion nonlinear flexural-flexural-torsional, J. Struct. Mech. 6 (1978) 437–448, http://dx.doi.org/10.1080/03601217808907348.
[53] E.C. Smith, I. Chopra, Formulation and evaluation of an analytical model for composite box-beams, J. Am. Helicopter Soc. 36 (1991) 23–35.
[54] R. Chandra, I. Chopra, Experimental-theoretical investigation of the vibration characteristics of rotating composite box beams, J. Aircr. 29 (1992) 657–664, http://dx.doi.org/10.2514/3.46216.
[55] S.N. Jung, V.T. Nagaraj, I. Chopra, Refined structural dynamics model for composite rotor blades, AIAA J. 39 (2001) 339–348, http://dx.doi.org/10.2514/2.1310.
[56] S.N. Jung, V.T. Nagaraj, I. Chopra, Refined structural model for thin- and thick-walled composite rotor blades, AIAA J. 40 (2002) 105–116.
[57] T. Kim, J. Dugundji, Nonlinear large amplitude vibration of composite helicopter blade at large static deflection, AIAA J. 31 (1993) 938–946, http://dx.doi.org/10.2514/3.11708.
[58] T. Kim, J. Dugundji, Nonlinear large amplitude aeroelastic behavior of composite rotor blades, AIAA J. 31 (1993) 1489–1497, http://dx.doi.org/10.2514/3.49082.
[59] I. Elishakoff, N. Zaza, J. Curtin, J. Hashemi, Apparently first closed-form solution for vibration of functionally graded rotating beams, AIAA J. 52 (2014) 2587–2593, http://dx.doi.org/10.2514/1.J053033.
[60] F. Ebrahimi, M. Hashemi, On vibration behavior of rotating functionally graded double-tapered beam with the effect of porosities, Proc. Inst. Mech. Eng. Part G J. Aerosp. Eng. (2015), http://dx.doi.org/10.1177/0954410015619647.
[61] S. Kumar, A. Mitra, Large amplitude free vibration analysis of axially functionally graded tapered rotating beam by energy method, Mech. Mach. Sci. 23 (2015) 473–483, http://dx.doi.org/10.1007/978-3-319-09918-7.
[62] B.K. Jiang, J. Xu, Y.H. Li, Flapwise vibration analysis of a rotating composite beam under hygrothermal environment, Compos. Struct. 117 (2014) 201–211, http://dx.doi.org/10.1016/j.compstruct.2014.04.008.
[63] C. DeValve, R. Pitchumani, Analysis of vibration damping in a rotating composite beam with embedded carbon nanotubes, Compos. Struct. 110 (2014) 289–296, http://dx.doi.org/10.1016/j.compstruct.2013.12.007.
[64] S.K. Sinha, Transient response of a multilayered composite rotating airfoil under slicing-impact loading, AIAA J. 52 (2014) 2701–2711, http://dx.doi.org/10.2514/1.J052888.
[65] R.-A. Jafari-Talookolaei, Analytical solution for the free vibration characteristics of the rotating composite beams with a delamination, Aerosp. Sci. Technol. 45 (2015) 346–358, http://dx.doi.org/10.1016/j.ast.2015.06.009.
[66] H.H. Yoo, S.H. Lee, S.H. Shin, Flapwise bending vibration analysis of rotating multi-layered composite beams, J. Sound Vib. 286 (2005) 745–761, http://dx.doi.org/10.1016/j.jsv.2004.10.007.
[67] O.O. Ozgumus, M.O. Kaya, Energy expressions and free vibration analysis of a rotating Timoshenko beam featuring bending – bending-torsion coupling, Arch. Appl. Mech. 83 (2013) 97–108, http://dx.doi.org/10.1007/s00419-012-0634-4.
[68] O. Ozdemir, M.O. Kaya, Energy derivation and extension-flapwise bending vibration analysis of a rotating piezolaminated composite timoshenko beam, Mech. Adv. Mater. Struct. 21 (2014) 477–489, http://dx.doi.org/10.1080/15376494.2012.697606.
[69] N.V.R. Maganti, M.R. Nalluri, Chordwise bending vibration analysis of functionally graded double-tapered rotating beams, Int. J. Comput. Methods Eng. Sci. Mech. (2014).
[70] M.N.V. Ramesh, N.M. Rao, Free vibration analysis of rotating functionally-graded cantilever beams, Int. J. Acoust. Vib. 19 (2014) 31–41.
[71] T. Aksencer, M. Aydogdu, Flapwise vibration of rotating composite beams, Compos. Struct. 134 (2015) 672–679, http://dx.doi.org/10.1016/j.compstruct.2015.08.130.
[72] F. Ebrahimi, M. Mokhtari, Vibration analysis of spinning exponentially functionally graded Timoshenko beams based on differential transform method, Proc. Inst. Mech. Eng. Part G J. Aerosp. Eng. 229 (2015) 2559–2571, http://dx.doi.org/10.1177/0954410015580801.
[73] N.V.R. Maganti, M.R. Nalluri, Flapwise bending vibration analysis of functionally graded rotating double-tapered beams, Int. J. Mech. Mater. Eng. 10 (2015) 21, http://dx.doi.org/10.1186/s40712-015-0040-0.
[74] R.-A. Jafari-Talookolaei, Analytical Solution for Vibration of a Rotating Delaminated Composite Beam with End Mass, Int. J. Struct. Stab. Dyn. (2015) 1550013, http://dx.doi.org/10.1142/S0219455415500133.
[75] F. Ebrahimi, M. Mokhtari, Transverse vibration analysis of rotating porous beam with functionally graded microstructure using the differential transform method, J. Braz. Soc. Mech. Sci. Eng. 37 (2015) 1435–1444, http://dx.doi.org/10.1007/s40430-014-0255-7.
[76] F. Ebrahimi, M. Mokhtari, Free vibration analysis of a rotating mori–tanaka-based functionally graded beam via differential transformation method, Arab. J. Sci. Eng. (2015) 577–590, http://dx.doi.org/10.1007/s13369-015-1689-7.
[77] J.-S. Fang, D. Zhou, Free Vibration analysis of rotating axially functionally graded tapered timoshenko beams, Int. J. Struct. Stab. Dyn. 16 (2016) 1550007, http://dx.doi.org/10.1142/S0219455415500078.
[78] H. Arvin, F. Bakhtiari-Nejad, Nonlinear free vibration analysis of rotating composite Timoshenko beams, Compos. Struct. 96 (2013) 29–43, http://dx.doi.org/10.1016/j.compstruct.2012.09.009.
[79] H. Arvin, W. Lacarbonara, A fully nonlinear dynamic formulation for rotating composite beams: nonlinear normal modes in flapping, Compos. Struct. 109 (2014) 93–105, http://dx.doi.org/10.1016/j.compstruct.2013.10.044.
[80] A.R. Atilgan, D.H. Hodges, Unified nonlinear analysis for nonhomogeneous anisotropic beams with closed cross sections, AIAA J. 29 (1991) 1990–1999, http://dx.doi.org/10.2514/3.10829.
[81] V.L. Berdichevskii, On the energy of an elastic rod, J. Appl. Math. Mech. 45 (1981) 518–529, http://dx.doi.org/10.1016/0021-8928(81)90097-6.
[82] C.E.S. Cesnik, D.H. Hodges, VABS: a new concept for composite Rotor blade cross-sectional Modeling, J. Am. Helicopter Soc. 42 (1997) 27, http://dx.doi.org/10.4050/JAHS.42.27.
[83] W. Yu, D.H. Hodges, J.C. Ho, Variational asymptotic beam sectional analysis - An updated version, Int. J. Eng. Sci. 59 (2012) 40–64, http://dx.doi.org/10.1016/j.ijengsci.2012.03.006.
[84] W. Yu, VABS Manual for Users, Dep. Mech. Aerosp. Eng. Utah State Univ. Logan, Utah. (2011), pp. 1–22.
[85] D.A. Danielson, D.H. Hodges, Nonlinear beam kinematics by decomposition of the rotation tensor, J. Appl. Mech. 54 (1987) 258–262, http://dx.doi.org/10.1115/1.3173004.
[86] D.H. Hodges, Geometrically exact, intrinsic theory for dynamics of curved and twisted anisotropic beams, AIAA J. 41 (2003) 1131–1137.
[87] Z. Sotoudeh, D.H. Hodges, Structural dynamics analysis of rotating blades using fully intrinsic equations, Part I: formulation and verification of single-load-path configurations, J. Am. Helicopter Soc. 58 (2013) 1–9, http://dx.doi.org/10.4050/JAHS.58.032003.
[88] Z. Sotoudeh, D.H. Hodges, Structural dynamics analysis of rotating blades using fully intrinsic equations, Part II: dual-load-path configurations, J. Am. Helicopter Soc. 58 (2013) 1–9, http://dx.doi.org/10.4050/JAHS.58.032004.
[89] D.H. Hodges, Modeling of Composite Beams and Plates for Static and Dynamic Analysis, 1990.
[90] C.E.S. Cesnik, D.H. Hodges, V.G. Sutyrin, Cross-sectional analysis of composite

beams including large initial twist and curvature effects, AIAA J. 34 (1996) 1913–1920, http://dx.doi.org/10.2514/3.13325.
[91] W. Yu, D.H. Hodges, V. Volovoi, C.E.S. Cesnik, On Timoshenko-like modeling of initially curved and twisted composite beams, Int. J. Solids Struct. 39 (2002) 5101–5121, http://dx.doi.org/10.1016/S0020-7683(02)00399-2.
[92] D.H. Hodges, H. Saberi, R.A. Ormiston, Development of nonlinear beam elements for rotorcraft comprehensive analyses, J. Am. Helicopter Soc. 52 (2007) 36, http://dx.doi.org/10.4050/JAHS.52.36.
[93] M.J. Patil, M. Althoff, Energy-consistent, Galerkin approach for the nonlinear dynamics of beams using intrinsic equations, J. Vib. Control. 17 (2011) 1748–1758, http://dx.doi.org/10.1177/1077546310385777.
[94] M. Althoff, M.J. Patil, J.P. Traugott, Nonlinear modeling and control design of active Helicopter blades, J. Am. Helicopter Soc. 57 (2012) 1–18, http://dx.doi.org/10.4050/Jahs.57.012002.
[95] M. Rafiee, F. Nitzsche, M. Labrosse, Rotating nanocomposite thin-walled beams undergoing large deformation, Compos. Struct. 150 (2016) 191–199, http://dx.doi.org/10.1016/j.compstruct.2016.05.014.
[96] F. Bekhoucha, S. Rechak, L. Duigou, J. Cadou, Nonlinear forced vibrations of rotating anisotropic beams, Nonlinear Dyn. 74 (2013) 1281–1296, http://dx.doi.org/10.1007/s11071-013-1040-3.
[97] M. Ghorashi, F. Nitzsche, Nonlinear dynamic response of an accelerating composite rotor blade using perturbations, J. Mech. Mater. Struct. 4 (2009) 693–718.
[98] M. Ghorashi, Nonlinear analysis of the dynamics of articulated composite rotor blades, Nonlinear Dyn. 67 (2012) 227–249, http://dx.doi.org/10.1007/s11071-011-9974-9.
[99] M.R. Amoozgar, H. Shahverdi, Analysis of nonlinear fully intrinsic equations of geometrically exact beams using generalized differential quadrature method, Acta Mech. (2016), http://dx.doi.org/10.1007/s00707-015-1528-7.
[100] V. Berdichevsky, E. Armanios, A. Badir, Theory of anisotropic thin-walled closed-cross-section beams, Compos. Eng. 2 (1992) 411–432, http://dx.doi.org/10.1016/0961-9526(92)90035-5.
[101] E.A. Armanios, A.M. Badir, Free vibration analysis of anisotropic thin-walled closed-section beams, AIAA J. 33 (1995) 1905–1910, http://dx.doi.org/10.2514/3.12744.
[102] R.E.N. Yongsheng, Y. Shulian, D.U. Xianghong, Modeling and free vibration behavior of rotating composite thin-walled closed-section beams with SMA fibers, Chin. J. Mech. Eng. 25 (2012) 1029–1043, http://dx.doi.org/10.3901/CJME.2012.05.1029.
[103] C.E.S. Cesnik, S. Shin, On the modeling of integrally actuated helicopter blades, Int. J. Solids Struct. 38 (2001) 1765–1789, http://dx.doi.org/10.1016/S0020-7683(00)00135-9.
[104] C. Saxton, F.F. Afagh, Modelling and dynamic stability of a hingeless active fibre composite blade, Arch. Appl. Mech. 80 (2010) 843–868, http://dx.doi.org/10.1007/s00419-009-0344-8.
[105] J.-S. Park, J.-H. Kim, Design and aeroelastic analysis of active twist rotor blades incorporating single crystal macro fiber composite actuators, Compos. Part B Eng. 39 (2008) 1011–1025, http://dx.doi.org/10.1016/j.compositesb.2007.11.006.
[106] J.P. Traugott, M.J. Patil, F. Holzapfel, Nonlinear modeling of integrally actuated beams, Aerosp. Sci. Technol. 10 (2006) 509–518, http://dx.doi.org/10.1016/j.ast.2006.06.003.
[107] F. Bekhoucha, S. Rechak, L. Duigou, J. Cadou, Branch switching at Hopf bifurcation analysis via asymptotic numerical method: application to nonlinear free vibrations of rotating beams, Commun. Nonlinear Sci. Numer. Simul. 22 (2015) 716–730, http://dx.doi.org/10.1016/j.cnsns.2014.09.001.
[108] W. Yu, M. Blair, GEBT: a general-purpose nonlinear analysis tool for composite beams, Compos. Struct. 94 (2012) 2677–2689, http://dx.doi.org/10.1016/j.compstruct.2012.04.007.
[109] O. a. Bauchau, Computational schemes for flexible, nonlinear multi-body Systems, Multibody Syst. Dyn. 2 (1998) 169–225, http://dx.doi.org/10.1023/A:1009710818135.
[110] W. Johnson, Rotorcraft Aerodynamics Models for a Comprehensive Analysis, in: Am. Helicopter Soc. 54th Annu. Forum, Washington, DC, 1999.
[111] K. Wei, G. Meng, H. Lu, S. Zhu, Dynamic analysis of rotating electrorheological composite beams, in: Electrorheological Fluids Magnetorheol. Suspens. (ERMR 2004), WORLD SCIENTIFIC (2005), pp. 222–228. ⟨http://dx.doi.org/10.1142/9789812702197_0034⟩.
[112] K. Wei, G. Meng, S. Zhou, J. Liu, Vibration control of variable speed/acceleration rotating beams using smart materials, J. Sound Vib. 298 (2006) 1150–1158, http://dx.doi.org/10.1016/j.jsv.2006.05.033.
[113] H. Zarrinzadeh, R. Attarnejad, A. Shahba, Free vibration of rotating axially functionally graded tapered beams, Proc. Inst. Mech. Eng. Part G J. Aerosp. Eng. 226 (2011) 363–379, http://dx.doi.org/10.1177/0954410011413531.
[114] B.P. Deepak, R. Ganguli, S. Gopalakrishnan, Dynamics of rotating composite beams: a comparative study between CNT reinforced polymer composite beams and laminated composite beams using spectral finite elements, Int. J. Mech. Sci. 64 (2012) 110–126, http://dx.doi.org/10.1016/j.ijmecsci.2012.07.009.
[115] A. Allahverdizadeh, J. Mahjoob, I. Eshraghi, P. Asgharifard, Effects of electrorheological fluid core and functionally graded layers on the vibration behavior of a rotating composite beam, Meccanica 47 (2012) 1945–1960, http://dx.doi.org/10.1007/s11012-012-9566-x.
[116] A. Allahverdizadeh, M.J. Mahjoob, N. Nasrollahzadeh, I. Eshraghi, Optimal parameters estimation and vibration control of a viscoelastic adaptive sandwich beam incorporating an electrorheological fluid layer, J. Vib. Control. 20 (2014) 1855–1868, http://dx.doi.org/10.1177/1077546313483159.
[117] S.N. Jung, S.J. Kim, Aeroelastic response of composite rotor blades considering transverse shear and structural damping, AIAA J. 32 (1994) 820–827, http://dx.doi.org/10.2514/3.12059.
[118] B.P. Patel, M. Ganapathi, M. Touratier, Free vibrations analysis of laminated composite rotating beam using C1 shear flexible element, Def. Sci. J. 49 (1999) 3–8.
[119] A. Baz, J. Ro, Vibration control of rotating beams with active constrained layer damping, Smart Mater. Struct. 10 (2001) 112–120, http://dx.doi.org/10.1088/0964-1726/10/1/311.
[120] K. Wei, G. Meng, W. Zhang, S. Zhou, Vibration characteristics of rotating sandwich beams filled with electrorheological fluids, J. Intell. Mater. Syst. Struct. 18 (2007) 1165–1173, http://dx.doi.org/10.1177/1045389×06072380.
[121] C.M. Saravia, S.P. Machado, V.H. Cortínez, Free vibration and dynamic stability of rotating thin-walled composite beams, Eur. J. Mech. / A Solids 30 (2011) 432–441, http://dx.doi.org/10.1016/j.euromechsol.2010.12.015.
[122] E. Carrera, M. Filippi, E. Zappino, Free vibration analysis of rotating composite blades via Carrera Unified Formulation, Compos. Struct. 106 (2013) 317–325, http://dx.doi.org/10.1016/j.compstruct.2013.05.055.
[123] R.-A. Jafari-Talookolaei, C. Della, Dynamic behavior of a rotating delaminated composite beam including rotary inertia and shear deformation effects, Ain Shams Eng. J. 6 (2015) 1031–1044, http://dx.doi.org/10.1016/j.asej.2015.03.002.
[124] T.H. Brockmann, R. Lammering, Finite beam Elements for rotating piezoelectric fiber composite structures Rotating Piezoelectric Fiber Composite Structures, in: K.J. Bathe (Ed.), Computational Fluid and Solid Mechanics, Elsevier, Amsterdam, 2003.
[125] T.H. Brockmann, R. Lammering, Beam finite elements for rotating piezoelectric fiber composite structures, J. Intell. Mater. Syst. Struct. 17 (2006) 431–448, http://dx.doi.org/10.1177/1045389×06058632.
[126] M.T. Piovan, R. Sampaio, A study on the dynamics of rotating beams with functionally graded properties, J. Sound Vib. 327 (2009) 134–143, http://dx.doi.org/10.1016/j.jsv.2009.06.015.
[127] K.M. Ravikumar, J.D. Humphrey, W. Hwang, Variable-order finite elements for nonlinear, fully intrinsic beam equations, J. Mech. Mater. Struct. 6 (2011) 479–493.
[128] M.C. Ray, D. Biswas, Active constrained layer damping of geometrically nonlinear vibration of rotating composite beams using 1-3 piezoelectric composite, Int. J. Mech. Mater. 9 (2013) 83–104, http://dx.doi.org/10.1007/s10999-012-9207-5.
[129] D. Thakkar, R. Ganguli, Helicopter vibration reduction in forward flight with induced-shear based piezoceramic actuation, Smart Mater. Struct. 13 (2004) 599–608, http://dx.doi.org/10.1088/0964-1726/13/3/01.
[130] S. Kumar, R. Kumar, Theoretical and experimental vibration analysis of rotating beams with combined ACLD and stressed layer damping treatment, Appl. Acoust. 74 (2013) 675–693, http://dx.doi.org/10.1016/j.apacoust.2012.11.002.
[131] C.-Y. Lin, L.-W. Chen, Dynamic stability of a rotating beam with a constrained damping layer, J. Sound Vib. 267 (2003) 209–225, http://dx.doi.org/10.1016/S0022-460X(02)01427-X.
[132] C.-Y. Lin, L.-W. Chen, Dynamic stability of rotating pre-twisted blades with a constrained damping layer, Compos. Struct. 61 (2003) 235–245, http://dx.doi.org/10.1016/S0263-8223(03)00048-5.
[133] M. Sabuncu, K. Evran, The dynamic stability of a rotating asymmetric cross-section Timoshenko beam subjected to lateral parametric excitation, Finite Elem. Anal. Des. 42 (2006) 454–469, http://dx.doi.org/10.1016/j.finel.2005.09.002.
[134] J.J. Epps, R. Chandra, The natural frequencies of rotating composite beams with tip sweep, J. Am. Helicopter Soc. 41 (1996) 29, http://dx.doi.org/10.4050/JAHS.41.29.
[135] S.W. Lee, Y.H. Kim, A new approach to the finite element modelling of beams with warping effect, Int. J. Numer. Methods Eng. 24 (1987) 2327–2341, http://dx.doi.org/10.1002/nme.1620241207.
[136] A.D. Stemple, S.W. Lee, Finite-element model for composite beams with arbitrary cross-sectional warping, AIAA J. 26 (1988) 1512–1520, http://dx.doi.org/10.2514/3.48797.
[137] A.D. Stemple, S.W. Lee, A finite element model for composite beams undergoing large deflection with arbitrary cross-sectional warping, Int. J. Numer. Methods Eng. 28 (1989) 2143–2160, http://dx.doi.org/10.1002/nme.1620280911.
[138] A.D. Stemple, Y.H. Kim, Vibration analysis of rotating composite beams using a finite element model with warping degrees of freedom, Comput. Mech. 16 (1995) 258–265.
[139] S.M. Jeon, I. Lee, Aeroelastic response and stability analysis of composite rotor blades in forward flight, Compos. Part B Eng. 32 (2001) 249–257, http://dx.doi.org/10.1016/S1359-8368(00)00061-5.
[140] Y.-J. Kee, J.-H. Kim, Vibration characteristics of initially twisted rotating shell type composite blades, Compos. Struct. 64 (2004) 151–159, http://dx.doi.org/10.1016/j.compstruct.2003.07.001.
[141] H.J. Lin, J.F. Tsai, Analysis of underwater free vibrations of a composite propeller blade, J. Reinf. Plast. Compos. 27 (2008) 447–458, http://dx.doi.org/10.1177/0731684407082539.
[142] Z.-c. Qiu, Y.-f. Xu, Vibration control of a rotating two-connected flexible beam using chattering-free sliding mode controllers, Proc. Inst. Mech. Eng. Part G J. Aerosp. Eng. 230 (2015) 444–468, http://dx.doi.org/10.1177/0954410015592436.
[143] H.-J. Lin, J.-J. Lin, Nonlinear hydroelastic behavior of propellers using a finite-element method and lifting surface theory, J. Mar. Sci. Technol. 1 (1996) 114–124, http://dx.doi.org/10.1007/BF02391167.
[144] A. Chattopadhyay, Q. Liu, H. Gu, Vibration reduction in rotor blades using active composite box beam, AIAA J. 38 (2000) 1125–1131, http://dx.doi.org/10.2514/2.1097.
[145] Y.-J. Kee, S.-J. Shin, Structural dynamic modeling for rotating blades using three dimensional finite elements, J. Mech. Sci. Technol. 29 (2015) 1607–1618, http://

dx.doi.org/10.1007/s12206-015-0332-6.
[146] S.S. Rao, M. Sunar, Piezoelectricity and its use in disturbance sensing and control of flexible structures - a survey, Appl. Mech. Rev. 47 (1994) 113–124.
[147] E.F. Crawley, Intelligent structures for aerospace - a technology overview and assessment, AIAA J. 32 (1994) 1689–1699, http://dx.doi.org/10.2514/3.12161.
[148] C.Y.K. Chee, L.Y. Tong, G.P. Steven, A review on the modelling of piezoelectric sensors and actuators incorporated in Intelligent structures, J. Intell. Mater. Syst. Struct. 9 (2006) 928–940 (doi:0803973233).
[149] I. Chopra, Review of state of art of smart structures and integrated systems, AIAA J. 40 (2002) 16–19.
[150] R. Ganguli, S.R. Viswamurthy, D. Thakkar, Smart Helicopter Rotors, Springer, London, 2016, http://dx.doi.org/10.1007/978-3-319-24768-7.
[151] A.A. Bent, N.W. Hagood, J.P. Rodgers, Anisotropic actuation with piezoelectric fiber composites, J. Intell. Mater. Syst. Struct. 6 (1995) 338–349, http://dx.doi.org/10.1177/1045389×9500600305.
[152] W.K. Wilkie, K.C. Park, An aeroelastic analysis of helicopter rotor blades incorporating piezoelectric fiber composite twist actuation, NASA TM-110252. NASA TM-11 ARL-MR-328, 1996.
[153] N. Mallik, M.C. Ray, Exact solutions for the analysis of piezoelectric fiber reinforced composites as distributed actuators for smart composite plates, Int. J. Mech. Mater. Des. 1 (2004) 347–364, http://dx.doi.org/10.1007/s10999-005-0516-9.
[154] D. Li, S.-C.M. Ho, G. Song, L. Ren, H. Li, A review of damage detection methods for wind turbine blades, Smart Mater. Struct. 24 (2015) 33001, http://dx.doi.org/10.1088/0964-1726/24/3/033001.
[155] S. Lin, I. Mao, J. Lin, Vibration of a rotating smart beam, AIAA J. 45 (2007) 382–389, http://dx.doi.org/10.2514/1.24692.
[156] K. Singh, J. Sirohi, I. Chopra, An improved shape memory alloy actuator for rotor blade tracking, J. Intell. Mater. Syst. Struct. 14 (2003) 767–786, http://dx.doi.org/10.1177/104538903039134.
[157] V. Giurgiutiu, Review of smart-materials actuation solutions for aeroelastic and vibration control, J. Intell. Mater. Syst. Struct. 11 (2000) 525–544, http://dx.doi.org/10.1106/HYTV-NC7R-BCMM-W3CH.
[158] R. Alkhatib, M.F. Golnaraghi, Active structural vibration control: a review, Shock Vib. Dig. 35 (2003) 367, http://dx.doi.org/10.1177/05831024030355002.
[159] P.P. Friedmann, On-Blade control of rotor vibration, noise, and performance: just around the corner? The 33rd Alexander Nikolsky honorary lecture, J. Am. Helicopter Soc. 59 (2014) 1–37, http://dx.doi.org/10.4050/JAHS.59.041001.
[160] S.B. Choi, M.S. Han, Vibration control of a rotating cantilevered beam using piezoactuators: experimental work, J. Sound Vib. 277 (2004) 436–442, http://dx.doi.org/10.1016/j.jsv.2003.11.021.
[161] S.-C. Choi, J.-S. Park, J.-H. Kim, Active damping of rotating composite thin-walled beams using MFC actuators and PVDF sensors, Compos. Struct. 76 (2006) 362–374, http://dx.doi.org/10.1016/j.compstruct.2005.05.010.
[162] M.N. Svendsen, S. Krenk, J. Hogsberg, Resonant vibration control of rotating beams, J. Sound Vib. 330 (2011) 1877–1890, http://dx.doi.org/10.1016/j.jsv.2010.11.008.
[163] J.K. Shim, S. Na, Modeling and vibration feedback control of rotating tapered composite thin-walled blade, KSME Int. J. 17 (2003) 380–390, http://dx.doi.org/10.1007/BF02984364.
[164] J.-S. Park, J.-H. Kim, Analytical development of single crystal Macro Fiber Composite actuators for active twist rotor blades, Smart Mater. Struct. 14 (2005) 745–753, http://dx.doi.org/10.1088/0964-1726/14/4/033.
[165] C.D. Shete, N.K. Chandiramani, Optimal control of a pretwisted shearable smart composite rotating beam, Acta Mech. 191 (2007) 37–58, http://dx.doi.org/10.1007/s00707-007-0443-y.
[166] A. Chattopadhyay, J.-S. Kim, Q. Liu, Aeromechanical stability analysis and control of smart composite rotor blades, J. Vib. Control. 8 (2002) 847–860, http://dx.doi.org/10.1177/1077546029187.
[167] D.N. Vadiraja, A.D. Sahasrabudhe, Vibration analysis and optimal control of rotating pre-twisted thin-walled beams using MFC actuators and sensors, Thin-Walled Struct. 47 (2009) 555–567, http://dx.doi.org/10.1016/j.tws.2008.10.004.
[168] D. Patt, L. Liu, P.P. Friedmann, Simultaneous vibration and noise reduction in rotorcraft using aeroelastic simulation, J. Am. Helicopter Soc. 51 (2006) 127, http://dx.doi.org/10.4050/JAHS.51.127.
[169] L. Liu, P.P. Friedmann, I. Kim, D.S. Bernstein, Rotor performance enhancement and vibration reduction in presence of dynamic stall using actively controlled flaps, J. Am. Helicopter Soc. 53 (2008) 338, http://dx.doi.org/10.4050/JAHS.53.338.
[170] M. Gennaretti, L. Poloni, F. Nitzsche, "Smart spring" identification for hovering rotor aeroelastic-stability augmentation, Aeronaut. J. 107 (2003) 233–240.
[171] F.F. Afagh, F. Nitzsche, N. Morozova, Dynamic modelling and stability of hingeless helicopter blades with a smart spring, Aeronaut. J. 108 (2004) 369–378.
[172] F. Nitzsche, D.G. Zimcik, V.K. Wickramasinghe, C. Yong, Control laws for an active tunable vibration absorber designed for rotor blade damping augmentation, Aeronaut. J. 108 (2004) 35–42.
[173] F. Nitzsche, Development of a maximum energy extraction control for the smart spring, J. Intell. Mater. Syst. Struct. 16 (2005) 1057–1066, http://dx.doi.org/10.1177/1045389×05059964.
[174] G. Oxley, F. Nitzsche, D. Feszty, Smart spring control of vibration on helicopter rotor blades, J. Aircr. 46 (2009) 692–696, http://dx.doi.org/10.2514/1.27914.
[175] J. Austruy, F. Gandhi, N. Lieven, Rotor vibration reduction using an embedded spanwise absorber, J. Am. Helicopter Soc. 57 (2012) 49–60, http://dx.doi.org/10.4050/JAHS.57.022008.
[176] P. Lv, S. Prothin, F. Mohd-Zawawi, E. Benard, J. Morlier, J.-M. Moschetta, Performance improvement of small-scale rotors by passive blade twist control, J. Fluids Struct. 55 (2015) 25–41, http://dx.doi.org/10.1016/j.jfluidstructs.2015.01.008.
[177] J. Ro, A. Baz, Vibration control of plates using self-sensing active constrained layer damping, Smart Mater. Struct. 5 (1996) 272–280, http://dx.doi.org/10.1117/12.349783.
[178] P. Machado, M.T. Piovan, Nonlinear dynamics of rotating box FGM beams using nonlinear normal modes, Thin-Walled Struct. J. 62 (2013) 158–168, http://dx.doi.org/10.1016/j.tws.2012.09.005.
[179] L. Li, D.G. Zhang, W.D. Zhu, Free vibration analysis of a rotating hub–functionally graded material beam system with the dynamic stiffening effect, J. Sound Vib. 333 (2014) 1526–1541, http://dx.doi.org/10.1016/j.jsv.2013.11.001.
[180] R. Inala, S. Mohanty, Flap wise bending vibration and dynamic stability of rotating functionally graded material plates in thermal environments, Proc. Inst. Mech. Eng. Part G J. Aerosp. Eng. (2016), http://dx.doi.org/10.1177/0954410016636152.
[181] S. Na, K.-W. Kim, B.-H. Lee, P. Marzocca, Dynamic response analysis of rotating functionally graded thin-walled blades exposed to steady temperature and external excitation, J. Therm. Stress. 32 (2009) 209–225, http://dx.doi.org/10.1080/01495730802507956.
[182] E.T. Thostenson, W.Z. Li, D.Z. Wang, Z.F. Ren, T.W. Chou, Carbon nanotube/carbon fiber hybrid multiscale composites, J. Appl. Phys. 91 (2002) 6034–6037, http://dx.doi.org/10.1063/1.1466880.
[183] E.T. Thostenson, T.-W. Chou, Aligned multi-walled carbon nanotube-reinforced composites: processing and mechanical characterization, J. Phys. D. Appl. Phys. 35 (2002) L77–L80, http://dx.doi.org/10.1088/0022-3727/35/16/103.
[184] X.Q. He, M. Rafiee, S. Mareishi, K.M. Liew, Large amplitude vibration of fractionally damped viscoelastic CNTs/fiber/polymer multiscale composite beams, Compos. Struct. 131 (2015) 1111–1123, http://dx.doi.org/10.1016/j.compstruct.2015.06.038.
[185] B. Glaz, J. Riddick, E. Habtour, H. Kang, Interfacial strain energy dissipation in hybrid nanocomposite beams under axial strain fields, AIAA J. 53 (2015) 1544–1554, http://dx.doi.org/10.2514/1.J053390.
[186] S.V. Hoa, Vibration frequency of a curved beam with tip mass, J. Sound Vib. 61 (1978) 427–436, http://dx.doi.org/10.1016/0022-460X(78)90390-5.
[187] S.V. Hoa, Vibration of a rotating beam with tip mass, J. Sound Vib. 67 (1979) 369–381, http://dx.doi.org/10.1016/0022-460X(79)90542-X.
[188] S.H. Lai, Geometrically nonlinear transient analysis of a rotating beam structure carrying a static payload, Mech. Res. Commun. 21 (1994) 473–482.
[189] G.P. Cai, J.Z. Hong, S.X. Yang, Dynamic analysis of a flexible hub-beam system with tip mass, Mech. Res. Commun. 32 (2005) 173–190, http://dx.doi.org/10.1016/j.mechrescom.2004.02.007.
[190] D. Das, P. Sahoo, K. Saha, Out-of-plane free vibration analysis of rotating tapered beams in post-elastic regime, Mater. Des. 30 (2009) 2875–2894, http://dx.doi.org/10.1016/j.matdes.2009.01.011.
[191] L. Li, D. Zhang, Dynamic analysis of rotating axially FG tapered beams based on a new rigid–flexible coupled dynamic model using the B-spline method, Compos. Struct. 124 (2015) 357–367, http://dx.doi.org/10.1016/j.compstruct.2015.01.018.
[192] N. Shafiei, A. Mousavi, M. Ghadiri, Vibration behavior of a rotating non-uniform FG microbeam based on the modified couple stress theory and GDQEM, Compos. Struct. 149 (2016) 157–169, http://dx.doi.org/10.1016/j.compstruct.2016.04.024.
[193] D.H. Hodges, X. Shang, C.E.S. Cesnik, Finite element solution of nonlinear intrinsic equations for curved composite beams, J. Am. Helicopter Soc. 41 (1996) 313, http://dx.doi.org/10.4050/JAHS.41.313.
[194] S.M. Lin, The instability and vibration of rotating beams with arbitrary pretwist and an elastically restrained root, J. Appl. Mech. 68 (2001) 844, http://dx.doi.org/10.1115/1.1408615.
[195] C.-Y. Lin, L.-W. Chen, Dynamic stability of rotating composite beams with a viscoelastic core, Compos. Struct. 58 (2002) 185–194, http://dx.doi.org/10.1016/S0263-8223(02)00127-7.
[196] S.A.A. Hosseini, S.E. Khadem, Vibration and reliability of a rotating beam with random properties under random excitation, Int. J. Mech. Sci. 49 (2007) 1377–1388, http://dx.doi.org/10.1016/j.ijmecsci.2007.04.008.
[197] S. Na, K. Kim, B. Lee, P. Marzocca, Dynamic response analysis of rotating functionally graded thin-walled blades exposed to steady temperature and external excitation, J. Therm. Stress. 32 (2009) 209–225, http://dx.doi.org/10.1080/01495730802507956.
[198] J.G. Yen, Effects of blade tip shape on dynamics, cost, weight, aerodynamic performance, and aeroelastic response, J. Am. Helicopter Soc. 39 (1994) 37, http://dx.doi.org/10.4050/JAHS.39.37.
[199] B.A.H. Abbas, Dynamic stability of a rotating Timoshenko beam with a flexible root, J. Sound Vib. 108 (1986) 25–32, http://dx.doi.org/10.1016/S0022-460X(86)80308-X.
[200] M.N. Hamdan, A.H. El-Sinawi, On the non-linear vibrations of an inextensible rotating arm with setting angle and flexible hub, J. Sound Vib. 281 (2005) 375–398, http://dx.doi.org/10.1016/j.jsv.2003.06.036.
[201] S.Y. Lee, Y.H. Kuo, Bending vibrations of a rotating non-uniform beam with an elastically restrained root, J. Sound Vib. 154 (1992) 441–451.
[202] S.M. Lin, S.Y. Lee, Free vibration of a rotating non-uniform beam with arbitrary pretwist, an elasticallyrestrained root and a tip mass, J. Sound Vib. 273 (2004) 477–492, http://dx.doi.org/10.1016/j.ijmecsci.2004.08.002.
[203] S.-Y. Lee, J.-J. Sheu, S.-M. Lin, In-plane vibrational analysis of rotating curved beam with elastically restrained root, J. Sound Vib. 315 (2008) 1086–1102, http://dx.doi.org/10.1016/j.jsv.2008.02.011.
[204] B. Yardimoglu, D.J. Inman, Coupled bending-bending-torsion vibration of a

rotating pre-twisted beam with aerofoil cross-section and flexible root by finite element method, Shock Vib. 11 (2004) 637–646, http://dx.doi.org/10.1155/2004/702380.
[205] J. Montoya, Coupled bending and torsional vibrations in a twisted rotating blade, Brown Boveri Rev. 53 (1966) 216–230.
[206] K.H. Low, A note on the effect of hub inertia and payload on the vibration of a flexible slewing link, J. Sound Vib. 204 (1997) 823–828, http://dx.doi.org/10.1016/0002-9610(92)90118-B.
[207] J. Latalski, J. Warminski, G. Rega, Bending-twisting vibrations of a rotating hub-thin-walled composite beam system, Math. Mech. Solids (2016), http://dx.doi.org/10.1177/1081286516629768.
[208] D.C. Kammer, A.L. Schlack Jr, Effects of nonconstant spin rate on the vibration of a rotating beam, J. Appl. Mech. 54 (1987) 305–310 ⟨http://link.aip.org/link/?JAMCAV/54/305/1⟩.
[209] S.M. Yang, S.M. Tsao, Dynamics of a pretwisted blade under nonconstant rotating speed, Comput. Struct. 62 (1997) 643–651, http://dx.doi.org/10.1016/S0045-7949(96)00227-1.
[210] B.S. Kallesøe, Equations of motion for a rotor blade, including gravity, pitch action and rotor speed variations, Wind Energy 10 (2007) 209–230, http://dx.doi.org/10.1002/we.217.
[211] D.H. Hodges, E.H. Dowell, Nonlinear equations of motion for the elastic bending and torsion of twisted nuniniform rotor blades, 1974.
[212] D. Younesian, E. Esmailzadeh, Non-linear vibration of variable speed rotating viscoelastic beams, Nonlinear Dyn. 60 (2010) 193–205, http://dx.doi.org/10.1007/s11071-009-9589-6.
[213] M.H. Yao, Y.P. Chen, W. Zhang, Nonlinear vibrations of blade with varying rotating speed, Nonlinear Dyn. 68 (2011) 487–504, http://dx.doi.org/10.1007/s11071-011-0231-z.
[214] S. Stoykov, P. Ribeiro, Vibration analysis of rotating 3D beams by the p-version finite element method, Finite Elem. Anal. Des. 65 (2013) 76–88, http://dx.doi.org/10.1016/j.finel.2012.10.008.
[215] M.A. Eltaher, M.E. Khater, S.A. Emam, A review on nonlocal elastic models for bending, buckling, vibrations, and wave propagation of nanoscale beams, Appl. Math. Model. 40 (2015) 4109–4128, http://dx.doi.org/10.1016/j.apm.2015.11.026.
[216] P. Minguet, J. Dugundji, Experiments and analysis for composite blades under large deflections. II - dynamic behavior, AIAA J. 28 (1990) 1580–1588, http://dx.doi.org/10.2514/3.25256.
[217] A.V. Srinivasan, D.G. Cutts, H.T. Shu, D.L. Sharpe, O.A. Bauchau, Structural dynamics of a helicopter rotor blade system, J. Am. Helicopter Soc. 35 (1990) 75, http://dx.doi.org/10.4050/JAHS.35.75.
[218] O. Rand, Experimental investigation of periodically excited rotating composite rotor blades, J. Aircr. 28 (1991) 876–884, http://dx.doi.org/10.2514/3.46112.
[219] O. Rand, Experimental study of the natural frequencies of rotating thin-walled composite blades, Thin-Walled Struct. 21 (1995) 191–207, http://dx.doi.org/10.1016/0263-8231(94)00041-W.
[220] R. Chandra, I. Chopra, Structural behavior of two-cell composite rotor blades with elastic couplings, AIAA J. 30 (1992) 2914–2921, http://dx.doi.org/10.2514/3.11637.
[221] R. Chandra, I. Chopra, Analytical-experimental investigation of free-vibration characteristics of rotating composite I-beams, J. Aircr. 30 (1993) 927–934, http://dx.doi.org/10.2514/3.46436.
[222] S.J. Shin, C.E.S. Cesnik, W.K. Wilkie, M.L. Wilbur, Design and manufacturing of a model-scale active twist rotor prototype blade, J. Intell. Mater. Syst. Struct. 19 (2008) 1443–1456, http://dx.doi.org/10.1177/1045389×07088051.
[223] J.B. Min, K.P. Duffy, B.B. Choi, A.J. Provenza, N. Kray, Numerical modeling methodology and experimental study for piezoelectric vibration damping control of rotating composite fan blades, Comput. Struct. 128 (2013) 230–242, http://dx.doi.org/10.1016/j.compstruc.2013.06.001.
[224] Z.-c. Qiu, J.-d. Han, J.-g. Liu, Experiments on fuzzy sliding mode variable structure control for vibration suppression of a rotating flexible beam, J. Vib. Control. 21 (2013) 343–358, http://dx.doi.org/10.1177/1077546313487760.
[225] K.-V. Truong, H. Yeo, R.A. Ormiston, Structural dynamics modeling of rectangular rotor blades, Aerosp. Sci. Technol. 30 (2013) 293–305, http://dx.doi.org/10.1016/j.ast.2013.08.014.
[226] C. Gao, W.Q. Meeker, D. Mayton, Detecting cracks in aircraft engine fan blades using vibrothermography nondestructive evaluation, Reliab. Eng. Syst. Saf. 131 (2014) 229–235, http://dx.doi.org/10.1016/j.ress.2014.05.009.
[227] D. Kumar, C.E. Cesnik, New strategy for designing composite rotor blades with active flaps, J. Intell. Mater. Syst. Struct. (2015) 1–13, http://dx.doi.org/10.1177/1045389×15586446.
[228] E. Villeneuve, D. Harvey, D. Zimcik, R. Aubert, J. Perron, Piezoelectric deicing system for rotorcraft, J. Am. Helicopter Soc. 60 (2015) 1–12, http://dx.doi.org/10.4050/JAHS.60.042001.
[229] X.Q. Zhou, D.Y. Yu, X.Y. Shao, S.Q. Zhang, S. Wang, Research and applications of viscoelastic vibration damping materials: a review, Compos. Struct. 136 (2016) 460–480, http://dx.doi.org/10.1016/j.compstruct.2015.10.014.
[230] P.F. Pai, High-fidelity sectional analysis of warping functions, stiffness values and wave properties of beams, Eng. Struct. 67 (2014) 77–95, http://dx.doi.org/10.1016/j.engstruct.2014.02.034.
[231] W.K. Wilkie, D.J. Inman, J.W. High, R.B. Williams, Recent Developments in NASA Piezocomposite Actuator Technology, in: 9th Int. Conf. New Actuators, Breman (2004), pp. 1–4.
[232] I.A. Henslee, D.A. Miller, T. Tempero, Fatigue life characterization for piezoelectric macrofiber composites, Smart Mater. Struct. 21 (2012) 105037, http://dx.doi.org/10.1088/0964-1726/21/10/105037.
[233] L. Wang, M. Zhang, J. Li, X. Gong, W. Wen, Logic control of microfluidics with smart colloid, Lab Chip. 10 (2010) 2869–2874, http://dx.doi.org/10.1039/C0LC00003E.
[234] D.K. Jha, T. Kant, R.K. Singh, A critical review of recent research on functionally graded plates, Compos. Struct. 96 (2013) 833–849, http://dx.doi.org/10.1016/j.compstruct.2012.09.001.
[235] G. Ware, Y. Park, C. Zhang, Z. Liang, B. Wang, Processing and characterization of epoxy/carbon fiber/carbon nanotube multiscale composites fabricated using VARTM, in: Proceedings SAMPE 2007 Fall Tech. Conference, Cincinnati, OH (2007).
[236] S.A. Sina, H. Haddadpour, Axial – torsional vibrations of rotating pretwisted thin walled composite beams, Int. J. Mech. Sci. 80 (2014) 93–101, http://dx.doi.org/10.1016/j.ijmecsci.2013.12.018.
[237] S.W. Shaw, Modal reduction of a nonlinear rotating beam through nonlinear normal modes, J. Vib. Acoust. 124 (2002) 229–236, http://dx.doi.org/10.1115/1.1426071.
[238] B. Fallahi, S.H.Y. Lai, An improved numerical scheme for characterizing dynamic behavior of high-speed rotating elastic beam structures, Comput. Struct. 50 (1994) 749–755.
[239] J.M. Mayo, D. García-Vallejo, J. Domínguez, Study of the geometric stiffening effect: comparison of different formulations, Multibody Syst. Dyn. 11 (2004) 321–341, http://dx.doi.org/10.1023/B:MUBO.0000040799.63053.d9.
[240] J.-C. Piedbœuf, B. Moore, On the foreshortening effects of a rotating flexible beam using different modeling methods, Mech. Struct. Mach. 30 (2002) 83–102, http://dx.doi.org/10.1081/SME-120001478.
[241] I. Sharf, Geometric stiffening in multibody dynamics formulations, J. Guid. Control. Dyn. 18 (1995) 882–890, http://dx.doi.org/10.2514/3.21473.
[242] C. Ling, W. Yi, K. Mo, Free vibration analysis of rotating Euler beams at high angular velocity, Comput. Struct. 88 (2010) 991–1001, http://dx.doi.org/10.1016/j.compstruc.2010.06.001.
[243] Q. Wenzhong, S. Jincai, Q. Yang, Active control of vibration using a fuzzy control method, J. Sound Vib. 275 (2004) 917–930, http://dx.doi.org/10.1016/S0022-460X(03)00795-8.
[244] G.-P. Cai, C.W. Lim, Active control of a flexible hub-beam system using optimal tracking control method, Int. J. Mech. Sci. 48 (2006) 1150–1162, http://dx.doi.org/10.1016/j.ijmecsci.2006.05.003.
[245] J. Warminski, J. Latalski, Saturation control for a rotating thin-walled composite beam structure, Procedia Eng. 144 (2016) 713–720, http://dx.doi.org/10.1016/j.proeng.2016.05.073.

Chapter 3

3. Rotating nanocomposite thin-walled beams undergoing large deformation

as published* in Composite Structures 150 (2016) 191–199

https://doi.org/10.1016/j.compstruct.2016.05.014

*In accordance with University of Ottawa regulations, the contact email address has been removed from this article.

Foreword

In this chapter, a mathematical model describing the effective material properties of MWCNTs-reinforced multiscale laminated composites was used to study the nonlinear steady state static response and free vibrations of nonrotating and rotating composite beams. Being analytical, the proposed model allows for convenient parametric analyses and is less expensive than a finite element model. However, it does not resort to one-dimensional governing equations, and therefore, it is expected to be more accurate than theories assuming a-priori knowledge of the cross-sectional deformation.

Composite Structures 150 (2016) 191–199

Contents lists available at ScienceDirect

Composite Structures

journal homepage: www.elsevier.com/locate/compstruct

Rotating nanocomposite thin-walled beams undergoing large deformation

Mohammad Rafiee [a,*], Fred Nitzsche [b], Michel Labrosse [a]

[a] Department of Mechanical Engineering, University of Ottawa, 161 Louis Pasteur, Ottawa, ON K1N 6N5, Canada
[b] Department of Mechanical and Aerospace Engineering, Carleton University, 1125 Colonel By Drive, Ottawa, ON K1S 5B6, Canada

A R T I C L E   I N F O

Article history:
Received 11 December 2015
Revised 22 March 2016
Accepted 2 May 2016
Available online 3 May 2016

Keywords:
Thin-walled beams
Nonlinear response
Rotating beams
Carbon nanotube-reinforced multiscale composites
Nanocomposite blades
Galerkin method

A B S T R A C T

A computational model was developed to study the nonlinear steady state static response and free vibration of thin-walled carbon nanotubes/fiber/polymer laminated multiscale composite beams and blades. A set of nonlinear intrinsic equations describing the response of rotating cantilever composite beams undergoing large deformations was established. The main assumptions were small local strains and local rotations, large deflections and global rotations. Halpin–Tsai equations and fiber micromechanics were used to predict the bulk material properties of the multiscale nanocomposite. The carbon nanotubes (CNTs) were assumed to be uniformly distributed and randomly oriented through the epoxy resin matrix. Discretized by the Galerkin approximation, eigenvalues and vectors and nonlinear steady state static response of the nanocomposite beams and blades were calculated. The volume fraction of fibers, weight percentage of single-walled and multi-walled carbon nanotubes (SWCNTs and MWCNTs) and their aspect ratio were investigated through a detailed parametric study for their effects on the nonlinear response of nanotubes-reinforced moving beams. It was found that natural frequencies are significantly influenced by a small percentage of CNTs. It was also found that the SWCNTs reinforcement produces more pronounced effect in comparison with MWCNTs on the nonlinear steady state static response and natural frequencies of the composite beams.

1. Introduction

Nanocomposite materials reinforced with high aspect ratios and low density carbon nanotubes and microscale high strength fibers are a new generation of multifunctional, high-performance engineering composites that have attracted considerable attention in recent years due to their unique properties [1–8]. The most important characteristics of carbon nanotubes are their extremely high strength combined with excellent resilience. Therefore, the introduction of carbon nanotubes into polymeric composites may improve their applications in the fields of reinforcing composites, electronic devices and more. With carbon nanotubes, the change in reinforcement scale relative to carbon fibers offers an opportunity to combine the potential benefits of nanoscale reinforcement with those, well-established, of fibrous composites to create multiscale hybrid micro/nanocomposites.

The problem of modeling thin-walled laminated composite beam, or beam-like slender structures having an open or closed cross-section, using one dimensional condensed beam elements has drawn a significant amount of attention over the last decades. A number of investigations have been carried out to study different aspects of this problem [1–3,9–54]. The advent of advanced composite materials has been a strong stimulus for such developments. Moreover, their incorporation is likely to expand the use and capabilities of thin-walled beam structures. The new and stringent requirements imposed on aeronautical/aerospace, turbomachinery and shaft structural systems will be best met by such new types of material structures.

An intrinsic formulation developed by Hodges and his coworkers [9,10,16,20] which covers the anisotropic beams with large deformations and small strains. The approach extracted from a three-dimensional elasticity formulation provides two streams of analyses: one stream is concerned with the cross section, providing elastic constants that might be used in a suitable set of beam equations, and the other stream being the beam equations themselves. Kim and Dugundji [11] studied the nonlinear large amplitude vibration of composite helicopter blade under large static deflection. Their model is based on the use of Euler angles, harmonic balance, and the finite difference solution of the basic large deflection equations. Thin-walled composite beam have been extensively

* Corresponding author.
E-mail addresses:

http://dx.doi.org/10.1016/j.compstruct.2016.05.014
0263-8223/

investigated by Librescu and Song [13,14,21] and their co-workers, e.g. [17–19]. These authors developed and refined thin-walled beam models of an arbitrary, closed or open cross-section. A number of non-classical effects such as the anisotropy and heterogeneity of constituent materials, transverse shear, primary and secondary warping phenomena (Vlasov effect) are considered in their works, with the assumption that the cross-section is rigid in its own plane. In the analysis performed on rotating systems [14], the effects of the centrifugal and Coriolis forces were taken into account as well. Furthermore, the importance of shear effects in composite material was emphasized. A complete theory for free torsion and bending of anisotropic thin-walled beams with closed cross-sectional contours was developed by Johnson et al. [15] using the stress formulation. Fazelzadeh et al. [22] performed the vibration analysis of functionally graded thin-walled rotating blades under high temperature supersonic flow using the differential quadrature method. Ghorashi and Nitzsche [23] studied the nonlinear dynamic response of an accelerating composite rotor blade using perturbations. Shooshtari and Rafiee [24] developed a mathematical model to study the nonlinear free and forced vibration analysis of clamped functionally graded beams. The nonlinear analysis of the dynamics of articulated composite rotor blades was performed by Ghorashi et al. [25]. Patil and Althoff [26] and Althoff et al. [27] developed a nonlinear model based on the Galerkin method to investigate the nonlinear response of rotating composite blades using intrinsic equations. Allahverdizadeh et al. [28] investigated the effects of electrorheological fluid core and functionally graded layers on the vibration behavior of a rotating composite beam. Deepak et al. [29] presented a comparative study between CNT-reinforced polymer composite beams and laminated composite beams in dynamic analysis using spectral elements. Arvin and his coworkers [30,31,40] presented a geometrically exact approach to the overall dynamics of elastic rotating blades. In another set of studies, Arvin and Bakhtiari-Nejad [32,33] studied the nonlinear vibration analysis of rotating composite Timoshenko beams. Bekhoucha et al. [34] investigated the nonlinear forced vibrations of rotating anisotropic beams. Rafiee et al. [35,36] studied the nonlinear free and forced thermo-electro-aero-elastic vibration and dynamic response of piezoelectric functionally graded laminated composite shells. Large amplitude, free and forced oscillations of functionally graded beams were analyzed by Hosseini et al. [37]. Sinha [38] studied the transient response of a multilayered composite rotating airfoil under slicing-impact loading. The equations of motion for a rotating composite beam with a nonconstant rotation speed and an arbitrary preset angle were derived by Georgiades et al. [39]. Sina and Haddadpour [41] analyzed the axial–torsional vibrations of rotating pre-twisted thin-walled composite beams.

The nonlinear response of multiscale nanocomposites and CNT-reinforced non-rotating composite beams and beam-type structures is also reported in the literature. A significant contribution in this area was made by Rafiee and his coworkers [1–3,42–48]. For example, they investigated the large amplitude free vibration [42,43], buckling and post buckling [44] and energy harvesting [45] in piezoelectric two-phase nanocomposite beams. They also considered large deformation and stress [1,46], post-buckling [46], nonlinear vibration [3,46], nonlinear dynamic stability [47] and piezoelectric power scavenging [48] in shear deformable piezoelectric laminated nanocomposite plates. Recently, He et al. [2] developed a study to investigate the large amplitude vibration of fractionally damped viscoelastic CNTs/fiber/polymer multiscale composite beams.

Even though the nonlinear analysis of rotating composite beams made of advanced materials is of a great importance, to date, no mathematical model has been available for the nonlinear deformation of CNTs-reinforced rotating composite beams or blades. Three dimensional finite-element methods (FEM), while possible, would be expensive. Ad hoc theories (e.g. von Karman and inextentional beam theories) based on the assumption of some a priori cross-sectional deformation, on the other hand, may lack accuracy [9] owing to one dimensional governing equations.

In the present work, we investigate the nonlinear steady state static response and vibration of CNTs/fiber/polymer laminated multiscale composite beams. A set of nonlinear, intrinsic equations describing the response of rotating cantilever composite beams undergoing large deformations is established. The main assumptions relate to small local strains and local rotations, large deflections and global rotations. The Halpin–Tsai equations and fiber micromechanics are used in hierarchy to predict the bulk material properties of the multiscale nanocomposite. The carbon nanotubes were assumed to be uniformly distributed and randomly oriented through the epoxy resin matrix. The nanocomposite beams and blades were discretized by the Galerkin approximation, and their eigenvalues, eigenvectors and nonlinear steady state static response calculated. The volume fraction of fibers, the weight percentage of single-walled and multi-walled carbon nanotubes (SWCNTs and MWCNTs), and their aspect ratio were investigated through a detailed parametric study for their effects on the nonlinear response of nanotubes-reinforced moving beams.

2. Theoretical formulation

The nonlinear, intrinsic, mixed equations for the dynamics of a general (nonuniform, twisted, curved, anisotropic) beam (See Fig. 1) undergoing small strains and large deformations are given below based on the generalized Timoshenko beam model [9]:

$$\mathbf{F}' + \left(\tilde{\mathbf{k}} + \tilde{\boldsymbol{\kappa}}\right)\mathbf{F} + \mathbf{f} = \dot{\mathbf{P}} + \tilde{\boldsymbol{\Omega}}\mathbf{P} \tag{1a}$$

$$\mathbf{M}' + \left(\tilde{\mathbf{k}} + \tilde{\boldsymbol{\kappa}}\right)\mathbf{M} + (\tilde{\mathbf{e}}_1 + \tilde{\gamma})\mathbf{F} + \mathbf{m} = \dot{\mathbf{H}} + \tilde{\boldsymbol{\Omega}}\mathbf{H} + \tilde{\mathbf{V}}\mathbf{P} \tag{1b}$$

$$\mathbf{V}' + \left(\tilde{\mathbf{k}} + \tilde{\boldsymbol{\kappa}}\right)\mathbf{V} + (\tilde{\mathbf{e}}_1 + \tilde{\gamma})\boldsymbol{\Omega} = \dot{\gamma} \tag{1c}$$

$$\boldsymbol{\Omega}' + \left(\tilde{\mathbf{k}} + \tilde{\boldsymbol{\kappa}}\right)\boldsymbol{\Omega} = \dot{\boldsymbol{\kappa}} \tag{1d}$$

where the prime denotes the partial derivative with respect to the undeformed beam reference line defined by the curvilinear coordinate x, the over dot denotes the partial derivative with respect to the time t; and internal forces $\mathbf{F} = [F_1\ F_2\ F_3]^{\mathrm{T}}$, internal moments $\mathbf{M} = [M_1\ M_2\ M_3]^{\mathrm{T}}$, generalized force strains $\gamma = [\gamma_{11} 2\gamma_{12} 2\gamma_{13}]^{\mathrm{T}}$,

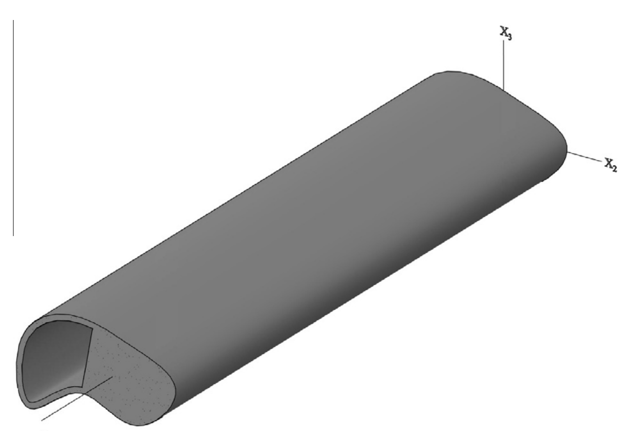

Fig. 1. General configuration of a nanocomposite beam with arbitrary cross-section.

generalized moment strains $\boldsymbol{\kappa} = [\kappa_1\ \kappa_2\ \kappa_3]^{\mathrm{T}}$, generalized curvatures $\mathbf{K} = [K_1\ K_2\ K_3]^{\mathrm{T}}$, linear momentums $\mathbf{P} = [P_1\ P_2\ P_3]^{\mathrm{T}}$, angular momentums $\mathbf{H} = [H_1\ H_2\ H_3]^{\mathrm{T}}$, linear velocities $\mathbf{V} = [V_1\ V_2\ V_3]^{\mathrm{T}}$, angular velocities $\boldsymbol{\Omega} = [\Omega_1\ \Omega_2\ \Omega_3]^{\mathrm{T}}$, and external forces $\mathbf{f} = [f_1\ f_2\ f_3]^{\mathrm{T}}$; and external moments $\mathbf{m} = [m_1\ m_2\ m_3]^{\mathrm{T}}$; γ_{11} is the extensional strain measure, and $2\gamma_{12}$ and $2\gamma_{13}$ are the transverse shear measures; and, finally, the tilde over certain terms denotes a skew-symmetric matrix (pseudovector) of the components of the column matrix of the same name, namely,

$$\widetilde{\mathbf{K}} = \tilde{\mathbf{k}} + \tilde{\boldsymbol{\kappa}} = \begin{bmatrix} 0 & -K_3 & K_2 \\ K_3 & 0 & -K_1 \\ -K_2 & K_1 & 0 \end{bmatrix}. \tag{2}$$

All measure numbers are calculated in the deformed cross-sectional frame. $\mathbf{k} = [k_1\ k_2\ k_3]^{\mathrm{T}}, k_1$ is the initial twist, k_2 and k_3 are the initial curvatures of the beam, and $\mathbf{e}_1 = [1\ 0\ 0]^{\mathrm{T}}$.

2.1. Constitutive equations

The generalized forces are related to the generalized strains via

$$\begin{Bmatrix} \gamma_{11} \\ 2\gamma_{12} \\ 2\gamma_{13} \\ \kappa_1 \\ \kappa_2 \\ \kappa_3 \end{Bmatrix} = \begin{bmatrix} R_{11} & R_{12} & R_{13} & S_{11} & S_{12} & S_{13} \\ R_{12} & R_{22} & R_{23} & S_{21} & S_{22} & S_{23} \\ R_{13} & R_{23} & R_{33} & S_{31} & S_{32} & S_{33} \\ S_{11} & S_{21} & S_{31} & T_{11} & T_{12} & T_{13} \\ S_{12} & S_{22} & S_{32} & T_{12} & T_{22} & T_{23} \\ S_{13} & S_{23} & S_{33} & T_{13} & T_{23} & T_{33} \end{bmatrix} \begin{Bmatrix} F_1 \\ F_2 \\ F_3 \\ M_1 \\ M_2 \\ M_3 \end{Bmatrix}. \tag{3}$$

The coefficients $R_{11}; R_{12}, \ldots, T_{33}$ are cross-sectional flexibility coefficients that can be obtained using the analytical thin-walled theory [15] or computational finite-element analysis [12,55] for general configurations. Being linear, the present material law is only valid for small local strains, which can, however, lead to large global deformations.

The generalized momenta are related to the generalized velocities via the cross-sectional beam inertia,

$$\begin{Bmatrix} P_1 \\ P_2 \\ P_3 \\ H_1 \\ H_2 \\ H_3 \end{Bmatrix} = \begin{bmatrix} \mu & 0 & 0 & 0 & \mu\bar{x}_3 & -\mu\bar{x}_2 \\ 0 & \mu & 0 & -\mu\bar{x}_3 & 0 & 0 \\ 0 & 0 & \mu & \mu\bar{x}_2 & 0 & 0 \\ 0 & -\mu\bar{x}_3 & \mu\bar{x}_2 & i_2 + i_3 & 0 & 0 \\ \mu\bar{x}_3 & 0 & 0 & 0 & i_2 & i_{23} \\ -\mu\bar{x}_2 & 0 & 0 & 0 & i_{23} & i_3 \end{bmatrix} \begin{Bmatrix} V_1 \\ V_2 \\ V_3 \\ \Omega_1 \\ \Omega_2 \\ \Omega_3 \end{Bmatrix}, \tag{4}$$

where $\mu(x)$ is the mass per unit length, $\bar{x}_2$ and $\bar{x}_3$ are offsets from the reference line of the cross sectional mass centroid; and i_2, i_3, and i_{23} are cross-sectional mass moments and product of inertia. Eqs. (3) and (4) may also be written as

$$\begin{Bmatrix} \boldsymbol{\gamma} \\ \boldsymbol{\kappa} \end{Bmatrix} = \begin{bmatrix} \mathbf{R} & \mathbf{S} \\ \mathbf{S}^{\mathrm{T}} & \mathbf{T} \end{bmatrix} \begin{Bmatrix} \mathbf{F} \\ \mathbf{M} \end{Bmatrix}, \tag{5a}$$

$$\begin{Bmatrix} \mathbf{P} \\ \mathbf{H} \end{Bmatrix} = \begin{bmatrix} \mathbf{G} & \mathbb{k} \\ \mathbb{k}^{\mathrm{T}} & \mathbf{I} \end{bmatrix} \begin{Bmatrix} \mathbf{V} \\ \boldsymbol{\Omega} \end{Bmatrix}. \tag{5b}$$

2.2. CNTs/fiber/polymer multi-scale composite material model

The key constituents of the three-phase CNTFPC multiscale beam are the isotropic matrix (epoxy resin), CNTs and fibers (E-Glass) with different alignment for each lamina through the thickness. The carbon nanotube composites are regarded as isotropic, as the CNTs are assumed to be uniformly distributed and randomly oriented through the matrix. It is further assumed that: (1) the CNT-matrix bonding and the CNT dispersion in the matrix are perfect; (2) each CNT has the same mechanical properties and aspect ratio; (3) all CNTs are straight rods; (4) there is no void in the matrix; and (5) fiber–matrix bonding is perfect. The constituent materials are finally assumed to be linear elastic throughout the deformation.

The effective material properties of the three-phase CNTs/fiber/polymer multiscale laminated composite (CNTFPC) can be predicted according to a combination of the Halpin–Tsai and micromechanics schemes [1–3] via two steps in the hierarchy as shown in Fig. 2. The effective material properties of the CNTFPC beam are assumed to be orthotropic and thus, can be predicted by [1–3]

$$E_{11h} = V_F E_{11}^F + V_{MNC} E^{MNC}, \tag{6a}$$

$$\frac{1}{E_{22h}} = \frac{V_F}{E_{22}^F} + \frac{V_{MNC}}{E^{MNC}} - V_F V_{MNC} \times \frac{\nu_F^2 E^{MNC}/E_{22}^F + \nu_{MNC}^2 E_{22}^F/E^{MNC} - 2\nu^F \nu^{MNC}}{V_F E_{22}^F + V_{MNC} E^{MNC}} \tag{6b}$$

$$\frac{1}{G_{12h}} = \frac{V_F}{G_{12}^F} + \frac{V_{MNC}}{G^{MNC}} \tag{6c}$$

$$\nu_{12h} = V_F \nu^F + V_{MNC} \nu^{MNC} \tag{6d}$$

$$\rho_h = V_F \rho^F + V_{MNC} \rho^{MNC} \tag{6e}$$

where $E_{11}^F, E_{22}^F, G_{12}^F, \nu^F$ and ρ^F are the fibers' Young's moduli, shear modulus, Poisson's ratio and mass density, respectively, and $E^{MNC}, G^{MNC}, \nu^{MNC}$ and ρ^{MNC} represent the corresponding properties of the isotropic matrix of nanocomposite. V_F and V_{MNC} refer to the volume fractions of the fibers and the nanocomposite matrix, respectively.

According to the Halpin–Tsai equation, the tensile modulus of nanocomposites can be expressed as [1–3]

$$E^{MNC} = \frac{E^{MER}}{8} \left[5 \left(\frac{1 + 2\beta_{dd} V_{CN}}{1 - \beta_{dd} V_{CN}} \right) + 3 \left(\frac{1 + 2\left(\frac{\ell^{CN}}{d^{CN}}\right) \beta_{dl} V_{CN}}{1 - \beta_{dl} V_{CN}} \right) \right] \tag{7a}$$

with

$$\beta_{dl} = \frac{\left(\frac{E_{11}^{CN}}{E^{MER}}\right) - \left(\frac{d^{CN}}{4t^{CN}}\right)}{\left(\frac{E_{11}^{CN}}{E^{MER}}\right) + \left(\frac{\ell^{CN}}{2t^{CN}}\right)}, \tag{7b}$$

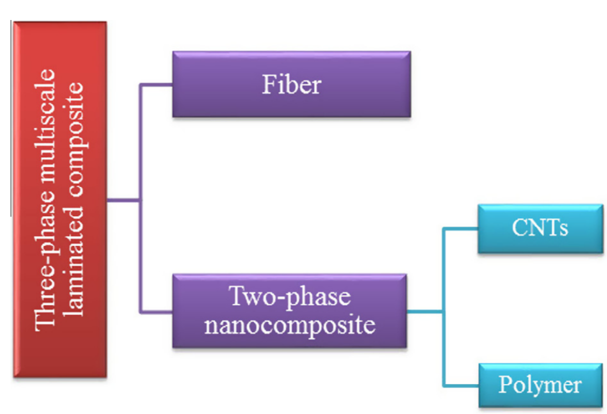

Fig. 2. Hierarchy of the three-phase CNTs/fiber/polymer multiscale composites [1].

$$\beta_{dd} = \frac{\left(\frac{E_{11}^{CN}}{E^{MER}}\right) - \left(\frac{d^{CN}}{4t^{CN}}\right)}{\left(\frac{E_{11}^{CN}}{E^{MER}}\right) + \left(\frac{d^{CN}}{2t^{CN}}\right)}. \tag{7c}$$

where $E_{11}^{CN}, V_{CN}, \ell^{CN}, d^{CN}$ and t^{CN} are the CNTs' Young's modulus, volume fraction, length, outer diameter and thickness, respectively, and V_{MER} and E^{MER} indicate the volume fraction and Young's modulus of the isotropic epoxy resin matrix, respectively.

The volume fraction of CNTs can be expressed as [1–3]

$$V_{CN} = \frac{w^{CN}}{w^{CN} + (\rho^{CN}/\rho^{MER}) - (\rho^{CN}/\rho^{MER})w^{CN}}, \tag{8}$$

where w^{CN} is the mass fraction of the carbon nanotubes, ρ^{CN} and ρ^{MER} are the mass densities of the carbon nanotube and epoxy resin matrix, respectively.

The Poisson's ratio and mass density ρ can be expressed as

$$\nu^{MNC} = \nu^{MER}, \tag{9a}$$

$$\rho^{MNC} = V_{CN}\rho^{CN} + V_{MER}\rho^{MER} \tag{9b}$$

where ν^{MER} is Poisson's ratio of the epoxy resin matrix. As the amount of CNTs is assumed to be small (equal or less than 10%), the Poisson's ratio of the carbon nanotube composite was assumed to be the same as that of the epoxy, 0.33 ([1–3]).

2.3. Equations of motion

A cantilever CNTFPC multiscale composite beam of length L is considered here. The associated boundary conditions for a given hinge-less fixed-free beam whose root ($x = 0$) is on the axis of rotation, the boundary conditions at the root and the tip are:

$$\mathbf{V}(0,t) = \mathbf{V}^0, \quad \mathbf{\Omega}(0,t) = \mathbf{\Omega}^0, \tag{10a}$$

$$\mathbf{F}(L,t) = \mathbf{F}^L, \quad \mathbf{M}(L,t) = \mathbf{M}^L. \tag{10b}$$

2.3.1. Discretization

The equations of motions (1a,b), the intrinsic kinematical Eqs. (1c,d) and the boundary conditions (10a,b) are discretized by expanding $\mathbf{V}$, $\mathbf{\Omega}$, $\mathbf{F}$ and $\mathbf{M}$ using the shifted Legendre polynomials $\mathbf{\Psi}_i(x)$ as trial functions as follows:

$$\begin{aligned} \mathbf{V}(x,t) &= \sum_{i=1}^{n_t} \underset{i}{\mathbf{\Psi}}(x)\underset{i}{\mathbf{v}}(t), \quad \mathbf{\Omega}(x,t) = \sum_{i=1}^{n_t} \underset{i}{\mathbf{\Psi}}(x)\underset{i}{\Theta}(t), \\ \mathbf{F}(x,t) &= \sum_{i=1}^{n_t} \underset{i}{\mathbf{\Psi}}(x)\underset{i}{\mathbb{F}}(t), \quad \mathbf{M}(x,t) = \sum_{i=1}^{n_t} \underset{i}{\mathbf{\Psi}}(x)\underset{i}{\mathfrak{M}}(t), \end{aligned} \tag{11}$$

where $\underset{i}{\mathbf{v}}(t), \underset{i}{\Theta}(t), \underset{i}{\mathbb{F}}(t)$ and $\underset{i}{\mathfrak{M}}(t)$ are three-component unknown vectors of time, and n_t is the number of trial functions used and

$$\underset{i}{\mathbf{\Psi}}(x) = \underset{i-1}{\Xi}\left(\frac{x}{L}\right)\begin{bmatrix} 1 & 0 & 0 \\ 0 & 1 & 0 \\ 0 & 0 & 1 \end{bmatrix} = \underset{i-1}{\Xi}(\xi)\begin{bmatrix} 1 & 0 & 0 \\ 0 & 1 & 0 \\ 0 & 0 & 1 \end{bmatrix}. \tag{12}$$

The shifted Legendre polynomial of degree i is denoted by $\underset{i}{\Xi}(\xi)$ (defined on the interval $(0, L)$) and may be generated by the recurrence formulae

$$\begin{aligned} &\underset{i+1}{\Xi}(\xi) = \frac{2i+1}{i+1}(2\xi - 1)\underset{i}{\Xi}(\xi) - \frac{i}{i+1}\underset{i-1}{\Xi}(\xi), \quad i = 1, 2, \ldots, \\ &\underset{0}{\Xi}(\xi) = 1, \underset{1}{\Xi}(\xi) = (2\xi - 1). \end{aligned} \tag{13}$$

Multiplying the Eqs. (1a-d) by the shifted Legendre functions and integrating over the domain, we obtain the following system of coupled nonlinear ordinary-differential equations in state space form:

$$\begin{aligned} &\int_0^L \sum_{j=1}^{n_t} \underset{j}{\mathbf{\Psi}}(x)\Bigg\{ \mathbf{G}\sum_{i=1}^{n_t} \underset{i}{\mathbf{\Psi}}(x)\underset{i}{\dot{\mathbf{v}}}(t) + \mathbb{k}\sum_{i=1}^{n_t} \underset{i}{\mathbf{\Psi}}(x)\underset{i}{\dot{\Theta}}(t) + \left(\sum_{k=1}^{n_t} \underset{k}{\widetilde{\mathbf{\Psi}(x)\Theta}}(t)\right) \\ &\times \left(\mathbf{G}\sum_{i=1}^{n_t} \underset{i}{\mathbf{\Psi}}(x)\underset{i}{\mathbf{v}}(t) + \mathbb{k}\sum_{i=1}^{n_t} \underset{i}{\mathbf{\Psi}}(x)\underset{i}{\Theta}(t)\right) - \sum_{i=1}^{n_t} \underset{i}{\mathbf{\Psi}'}(x)\underset{i}{\mathbb{F}}(t) \\ &- \left(\tilde{\mathbf{k}} + \left(\mathbf{S}^{\mathrm{T}}\sum_{k=1}^{n_t} \underset{k}{\widetilde{\mathbf{\Psi}(x)\mathbb{F}}}(t)\right) + \left(\mathbf{T}\sum_{k=1}^{n_t} \underset{k}{\widetilde{\mathbf{\Psi}(x)\mathfrak{M}}}(t)\right)\right)\sum_{i=1}^{n_t} \underset{i}{\mathbf{\Psi}}(x)\underset{i}{\mathbb{F}}(t) - \mathbf{f}\Bigg\}\mathrm{d}x \\ &+ \sum_{j=1}^{n_t} \underset{j}{\mathbf{\Psi}}(L)\left(\sum_{i=1}^{n_t} \underset{i}{\mathbf{\Psi}}(L)\underset{i}{\mathbb{F}}(t) - \mathbf{F}^L\right) = 0, \end{aligned} \tag{14a}$$

$$\begin{aligned} &\int_0^L \sum_{j=1}^{n_t} \underset{j}{\mathbf{\Psi}}(x)\Bigg\{ \mathbb{k}^{\mathrm{T}}\sum_{i=1}^{n_t} \underset{i}{\mathbf{\Psi}}(x)\underset{i}{\dot{\mathbf{v}}}(t) + \mathbf{I}\sum_{i=1}^{n_t} \underset{i}{\mathbf{\Psi}}(x)\underset{i}{\dot{\Theta}}(t) + \left(\sum_{k=1}^{n_t} \underset{k}{\widetilde{\mathbf{\Psi}(x)\Theta}}(t)\right) \\ &\times \left(\mathbb{k}^{\mathrm{T}}\sum_{i=1}^{n_t} \underset{i}{\mathbf{\Psi}}(x)\underset{i}{\mathbf{v}}(t) + \mathbf{I}\sum_{i=1}^{n_t} \underset{i}{\mathbf{\Psi}}(x)\underset{i}{\Theta}(t)\right) + \left(\sum_{k=1}^{n_t} \underset{k}{\widetilde{\mathbf{\Psi}(x)\mathbf{v}}}(t)\right) \\ &\times \left(\mathbf{G}\sum_{i=1}^{n_t} \underset{i}{\mathbf{\Psi}}(x)\underset{i}{\mathbf{v}}(t) + \mathbb{k}\sum_{i=1}^{n_t} \underset{i}{\mathbf{\Psi}}(x)\underset{i}{\Theta}(t)\right) - \sum_{i=1}^{n_t} \underset{i}{\mathbf{\Psi}'}(x)\underset{i}{\mathfrak{M}}(t) \\ &- \left(\tilde{\mathbf{k}} + \left(\mathbf{S}^{\mathrm{T}}\sum_{k=1}^{n_t} \underset{k}{\widetilde{\mathbf{\Psi}(x)\mathbb{F}}}(t)\right) + \left(\mathbf{T}\sum_{k=1}^{n_t} \underset{k}{\widetilde{\mathbf{\Psi}(x)\mathfrak{M}}}(t)\right)\right)\sum_{i=1}^{n_t} \underset{i}{\mathbf{\Psi}}(x)\underset{i}{\mathfrak{M}}(t) \\ &- \left(\tilde{\mathbf{e}}_1 + \left(\mathbf{R}\sum_{k=1}^{n_t} \underset{k}{\widetilde{\mathbf{\Psi}(x)\mathbb{F}}}(t)\right) + \left(\mathbf{S}\sum_{k=1}^{n_t} \underset{k}{\widetilde{\mathbf{\Psi}(x)\mathfrak{M}}}(t)\right)\right)\sum_{i=1}^{n_t} \underset{i}{\mathbf{\Psi}}(x)\underset{i}{\mathbb{F}}(t) - \mathbf{m}\Bigg\}\mathrm{d}x \\ &+ \sum_{j=1}^{n_t} \underset{j}{\mathbf{\Psi}}(L)\left(\sum_{i=1}^{n_t} \underset{i}{\mathbf{\Psi}}(L)\underset{i}{\mathfrak{M}}(t) - \mathbf{M}^L\right) = 0, \end{aligned} \tag{14b}$$

$$\begin{aligned} &\sum_{j=1}^{n_t} \underset{j}{\mathbf{\Psi}}(x)\Bigg\{ \mathbf{R}\sum_{i=1}^{n_t} \underset{i}{\mathbf{\Psi}}(x)\underset{i}{\dot{\mathbb{F}}}(t) + \mathbf{S}\sum_{i=1}^{n_t} \underset{i}{\mathbf{\Psi}}(x)\underset{i}{\dot{\mathfrak{M}}}(t) - \sum_{i=1}^{n_t} \underset{i}{\mathbf{\Psi}'}(x)\underset{i}{\mathbf{v}}(t) \\ &- \left(\tilde{\mathbf{k}} + \left(\mathbf{S}^{\mathrm{T}}\sum_{k=1}^{n_t} \underset{k}{\widetilde{\mathbf{\Psi}(x)\mathbb{F}}}(t)\right) + \left(\mathbf{T}\sum_{k=1}^{n_t} \underset{k}{\widetilde{\mathbf{\Psi}(x)\mathfrak{M}}}(t)\right)\right)\sum_{i=1}^{n_t} \underset{i}{\mathbf{\Psi}}(x)\underset{i}{\mathbf{v}}(t) \\ &- \left(\tilde{\mathbf{e}}_1 + \left(\mathbf{R}\sum_{k=1}^{n_t} \underset{k}{\widetilde{\mathbf{\Psi}(x)\mathbb{F}}}(t)\right) + \left(\mathbf{S}\sum_{k=1}^{n_t} \underset{k}{\widetilde{\mathbf{\Psi}(x)\mathfrak{M}}}(t)\right)\right)\sum_{i=1}^{n_t} \underset{i}{\mathbf{\Psi}}(x)\underset{i}{\Theta}(t)\Bigg\}\mathrm{d}x \\ &- \sum_{j=1}^{n_t} \underset{j}{\mathbf{\Psi}}(0)\left(\sum_{i=1}^{n_t} \underset{i}{\mathbf{\Psi}}(0)\underset{i}{\mathbf{v}}(t) - \mathbf{V}^0\right) = 0, \end{aligned} \tag{14c}$$

$$\begin{aligned} &\sum_{j=1}^{n_t} \underset{j}{\mathbf{\Psi}}(x)\Bigg\{ \mathbf{S}^{\mathrm{T}}\sum_{i=1}^{n_t} \underset{i}{\mathbf{\Psi}}(x)\underset{i}{\dot{\mathbb{F}}}(t) + \mathbf{T}\sum_{i=1}^{n_t} \underset{i}{\mathbf{\Psi}}(x)\underset{i}{\dot{\mathfrak{M}}}(t) - \sum_{i=1}^{n_t} \underset{i}{\mathbf{\Psi}'}(x)\underset{i}{\Theta}(t) \\ &- \left(\tilde{\mathbf{k}} + \left(\mathbf{S}^{\mathrm{T}}\sum_{k=1}^{n_t} \underset{k}{\widetilde{\mathbf{\Psi}(x)\mathbb{F}}}(t)\right) + \left(\mathbf{T}\sum_{k=1}^{n_t} \underset{k}{\widetilde{\mathbf{\Psi}(x)\mathfrak{M}}}(t)\right)\right)\sum_{i=1}^{n_t} \underset{i}{\mathbf{\Psi}}(x)\underset{i}{\Theta}(t)\Bigg\}\mathrm{d}x \\ &- \sum_{j=1}^{n_t} \underset{j}{\mathbf{\Psi}}(0)\left(\sum_{i=1}^{n_t} \underset{i}{\mathbf{\Psi}}(0)\underset{i}{\Theta}(t) - \mathbf{\Omega}^0\right) = 0. \end{aligned} \tag{14d}$$

After simplification, one may obtain

$$
\begin{bmatrix} {}_1\mathbf{A}_{ji} & {}_1\mathbf{B}_{ji} & 0 & 0 \\ {}_2\mathbf{A}_{ji} & {}_2\mathbf{B}_{ji} & 0 & 0 \\ 0 & 0 & {}_3\mathbf{A}_{ji} & {}_1\mathbf{B}_{ji} \\ 0 & 0 & {}_4\mathbf{A}_{ji} & {}_4\mathbf{B}_{ji} \end{bmatrix}
\begin{bmatrix} \underset{i}{\dot{\mathbf{v}}}(t) \\ \underset{i}{\dot{\Theta}}(t) \\ \underset{i}{\dot{\mathbb{F}}}(t) \\ \underset{i}{\dot{\mathfrak{M}}}(t) \end{bmatrix}
+
\begin{bmatrix} 0 & 0 & -{}_1\mathbf{E}_{ji} & 0 \\ 0 & 0 & -{}_2\mathbf{U}_{ji} & -{}_1\mathbf{E}_{ji} \\ -{}_3\mathbf{E}_{ji} & -{}_2\mathbf{U}_{ji} & 0 & 0 \\ 0 & -{}_3\mathbf{E}_{ji} & 0 & 0 \end{bmatrix}
\begin{Bmatrix} \underset{i}{\mathbf{v}}(t) \\ \underset{i}{\Theta}(t) \\ \underset{i}{\mathbb{F}}(t) \\ \underset{i}{\mathfrak{M}}(t) \end{Bmatrix}
$$

$$
+ \begin{bmatrix}
{}_1\mathbf{C}_{jki}\underset{k}{\tilde{\Theta}}(t) & {}_1\mathbf{D}_{jki}\underset{k}{\tilde{\Theta}}(t) & -{}_1\mathbf{W}_{jki}\underset{k}{\tilde{\mathbb{F}}}(t) - {}_1\mathbf{X}_{jki}\underset{k}{\tilde{\mathbb{M}}}(t) & 0 \\
{}_2\mathbf{N}_{jki}\underset{k}{\tilde{\Theta}}(t) + {}_1\mathbf{C}_{jki}\underset{k}{\tilde{\mathbf{v}}}(t) & {}_1\mathbf{D}_{jki}\underset{k}{\tilde{\mathbf{v}}}(t) + {}_2\mathbf{L}_{jki}\underset{k}{\tilde{\Theta}}(t) & -{}_2\mathbf{O}_{jki}\underset{k}{\tilde{\mathbb{F}}}(t) - {}_2\mathbf{Q}_{jki}\underset{k}{\tilde{\mathfrak{M}}}(t) & -{}_1\mathbf{W}_{jki}\underset{k}{\tilde{\mathbb{F}}}(t) - {}_1\mathbf{X}_{jki}\underset{k}{\tilde{\mathfrak{M}}}(t) \\
-{}_1\mathbf{W}_{jki}\underset{k}{\tilde{\mathbb{F}}}(t) - {}_1\mathbf{X}_{jki}\underset{k}{\tilde{\mathfrak{M}}}(t) & -{}_2\mathbf{O}_{jki}\underset{k}{\tilde{\mathbb{F}}}(t) - {}_2\mathbf{Q}_{jki}\underset{k}{\tilde{\mathfrak{M}}}(t) & 0 & 0 \\
0 & -{}_1\mathbf{W}_{jki}\underset{k}{\tilde{\mathbb{F}}}(t) - {}_1\mathbf{X}_{jki}\underset{k}{\tilde{\mathfrak{M}}}(t) & 0 & 0
\end{bmatrix}
\begin{Bmatrix} \underset{i}{\mathbf{v}}(t) \\ \underset{i}{\Theta}(t) \\ \underset{i}{\mathbb{F}}(t) \\ \underset{i}{\mathfrak{M}}(t) \end{Bmatrix} \tag{15}
$$

$$
+ \begin{bmatrix} -{}_1\mathbf{Y}_j & 0 & 0 & 0 \\ 0 & {}_1\mathbf{Y}_j & 0 & 0 \\ 0 & 0 & 0 & 0 \\ 0 & 0 & 0 & 0 \end{bmatrix}
\begin{Bmatrix} \mathbf{f} \\ \mathbf{m} \\ 0 \\ 0 \end{Bmatrix}
+ \begin{bmatrix} -{}_1\mathbf{Z}_j & 0 & 0 & 0 \\ 0 & -{}_1\mathbf{Z}_j & 0 & 0 \\ 0 & 0 & {}_3\mathbf{Z}_j & 0 \\ 0 & 0 & 0 & {}_3\mathbf{Z}_j \end{bmatrix}
\begin{Bmatrix} \mathbf{F}^L \\ \mathbf{M}^L \\ \mathbf{V}^0 \\ \mathbf{\Omega}^0 \end{Bmatrix} = 0
$$

It can be shown that for quadratic nonlinearity, the Newton–Raphson method leads to a converged solution.

where coefficient matrices are known values obtained by Eqs. (14).

The general set of Eqs. (15) can be written in the following form:

$$
\Gamma_{1ji}\dot{\Lambda}_i + \Gamma_{2ji}\Lambda_i + \Gamma_{3jik}\Lambda_i\Lambda_j + \Gamma_{4ji}\mathbf{f} + \Gamma_{5ji}\mathbf{m} + \Gamma_{6ji}\mathfrak{R} = \mathbf{0} \tag{16}
$$

where

$$
\Lambda_i = \begin{Bmatrix} \Lambda_1 \\ \Lambda_2 \\ \vdots \\ \Lambda_{n_t} \end{Bmatrix} = \left\{ \underset{1}{v} \quad \underset{1}{\Theta} \quad \underset{1}{\mathbb{F}} \quad \underset{1}{\mathfrak{M}} \quad \cdots \quad \cdots \quad \underset{n_t}{v} \quad \underset{n_t}{\Theta} \quad \underset{n_t}{\mathbb{F}} \quad \underset{n_t}{\mathfrak{M}} \right\}^{\mathrm{T}}. \tag{17}
$$

The nonlinear steady-state solution is calculated by canceling the time dependent coefficients in Eq. (16)

$$
\Gamma_{2ji}\bar{\Lambda}_i + \Gamma_{3jik}\bar{\Lambda}_i\bar{\Lambda}_j + \Gamma_{4ji}\bar{\mathbf{f}} + \Gamma_{5ji}\bar{\mathbf{m}} + \Gamma_{6ji}\bar{\mathfrak{R}} = \mathbf{0} \tag{18}
$$

where $\bar{\Lambda}$ refers to the steady-state solution due to steady-state forcing $\bar{\mathbf{f}}, \bar{\mathbf{m}}$ and $\bar{\mathfrak{R}}$. The Newton–Raphson method is used as an iterative process to approach the solution for the given boundary conditions. The Jacobian required for the iteration can be easily calculated as

$$
\mathfrak{I} = \Gamma_{2ji} + \Gamma_{3jik}\Lambda_k + \Gamma_{3jki}\Lambda_k. \tag{19}
$$

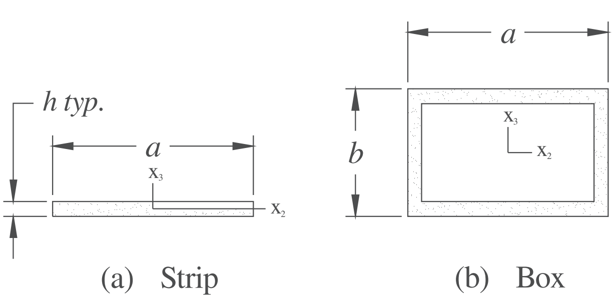

Fig. 3. The cross-sections of the two beams studied in the examples.

Let the total applied force and the corresponding solution be given by

$$
\mathbf{f} + \mathbf{m} + \mathfrak{R} = \bar{\mathbf{f}} + \bar{\mathbf{m}} + \bar{\mathfrak{R}} + \hat{\mathbf{f}}(t) + \hat{\mathbf{m}}(t) + \hat{\mathfrak{R}}(t), \tag{20a}
$$

$$
\Lambda = \bar{\Lambda} + \hat{\Lambda}(t). \tag{20b}
$$

Substituting those in the equations of motion, the linear natural frequencies of the nanocomposite beam can be obtained by using the linearized eigenvalue problem in steady state:

$$
\hat{\Gamma}_{1ji}\dot{\hat{\Lambda}}_i + \hat{\Gamma}_{2ji}\hat{\Lambda}_i + \hat{\Gamma}_{4ji}\hat{\mathbf{f}} + \hat{\Gamma}_{5ji}\hat{\mathbf{m}} + \hat{\Gamma}_{6ji}\hat{\mathfrak{R}} = \mathbf{0}. \tag{21}
$$

where

$$
\begin{aligned} \hat{\Gamma}_{1ji} &= \Gamma_{1ji}, \\ \hat{\Gamma}_{2ji} &= \Gamma_{2ji} + \Gamma_{3jik}\Lambda_k + \Gamma_{3jki}\Lambda_k. \end{aligned} \tag{22}
$$

3. Numerical results and discussions

In this section, we analyze the eigenvalues and nonlinear steady state static response of rotating CNTs/fiber/polymer laminated multiscale composite beams. The numerical results to be presented are for the laminated beams having two different types of cross-sections: Strip and Circumferentially Uniform Stiffness (CUS) Box. These cases are shown in Fig. 3. Typical geometric parameters, material properties and loading conditions are listed in Tables 1 and 2 unless otherwise specified. The material properties for CNTs-reinforced strip and box profiles are calculated using the Variational Asymptotic Beam Sectional Analysis program (VABS) [55]. The material properties for the active twist rotor (ATR) profile in Table 2 are from Ref. [27]. Results are presented for the case of n_t= 6 where all the variables are essentially approximated using quadratic polynomials leading to a total of 72 degrees of freedom.

To validate the proposed theory, the results for the linear natural frequencies of the ATR, for non-rotating and rotating cases, are compared to those from Bekhoucha et al. [34], which were obtained using the Galerkin method for nonlinear intrinsic and geometrically exact equations of motion. The geometric parameters and material properties for the ATR are listed in Table 2, and

Table 1
Typical material properties of nanocomposite beam used in examples unless otherwise specified [1].

Source	Symbol	Value	Unit	Description
Geometric and loading parameters				
	h	10×10^{-3}	m	Thickness of profile
	a	100×10^{-3}	m	Length of profile
	b	60×10^{-3}	m	Height of profile
	L	1.3970	m	Length of the blade
	Ω_3	10	rad/s	Rotational speed
Single-walled carbon nanotubes				
	t^{CN}	0.34×10^{-9}	m	Thickness of carbon nanotubes
	d^{CN}	1.4×10^{-9}	m	Outer diameter of carbon nanotubes
	ℓ^{CN}	25×10^{-6}	m	Length of carbon nanotubes
	w^{CN}	5	%	Weight percentage of carbon nanotubes
	ρ^{CN}	1350	kg/m^3	Mass density of carbon nanotubes
	E_{11}^{CN}	640×10^9	kg/m^2	Young's modulus of carbon nanotubes
	α_{11}^{CN}	3.4584×10^{-6}	1/K	Thermal expansion coefficient
	ν_{12}^{CN}	0.33	-	Poisson's ratio of carbon nanotubes
Multi-walled walled carbon nanotubes				
	t^{CN}	0.34×10^{-9}	m	Thickness of carbon nanotubes
	d^{CN}	20×10^{-9}	m	Outer diameter of carbon nanotubes
	ℓ^{CN}	50×10^{-6}	m	Length of carbon nanotubes
	w^{CN}	0	%	Weight percentage of carbon nanotubes
	ρ^{CN}	1350	kg/m^3	Mass density of carbon nanotubes
	E_{11}^{CN}	400×10^9	kg/m^2	Young's modulus of carbon nanotubes
	ν_{12}^{CN}	0.33	–	Poisson's ratio of carbon nanotubes
Epoxy resin polymer matrix				
	ρ^{MER}	1200	kg/m^3	Mass density of epoxy resin matrix
	E^{MER}	2.72×10^9	kg/m^2	Young's modulus of epoxy resin matrix
	α^{MER}	45×10^{-6}	1/K	Thermal expansion coefficient of epoxy resin matrix
	ν^{MER}	0.33	–	Poisson's ratio of epoxy resin matrix
E-Glass fibers				
	ρ^F	1200	kg/m^3	Mass density of E-Glass fibers
	E_{11}^F	69×10^9	kg/m^2	Young's modulus of E-Glass fibers
	ν^F	0.2	–	Poisson's ratio of E-Glass fibers
	V^F	0.3	–	Volume fraction of E-Glass fibers

Table 2
Structural parameters for different profiles.

Section	$\mathbf{R} = \begin{bmatrix} R_{11} & 0 & 0 \\ 0 & R_{22} & 0 \\ 0 & 0 & R_{33} \end{bmatrix}$	$\mathbf{S} = \begin{bmatrix} 0 & 0 & S_{13} \\ 0 & 0 & 0 \\ S_{31} & 0 & 0 \end{bmatrix}$	$\mathbf{T} = \begin{bmatrix} T_{11} & 0 & 0 \\ 0 & T_{22} & 0 \\ 0 & 0 & T_{33} \end{bmatrix}$	Other
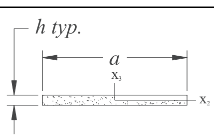	$R_{11} = 3.7190 \times 10^{-8}$ $R_{22} = 1.6862 \times 10^{-7}$ $R_{33} = 2.8754 \times 10^{-7}$	$S_{13} \approx S_{31} \approx 0$	$T_{11} = 4.4860 \times 10^{-3}$ $T_{22} = 4.1073 \times 10^{-3}$ $T_{33} = 4.4631 \times 10^{-5}$	$\mu = 9.5269 \times 10^{-1}$ $\bar{x}_2 = \bar{x}_3 = i_{23} = 0$ $i_2 = 7.9391 \times 10^{-6}$ $i_3 = 7.9391 \times 10^{-4}$
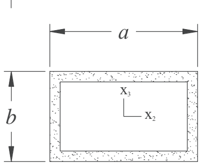	$R_{11} = 6.4375 \times 10^{-7}$ $R_{22} = 4.9262 \times 10^{-6}$ $R_{33} = 4.4389 \times 10^{-5}$	$S_{13} \approx S_{31} \approx 0$	$T_{11} = 4.4873 \times 10^{-5}$ $T_{22} = 2.7009 \times 10^{-5}$ $T_{33} = 1.1274 \times 10^{-5}$	$\mu = 2.6675$ $\bar{x}_2 = \bar{x}_3 = i_{23} = 0$ $i_2 = 1.3084 \times 10^{-3}$ $i_3 = 3.1375 \times 10^{-3}$
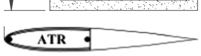	$R_{11} = 6.4375 \times 10^{-7}$ $R_{22} = 4.9262 \times 10^{-6}$ $R_{33} = 4.4389 \times 10^{-5}$	$S_{13} = 5.5420 \times 10^{-6}$ $S_{31} = 1.8621 \times 10^{-4}$	$T_{11} = 2.9056 \times 10^{-2}$ $T_{22} = 2.5038 \times 10^{-2}$ $T_{33} = 9.2640 \times 10^{-4}$	$\mu = 6.9310 \times 10^{-1}$ $\bar{x}_2 = -6.9240 \times 10^{-4}$ $\bar{x}_3 = i_{23} = 0$ $i_2 = 6.4630 \times 10^{-6}$ $i_3 = 3.7018 \times 10^{-4}$

Table 3
Comparison of the linear natural frequencies of the ATR, for non-rotating and rotating cases.

Mode	Ω_3 = 0 rad/s		Ω_3 = 10 rad/s		Ω_3 = 20 rad/s	
	[34]	Present	[34]	Present	[34]	Present
1st/z	13.64	13.65	17.44	16.97	25.53	24.20
1st/y	70.60	70.60	70.73	70.73	71.10	71.10
2nd/z	84.40	84.46	88.13	88.12	98.47	98.26
3rd/z	232.0	234.5	235.5	238.22	246.5	248.92

Table 4
Effect of SWCNTs weight percentages w^{CN} on the fundamental natural linear frequency of the cantilever rotating and non-rotating CNTFPC blades.

Case	Ω_3 = 0 rad/s w^{CN}			Ω_3 = 10 rad/s w^{CN}		
	0%	5%	10%	0%	5%	10%
Strip	24.2744	28.7979 [18.63%]*	32.4403 [33.64%]	26.4403	30.6478 [15.91%]	34.0946 [28.95%]
Box	154.9875	210.5126 [35.83%]	232.879 [50.26%]	155.3577	210.788 [35.68%]	233.116 [50.05%]

* [X%]: $X\% = 100\% \frac{Freq.|_{n\%SWCNT} - Freq.|_{0\%SWCNT}}{Freq.|_{0\%SWCNT}}$.

Table 5
Effect of volume fraction of fibers V^F on the fundamental natural linear frequency of the cantilever rotating and non-rotating CNTFPC blades.

Case	V^F					
	Ω_3 = 0 rad/s			Ω_3 = 10 rad/s		
	0.3	0.4	0.5	0.3	0.4	0.5
Strip	24.2744	31.7515 [30.80%]*	34.2376 [41.04]	26.4403	33.4297 [26.43%]	35.7965 [35.39%]
Box	154.9875	226.5541 [46.18%]	240.592 [55.23%]	155.3577	226.810 [45.99%]	240.833 [55.02%]

* [X%]: $X\% = 100\% \frac{Freq.|_{V^F} - Freq.|_{V^F=0.3}}{Freq|_{V^F=0.3}}$.

the results obtained are listed in Table 3. It can be observed that the results from the proposed theory are in excellent agreement with the reference results.

The effect of SWCNTs weight percentages w^{CN} on the fundamental linear natural frequency of the cantilever rotating and non-rotating CNTFPC blades was investigated and the results are listed in Table 4. Our findings suggest that a small amount of single-walled carbon nanotubes (5%) can significantly increase the natural frequencies of the fiber reinforced laminated composite beams. For instance, an increase of 18.63% was obtained in the case of non-rotating strip beams with 5% contribution of carbon nanotubes or 15.91% in the case of rotating strip beams at Ω_3 = 10 rad/s with the same 5% contribution. Another observation can be made from the results presented in Table 4 that the rise in fundamental natural frequency of beams due to addition of CNTs is more significant in nonrotating rather than the rotating cases. This could be predicted because the stiffness of the structure is increased upon rotation, and therefore, the addition of CNTs becomes less noticeable. Our findings also confirm that beams with the CUS Box profile produce higher increase in fundamental natural frequency in comparison with the strip cross-section. For example, there was a 35.83% increase in fundamental natural frequency of a CUS box beam, versus 18.63% for the strip profile, by addition of 5% of weight percentage for single-walled carbon nanotubes. Our simulations also show that the increase in fundamental natural frequencies of nanocomposite beams is not linearly dependent on the weight percentage of SWCNTs.

Table 5 illustrates the effect of volume fraction of fibers V^F on the fundamental linear natural frequency of the cantilever rotating and non-rotating CNTFPC blades. While the baseline amount of 30% for volume fraction of fibers is considered in this study, it can be seen that a higher value of fibers volume fraction can drastically increase the stiffness of the system and therefore the fundamental natural frequency. However, this increase is more noticeable in nonrotating rather than in rotating blades. It can be seen that the CUS box profile stiffness benefits more from an increase in volume fraction of fibers rather than the strip profile.

The influence of aspect ratio and type of the nanotubes on the fundamental natural linear frequency of the cantilever rotating and non-rotating CNTFPC blades is illustrated in Table 6. One can observe that the fundamental natural frequency of the CNTFPC beams increases with an increase in CNT percentage and this increase is more significant in SWCNTs than MWCNTs. In other words, single walled carbon nanotube reinforced composite beams exhibit better resistance to flexural deflection and vibration in comparison with multiwalled carbon nanotube reinforced beams.

Table 6
Effect of aspect ratio and type of the nanotubes on the fundamental natural linear frequency of the cantilever rotating and non-rotating CNTFPC blades.

Case	ℓ^{CN}/d^{CN}	Ω_3 = 0 rad/s			Ω_3 = 10 rad/s		
		SWCNTs	MWCNTs	Difference	SWCNTs	MWCNTs	Difference
Strip	100	26.6496	24.5043	[−8.05%]*	28.6383	26.6530	[−6.93%]
	10,000	28.7794	24.5128	[−14.83%]	30.6304	26.6608	[−12.96%]
Box	100	187.0501	159.0431	[−14.97%]	187.3596	159.4047	[−14.92%]
	10,000	210.3223	159.1685	[−24.32%]	210.5982	159.5299	[−24.25%]

* [X%]: $X\% = 100\% \frac{Freq.|_{MWCNTs} - Freq.|_{SWCNTs}}{Freq.|_{SWCNTs}}$.

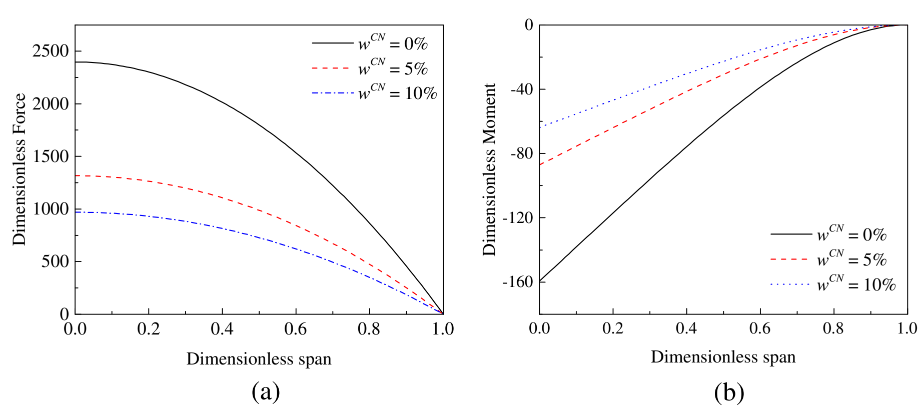

Fig. 4. Effect of weight percentages of SWCNTs on the dimensionless (a) Axial force F_1, and (b) Moment M_3 of the cantilever rotating CNTFPC blades with strip profile.

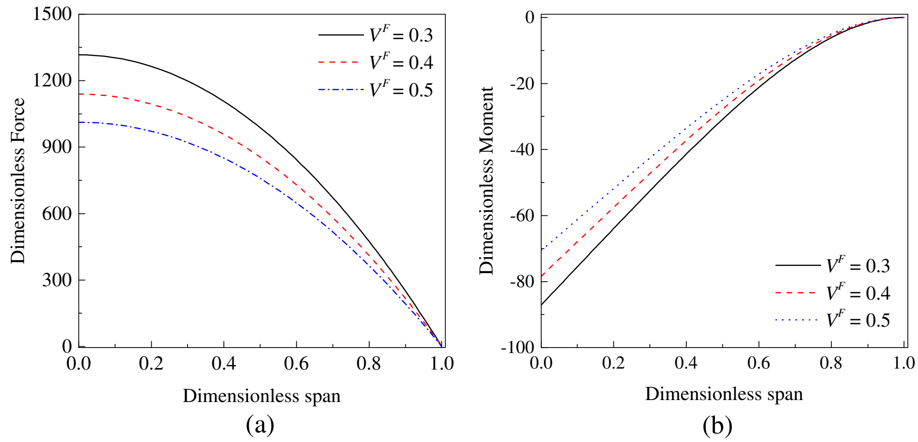

Fig. 5. Effect of volume fraction of fibers on the dimensionless (a) Axial force F_1, and (b) Moment M_3 of the cantilever rotating CNTFPC blades with strip profile.

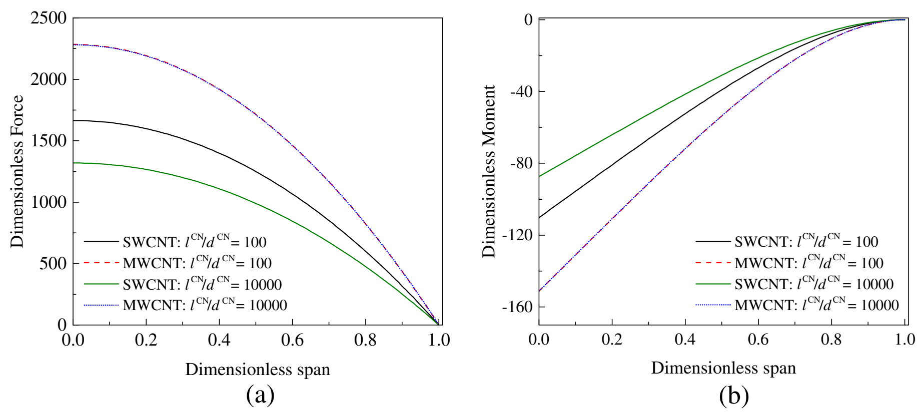

Fig. 6. Effect of CNTs aspect ratio and nanotube wall type on the dimensionless (a) Axial force F_1, and (b) Moment M_3 of the cantilever rotating CNTFPC blades with strip profile.

The influence of volume fraction of fibers and addition of carbon nanotubes on the nonlinear steady state response of the multiscale nanocomposite beam is shown in Figs. 4–6. Forces and moments in these graphs are nondimensionalized as follows:

$$\overline{F} = \frac{F_3 L^4}{U_{11} h^4}, \quad \overline{M}_3 = \frac{M_3 L^4}{U_{11} h^5}, \quad U_{11} = \frac{R_{11}}{\begin{vmatrix} \mathbf{R} & \mathbf{S} \\ \mathbf{S}^T & \mathbf{T} \end{vmatrix}} \tag{23}$$

It can be observed that higher percentage of the volume fraction or the addition of carbon nanotubes, especially in high aspect ratio SWCNTs, can significantly improve the mechanical response of the system and lead to a stiffer design. As shown in Fig. 6, the aspect ratio in MWCNTs did not significantly change the steady state static response of rotating blades. This confirms the observation already made about the fundamental natural frequency of the blades discussed earlier. The results presented in Figs. 4–6 may be used to help design rotating blades made of nanocomposite materials.

4. Conclusions

A set of nonlinear, intrinsic equations describing the response of rotating multiscale nanocomposite blades undergoing large deformations has been developed. The governing equations of motions were discretized by the Galerkin method, and the natural frequencies and nonlinear steady state static response of the nanocomposite blades were determined. Being analytical, the proposed model allows for convenient parametric analyses and is less expensive than a finite element model. However, it does not resort to one-dimensional governing equations, and therefore, it is expected to be more accurate than theories assuming a priori knowledge of the cross-sectional deformation. Numerical results showed that the natural frequencies significantly increase with a small content of CNTs. It was also found that the SWCNTs reinforcement produces more pronounced effect on the natural frequencies of the beam in comparison with MWCNTs. This may be attributed to the defect-free structure of SWCNTs. The results also confirmed that low aspect ratio CNTs in laminated composite beams bring about less significant improvement in nonlinear steady state response and natural frequencies of the composite beams. Another finding was that the rise in fundamental natural frequency of beams due to addition of carbon nanotubes is more significant in nonrotating condition than rotating one. The results and tools presented in this study may assist in the design of a new generation of rotating blades made of nanocomposite materials.

Acknowledgements

The first author thanks Professor Carlos E. S. Cesnik from University of Michigan, Ann Arbor and Dr. Matthias Althoff from Technische Universität München, Germany, for their technical supports. The first author also gratefully acknowledges the financial support from Ontario Trillium Scholarship (OTS), Government of Ontario, Canada.

References

[1] Rafiee M, He XQ, Mareishi S, Liew KM. Modeling and stress analysis of smart CNTs/fiber/polymer multiscale composite plates. Int J Appl Mech 2014;6(03):1450025.
[2] He XQ, Rafiee M, Mareishi S, Liew KM. Large amplitude vibration of fractionally damped viscoelastic CNTs/fiber/polymer multiscale composite beams. Compos Struct 2015;131:1111–23.
[3] Rafiee M, Liu XF, He XQ, Kitipornchai S. Geometrically nonlinear free vibration of shear deformable carbon nanotube/fiber/polymer multiscale laminated composite plates. J Sound Vib 2014;333(14):3236–51.
[4] Bekyarova E, Thostenson ET, Yu A, Kim H, Gao J, Tang J, Hahn HT, Chou TW, Itkis ME, Haddon RC. Multiscale carbon nanotube-carbon fiber reinforcement for advanced epoxy composites. Langmuir 2007;23:3970–4.
[5] Kim M, Park YB, Okoli OI, Zhang C. Processing, characterization, and modeling of carbon nanotube-reinforced multiscale composites. Compos Sci Technol 2009;69(3):335–42.
[6] Thostenson ET, Li WZ, Wang DZ, Ren ZF, Chou TW. Carbon nanotube/carbon fiber hybrid multiscale composites. J Appl Phys 2002;91(9):6034–7.
[7] Godara A, Mezzo L, Luizi F, Warrier A, Lomov SV, Van Vuure AW, et al. Influence of carbon nanotube reinforcement on the processing and the mechanical behaviour of carbon fiber/epoxy composites. Carbon 2009;47:2914–23.
[8] Green KJ, Dean DR, Vaidya UK, Nyairo E. Multiscale fiber reinforced composites based on a carbon nanofiber/epoxy nanophased polymer matrix: synthesis, mechanical, and thermomechanical behavior. Compos Part A: Appl Sci Manuf 2009;40(9):1470–5.
[9] Hodges DH. A mixed variational formulation based on exact intrinsic equations for dynamics of moving beams. Int J Solids Struct 1990;26(11):1253–73.
[10] Hodges DH, Atilgan AR, Cesnik CES, Fulton MV. On a simplified strain energy function for geometrically nonlinear behavior of anisotropic beams. Compos Eng 1992;2(5-7):513–26.
[11] Kim T, Dugundji J. Nonlinear large amplitude vibration of composite helicopter blade at large static deflection. AIAA J 1993;31(5):938–46.
[12] Cesnik CES, Hodges DH. VABS: a new concept for composite rotor blade cross-sectional modeling. J Am Helicopter Soc 1997;42(1):27–38.
[13] Song O, Librescu L. Free vibration of anisotropic composite thin-walled beams of closed cross-section contour. J Sound Vib 1993;167(1):129–47.
[14] Song O, Librescu L. Structural modeling and free vibration analysis of rotating composite thin-walled beams. J Am Helicopter Soc 1997;42(4):358–69.
[15] Johnson ER, Vasiliev VV, Vasiliev DV. Anisotropic thin-walled beams with closed cross-sectional contours. AIAA J 2001;39(12):2389–93.
[16] Yu W, Volovoi VV, Hodges DH, Hong X. Validation of the variational asymptotic beam sectional analysis. AIAA J 2002;40(10):2105–12.
[17] Oh SY, Song O, Librescu L. Effects of pretwist and presetting on coupled bending vibrations of rotating thinwalled composite beams. Int J Solids Struct 2003;40(5):1203–24.
[18] Qin Z, Librescu L. On a shear-deformable theory of anisotropic thin-walled beams: further contribution and validations. Compos Struct 2002;56(4):345–58.
[19] Oh SY, Song O, Librescu L. Effects of pretwist and presetting on coupled bending vibrations of rotating thin-walled composite beams. Int J Solids Struct 2003;40:1203–24.
[20] Hodges DH. Nonlinear composite beam theory. Progress in astronautics and aeronautics series, vol. 213. Reston, VA: AIAA; 2006.
[21] Librescu L, Song O. Thin-walled composite beams: theory and application. Dordrecht: Springer; 2006.
[22] Fazelzadeh SA, Malekzadeh P, Zahedinejad P, Hosseini M. Vibration analysis of functionally graded thin-walled rotating blades under high temperature supersonic flow using the differential quadrature method. J Sound Vib 2007;306(1):333–48.
[23] Ghorashi M, Nitzsche F. Nonlinear dynamic response of an accelerating composite rotor blade using perturbations. J Mech Mater Struct 2009;4(4):693–718.
[24] Shooshtari A, Rafiee M. Nonlinear forced vibration analysis of clamped functionally graded beams. Acta Mech 2011;221:23–38.
[25] Ghorashi M. Nonlinear analysis of the dynamics of articulated composite rotor blades. Nonlinear Dyn 2012;67(1):227–49.
[26] Patil MJ, Althoff M. Energy-consistent, Galerkin approach for the nonlinear dynamics of beams using intrinsic equations. J Vib Control 2010;17(11):1748–58.
[27] Althoff M, Patil MJ, Traugott JP. Nonlinear modeling and control design of active helicopter blades. J Am Helicopter Soc 2012;57(1):1–11.
[28] Allahverdizadeh A, Mahjoob MJ, Eshraghi I, Asgharifard-S P. Effects of electrorheological fluid core and functionally graded layers on the vibration behavior of a rotating composite beam. Meccanica 2012;47(8):1945–60.
[29] Deepak BP, Ganguli R, Gopalakrishnan S. Dynamics of rotating composite beams: a comparative study between CNT reinforced polymer composite beams and laminated composite beams using spectral finite elements. Int J Mech Sci 2012;64(1):110–26.
[30] Lacarbonara W, Arvin H, Bakhtiari-Nejad F. A geometrically exact approach to the overall dynamics of elastic rotating blades—part 1: linear modal properties. Nonlinear Dyn 2012;70(1):659–75.
[31] Arvin H, Lacarbonara W, Bakhtiari-Nejad F. A geometrically exact approach to the overall dynamics of elastic rotating blades—part 2: flapping nonlinear normal modes. Nonlinear Dyn 2012;70(3):2279–301.
[32] Arvin H, Bakhtiari-Nejad F. Nonlinear free vibration analysis of rotating composite Timoshenko beams. Compos Struct 2013;96:29–43.
[33] Arvin H, Bakhtiari-Nejad F. Nonlinear modal interaction in rotating composite Timoshenko beams. Compos Struct 2013;96:121–34.
[34] Bekhoucha F, Rechak S, Duigou L, Cadou JM. Nonlinear forced vibrations of rotating anisotropic beams. Nonlinear Dyn 2013;74(4):1281–96.
[35] Rafiee M, Mohammadi M, Sobhani Aragh B, Yaghoobi H. Nonlinear free and forced thermo-electro-aero-elastic vibration and dynamic response of piezoelectric functionally graded laminated composite shells, Part I: theory and analytical solutions. Compos Struct 2013;103:179–87.
[36] Rafiee M, Mohammadi M, Sobhani Aragh B, Yaghoobi H. Nonlinear free and forced thermo-electro-aero-elastic vibration and dynamic response of piezoelectric functionally graded laminated composite shells, Part II: numerical results. Compos. Struct. 2013;103:188–96.
[37] Hosseini SM, Mareishi S, Kalhori H, Rafiee M. Large amplitude free and forced oscillations of functionally graded beams. Mech Adv Mater Struct 2014;21(4):255–62.
[38] Sinha SK. Transient response of a multilayered composite rotating airfoil under slicing-impact loading. AIAA J 2014;52(12):2701–11.
[39] Georgiades F, Latalski J, Warminski J. Equations of motion of rotating composite beam with a nonconstant rotation speed and an arbitrary preset angle. Meccanica 2014;49(8):1833–58.
[40] Arvin H, Lacarbonara W. A fully nonlinear dynamic formulation for rotating composite beams: nonlinear normal modes in flapping. Compos Struct 2014;109:93–105.
[41] Sina SA, Haddadpour H. Axial–torsional vibrations of rotating pretwisted thin walled composite beams. Int J Mech Sci 2014;80:93–101.
[42] Rafiee M, Yang J, Kitipornchai S. Large amplitude vibration of carbon nanotube reinforced functionally graded composite beams with piezoelectric layers. Compos Struct 2013;96:716–25.
[43] Mareishi S, Kalhori H, Rafiee M, Hosseini SM. Nonlinear forced vibration response of smart two-phase nano-composite beams to external harmonic excitations. Curved Layered Struct 2015;2(1):50–161.
[44] Rafiee M, Yang J, Kitipornchai S. Thermal bifurcation buckling of piezoelectric carbon nanotube reinforced composite beams. Comput Math Appl 2013;66(7):1147–60.
[45] He XQ, Rafiee M, Mareishi S. Nonlinear dynamics of piezoelectric nanocomposite energy harvesters under parametric resonance. Nonlinear Dyn 2015;79(3):1863–80.
[46] Rafiee M, He XQ, Mareishi S, Liew KM. Nonlinear response of piezoelectric nanocomposite plates: large deflection, post-buckling and large amplitude vibration. Int J Appl Mech 2014;7(05):1550074.
[47] Rafiee M, He XQ, Liew KM. Non-linear dynamic stability of piezoelectric functionally graded carbon nanotube-reinforced composite plates with initial geometric imperfection. Int J Non-Linear Mech 2014;59:37–51.
[48] Rafiee M, He XQ, Liew KM. Nonlinear analysis of piezoelectric nanocomposite energy harvesting plates. Smart Mater Struct 2014;23(6):065001.
[49] Silvestre N, Camotim D. Second-order generalised beam theory for arbitrary orthotropic materials. Thin-Walled Struct 2002;40(9):791–820.
[50] Schardt R. Lateral torsional and distortional buckling of channel-and hat-sections. J Constr Steel Res 1994;31(2):243–65.
[51] Schardt R, Heinz D. Vibrations of thin-walled prismatic structures under simultaneous static load using generalized beam theory. In: Kratzig W et al., editors. Structural dynamics. Rotterdam. Chap: Balkema; 1991. p. 921–7.
[52] Carrera E, Filippi M. Variable kinematic one-dimensional finite elements for the analysis of rotors made of composite materials. J Eng Gas Turbines Power 2014;136(9):092501.
[53] Carrera E, Filippi EM, Zappino E. Analysis of rotor dynamic by one-dimensional variable kinematic theories. J Eng Gas Turbines Power 2013;135(9):092501.
[54] Carrera E, Filippi M, Zappino E. Free vibration analysis of rotating composite blades via Carrera Unified Formulation. Compos Struct 2013;106:317–25.
[55] Yu W. VABS manual for users. Logan, Utah: Department of Mechanical and Aerospace Engineering, Utah State University; 2011.

Chapter 4

4. Cross-Sectional Design and Analysis of Multiscale Carbon Nanotubes-Reinforced Composite Beams and Blades

as published* in International Journal of Applied Mechanics 10(3) (2018) 1850032 (26 pages)

https://doi.org/10.1142/S1758825118500321

*In accordance with University of Ottawa regulations, the contact email address has been removed from this article.

Foreword

This chapter differs from the previous chapter in the sense that it is not focused on mechanical behaviour, but is instead focused on the effect of MWCNTs on the cross-sectional properties of beam-type structures. Based on the variational asymptotic method (VAM), the governing equations of 3D elasticity can be rigorously split into a 1D problem and a complementary 2D problem over the cross-sectional plane. The former governs the global deformation, while the latter provides cross-sectional elastic constants and stress/strain recovery relations over the cross-section.

A structure should be slender to be modeled as a beam. The structure should satisfy $a/l \ll 1$ and $a/R \ll 1$, where a is the characteristic length of the cross-section, l is the characteristic wavelength of the deformation along the axial direction, and R is the characteristic radius of initial curvatures and twist of the beam. We have assumed both the 3D strain field and the 1D strain field to be small as we are only interested in a geometrically nonlinear, but material linear theory.

The 2D cross-sectional analysis for simple geometries can be done using analytical methods. However, for complicated geometries and anisotropic material properties, numerical methods such as finite element analysis (FEA) is needed. VABS (Variational Asymptotic Beam Sectional Analysis) [1] is a code implementing the cross-sectional analysis based on the concept of VAM. VABS takes a finite element mesh of the cross section, including all the details of geometry and material as inputs, to calculate the sectional properties, including structural properties and inertial properties. In this chapter, VABS was used to calculate the cross-sectional properties of the nanocomposite beams and blades. The same effective material properties as in Chapter 3 were used to calculate the cross-sectional properties of multiscale composites.

References:

Cesnik, Carlos ES, and Dewey H. Hodges. "VABS: a new concept for composite rotor blade cross-sectional modeling." Journal of the American helicopter society 42.1 (1997): 27-38.

International Journal of Applied Mechanics
Vol. 10, No. 3 (2018) 1850032 (26 pages)

DOI: 10.1142/S1758825118500321

Cross-Sectional Design and Analysis of Multiscale Carbon Nanotubes-Reinforced Composite Beams and Blades

M. Rafiee*

Department of Mechanical Engineering, University of Ottawa
161 Louis Pasteur, Ottawa, ON K1N 6N5, Canada

F. Nitzsche

Department of Mechanical and Aerospace Engineering, Carleton University
1125 Colonel By Drive, Ottawa, ON K1S 5B6, Canada

M. R. Labrosse

Department of Mechanical Engineering, University of Ottawa
161 Louis Pasteur, Ottawa, ON K1N 6N5, Canada

Received 16 January 2018
Revised 26 February 2018
Accepted 5 March 2018
Published 26 April 2018

The present work addresses with the cross-sectional design and analysis of fiber-reinforced multiscale composite beams of general cross-sectional shape and arbitrary anisotropic material properties and investigates the effect of carbon nanotubes (CNTs) on their stiffness properties. The three-dimensional strain field was formulated in terms of one-dimensional strains and a three-dimensional warping displacement. The bulk material properties of the multiscale composite were predicted using Halpin–Tsai equations and fiber micromechanics. The carbon nanotubes were assumed to be uniformly distributed and randomly oriented throughout the polymer matrix. The variational asymptotic beam section (VABS) was used to numerically evaluate the stiffness and mass matrices of four test cases: strip, circular pipe, box beam and airfoil. The influence of CNTs weight percentage and volume fraction of fibers was investigated through a detailed parametric study. The numerical results indicate that the inclusion of a small weight percentage of carbon nanotubes in the polymer matrix is sufficient to induce a significant improvement in stiffness properties.

Keywords: Carbon nanotubes; multiscale composites; cross-section design; fiber-reinforced nanocomposite; VABS; airfoil section.

1. Introduction

Beams are three-dimensional (3D) bodies in which one dimension is large compared to the other two. This enables the separation of the 3D problem into two parts: a 2D

*Corresponding author.

local deformation field within the cross-section that is used to calculate the section properties and a 1D global deformation field that is used to calculate the response of the beam [Rafiee *et al.*, 2017]. A comprehensive review of composite beam theories can be found in Rafiee *et al.* [2017]. The cross-sectional properties can be obtained using either ad hoc assumptions [Jung *et al.*, 2002; Pai and Nayfeh, 1990; Rafiee *et al.*, 2017; Song and Librescu, 1997] or asymptotic methods [Berdichevsky *et al.*, 1992; Cesnik and Shin, 2001; Hodges, 2003; Rafiee *et al.*, 2017; Rafiee *et al.*, 2016]. In general, a fully populated matrix of cross-sectional stiffness properties is expected [Hodges, 2006]. Analytical analyses are available for simple geometries; however, arbitrary cross-sections require numerical solutions such as finite element analysis (FEA). One of the most common FEA-based tools is the Variational Asymptotic Beam Section (VABS) [Cesnik and Hodges, 1997; Yu, 2011; Yu *et al.*, 2012]. The mathematical basis of VABS is the variational asymptotic method (VAM). VAM allows one to replace a three-dimensional structural model with a reduced-order model in terms of an asymptotic series of certain small parameters inherent to the structure [Berdichevsky *et al.*, 1992]. Based on this method, Hodges and his coworkers developed theoretical foundations for the analysis of anisotropic composite beams [Cesnik *et al.*, 1996; Danielson and Hodges, 1987; Hodges, 2003, 2006, 2015; Hodges *et al.*, 2007; Yu *et al.*, 2012; Yu *et al.*, 2002]. Many researchers extended the research done by Hodges [1990, 2003] to study the statics and dynamics of composite beams. For instance, Traugott *et al.* [2006] developed a set of nonlinear, intrinsic equations describing the dynamics of beam structures undergoing large deformations of active helicopters blade. Their active structural model could be coupled with a suitable aerodynamic model for aeroelastic simulation and aeroelastic control design. Ghorashi and Nitzsche [2009] studied the nonlinear dynamic response of an accelerating composite rotor blade using perturbations. In another study, Ghorashi [2012] also investigated the elasto-dynamic response of a rotating articulated blade. He used the linear VAM cross-sectional analysis, together with an improved damped nonlinear model for the rigid-body motion analysis of helicopter blades in coupled flap and lead-lag motions. Very recently, Rafiee *et al.* [2016] presented a computational model to investigate the static and vibration response of rotating and non-rotating nanocomposite beams and blades based on VAM.

Multiscale composites containing reinforcing elements from different length scales (i.e., macro, micro and/or nano) are a class of innovative and high-performance materials with a wide range of applications in the high-end industrial sectors [Bekyarova *et al.*, 2007; Díez-Pascual *et al.*, 2011; Hosseini *et al.*, 2017; Kim *et al.*, 2009; Nejad *et al.*, 2017; Nejad *et al.*, 2016; Rafiee *et al.*, 2014b, 2014c, 2014d; Rafiee *et al.*, 2016; Rana and Fangueiro, 2016; Wang *et al.*, 2011]. The most important characteristics of carbon nanotubes are their extremely high strength combined with excellent resilience. Therefore, the introduction of carbon nanotubes into polymeric composites may improve their applications in the fields of reinforcing composites, electronic devices and more. With carbon nanotubes, the change in reinforcement scale relative to carbon fibers offers an opportunity to combine the potential benefits of nanoscale reinforcement with those, well-established, of fibrous composites to create multiscale hybrid micro/nanocomposites. To date, multiscale composites have been developed using different types of nanomaterials. The most common are the nanomaterials with high aspect ratios such as nanotubes. There are two approaches of fabricating fiber reinforced polymer (FRP) multiscale composites: (a) by dispersing nanotubes within a polymeric matrix and, subsequently, impregnating the conventional fibers with this nanodispersed resin system, and (b) incorporating nanotubes within fibers, followed by their impregnation with a pure matrix as shown schematically in Fig. 1. Some researchers investigated the effect of carbon nanotubes-reinforced composite materials on the static and dynamic behavior of beams and plates [He *et al.*, 2014; Rafiee *et al.*, 2014a, 2014b, 2014c, 2014d; He *et al.*, 2015; Rafiee *et al.*, 2015; Rafiee *et al.*, 2013a, 2013b; Rafiee *et al.*, 2016]. Geometrically nonlinear analysis of piezoelectric nanocomposite energy harvesters under principle parametric resonance in pre-buckling and postbuckling domains were studied by He *et al.* [2014]. Based on Halpin–Tsai equations and fiber micromechanics, Rafiee *et al.* [2016] investigated the statics and dynamics of carbon

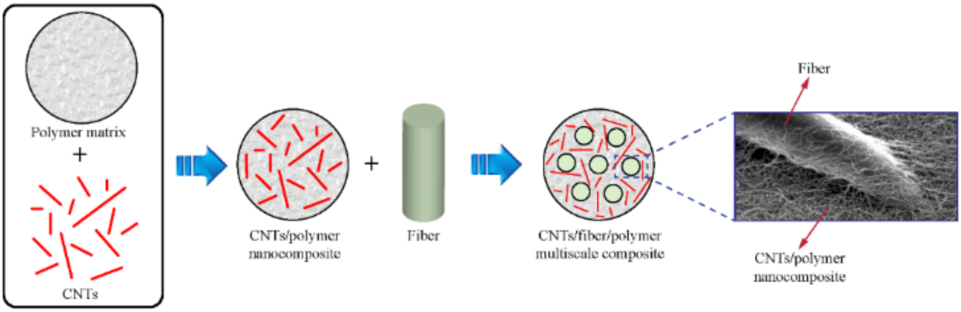

(a)

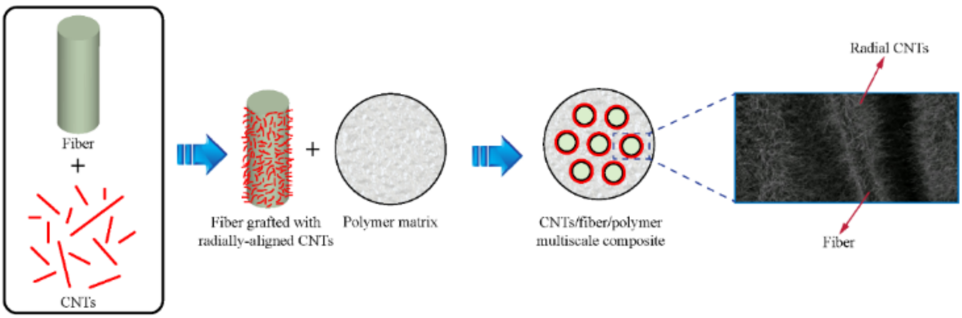

(b)

Fig. 1. Two different approaches of manufacturing multiscale CNTs/polymer nanocomposites: (a) dispersing CNTs in polymer matrix and (b) grafting CNTs on the surface of fibers.

nanotubes reinforced composite cantilever beams. The large amplitude vibration of rectangular cross-section beams made of multiscale composites was also studied by He *et al.* [2015].

Although multiscale composites have been studied and the research efforts on this topic are increasing, modelling and simulation techniques to predict the stiffness properties of beams made of multiscale composites are still needed toward the design of composite structures with targeted sets of properties.

This work addresses with cross-sectional design and investigates the effectiveness of carbon nanotubes reinforcements on the cross-sectional properties of beams and blades made of multiscale composite materials. Halpin–Tsai equations and fiber micromechanics were used in hierarchy to predict the bulk material properties of the multiscale composite. The carbon nanotubes were assumed to be uniformly distributed and randomly oriented through the epoxy resin matrix. We use VABS approach for numerical calculation of mass and stiffness matrices for four different cross-sections: strip, circular pipe, box beam and airfoil. The volume fraction of fibers, the weight percentage of single-walled and multi-walled carbon nanotubes (SWCNTs and MWCNTs) were investigated through a detailed parametric study for their effects on the stiffness properties of composite beams and blades.

2. Mathematical Modeling

As mentioned earlier, VAM enables the separation of the 3D problem into two parts: a 2D analysis at each cross-section with curvilinear coordinates x_2 and x_3 and a 1D analysis along the reference line with coordinate x_1. The final 3D elastic field can be recovered by combination of the results of the two sub-problems as shown in Fig. 2

$$\Gamma = \Gamma_h \hat{w} + \Gamma_\varepsilon \varepsilon + \Gamma_R \hat{w} + \Gamma_\ell \hat{w}' \tag{1}$$

where $\hat{w}$ is the warping function, ε is the 1D strain and matrices $\Gamma_h, \Gamma_\varepsilon, \Gamma_R$, and Γ_ℓ are

$$\Gamma_h = \begin{bmatrix} 0 & 0 & 0 \\ \dfrac{\partial}{\partial \zeta_2} & 0 & 0 \\ \dfrac{\partial}{\partial \zeta_3} & 0 & 0 \\ 0 & \dfrac{\partial}{\partial \zeta_2} & 0 \\ 0 & \dfrac{\partial}{\partial \zeta_3} & \dfrac{\partial}{\partial \zeta_2} \\ 0 & 0 & \dfrac{\partial}{\partial \zeta_3} \end{bmatrix}, \quad \Gamma_\varepsilon = \frac{1}{\sqrt{g}} \begin{bmatrix} 1 & 0 & -\zeta_3 & \zeta_2 \\ 0 & \zeta_3 & 0 & 0 \\ 0 & -\zeta_2 & 0 & 0 \\ 0 & 0 & 0 & 0 \\ 0 & 0 & 0 & 0 \\ 0 & 0 & 0 & 0 \end{bmatrix},$$

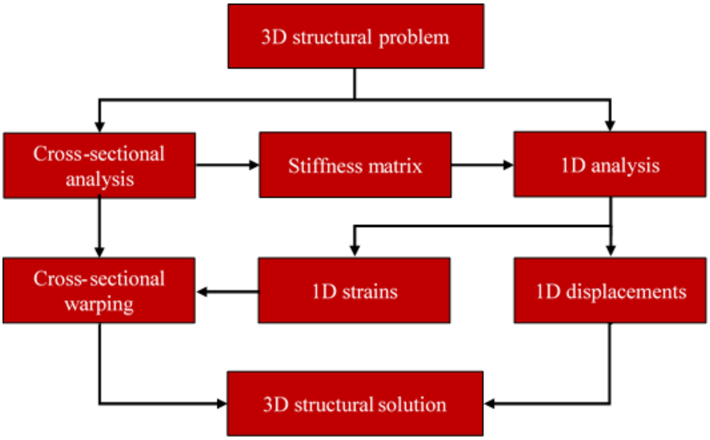

Fig. 2. Hierarchy of solution for a 3D structural problem.

$$\Gamma_R = \frac{1}{\sqrt{g}}\begin{bmatrix} \tilde{k} + k_1 I\left(\zeta_3\dfrac{\partial}{\partial\zeta_2} - \zeta_2\dfrac{\partial}{\partial\zeta_3}\right) \\ 0 \end{bmatrix}, \quad \Gamma_\ell = \frac{1}{\sqrt{g}}\begin{bmatrix} I \\ 0 \end{bmatrix},$$
$$\varepsilon = [\gamma_{11} \quad \kappa_1 \quad \kappa_2 \quad \kappa_3]^T, \quad \hat{w} = [w_1 \quad w_2 \quad w_3]^T,$$
$$\hat{\Gamma} = [\Gamma_{11} \quad 2\Gamma_{12} \quad 2\Gamma_{13} \quad \Gamma_{22} \quad 2\Gamma_{23} \quad \Gamma_{33}]. \tag{2}$$

In Eq. (2), $\sqrt{g} = 1 - x_2 k_3 + x_3 k_2$, where k_α are the initial curvatures and the notation tilde ($\sim$) forms an antisymmetric matrix from a vector according to $()^\sim = -e_{ijk}()_k$ using the permutation symbol e_{ijk} with $()' = \frac{\partial}{\partial x_1}$. The internal energy density is defined by the strain energy associated with this strain field

$$2U = \langle \Gamma^T D \Gamma \rangle \tag{3}$$

where D is the 6×6 symmetric material matrix and the notation

$$\langle \bullet \rangle = \int_S \bullet \sqrt{g}\, dx_2 dx_3 = h^2 \int_S \bullet \sqrt{g}\, d\zeta_2 d\zeta_3. \tag{4}$$

The characteristic size of the domain S is denoted by h and the dimensionless coordinates $\zeta \equiv \{\zeta_2 \equiv x_2/h, \zeta_3 \equiv x_3/h\}$ are introduced.

2.1. *Discretization*

The dimensional reduction from the original 3D structure to a 1D beam model can only be done approximately. As demonstrated in various applications, VAM can be used to construct a 1D formulation with minimum accuracy loss in comparison with the original 3D formulation. In order to deal with the arbitrary cross-sectional geometry and anisotropic materials, we need to turn to a numerical approach, such as the finite element method (FEM), to find the warping functions. Therefore, we discretize the warping field using the finite element method at the cross-sectional level. By doing this, the unknown warping field is reduced to the displacements at the nodes of the mesh,

$$\hat{w}(x_1, x_2, x_3) = S(x_2, x_3)V(x_1), \tag{5}$$

with $S(x_2, x_3)$ representing the element shape functions and V as a column matrix of the nodal values of the warping functions over the cross-section. Substituting Eq. (5) into Eq. (1) and then into Eq. (3), we obtain

$$\begin{aligned}
2U = {} & \left(\frac{1}{h}\right)^2 V^T\langle[\Gamma_h S]D[\Gamma_h S]\rangle V \\
& + \left(\frac{1}{h}\right) 2V^T(\langle[\Gamma_h S]D\Gamma_\varepsilon\rangle\varepsilon + \langle[\Gamma_h S]D[\Gamma_R S]\rangle V + \langle[\Gamma_h S]D[\Gamma_\ell S]\rangle V') \\
& + \varepsilon^T\langle[\Gamma_\varepsilon]^T D\Gamma_\varepsilon\rangle\varepsilon + V^T\langle[\Gamma_R S]D[\Gamma_R S]\rangle V + V'^T\langle[\Gamma_\ell S]D[\Gamma_\ell S]\rangle V' \\
& + 2V^T\langle[\Gamma_R S]D[\Gamma_\varepsilon]\rangle\varepsilon + 2V'^T\langle[\Gamma_\ell S]D[\Gamma_\varepsilon]\rangle\varepsilon + 2V^T\langle[\Gamma_R S]D[\Gamma_\ell S]\rangle V'.
\end{aligned} \tag{6}$$

2.2. *Stiffness matrix*

Depending on how we consider the displacement field component V, a specific form of strain energy can be derived. Here, we will assume that there is a known component of the warping, which corresponds to a set of non-classical degrees of freedom (d.o.f.) in the final beam model. If Ψ_q is the column matrix with these assumed deformation modes, the decomposition of the warping field can be written as

$$V = \Psi_q q(x) + W(x). \tag{7}$$

The vector of modal amplitudes, q, is a column matrix of one or more new unknown functions, and W is the new warping to be found. Through integration by parts, the potential of the generalized Timoshenko model can be written as

$$2U = \begin{bmatrix} \gamma_{11} \\ 2\gamma_{12} \\ 2\gamma_{13} \\ \kappa_1 \\ \kappa_2 \\ \kappa_3 \end{bmatrix}^T \begin{bmatrix} S_{11} & S_{12} & S_{13} & S_{14} & S_{15} & S_{16} \\ S_{21} & S_{22} & S_{23} & S_{24} & S_{25} & S_{26} \\ S_{31} & S_{32} & S_{33} & S_{34} & S_{35} & S_{36} \\ S_{41} & S_{42} & S_{43} & S_{44} & S_{45} & S_{46} \\ S_{51} & S_{52} & S_{53} & S_{54} & S_{55} & S_{56} \\ S_{61} & S_{62} & S_{63} & S_{64} & S_{65} & S_{66} \end{bmatrix} \begin{bmatrix} \gamma_{11} \\ 2\gamma_{12} \\ 2\gamma_{13} \\ \kappa_1 \\ \kappa_2 \\ \kappa_3 \end{bmatrix}. \tag{8}$$

3. Material Model

3.1. *CNTs/fiber/polymer multi-scale composite material model*

The three-phase multiscale composites considered herein comprised of isotropic matrix, CNTs and fibers and were assumed to be fabricated by dispersing nanotubes within an isotropic polymeric matrix and, impregnating the conventional fibers with this nanodispersed resin system. The alignment of fibers could be different for each lamina through the thickness. The CNTs were assumed to be isotropic and uniformly distributed and randomly oriented through the matrix. It was also assumed that the bonding between CNTs and matrix and the CNTs dispersion in the matrix are perfect; each CNT has the same mechanical properties depending on the aspect ratio; all CNTs are straight rods; there is no void in the matrix; fiber-matrix bonding was assumed to be perfect. The constituent materials were assumed to be linear elastic throughout the deformation. The effective material properties of the three-phase CNTs/fiber/polymer multiscale laminated composite can be predicted according to a hierarchical combination of Halpin-Tsai and micromechanics approaches via two steps as shown in Fig. 3.

The effective material properties of the multiscale composite were assumed to be orthotropic and can be predicted by [Rafiee *et al.*, 2014c]

$$E_{11h} = V_F E_{11}^F + V_{MNC} E^{MNC}, \tag{9a}$$

$$\frac{1}{E_{22h}} = \frac{V_F}{E_{22}^F} + \frac{V_{MNC}}{E^{MNC}} - V_F V_{MNC} \frac{\nu_F^2 E^{MNC}/E_{22}^F + \nu_{MNC}^2 E_{22}^F/E^{MNC} - 2\nu^F \nu^{MNC}}{V_F E_{22}^F + V_{MNC} E^{MNC}} \tag{9b}$$

$$\frac{1}{G_{12h}} = \frac{V_F}{G_{12}^F} + \frac{V_{MNC}}{G^{MNC}} \tag{9c}$$

$$\nu_{12h} = V_F \nu^F + V_{MNC} \nu^{MNC} \tag{9d}$$

$$\rho_h = V_F \rho^F + V_{MNC} \rho^{MNC} \tag{9e}$$

where E_{11}^F, E_{22}^F, G_{12}^F, ν^F and ρ^F are the Young's moduli, shear modulus, Poisson's ratio and mass density of fibers, respectively, and E^{MNC}, G^{MNC}, ν^{MNC} and ρ^{MNC}

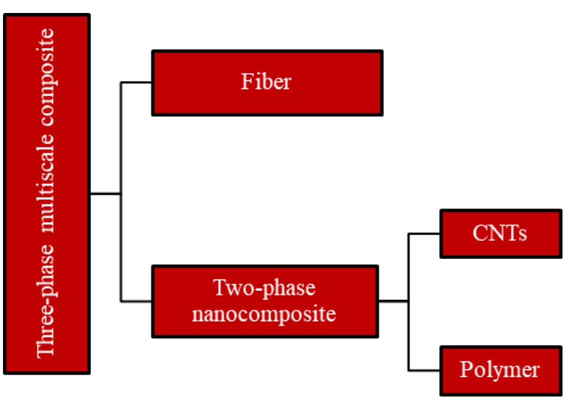

Fig. 3. Hierarchy of the three-phase CNTs/fiber/polymer multiscale composites [Rafiee *et al.*, 2014c].

represent the corresponding properties of the isotropic matrix of nanocomposite. V_F and V_{MNC} refer to the volume fractions of the fibers and the nanocomposite matrix, respectively.

According to the Halpin–Tsai equation, the tensile modulus of nanocomposites can be expressed as [Gojny *et al.*, 2004; Peeterbroeck *et al.*, 2007; Thostenson and Chou, 2003]

$$E^{MNC} = \frac{E^{MER}}{8}\left[5\left(\frac{1+2\beta_{dd}V_{\mathrm{CN}}}{1-\beta_{dd}V_{\mathrm{CN}}}\right)+3\left(\frac{1+2\left(\frac{\ell^{\mathrm{CN}}}{d^{\mathrm{CN}}}\right)\beta_{dl}V_{\mathrm{CN}}}{1-\beta_{dl}V_{\mathrm{CN}}}\right)\right] \tag{10a}$$

$$\beta_{dl} = \frac{\left(\frac{E_{11}^{\mathrm{CN}}}{E^{MER}}\right)-\left(\frac{d^{\mathrm{CN}}}{4t^{\mathrm{CN}}}\right)}{\left(\frac{E_{11}^{\mathrm{CN}}}{E^{MER}}\right)+\left(\frac{\ell^{\mathrm{CN}}}{2t^{\mathrm{CN}}}\right)} \tag{10b}$$

$$\beta_{dd} = \frac{\left(\frac{E_{11}^{\mathrm{CN}}}{E^{MER}}\right)-\left(\frac{d^{\mathrm{CN}}}{4t^{\mathrm{CN}}}\right)}{\left(\frac{E_{11}^{\mathrm{CN}}}{E^{MER}}\right)+\left(\frac{d^{\mathrm{CN}}}{2t^{\mathrm{CN}}}\right)}. \tag{10c}$$

where E_{11}^{CN}, V_{CN}, ℓ^{CN}, d^{CN} and are the Young's modulus, volume fraction, length, outer diameter and the thickness of carbon nanotubes, respectively, V_{MER} and E^{MER} indicate the volume fraction and Young's modulus of the isotropic epoxy resin matrix, respectively.

The volume fraction of carbon nanotubes can be expressed as [Rafiee *et al.*, 2014c]

$$V_{\mathrm{CN}} = \frac{w^{\mathrm{CN}}}{w^{\mathrm{CN}}+(\rho^{\mathrm{CN}}/\rho^{MER})-(\rho^{\mathrm{CN}}/\rho^{MER})w^{\mathrm{CN}}}, \tag{11}$$

where w^{CN} is the mass fraction of the carbon nanotubes, ρ^{CN} and ρ^{MER} are the mass densities of the carbon nanotube and epoxy resin matrix, respectively.

Poisson's ratio and mass density ρ can be expressed as

$$\nu^{MNC} = \nu^{MER} \tag{12a}$$

$$\rho^{MNC} = V_{\mathrm{CN}}\rho^{\mathrm{CN}} + V_{MER}\rho^{MER} \tag{12b}$$

where ρ^{CN}, ρ^{MER} are mass densities of the carbon nanotubes and matrix and is Poisson's ratio for the epoxy resin matrix, respectively. As the amount of CNTs was small, Poisson's ratio for the CNT composite was assumed to be the same as that of epoxy, 0.33 [Rafiee *et al.*, 2014c].

4. Numerical Study

Four different cross-sectional shapes were considered in this study: strip and circumferentially uniform stiffness (CUS) box, circular pipe, and Bell540 airfoil. These test cases are shown in Fig. 4. Their geometric parameters, material properties and stacking sequences are listed in Tables 1–3 unless otherwise specified. The

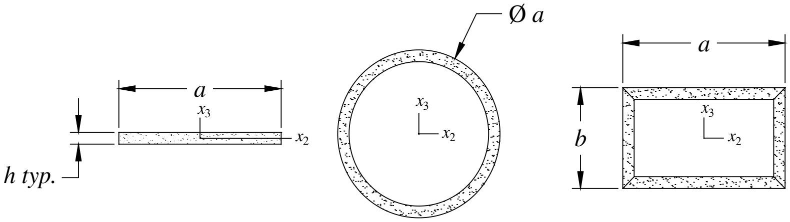

(a) Strip (b) Pipe (c) Box

Fig. 4. The cross-sections of the (a) strip, (b) pipe and (c) box beams studied in the examples.

Table 1. Typical material properties of nanocomposite beam used in examples unless otherwise specified [Rafiee *et al.*, 2014c].

Source	Symbol	Value	Unit	Description
Single-walled carbon nanotubes				
	t^{CN}	0.34×10^{-9}	m	Thickness of carbon nanotubes
	d^{CN}	1.4×10^{-9}	m	Outer diameter of carbon nanotubes
	ℓ^{CN}	25×10^{-6}	m	Length of carbon nanotubes
	w^{CN}	1	%	Weight percentage of carbon nanotubes
	ρ^{CN}	1350	kg/m3	Mass density of carbon nanotubes
	E_{11}^{CN}	640×109	kg/m2	Young's modulus of carbon nanotubes
	$\alpha_{11}^{\mathrm{CN}}$	3.4584×10^{-6}	1/K	Thermal expansion coefficient
	ν_{12}^{CN}	0.33	—	Poisson's ratio of carbon nanotubes
Multi-walled carbon nanotubes				
	t^{CN}	0.34×10^{-9}	m	Thickness of carbon nanotubes
	d^{CN}	20×10^{-9}	m	Outer diameter of carbon nanotubes
	ℓ^{CN}	50×10^{-6}	m	Length of carbon nanotubes
	w^{CN}	0	%	Weight percentage of carbon nanotubes
	ρ^{CN}	1350	kg/m3	Mass density of carbon nanotubes
	E_{11}^{CN}	400×109	kg/m2	Young's modulus of carbon nanotubes
	ν_{12}^{CN}	0.33	—	Poisson's ratio of carbon nanotubes
Epoxy resin polymer matrix				
	ρ^{MER}	1200	kg/m3	Mass density of epoxy resin matrix
	E^{MER}	2.72×109	kg/m2	Young's modulus of epoxy resin matrix
	α^{MER}	45×10^{-6}	1/K	Thermal expansion coefficient of epoxy resin matrix
	ν^{MER}	0.33	—	Poisson's ratio of epoxy resin matrix
E-Glass fibers				
	ρ^{F}	1200	kg/m3	Mass density of E-Glass fibers
	E_{11}^{F}	69×109	kg/m2	Young's modulus of E-Glass fibers
	ν^{F}	0.2	—	Poisson's ratio of E-Glass fibers
	V^{F}	0.5	—	Volume fraction of E-Glass fibers
Foam (For airfoil test case)				
	E^{Foam}	72.4×109	kg/m2	Young's modulus of airfoil foam
	ρ^{Foam}	160	kg/m3	Mass density of airfoil foam
	ν^{Foam}	0.3	—	Poisson's ratio of airfoil foam

Table 2. Properties of CAS box-beam.

Geometry	Lay up	Material properties
$a = 0:953$ in.	Right wall: $[15°/-15°]_3$	$E_{11} = 20:59 \times 10^6$ psi
$b = 0:53$ in.	Left wall: $[-15°/15°]_3$	$E_{22} = E_{33} = 1:42 \times 10^6$ psi
$h = 0:03$ in.	Upper wall: $[-15°]_6$	$G_{12} = 8:7 \times 10^6$ psi
	Lower wall: $[15°]_6$	$G_{13} = G_{23} = 6:96 \times 10^6$ psi
		$\upsilon_{12} = \upsilon_{13} = 0:42$

Table 3. Properties of beams cross-sections studied in the examples.

Case	Geometry	Lay-up
Strip	$a = 0.1\,\text{m}$ $h = 0.012\,\text{m}$	$[-45°/45°]_3$
Circular Pipe	Outer diameter $a = 0.05$ $h = 0.012\,\text{m}$	$[-45°/45°]$
CUS	$a = 0.1\,\text{m}$ $b = 0.06\,\text{m}$	Right wall: $[45°]_6$ Left wall: $[45°]_6$ Upper wall: $[45°]_6$ Lower wall: $[45°]_6$
Airfoil	See Fig. 5	See Fig. 5

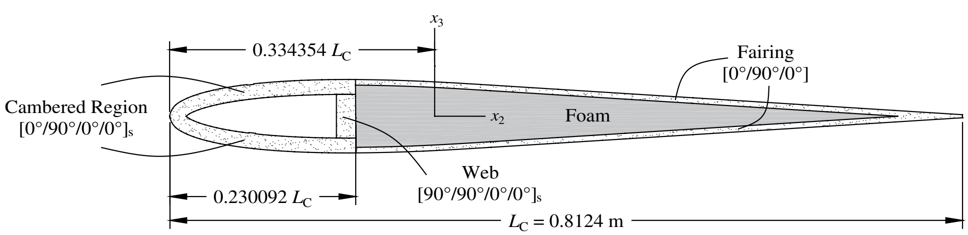

Fig. 5. Profile of the Bell540 airfoil blade and ply-up.

theoretical development presented in the previous section was numerically implemented in VABS and some of the numerical predictions were validated against available measurements.

Not all stiffness components are shown since the stiffness matrix is symmetric. All results are given at the area centroid and the 6×6 stiffness matrix is arranged as 1: extension; 2: chordwise transverse shear; 3: flatwise transverse shear; 4: torsion; 5: flatwise bending; and 6: chordwise bending. It should be noted that stiffness components with relatively small values compared to the others are neglected in the tabular data and figures.

4.1. *Validation*

To validate the theory and implementation, a circumferentially asymmetric stiffness (CAS) configuration was studied. The geometry and ply lay-up is shown in Fig. 4

Table 4. Stiffness for CAS box-beam (results are given at the area centroid) — 1: extension; 2: chordwise transverse shear; 3: flatwise transverse shear; 4: torsion; 5: flatwise bending; 6: chordwise bending ($\mu \approx 1.08\,\mathrm{kg/m}$, $\bar{x}_2 = \bar{x}_3 = 0$, $i_2 = 1.296 \times 10^{-5}\,\mathrm{kgm}$, $i_3 = 9 \times 10^{-4}\,\mathrm{kgm}$, $i_{23} = 0\,\mathrm{kgm}$).

Stiffness	Popescu *et al.* [2000]	Yu *et al.* [2002]	NABSA Giavotto *et al.* [1983]	Present
S_{11}(N)	0.137×10^7	0.137×10^7	0.137×10^7	1.3668×10^6
S_{22}(N)	0.883×10^5	0.884×10^5	0.885×10^5	8.8300×10^4
S_{33}(N)	0.775×10^4	0.389×10^5	0.387×10^5	3.8613×10^4
S_{44}(Nm^2)	0.174×10^5	0.170×10^5	0.170×10^5	1.6913×10^4
S_{55}(Nm^2)	0.608×10^5	0.591×10^5	0.591×10^5	5.9056×10^4
S_{66}(Nm^2)	0.143×10^6	0.141×10^6	0.141×10^6	1.4115×10^5
S_{12}(Nm)	-0.184×10^6	-0.184×10^6	-0.184×10^6	-1.8395×10^5
S_{13}(Nm)	-0.176×10^3	-0.131×10^3	-0.150×10^3	1.2864×10^2
S_{23}(N)	-0.842×10^2	0.719×10^2	0.803×10^2	-8.0210×10^1
S_{45}(Nm)	0.180×10^5	0.176×10^5	0.176×10^5	1.7599×10^4
S_{46}(Nm)	-0.362×10^3	-0.351×10^3	-0.349×10^3	3.5501×10^2
S_{56}(Nm^2)	-0.372×10^3	-0.371×10^3	-0.371×10^3	3.7115×10^2

and Table 2. The results presented in Table 4 clearly show the excellent agreement between the results from the present work and those of Popescu *et al.* [2000], Giavotto *et al.* [1983] and Yu *et al.* [2002].

4.2. *Strip*

To illustrate how CNTs affect the 6 × 6 stiffness matrix, we first investigated a beam with thin rectangular cross-section called Strip (see Fig. 4(a) and Table 3 for geometry and lay-up configuration). The cross-section meshed with 100×12 8-noded quadrilateral elements (7,650 d.o.f. in total). Stiffness results are listed in Tables 5–7 and Fig. 6. The symmetric lay-up of $[-45°/45°]_3$ introduced extension-torsion (S_{14}) and chordwise transverse shear-flatwise bending (S_{25}) couplings.

The effect of SWCNTs weight percentages w^{CN} on the stiffness properties per unit length of strip configuration ($\mu \approx 1.08\,\mathrm{kg/m}$, $\bar{x}_2 = \bar{x}_3 = 0$, $i_2 = 1.296 \times 10^{-5}\,\mathrm{kgm}$, $i_3 = 9 \times 10^{-4}\,\mathrm{kgm}$, $i_{23} = 0\,\mathrm{kgm}$) is shown in Table 5. One can observe from Tables 5 and 6 that the inclusion of a small weight percentage of carbon nanotubes was sufficient to significantly improve the stiffness properties. This improvement is more substantial with SWCNTs than with MWCNTs. This may be because of the lower specific surface area and defect structure of MWCNTs [Rafiee *et al.*, 2014c; Rafiee *et al.*, 2016]. Table 5 shows that adding 1% of SWCNTs improved the extension-extension coupling by 59.6% and the flatwise transverse shear coupling by 195%. However, addition of 1% and 2.5% of SWCNTs decreased the coupling between the chordwise transverse shear and the flatwise bending by −4.6% and −15.9%, respectively.

The influence of volume fraction of fibers on the stiffness properties per unit length of strip configuration ($\bar{x}_2 = \bar{x}_3 = 0$, $i_{23} = 0\,\mathrm{kgm}$) is also shown in Table 7. As one would expect, the stiffness components increased with the increase in the

Table 5. Effect of SWCNTs weight percentages w^{CN} on the stiffness properties per unit length of strip configuration ($\mu \approx 15.8533\,\mathrm{kg/m}$, $\bar{x}_2 = \bar{x}_3 = 0$, $i_2 \approx 7.894 \times 10^{-3}\,\mathrm{kgm}$, $i_3 \approx 7.504 \times 10^{-1}\,\mathrm{kgm}$, $i_{23} \approx 0\,\mathrm{kgm}$).

Stiffness	$w^{\mathrm{CN}} = 0\%$	$w^{\mathrm{CN}} = 1\%$	$w^{\mathrm{CN}} = 2.5\%$	$100 \times \frac{S_{ij}\|_{1\%} - S_{ij}\|_{0\%}}{S_{ij}\|_{0\%}}$	$100 \times \frac{S_{ij}\|_{2.5\%} - S_{ij}\|_{0\%}}{S_{ij}\|_{0\%}}$
$S_{11}(\mathrm{N})$	8.9563×10^6	1.4293×10^7	2.1101×10^7	59.6	135.6
$S_{22}(\mathrm{N})$	9.9733×10^6	1.1007×10^7	1.2404×10^7	10.4	24.4
$S_{33}(\mathrm{N})$	9.1548×10^4	2.7007×10^5	7.0678×10^5	195.0	672.0
$S_{44}(\mathrm{Nm}^2)$	4.6886×10^2	5.4390×10^2	6.3243×10^2	16.0	34.9
$S_{55}(\mathrm{Nm}^2)$	1.0953×10^2	1.7286×10^2	2.5389×10^2	57.8	131.8
$S_{66}(\mathrm{Nm}^2)$	7.4169×10^3	1.1866×10^4	1.7550×10^4	60.0	136.6
$S_{14}(\mathrm{Nm})$	5.0446×10^3	6.2909×10^3	6.6439×10^3	24.7	31.7
$S_{25}(\mathrm{Nm})$	-5.3354×10^3	-5.0877×10^3	-4.4855×10^3	−4.6	−15.9

Table 6. Effect of MWCNTs weight percentages w^{CN} on the stiffness properties per unit length of strip configuration ($\mu \approx 1.08\,\mathrm{kg/m}$, $\bar{x}_2 = \bar{x}_3 = 0$, $i_2 = 1.296 \times 10^{-5}\,\mathrm{kgm}$, $i_3 = 9 \times 10^{-4}\,\mathrm{kgm}$, $i_{23} = 0\,\mathrm{kgm}$).

Stiffness	$w^{\mathrm{CN}} = 0\%$	$w^{\mathrm{CN}} = 1\%$	$w^{\mathrm{CN}} = 2.5\%$	$100 \times \frac{S_{ij}\|_{1\%} - S_{ij}\|_{0\%}}{S_{ij}\|_{0\%}}$	$100 \times \frac{S_{ij}\|_{2.5\%} - S_{ij}\|_{0\%}}{S_{ij}\|_{0\%}}$
$S_{11}(\mathrm{N})$	8.9563×10^6	9.2753×10^6	9.7513×10^6	3.6	8.9
$S_{22}(\mathrm{N})$	9.9733×10^6	1.0033×10^7	1.0123×10^7	0.6	1.5
$S_{33}(\mathrm{N})$	9.1548×10^4	9.8939×10^4	1.1067×10^5	8.1	20.9
$S_{44}(\mathrm{Nm}^2)$	4.6886×10^2	4.7367×10^2	4.8072×10^2	1.0	2.5
$S_{55}(\mathrm{Nm}^2)$	1.0953×10^2	1.1332×10^2	1.1896×10^2	3.5	8.6
$S_{66}(\mathrm{Nm}^2)$	7.4169×10^3	7.6825×10^3	8.0788×10^3	3.6	8.9
$S_{14}(\mathrm{Nm})$	5.0446×10^3	5.1519×10^3	5.3033×10^3	2.1	5.1
$S_{25}(\mathrm{Nm})$	-5.3354×10^3	-5.3316×10^3	-5.3225×10^3	−0.1	−0.2

Table 7. Effect of volume fraction of fibers on the stiffness properties per unit length of strip configuration ($\bar{x}_2 = \bar{x}_3 = 0$, $i_{23} = 0$ kgm).

Stiffness	$V_F = 0.5$	$V_F = 0.6$	$V_F = 0.7$	$100 \times \frac{S_{ij}\|_{V_F=0.6} - S_{ij}\|_{V_F=0.5}}{S_{ij}\|_{V_F=0.5}}$	$100 \times \frac{S_{ij}\|_{V_F=0.7} - S_{ij}\|_{V_F=0.5}}{S_{ij}\|_{V_F=0.5}}$
S_{11} (N)	1.4293×10^7	1.7410×10^7	2.1923×10^7	21.8	53.4
S_{22} (N)	1.1007×10^7	1.2827×10^7	1.4823×10^7	16.5	34.7
S_{33} (N)	2.7007×10^5	3.7522×10^5	5.8458×10^5	38.9	116.5
S_{44} (Nm^2)	5.4390×10^2	6.3597×10^2	7.4151×10^2	16.9	36.3
S_{55} (Nm^2)	1.7286×10^2	2.1057×10^2	2.6481×10^2	21.8	53.2
S_{66} (Nm^2)	1.1866×10^4	1.4446×10^4	1.8193×10^4	21.7	53.3
S_{14} (Nm)	6.2909×10^3	8.0584×10^3	9.9750×10^3	28.1	58.6
S_{25} (Nm)	-5.0877×10^3	-6.2724×10^3	-7.2824×10^3	23.3	43.1
μ(kg/m)	1.081	1.095	1.138	1.3	5.3
i_2(kgm)	1.297×10^{-5}	1.314×10^{-5}	1.366×10^{-5}	1.3	5.3
i_3(kgm)	9.007×10^{-4}	9.125×10^{-4}	9.484×10^{-4}	1.3	5.3

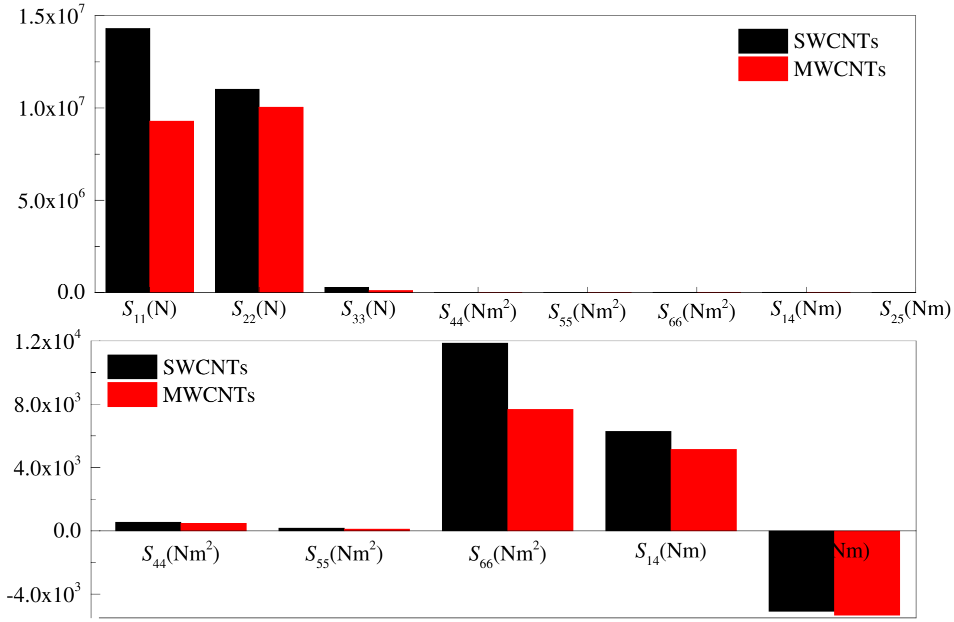

Fig. 6. Effect of CNTs structure on the stiffness properties per unit length of strip configuration ($w^{\mathrm{CN}} = 1\%$, $\mu \approx 1.08\,\mathrm{kg/m}$, $\bar{x}_2 = \bar{x}_3 = 0$, $i_2 = 1.296 \times 10^{-5}\,\mathrm{kgm}$, $i_3 = 9 \times 10^{-4}\,\mathrm{kgm}$, $i_{23} = 0\,\mathrm{kgm}$).

volume fraction of fibers. This is consistent with earlier reports [He *et al.*, 2015; Rafiee *et al.*, 2014a, 2014b, 2014c, 2014d; Rafiee *et al.*, 2016]. From the results shown in Table 7, one can see that the flatwise transverse shear coupling had the most significant improvement.

4.3. *Circular pipe*

The next test case considered was a circular pipe beam. The geometry and stacking sequence of this cross-section is shown in Fig. 4(b) and Table 3. The stiffness results, using 2,320 8-noded quadrilaterals elements (14,848 d.o.f.) to discretize the cross-section, can be found in Table 10 and Fig. 7. The ply-up of $[-45°/45°]$ generated extension-torsion (S_{14}), chordwise transverse shear-flatwise bending (S_{25}), and flatwise transverse shear-chordwise bending (S_{36}) couplings.

As one can observe from the results, a small weight percentage of carbon nanotubes was also able to improve the stiffness properties of circular pipe cross-section. The extension (S_{11}), flatwise bending (S_{55}) and chordwise bending (S_{66}) components of coupling received the most significant improvements. However, addition of CNTs weakened the coupling between (a) extension-torsion (S_{14}), (b) chordwise transverse shear-flatwise bending (S_{25}) and (c) flatwise transverse shear-chordwise bending (S_{36}). This could be used toward elastically tailoring circular pipe beams to meet stability requirements. The stiffness components also increased with the increase of the volume fraction of fibers (see Table 9).

Table 8. Effect of MWCNTs weight percentages w^{CN} on the stiffness properties per unit length of circular pipe configuration ($\mu \approx 2.99\,\mathrm{kg/m}$, $\bar{x}_2 = \bar{x}_3 = 0$, $i_2 = i_3 = 2.944 \times 10^{-3}\,\mathrm{kgm}$, $i_{23} = 0\,\mathrm{kgm}$).

Stiffness	$w^{\mathrm{CN}} = 0\%$	$w^{\mathrm{CN}} = 1\%$	$w^{\mathrm{CN}} = 2.5\%$	$100 \times \frac{S_{ij}\|_{1\%} - S_{ij}\|_{0\%}}{S_{ij}\|_{0\%}}$	$100 \times \frac{S_{ij}\|_{2.5\%} - S_{ij}\|_{0\%}}{S_{ij}\|_{0\%}}$
S_{11}(N)	2.4944×10^7	2.5824×10^7	2.7138×10^7	3.5	8.8
S_{22}(N)	1.6811×10^7	1.6930×10^7	1.7105×10^7	0.7	1.7
S_{33}(N)	1.6811×10^7	1.6930×10^7	1.7105×10^7	0.7	1.7
S_{44}(Nm^2)	6.5397×10^4	6.5791×10^4	6.6379×10^4	0.6	1.5
S_{55}(Nm^2)	2.4656×10^4	2.5520×10^4	2.6809×10^4	3.5	8.7
S_{66}(Nm^2)	2.4656×10^4	2.5520×10^4	2.6809×10^4	3.5	8.7
S_{14}(Nm)	9.1691×10^4	9.1584×10^4	9.1385×10^4	−0.1	−0.3
S_{25}(Nm)	-5.5693×10^4	-5.4990×10^4	-5.3950×10^4	−1.3	−3.1
S_{36}(Nm)	-5.5693×10^4	-5.4990×10^4	-5.3950×10^4	−1.3	−3.1

Table 9. Effect of volume fraction of fibers on the stiffness properties per unit length of circular pipe configuration ($\bar{x}_2 = \bar{x}_3 = 0$, $i_{23} = 0\,\mathrm{kgm}$).

Stiffness	$V_F = 0.5$	$V_F = 0.6$	$V_F = 0.7$	$100 \times \frac{S_{ij}\|_{V_F=0.6} - S_{ij}\|_{V_F=0.5}}{S_{ij}\|_{V_F=0.5}}$	$100 \times \frac{S_{ij}\|_{V_F=0.7} - S_{ij}\|_{V_F=0.5}}{S_{ij}\|_{V_F=0.5}}$
S_{11}(N)	3.9667×10^7	4.8314×10^7	6.0811×10^7	21.8	53.3
S_{22}(N)	1.8732×10^7	2.1837×10^7	2.5257×10^7	16.6	34.8
S_{33}(N)	1.8732×10^7	2.1837×10^7	2.5257×10^7	16.6	34.8
S_{44}(Nm^2)	7.2141×10^4	8.4060×10^4	9.7123×10^4	16.5	34.6
S_{55}(Nm^2)	3.9126×10^4	4.7649×10^4	5.9962×10^4	21.8	53.3
S_{66}(Nm^2)	3.9126×10^4	4.7649×10^4	5.9962×10^4	21.8	53.3
S_{12}(Nm)	8.7650×10^4	1.0742×10^5	1.2461×10^5	22.6	42.2
S_{35}(Nm)	-4.4888×10^4	-5.3339×10^4	-5.8546×10^4	18.8	30.4
S_{36}(Nm)	-4.4888×10^4	-5.3339×10^4	-5.8546×10^4	18.8	30.4
μ(kg/m)	2.99	3.03	3.15	1.3	5.3
i_2(kgm)	2.95×10^{-3}	2.98×10^{-3}	3.10×10^{-3}	1.3	5.3
i_3(kgm)	2.95×10^{-3}	2.98×10^{-3}	3.10×10^{-3}	1.3	5.3

Table 10. Effect of SWCNTs weight percentages w^{CN} on the stiffness properties per unit length of circular pipe configuration ($\mu \approx 2.99\,\mathrm{kg/m}$, $\bar{x}_2 = \bar{x}_3 = 0$, $i_2 = i_3 = 2.944 \times 10^{-3}\,\mathrm{kgm}$, $i_{23} = 0\,\mathrm{kgm}$).

Stiffness	$w^{\mathrm{CN}} = 0\%$	$w^{\mathrm{CN}} = 1\%$	$w^{\mathrm{CN}} = 2.5\%$	$100 \times \frac{S_{ij}\vert_{1\%} - S_{ij}\vert_{0\%}}{S_{ij}\vert_{0\%}}$	$100 \times \frac{S_{ij}\vert_{2.5\%} - S_{ij}\vert_{0\%}}{S_{ij}\vert_{0\%}}$
S_{11}(N)	2.4944×10^7	3.9667×10^7	5.8442×10^7	59.0	134.3
S_{22}(N)	1.6811×10^7	1.8732×10^7	2.1178×10^7	11.4	26.0
S_{33}(N)	1.6811×10^7	1.8732×10^7	2.1178×10^7	11.4	26.0
S_{44}(Nm^2)	6.5397×10^4	7.2141×10^4	8.1240×10^4	10.3	24.2
S_{55}(Nm^2)	2.4656×10^4	3.9126×10^4	5.7619×10^4	58.7	133.7
S_{66}(Nm^2)	2.4656×10^4	3.9126×10^4	5.7619×10^4	58.7	133.7
S_{14}(Nm)	9.1691×10^4	8.7650×10^4	7.8023×10^4	−4.4	−14.9
S_{25}(Nm)	-5.5693×10^4	-4.4888×10^4	-3.4138×10^4	−19.4	−38.7
S_{36}(Nm)	-5.5693×10^4	-4.4888×10^4	-3.4138×10^4	−19.4	−38.7

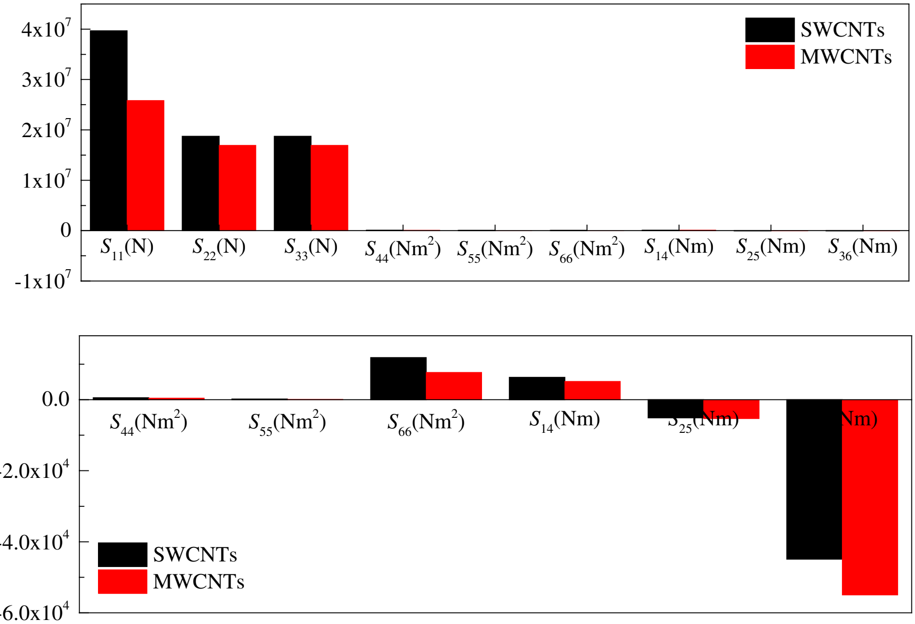

Fig. 7. Effect of CNTs structure on the stiffness properties per unit length of circular pipe configuration ($w^{\mathrm{CN}} = 1\%$, $\mu \approx 2.99\,\mathrm{kg/m}$, $\bar{x}_2 = \bar{x}_3 = 0$, $i_2 = i_3 = 2.944 \times 10^{-3}\,\mathrm{kgm}$, $i_{23} = 0\,\mathrm{kgm}$).

4.4. *CUS box*

To exemplify the effects of CNTs and volume fraction of fibers on the stiffness of composite beams, a CUS box-beam was also considered. The geometry and stacking sequence of circular pipe beam cross-section is shown in Fig. 4(c) and Table 3. The cross-section meshed with 1,920 8-noded quadrilateral elements (12,800 d.o.f. in total). The lay-up in every wall was $[45°]_6$, and the beam exhibited extension-twist (S_{14}) and shear-bending (S_{25} and S_{36}) couplings. The results are presented in Tables 11–13 and Fig. 8. When we reinforced the beam with CNTs, the values of all stiffness components were significantly affected. Similarly to previous cases, this improvement was more prominent with SWCNTs than with MWCNTs. The effect of CNTs structure on the stiffness properties per unit length of CUS configuration is shown in Fig. 8. From Fig. 8, one can see that the extension-twist coupling was relatively stronger than shear-bending couplings.

4.5. *Airfoil*

The last test case considered was a Bell540 airfoil-shape cross-section (see Fig. 5). The complete blade had a span of 0.8124 m (beyond the clamping area at the root). The blade geometry and material properties are shown in Fig. 5. The right cell of the airfoil was filled with foam. A finite element mesh with 9,885 6-noded triangular elements (40,850 d.o.f.) was used. The predicted stiffness coefficients are

Table 11. Effect of SWCNTs weight percentages w^{CN} on the stiffness properties per unit length of CUS configuration ($\mu \approx 2.9376\,\mathrm{kg/m}$, $\bar{x}_2 = \bar{x}_3 = 0$, $i_2 = 1.354 \times 10^{-3}\,\mathrm{kgm}$, $i_3 = 3.315 \times 10^{-3}\,\mathrm{kgm}$, $i_{23} = 0\,\mathrm{kgm}$).

Stiffness	$w^{\mathrm{CN}} = 0\%$	$w^{\mathrm{CN}} = 1\%$	$w^{\mathrm{CN}} = 2.5\%$	$100 \times \frac{S_{ij}\|_{1\%} - S_{ij}\|_{0\%}}{S_{ij}\|_{0\%}}$	$100 \times \frac{S_{ij}\|_{2.5\%} - S_{ij}\|_{0\%}}{S_{ij}\|_{0\%}}$
S_{11}(N)	2.4483×10^7	3.8986×10^7	5.7474×10^7	59.2	134.8
S_{22}(N)	1.2864×10^7	1.7774×10^7	2.2786×10^7	38.2	77.1
S_{33}(N)	5.7782×10^6	8.0760×10^6	1.0427×10^7	39.8	80.5
S_{44}(Nm^2)	2.1137×10^4	2.9572×10^4	3.8154×10^4	39.9	80.5
S_{55}(Nm^2)	1.1358×10^4	1.7992×10^4	2.6487×10^4	58.4	133.2
S_{66}(Nm^2)	2.7752×10^4	4.4066×10^4	6.4889×10^4	58.8	133.8
S_{14}(Nm)	-2.5288×10^5	-3.0486×10^5	-3.1517×10^5	20.6	24.6
S_{25}(Nm)	1.3122×10^5	1.5527×10^5	1.5903×10^5	18.3	21.2
S_{36}(Nm)	1.3564×10^5	1.6291×10^5	1.6809×10^5	20.1	23.9

Table 12. Effect of MWCNTs weight percentages w^{CN} on the stiffness properties per unit length of CUS configuration ($\mu \approx 2.9376\,\mathrm{kg/m}$, $\bar{x}_2 = \bar{x}_3 = 0$, $i_2 = 1.354 \times 10^{-3}\,\mathrm{kgm}$, $i_3 = 3.315 \times 10^{-3}\,\mathrm{kgm}$, $i_{23} = 0\,\mathrm{kgm}$).

Stiffness	$w^{\mathrm{CN}} = 0\%$	$w^{\mathrm{CN}} = 1\%$	$w^{\mathrm{CN}} = 2.5\%$	$100 \times \frac{S_{ij}\|_{1\%} - S_{ij}\|_{0\%}}{S_{ij}\|_{0\%}}$	$100 \times \frac{S_{ij}\|_{2.5\%} - S_{ij}\|_{0\%}}{S_{ij}\|_{0\%}}$
S_{11}(N)	2.4483×10^7	2.5350×10^7	2.6644×10^7	3.5	8.8
S_{22}(N)	1.2864×10^7	1.3193×10^7	1.3673×10^7	2.6	6.3
S_{33}(N)	5.7782×10^6	5.9317×10^6	6.1562×10^6	2.7	6.5
S_{44}(Nm^2)	2.1137×10^4	2.1701×10^4	2.2526×10^4	2.7	6.6
S_{55}(Nm^2)	1.1358×10^4	1.1754×10^4	1.2344×10^4	3.5	8.7
S_{66}(Nm^2)	2.7752×10^4	2.8727×10^4	3.0183×10^4	3.5	8.8
S_{14}(Nm)	-2.5288×10^5	-2.5751×10^5	-2.6401×10^5	1.8	4.4
S_{25}(Nm)	1.3122×10^5	1.3340×10^5	1.3644×10^5	1.7	4.0
S_{36}(Nm)	1.3564×10^5	1.3808×10^5	1.4151×10^5	1.8	4.3

Table 13. Effect of volume fraction of fibers on the stiffness properties per unit length of CUS configuration ($\bar{x}_2 = \bar{x}_3 = 0$, $i_{23} = 0\,\mathrm{kgm}$).

Stiffness	$w^{\mathrm{CN}} = 0\%$	$w^{\mathrm{CN}} = 1\%$	$w^{\mathrm{CN}} = 2.5\%$	$100 \times \frac{S_{ij}\|_{1\%} - S_{ij}\|_{0\%}}{S_{ij}\|_{0\%}}$	$100 \times \frac{S_{ij}\|_{2.5\%} - S_{ij}\|_{0\%}}{S_{ij}\|_{0\%}}$
S_{11} (N)	3.8986×10^7	4.7493×10^7	5.9792×10^7	21.8	53.4
S_{22} (N)	1.7774×10^7	2.0396×10^7	2.4049×10^7	14.7	35.3
S_{33} (N)	8.0760×10^6	9.3087×10^6	1.1022×10^7	15.3	36.5
S_{44} (Nm^2)	2.9572×10^4	3.3949×10^4	4.0110×10^4	14.8	35.6
S_{55} (Nm^2)	1.7992×10^4	2.1906×10^4	2.7558×10^4	21.8	53.2
S_{66} (Nm^2)	4.4066×10^4	5.3672×10^4	6.7542×10^4	21.8	53.3
S_{14} (Nm)	-3.0486×10^5	-3.8847×10^5	-4.7711×10^5	27.4	56.5
S_{25} (Nm)	1.5527×10^5	1.9742×10^5	2.4163×10^5	27.1	55.6
S_{36} (Nm)	1.6291×10^5	2.0813×10^5	2.5580×10^5	27.8	57.0
μ(kg/m)	2.9398	2.9785	3.0956	1.3	5.3
i_2(kgm)	1.3551×10^{-3}	1.3729×10^{-3}	1.4269×10^{-3}	1.3	5.3
i_3(kgm)	3.3172×10^{-3}	3.3609×10^{-3}	3.49×10^{-3}	1.3	5.3

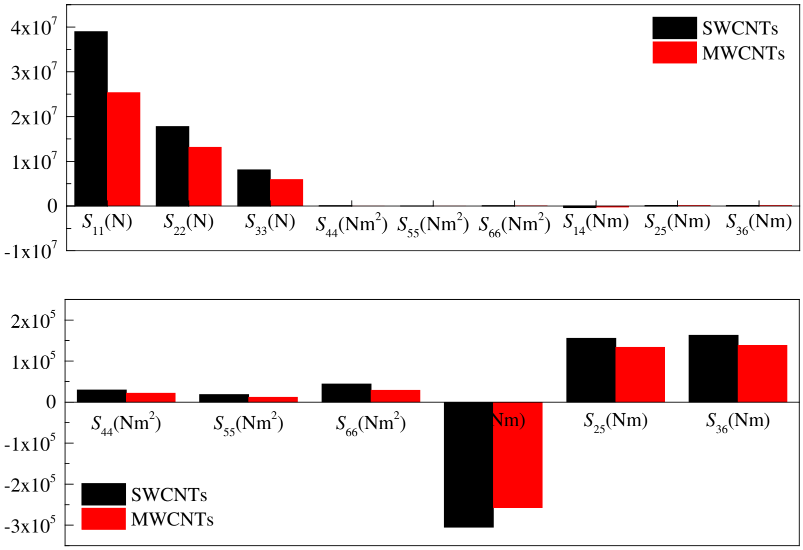

Fig. 8. Effect of CNTs structure on the stiffness properties per unit length of CUS configuration ($\mu \approx 2.9376\,\text{kg/m}$, $\bar{x}_2 = \bar{x}_3 = 0$, $i_2 = 1.354 \times 10^{-3}\,\text{kgm}$, $i_3 = 3.315 \times 10^{-3}\,\text{kgm}$, $i_{23} = 0\,\text{kgm}$).

given in Table 14 through 16 and Fig. 9. The beam exhibited extension-chordwise bending (S_{16}) and flatwise transverse shear-twist (S_{34}) couplings. From the results, one can see that the inclusion of the SWCNTS significantly stiffened the structure. However, this improvement is more obvious in chordwise transverse shear coupling (S_{22}) with 19.4%, flatwise transverse shear coupling (S_{33}) with 42.6% and flatwise transverse shear-twist (S_{34}) coupling as a result of adding 1% of SWCNTs. The same couplings were also significantly influenced as a result of adding 1% of MWCNTs. However, as in the previous cases, reinforcement achieved by MWCNTs was much lower than with SWCNTs. Nevertheless, MWCNTs can still be an interesting choice due to the higher cost of large scale use of using SWCNTs in mass production applications.

The effect of volume fraction of E-Glass fibers on the stiffness properties per unit length of Bell540 airfoil configuration ($\bar{x}_2 = \bar{x}_3 = 0$, $i_{23} = 0\,\text{kgm}$) is presented in Table 16. Based on these results, increasing the volume fraction of fibers also improved the stiffness properties of airfoil cross-section studied (see Table 16). However, an increase in fiber volume fraction weakened the flatwise transverse shear-twist (S_{34}).

The effect of CNTs structure on the stiffness properties per unit length of Bell540 airfoil configuration ($w^{\text{CN}} = 1\%$, $\mu \approx 2.9376\,\text{kg/m}$, $\bar{x}_2 = \bar{x}_3 = 0$, $i_2 = 1.354 \times 10^{-3}\,\text{kgm}$, $i_3 = 3.315 \times 10^{-3}\,\text{kgm}$, $i_{23} = 0\,\text{kgm}$). The results from Fig. 9 reveal that both of SWCNTs and MWCNTs brought about approximately the same improvements. This is especially noticeable when we compare this test case with the previous test cases. Figure 9 also shows that the most significant coupling terms

Table 14. Effect of SWCNTs weight percentages w^{CN} on the stiffness properties per unit length of Bell540 airfoil configuration ($\mu \approx 15.8533\,\mathrm{kg/m}$, $\bar{x}_2 = \bar{x}_3 = 0$, $i_2 \approx 7.894 \times 10^{-3}\,\mathrm{kgm}$, $i_3 \approx 7.504 \times 10^{-1}\,\mathrm{kgm}$, $i_{23} \approx 0\,\mathrm{kgm}$).

Stiffness	$w^{\mathrm{CN}} = 0\%$	$w^{\mathrm{CN}} = 1\%$	$w^{\mathrm{CN}} = 2.5\%$	$100 \times \frac{S_{ij}\|_{1\%} - S_{ij}\|_{0\%}}{S_{ij}\|_{0\%}}$	$100 \times \frac{S_{ij}\|_{2.5\%} - S_{ij}\|_{0\%}}{S_{ij}\|_{0\%}}$
S_{11}(N)	1.8476×10^9	1.8764×10^9	1.9163×10^9	1.6	3.7
S_{22}(N)	4.1397×10^8	4.9422×10^8	5.5962×10^8	19.4	35.2
S_{33}(N)	5.6780×10^7	8.0989×10^7	1.0299×10^8	42.6	81.4
S_{44}(Nm^2)	5.0140×10^5	5.5416×10^5	6.2546×10^5	10.5	24.7
S_{55}(Nm^2)	5.3122×10^5	5.4733×10^5	5.6964×10^5	3.0	7.2
S_{66}(Nm^2)	6.1994×10^7	6.3599×10^7	6.5816×10^7	2.6	6.2
S_{16}(Nm)	-1.6268×10^8	-1.6381×10^8	-1.6538×10^8	0.7	1.7
S_{34}(Nm)	5.6853×10^5	7.0067×10^5	7.0972×10^5	23.2	24.8

Table 15. Effect of MWCNTs weight percentages w^{CN} on the stiffness properties per unit length of Bell540 airfoil configuration ($\mu \approx 15.8533\,\mathrm{kg/m}$, $\bar{x}_2 = \bar{x}_3 = 0$, $i_2 \approx 7.894 \times 10^{-3}\,\mathrm{kgm}$, $i_3 \approx 7.504 \times 10^{-1}\,\mathrm{kgm}$, $i_{23} \approx 0\,\mathrm{kgm}$).

Stiffness	$w^{\mathrm{CN}} = 0\%$	$w^{\mathrm{CN}} = 1\%$	$w^{\mathrm{CN}} = 2.5\%$	$100 \times \frac{S_{ij}\|_{1\%} - S_{ij}\|_{0\%}}{S_{ij}\|_{0\%}}$	$100 \times \frac{S_{ij}\|_{2.5\%} - S_{ij}\|_{0\%}}{S_{ij}\|_{0\%}}$
S_{11}(N)	1.8476×10^9	1.8492×10^9	1.8517×10^9	0.1	0.2
S_{22}(N)	4.1397×10^8	4.2009×10^8	4.2881×10^8	1.5	3.6
S_{33}(N)	5.6780×10^7	5.8429×10^7	6.0840×10^7	2.9	7.2
S_{44}(Nm^2)	5.0140×10^5	5.0446×10^5	5.0905×10^5	0.6	1.5
S_{55}(Nm^2)	5.3122×10^5	5.3215×10^5	5.3353×10^5	0.2	0.4
S_{66}(Nm^2)	6.1994×10^7	6.2086×10^7	6.2224×10^7	0.1	0.4
S_{16}(Nm)	-1.6268×10^8	-1.6274×10^8	-1.6284×10^8	0.0	0.1
S_{34}(Nm)	5.6853×10^5	5.8034×10^5	5.9700×10^5	2.1	5.0

Table 16. Effect of volume fraction of fibers on the stiffness properties per unit length of Bell540 airfoil configuration ($\bar{x}_2 = \bar{x}_3 = 0$, $i_{23} = 0\,\text{kgm}$).

Stiffness	$w^{\text{CN}} = 0\%$	$w^{\text{CN}} = 1\%$	$w^{\text{CN}} = 2.5\%$	$100 \times \frac{S_{ij}\|_{1\%} - S_{ij}\|_{0\%}}{S_{ij}\|_{0\%}}$	$100 \times \frac{S_{ij}\|_{2.5\%} - S_{ij}\|_{0\%}}{S_{ij}\|_{0\%}}$
S_{11} (N)	1.8764×10^9	1.9449×10^9	2.0181×10^9	3.7	7.6
S_{22} (N)	4.9422×10^8	5.1719×10^8	5.5157×10^8	4.6	11.6
S_{33} (N)	8.0989×10^7	8.4876×10^7	9.3002×10^7	4.8	14.8
S_{44} (Nm^2)	5.5416×10^5	5.8103×10^5	6.2421×10^5	4.8	12.6
S_{55} (Nm^2)	5.4733×10^5	5.8696×10^5	6.2914×10^5	7.2	14.9
S_{66} (Nm^2)	6.3599×10^7	6.7314×10^7	7.1294×10^7	5.8	12.1
S_{16} (Nm)	-1.6381×10^8	-1.6555×10^8	-1.6749×10^8	1.1	2.2
S_{34} (Nm)	7.0067×10^5	5.0632×10^5	3.1233×10^5	−27.7	−55.4
μ(kg/m)	1.59×10^1	1.60×10^1	1.65×10^1	1.0	4.2
i_2(kgm)	7.90×10^{-3}	7.99×10^{-3}	8.28×10^{-3}	1.2	4.8
i_3(kgm)	7.51×10^{-1}	7.60×10^{-1}	7.87×10^{-1}	1.2	4.8

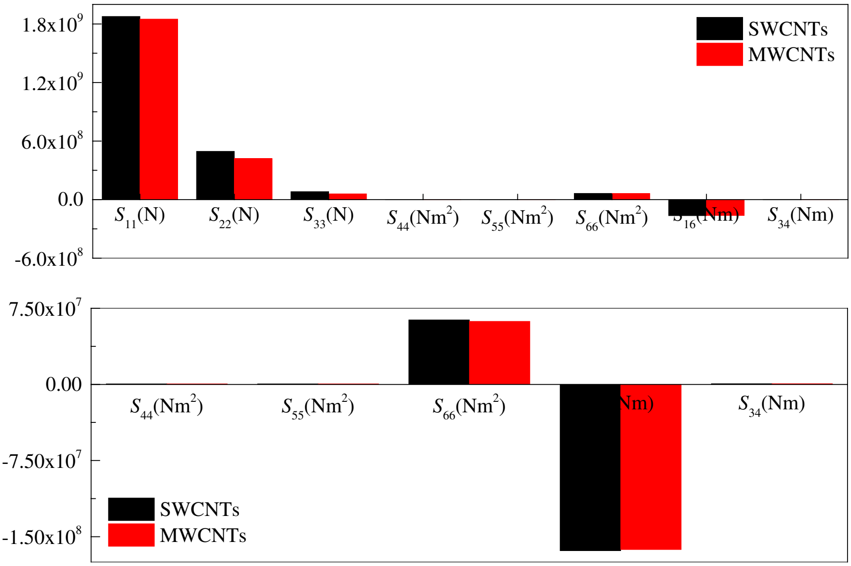

Fig. 9. Effect of CNTs structure on the stiffness properties per unit length of Bell540 airfoil configuration ($w^{\mathrm{CN}} = 1\%$, $\mu \approx 2.9376\,\mathrm{kg/m}$, $\bar{x}_2 = \bar{x}_3 = 0$, $i_2 = 1.354 \times 10^{-3}\,\mathrm{kgm}$, $i_3 = 3.315 \times 10^{-3}\,\mathrm{kgm}$, $i_{23} = 0\,\mathrm{kgm}$).

were extension (S_{11}), chordwise transverse shear (S_{22}) and extension-chordwise bending (S_{16}).

5. Conclusion

A finite-element-based, cross-sectional analysis for CNTs-reinforced multiscale composite beams was formulated from geometrically nonlinear, 3D elasticity. The 3D strain field was formulated in terms of 1D generalized strains and a 3D warping displacement. The developed formulation was numerically implemented in the VABS to compute the cross-section stiffness matrices and mass properties. Several numerical test cases were used to support the validation and application of the proposed theory. The results indicated that the inclusion of a small weight percentage of carbon nanotubes in the polymer matrix was sufficient to induce a significant improvement in stiffness properties. In some cases, however, CNTs may be used to weaken some specific structural couplings. SWCNTs were shown to have more significant effects than MWCNTs on the stiffness properties. This may be due to lower specific surface area and defect structure of MWCNTs. Overall, CNTs can be used to tailor the design of beams and blades for specific stiffness properties.

Acknowledgments

The first author thanks Fang Jiang from Purdue University for his technical help on preparation of VABS input file for pipe test case. The first author also gratefully acknowledges the financial support from Ontario Trillium Scholarship (OTS), University of Ottawa and Government of Ontario, Canada.

References

Bekyarova, E., Thostenson, E. T., Yu, A., Kim, H., Gao, J., Tang, J., Hahn, H. T., Chou, T.-W., Itkis, M. E., and Haddon, R. C. [2007] "Multiscale carbon nanotube-carbon fiber reinforcement for advanced epoxy composites," *Langmuir: The ACS Journal of Surfaces and Colloids* **23**(7), 3970–3974.

Berdichevsky, V., Armanios, E. and Badir, A. [1992] "Theory of anisotropic thin-walled closed-cross-section beams," *Composites Engineering* **2**(5–7), 411–432.

Cesnik, C. E. S. and Hodges, D. H. [1997] "VABS: A new concept for composite rotor blade cross-sectional modeling," *Journal of the American Helicopter Society* **42**, 27.

Cesnik, C. E. S., Hodges, D. H. and Sutyrin, V. G. [1996] "Cross-sectional analysis of composite beams including large initial twist and curvature effects," *AIAA Journal* **34**(9), 1913–1920.

Cesnik, C. E. S. and Shin, S. [2001] "On the modeling of integrally actuated helicopter blades," *International Journal of Solids and Structures* **38**(10–13), 1765–1789.

Danielson, D. A. and Hodges, D. H. [1987] "Nonlinear beam kinematics by decomposition of the rotation tensor," *Journal of Applied Mechanics* **54**, 258–262.

Díez-Pascual, A. M., Ashrafi, B., Naffakh, M., González-Domínguez, J. M., Johnston, A., Simard, B. and Gómez-Fatou, M. A. [2011] "Influence of carbon nanotubes on the thermal, electrical and mechanical properties of poly(ether ketone)/glass fiber laminates," *Carbon* **49**(8), 2817–2833.

Ghorashi, M. [2012] "Nonlinear analysis of the dynamics of articulated composite rotor blades," *Nonlinear Dynamics* **67**, 227–249.

Ghorashi, M. and Nitzsche, F. [2009] "Nonlinear dynamic response of an accelerating composite rotor blade using perturbations," *Journal of Mechanics of Materials And Structures* **4**(4), 693–718.

Giavotto, V., Borri, M., Mantegazza, P., Ghiringhelli, G., Carmaschi, V., Maffioli, G. C. and Mussi, F. [1983] "Anisotropic beam theory and applications," *Computers and Structures* **16**(1–4), 403–413.

Gojny, F. H., Wichmann, M. H. G., Köpke, U., Fiedler, B. and Schulte, K. [2004] "Carbon nanotube-reinforced epoxy-composites: Enhanced stiffness and fracture toughness at low nanotube content," *Composites Science and Technology* **64**(15), 2363–2371.

He, X. Q., Rafiee, M. and Mareishi, S. [2014] "Nonlinear dynamics of piezoelectric nanocomposite energy harvesters under parametric resonance," *Nonlinear Dynamics* **79**(3), 1863–1880.

He, X. Q., Rafiee, M., Mareishi, S. and Liew, K. M. [2015] "Large amplitude vibration of fractionally damped viscoelastic CNTs/fiber/polymer multiscale composite beams," *Composite Structures* **131**, 1111–1123.

Hodges, D. H. [1990] "A mixed variational formulation based on exact intrinsic equations for dynamics of moving beams," *International Journal of Solids and Structures* **26**(11), 1253–1273.

Hodges, D. H. [2003] "Geometrically exact , intrinsic theory for dynamics of curved and twisted anisotropic beams," *AIAA Journal* **41**(6), 1131–1137.

Hodges, D. H. [2006] *Nonlinear Composite Beam Thery. AIAA*. AIAA.

Hodges, D. H. [2015] "Unified approach for accurate and efficient modeling of composite rotor blade dynamics the Alexander A. Nikolsky honorary lecture," *Journal of the American Helicopter Society* **60**(1), 1–28.

Hodges, D. H., Saberi, H. and Ormiston, R. A. [2007] "Development of nonlinear beam elements for rotorcraft comprehensive analyses," *Journal of the American Helicopter Society* **52**(1), 36.

Hosseini, M., Gorgani, H. H., Shishesaz, M. and Hadi, A. [2017] "Size-dependent stress analysis of single-wall carbon nanotube based on strain gradient theory," *International Journal of Applied Mechanics* **9**(6).

Jung, S. N., Nagaraj, V. T. and Chopra, I. [2002] "Refined structural model for thin- and thick-walled composite rotor blades," *AIAA Journal* **40**(1), 105–116.

Kim, M., Park, Y. Bin, Okoli, O. I. and Zhang, C. [2009] "Processing, characterization, and modeling of carbon nanotube-reinforced multiscale composites," *Composites Science and Technology* **69**(3–4), 335–342.

Nejad, M. Z., Hadi, A. and Farajpour, A. [2017] "Consistent couple-stress theory for free vibration analysis of Euler-Bernoulli nano-beams made of arbitrary bi-directional functionally graded materials," *Structural Engineering and Mechanics* **63**(2), 161–169.

Nejad, M. Z., Hadi, A. and Rastgoo, A. [2016] "Buckling analysis of arbitrary two-directional functionally graded Euler-Bernoulli nano-beams based on nonlocal elasticity theory," *International Journal of Engineering Science* **103**, 1–10.

Pai, P. F. and Nayfeh, A. H. [1990] "Three-dimensional nonlinear vibrations of composite beams — I: Equations of motion," *Nonlinear Dynamics* **1**, 477–502.

Peeterbroeck, S., Breugelmans, L., Alexandre, M., BNagy, J., Viville, P., Lazzaroni, R. and Dubois, P. [2007] "The influence of the matrix polarity on the morphology and properties of ethylene vinyl acetate copolymers-carbon nanotube nanocomposites," *Composites Science and Technology* **67**(7–8), 1659–1665.

Popescu, B. and Hodges, D. H. [2000] "On asymptotically correct Timoshenko-like anisotropic beam theory," *International Journal of Solids and Structures* **37**(3), 535–558.

Popescu, B., Hodges, D. H. and Cesnik, C. E. S. [2000] "Obliqueness effects in asymptotic cross-sectional analysis of composite beams," *Computers and Structures* **76**(4), 533–543.

Rafiee, M., He, X. Q. and Liew, K. M. [2014a] "Non-linear dynamic stability of piezoelectric functionally graded carbon nanotube-reinforced composite plates with initial geometric imperfection," *International Journal of Non-Linear Mechanics* **59**, 37–51.

Rafiee, M., He, X. Q. and Liew, K. M. [2014b] "Nonlinear analysis of piezoelectric nanocomposite energy harvesting plates," *Smart Materials and Structures* **23**(6), 65001.

Rafiee, M., He, X. Q., Mareishi, S. and Liew, K. M. [2014c] "Modeling and stress analysis of smart CNTs/fiber/polymer multiscale composite plates," *International Journal of Applied Mechanics* **6**(3), 1450025.

Rafiee, M., Liu, X. F., He, X. Q. and Kitipornchai, S. [2014d] "Geometrically nonlinear free vibration of shear deformable piezoelectric carbon nanotube/fiber/polymer multiscale laminated composite plates," *Journal of Sound and Vibration* **333**(14), 3236–3251.

Rafiee, M., He, X. Q., Mareishi, S. and Liew, K. M. [2015] "Nonlinear response of piezoelectric nanocomposite plates: Large deflection, post-buckling and large amplitude vibration," *International Journal of Applied Mechanics* **7**(5).

Rafiee, M., Nitzsche, F. and Labrosse, M. [2016] "Rotating nanocomposite thin-walled beams undergoing large deformation," *Composite Structures* **150**, 191–199.

Rafiee, M., Nitzsche, F. and Labrosse, M. [2017] "Dynamics, vibration and control of rotating composite beams and blades: A critical review," *Thin-Walled Structures* **119**, 795–819.

Rafiee, M., Yang, J. and Kitipornchai, S. [2013a] "Large amplitude vibration of carbon nanotube reinforced functionally graded composite beams with piezoelectric layers," *Composite Structures* **96**, 716–725.

Rafiee, M., Yang, J. and Kitipornchai, S. [2013b] "Thermal bifurcation buckling of piezoelectric carbon nanotube reinforced composite beams," *Computers and Mathematics with Applications* **66**(7), 1147–1160.

Rana, S. and Fangueiro, R. [2016] *Advanced Composite Materials for Aerospace Engineering*: *Processing*, *Properties and Applications*, 1st edn. (Woodhead Publishing, United Kingdom).

Song, O. and Librescu, L. [1997] "Structural modeling and free vibration analysis of rotating composite thin-walled beams," *Journal of the American Helicopter Society* **42**(4), 358.

Thostenson, E. T. and Chou, T.-W. [2003] "On the elastic properties of carbon nanotube-based composites: modelling and characterization," *Journal of Physics D*: *Applied Physics* **36**, 573–582.

Traugott, J. P., Patil, M. J. and Holzapfel, F. [2006] "Nonlinear modeling of integrally actuated beams," *Aerospace Science and Technology* **10**(6), 509–518.

Wang, Y., Xu, Z., Chen, L., Jiao, Y. and Wu, X. [2011] "Multi-scale hybrid composites-based carbon nanotubes," *Polymer Composites* **32**(2), 159–167.

Yu, W. [2011] "VABS manual for users," *Department of Mechanical and Aerospace Engineering*, Utah State University, Logan, Utah, pp. 1–22.

Yu, W., Hodges, D. H. and Ho, J. C. [2012] "Variational asymptotic beam sectional analysis — An updated version," *International Journal of Engineering Science* **59**, 40–64.

Yu, W., Hodges, D. H., Volovoi, V. and Cesnik, C. E. S. [2002] "On Timoshenko-like modeling of initially curved and twisted composite beams," *International Journal of Solids and Structures* **39**(19), 5101–5121.

Chapter 5

5. Modeling and mechanical analysis of multiscale fiber-reinforced graphene composites: Nonlinear bending, thermal post-buckling and large amplitude vibration

as published* in International Journal of Non-Linear Mechanics 103 (2018) 104–112

https://doi.org/10.1016/j.ijnonlinmec.2018.05.004

*In accordance with University of Ottawa regulations, the contact email address has been removed from this article.

Foreword

This chapter provides a mathematical model to predict the effective material properties of GNPs/fiber/polymer multiscale composites. The large deflection, post-buckling and free nonlinear vibrations of GNPs-reinforced multiscale composite beams were studied through a theoretical study. The nonlinear bending and post-buckling equations were numerically solved by the Newton method, and the multiple timescales method was used to study the nonlinear free vibrations and dynamic response of laminated nanocomposite beam under two set of boundary conditions. A parametric study was carried out. The numerical results investigated the effect of GNPs on the central deflection, buckling load and natural frequencies of the multiscale composites.

International Journal of Non-Linear Mechanics 103 (2018) 104–112

Contents lists available at ScienceDirect

International Journal of Non-Linear Mechanics

journal homepage: www.elsevier.com/locate/nlm

Modeling and mechanical analysis of multiscale fiber-reinforced graphene composites: Nonlinear bending, thermal post-buckling and large amplitude vibration

M. Rafiee [a,*], F. Nitzsche [b], M.R. Labrosse [a]

[a] Department of Mechanical Engineering, University of Ottawa, 161 Louis Pasteur, Ottawa, ON K1N 6N5, Canada
[b] Department of Mechanical and Aerospace Engineering, Carleton University, 1125 Colonel By Drive, Ottawa, ON K1S 5B6, Canada

ARTICLE INFO

Keywords:
Mathematical modeling
Graphene nanoplatelets
Multiscale laminated composites beam
Nonlinear bending
Thermal buckling and postbuckling
Nonlinear vibration

ABSTRACT

In this paper, a mathematical model was developed to predict the effective material properties of graphene nanoplatelets/fiber/polymer multiscale composites (GFPMC). The large deflection, post-buckling and free nonlinear vibration of graphene nanoplatelets-reinforced multiscale composite beams were studied through a theoretical study. The governing equations of laminated nanocomposite beams were derived from the Euler–Bernoulli beam theory with von Kármán geometric nonlinearity. Halpin–Tsai equations and fiber micromechanics were used in hierarchy to predict the bulk material properties of the multiscale composite. Graphene nanoplatelets (GNPs) were assumed to be uniformly distributed and randomly oriented through the epoxy resin matrix. A semi-analytical approach was used to calculate the large static deflection and critical buckling temperature of multiscale multifunctional nanocomposite beams. A perturbation scheme was also employed to determine the nonlinear dynamic response and the nonlinear natural frequencies of the beams with clamped–clamped, and hinged–hinged boundary conditions. The effects of weight percentage of graphene nanoplatelets, volume fraction of fibers, and boundary conditions on the static deflection, thermal buckling and post-buckling and linear and nonlinear natural frequencies of the GFPMC beams were investigated in detail. The numerical results showed that the central deflection and natural frequency were significantly improved by a small percentage of GNPs. However, addition of GNPs led to a lower critical buckling temperature.

1. Introduction

GNPs/fiber/polymer multiscale laminated composite materials consist of high strength and modulus fibers, graphene nanoplatelets (GNPs) and a polymer matrix. GNPs/fiber/polymer multiscale composites can significantly reduce weight with the same or better performance than that of metal materials and, as such, have drawn significant attention in recent years. GNPs/fiber/polymer composites have been widely used in many structural applications, such as aircrafts, space vehicles, automotive industry, sporting goods, and marine industry in which weight reduction is crucial for higher speeds and increased payloads. GNPs are excellent candidates for nanoscale reinforcement toward improvement of multifunctionality of fiber-reinforced composites. They are expected to have extraordinary properties such as high thermal conductivity, superior mechanical properties, and superb electronic transport properties. These essential properties of graphene have generated huge attention for their possible application in several devices [1]. Graphene may be preferred over other conventional nanofillers (such as sodium montmorillonite, carbon nanotube (CNT), carbon nanofiber (CNF), graphite, and exfoliated graphite (EG)), due to high surface area, aspect ratio, tensile strength, thermal and electrical conductivity, electromagnetic interference (EMI) shielding ability, flexibility, transparency, and low coefficient of thermal expansion [2].

The analytical Halpin–Tsai model can predict the material properties of composite materials based on the geometry and orientation of the filler and the elastic properties of the filler and matrix [3]. An excellent survey of the research on different modeling techniques for predicting the mechanical behavior of polymer composites was presented by Valavala and Odegard [4]. Thostenson and Chou [5] showed that MWNT/polystyrene composite elastic properties are sensitive to nanotube diameter by an approach based on the Halpin–Tsai micromechanical method. Mechanical properties of high-density polyethylene composites reinforced with CNTs were presented by Kanagaraj et al. [6]. They employed both the Halpin–Tsai model and a modified form of

* Corresponding author.
E-mail addresses:

https://doi.org/10.1016/j.ijnonlinmec.2018.05.004
Received 5 February 2018; Received in revised form 7 May 2018; Accepted 7 May 2018

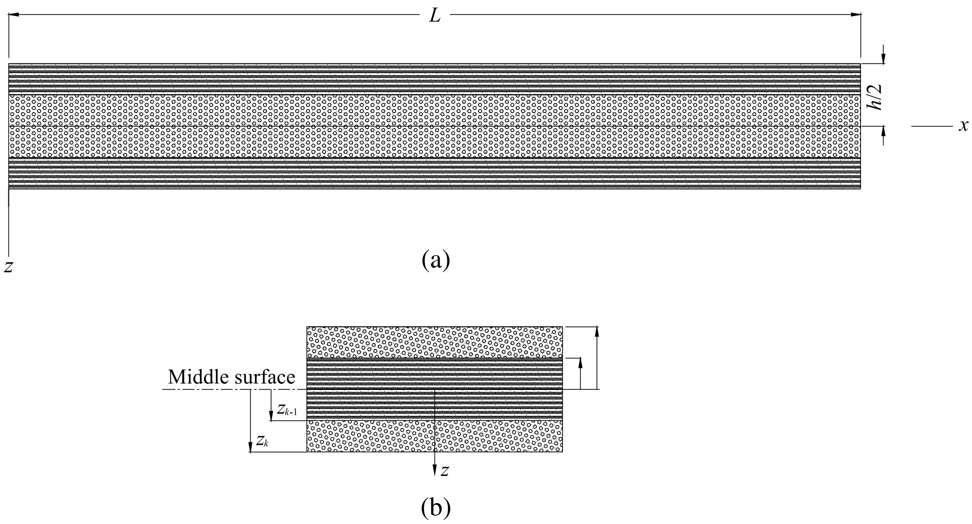

Fig. 1. Configuration of a multilayered GNPs/fiber/epoxy multiscale laminated composite beam: (a) front view and (b) cross section.

the rule of mixture model to make a comparison between theoretical and experimental results. Rafiee [3] used the Halpin–Tsai equations and fiber micromechanics in hierarchy to predict the bulk material properties of the multiscale composite. This approach was used further to study the vibration of nanocomposite beams [7]. Recently, Rafiee et al. [8] addressed the cross-sectional design and analysis of fiber-reinforced multiscale composite beams of general cross-sectional shape and arbitrary anisotropic material properties using Halpin–Tsai equations and fiber micromechanics. The influence of CNTs weight percentage and volume fraction of fibers was investigated in their work.

Most of the previous research regarding graphene-reinforced composite materials has mainly focused on the characterization and modeling of two-phase composites. Reports on the experimental development of advanced polymer composites reinforced by graphene and reduced graphene oxide have been given in the literature [9–19]. There few works devoted to the morphological and mechanical properties of multiscale multifunctional GFPMCs [20–24]. For instance, Kamar et al. [20] investigated the ability of GNPs to improve the interlaminar mechanical properties of glass-reinforced multilayer composites. Their results showed that the impact-side damage area decreased with increasing concentration of GNPs, while the back-side damage area increased. Hsieh et al. [21] studied the effect of environmental aging on interlaminar properties of graphene nanoplatelets reinforced epoxy/carbon fiber composite laminates. Their experimental results showed that the composite laminates containing graphene nanoplatelets presented appreciable improvement. Recently, Seretis et al. [24] investigated the bending and tensile performance of hand lay-up produced glass fabric/epoxy laminated composites after matrix reinforcement with pre-dried graphene nanoplatelets (GNPs) up to 30% wt. content.

Structural modeling of CNTs and GNPs-reinforced laminated composite beams has been a topic of active research in the recent years. Among those available in the literature, Rafiee and his coworkers developed a structural model for the analysis of three-phase multiscale laminated CNTs-reinforced composite beams ([7,25,26]) and plates ([3,27,28]). For beam-type structures, they studied the bending [26] and free vibration [7,26] of carbon nanotubes-reinforced multiscale laminated composite beams. Static bending [3,27], and free vibration [27,28] were also investigated for carbon nanotubes-reinforced laminated multiscale composite plates. Very few studies related to the structural modeling of two-phase GNPs-reinforced composite beams are available in the literature [29–31]. Modeling and analysis of thermal postbuckling and nonlinear bending of graphene-reinforced composite (GRC) laminated beams in a thermal environment and resting on elastic foundations have been presented by Shen et al. [29]. Yang et al. [30] studied the buckling and postbuckling of functionally graded multilayer GNPs-reinforced laminated composite beams resting on an elastic foundation from the perspective of a first-order shear deformation theory. Feng et al. [31] investigated the linear and nonlinear free vibration behaviors of nanocomposite beams reinforced with non-uniformly distributed GNPs within the framework of Timoshenko beam theory and von Kármán nonlinear strain–displacement relationship. They found that adding a very small amount of GPL to the polymer matrix can significantly increase the natural frequency of the composite beam.

Despite the great importance of graphene multifunctional composites, no mathematical model has been available for the simulation of bending, buckling and vibration response of graphene nanoplatelets/fiber/polymer laminated multiscale composite beams.

To fill this gap, the nonlinear static, thermal bifurcation buckling and postbuckling, and free vibration of GNPs/fiber/polymer laminated composite beams were investigated in the present work. The governing equations of the GFPMC multiscale laminated beam were derived from the Euler–Bernoulli beam theory and the von Kármán geometric nonlinearity. Halpin–Tsai equations and fiber micromechanics were used to predict the bulk material properties of the multiscale composite. The GNPs were assumed to be uniformly distributed and randomly oriented through the epoxy resin matrix. The Galerkin procedure yielded a time-wise equation with cubic nonlinear terms. The method of multiple time scales was employed to determine the dynamic response and nonlinear natural frequencies of the beams with clamped–clamped, and hinged–hinged boundary conditions. The effects of weight percentage of GNPs, boundary conditions, and volume fraction of fibers on large deflections, critical buckling temperature and linear and nonlinear frequencies of the GFPMC beams were investigated through a comprehensive parametric study.

2. Governing equations

2.1. Material properties

A GFPMC beam of length L and thickness h is shown in Fig. 1. The three-phase GFPMC multiscale beam was assumed to be made of a mixture of isotropic matrix (epoxy resin), GNPs and fibers (E-Glass) with different fiber alignment for each lamina through the thickness. The graphene nanoplatelets composite was regarded as isotropic, as the GNPs were assumed to be uniformly distributed and randomly oriented through the matrix. It was also assumed that the GNPs-matrix bonding and GNPs dispersion in the matrix were perfect, that each GNP had the same mechanical properties and aspect ratio, that all GNPs were rectangular planes, that there was no void in the matrix, and that the fiber–matrix bonding was also perfect. The constituent materials were assumed to be linearly elastic throughout the deformation.

Fig. 2 illustrates the concept of a multiscale multifunctional composite employing graphene nanoplatelets and traditional fibers.

The effective material properties of the three-phase GNPs/fiber/polymer multiscale laminated composite can be predicted according to a combination of the Halpin–Tsai scheme and micromechanics approach via two steps in the hierarchy shown in Fig. 3. The effective material properties of the GFPMC were assumed to be orthotropic and were predicted by

$$E_{11} = V_F E_{11}^F + V_{\mathrm{MNC}} E^{\mathrm{MNC}}, \tag{1a}$$

$$\frac{1}{E_{22}} = \frac{V_F}{E_{22}^F} + \frac{V_{\mathrm{MNC}}}{E^{\mathrm{MNC}}} - V_F V_{\mathrm{MNC}} \times \frac{v_F^2 E^{\mathrm{MNC}}/E_{22}^F + v_{\mathrm{MNC}}^2 E_{22}^F/E^{\mathrm{MNC}} - 2v^F v^{\mathrm{MNC}}}{V_F E_{22}^F + V_{\mathrm{MNC}} E^{\mathrm{MNC}}} \tag{1b}$$

$$\frac{1}{G_{12}} = \frac{V_F}{G_{12}^F} + \frac{V_{\mathrm{MNC}}}{G^{\mathrm{MNC}}} \tag{1c}$$

$$v_{12} = V_F v^F + V_{\mathrm{MNC}} v^{\mathrm{MNC}} \tag{1d}$$

$$\rho = V_F \rho^F + V_{\mathrm{MNC}} \rho^{\mathrm{MNC}} \tag{1e}$$

where E_{11}^F, E_{22}^F, G_{12}^F, v^F and ρ^F are the Young's moduli, shear modulus, Poisson's ratio and mass density of fibers, respectively, and E^{MNC}, G^{MNC}, v^{MNC} and ρ^{MNC} represent the corresponding properties of the isotropic matrix of nanocomposite. V_F and V_{MNC} refer to the volume fractions of the fibers and the nanocomposite matrix, respectively.

The thermal expansion coefficients in the longitudinal and transverse directions were expressed as

$$\alpha_{11} = \frac{V_F E_{11}^F \alpha_{11}^F + V_{\mathrm{MNC}} E^{\mathrm{MNC}} \alpha^{\mathrm{MNC}}}{V_F E_{11}^F + V_{\mathrm{MNC}} E^{\mathrm{MNC}}} \tag{2a}$$

$$\alpha_{22} = (1 + v^F) V_F \alpha_{22}^F + (1 + v^{\mathrm{MNC}}) V_{\mathrm{MNC}} \alpha^{\mathrm{MNC}} - v_{12}\alpha_{11} \tag{2b}$$

where α_{11}^F; α_{22}^F and α^{MNC} are thermal expansion coefficients, and v_{12}^F and v^{MNC} are Poisson's ratios, respectively, of the fibers and nanocomposite matrix.

According to the Halpin–Tsai equation, the Young modulus of nanocomposites was expressed as [3]:

$$E^{\mathrm{MNC}} = \frac{E^{\mathrm{MER}}}{8}\left[5\left(\frac{1 + 2\left(\frac{\mathfrak{M}_{\mathrm{GNP}}}{\hbar_{\mathrm{GNP}}}\right)\beta_{\mathfrak{M}} V_{\mathrm{GNP}}}{1 - \beta_{\mathfrak{M}} V_{\mathrm{GNP}}}\right) + 3\left(\frac{1 + 2\left(\frac{\ell_{\mathrm{GNP}}}{\hbar_{\mathrm{GNP}}}\right)\beta_{\ell} V_{\mathrm{GNP}}}{1 - \beta_{\ell} V_{\mathrm{GNP}}}\right)\right], \tag{3a}$$

$$\beta_{\ell} = \frac{\left(\frac{E_{11}^{\mathrm{GNP}}}{E^{\mathrm{MER}}}\right) - 1}{\left(\frac{E_{11}^{\mathrm{GNP}}}{E^{\mathrm{MER}}}\right) + \left(\frac{\ell_{\mathrm{GNP}}}{2\hbar_{\mathrm{GNP}}}\right)}, \tag{3b}$$

$$\beta_{\mathfrak{M}} = \frac{\left(\frac{E_{11}^{\mathrm{GNP}}}{E^{\mathrm{MER}}}\right) - 1}{\left(\frac{E_{11}^{\mathrm{GNP}}}{E^{\mathrm{MER}}}\right) + \left(\frac{\mathfrak{M}_{\mathrm{GNP}}}{2\hbar_{\mathrm{GNP}}}\right)}. \tag{3c}$$

where E_{11}^{GNP}, V_{GNP}, ℓ_{GNP}, $\mathfrak{M}_{\mathrm{GNP}}$ and $\hbar_{\mathrm{GNP}}$ are the Young's modulus, volume fraction, length, width and the thickness of graphene nanoplatelets, respectively, and V_{MER} and E^{MER} indicate the volume fraction and Young's modulus of the isotropic epoxy resin matrix, respectively.

The volume fraction of graphene nanoplatelets was expressed as

$$V_{\mathrm{GNP}} = \frac{w^{\mathrm{GNP}}}{w^{\mathrm{GNP}} + (\rho^{\mathrm{GNP}}/\rho^{\mathrm{MER}}) - (\rho^{\mathrm{GNP}}/\rho^{\mathrm{MER}}) w^{\mathrm{GNP}}}, \tag{4}$$

where w^{GNP} is the mass fraction of the graphene nanoplatelets, ρ^{GNP} and ρ^{GNP} are the mass densities of the graphene nanoplatelets and epoxy resin matrix, respectively.

The mass density ρ, Poisson's ratio v and thermal expansion coefficient α were expressed as

$$\rho^{\mathrm{MNC}} = V_{\mathrm{GNP}} \rho^{\mathrm{GNP}} + V_{\mathrm{MER}} \rho^{\mathrm{MER}} \tag{5a}$$

$$v^{\mathrm{MNC}} = V_{\mathrm{GNP}} v^{\mathrm{GNP}} + V_{\mathrm{MER}} v^{\mathrm{MER}} \tag{5b}$$

$$\alpha^{\mathrm{MNC}} = V_{\mathrm{GNP}} \alpha^{\mathrm{GNP}} + V_{\mathrm{MER}} \alpha^{\mathrm{MER}}. \tag{5c}$$

2.2. Mathematical model

The constitutive equation with respect to the plane (laminate) coordinates (x, y, z), was taken as

$$\sigma_{xxk} = \bar{Q}_{11k} \varepsilon_k \tag{6}$$

where ε and σ_{xx} are the strain and stress, and the transformed reduced elastic modulus of each layer for the beam structures can be expressed as:

$$\bar{Q}_{11k} = E_k \cos^4 \varphi_k \tag{7}$$

where E_k is the untransformed reduced elastic modulus of the kth layer of whole structure and φ_k is the direction of the kth lamina.

The displacement fields for the Euler–Bernoulli beam theory denoted by $u(x, z, t)$ and $w(x, z, t)$ respectively, were defined as

$$u(x, z, t) = u_0(x, t) - z\frac{\partial w_0(x, t)}{\partial x}, \tag{8}$$

$$v(x, z, t) = 0, \tag{9}$$

$$w(x, z, t) = w_0(x, t) \tag{10}$$

where it is assumed that the displacement in the y-direction is neglected and $u_0(x, t)$ is the displacements due to extension, $w_0(x, t)$ is the displacement due to bending deformation and t is time. The von Kármán nonlinear strain–displacement relationship gives

$$\varepsilon_x = \frac{\partial u_0}{\partial x} - z\frac{\partial^2 w_0}{\partial x^2} + \frac{1}{2}\left(\frac{\partial w_0}{\partial x}\right)^2 - \alpha_{11}\Delta T \tag{11}$$

It should be mentioned that the beam was initially stress-free at T_0 (in Kelvin) and was subjected to a uniform temperature variation $\Delta T = T - T_0$.

Substituting Eq. (11) into Eq. (6) and integrating through the beam thickness, one obtains the stress resultants

$$N_x = A_{11}\left[u_{,x} + \frac{1}{2}w_{,x}^2\right] + B_{11} w_{,xx} - N^T, \tag{12a}$$

$$M_x = B_{11}\left[u_{,x} + \frac{1}{2}w_{,x}^2\right] + D_{11} w_{,xx} - M^T, \tag{12b}$$

A_{11}, B_{11} and D_{11} in Eq. (12) are the transformed stretching stiffness, stretching–bending coupling stiffness and bending stiffness coefficients, respectively, which are defined as

$$A_{11} = \sum_{k=1}^{K} \bar{E}_k \left(z_k - z_{k-1}\right), \quad B_{11} = \frac{1}{2}\sum_{k=1}^{K} \bar{E}_k \left(z_k^2 - z_{k-1}^2\right), \quad D_{11} = \frac{1}{3}\sum_{k=1}^{K} \bar{E}_k \left(z_k^3 - z_{k-1}^3\right), \tag{13}$$

and K is the total number of layers and z_k is defined in Fig. 1b. Note that $z_0 = -h/2$, $z_K = h/2$.

Superscript "T" in Eq. (12) represents the thermal load, and N^T, M^T are defined as

$$\left(N^T \quad M^T\right) = \int_{-h/2}^{h/2} \left(\bar{Q}_{11k}\alpha_{11}\Delta T \quad z\bar{Q}_{11k}\alpha_{11}\Delta T\right) dz \tag{14}$$

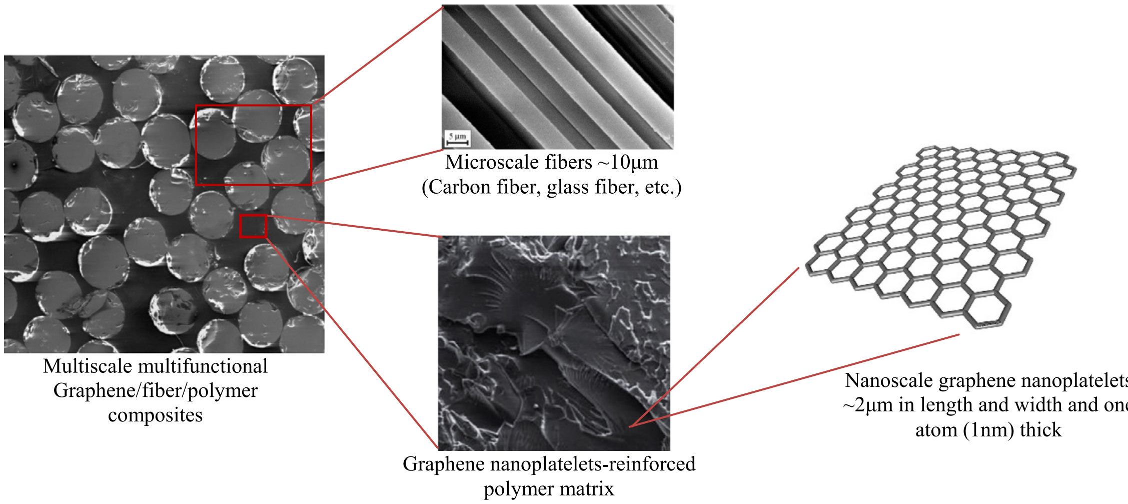

Fig. 2. Concept of multiscale multifunctional graphene nanoplatelets-reinforced polymer composites.

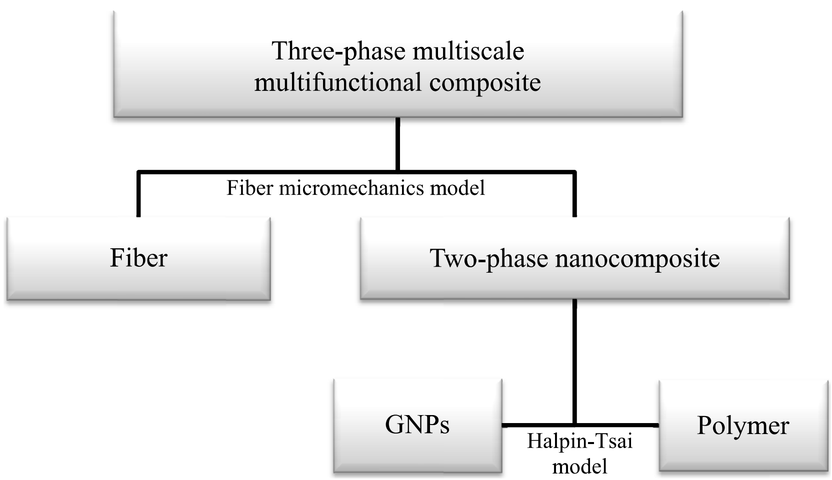

Fig. 3. Hierarchy of the three-phase GNPs/fiber/polymer multiscale composites.

For beams with fixed ends, the governing equation of free vibration for GNPs/fiber/polymer laminated multiscale composite beams can be obtained as

$$-\left(\bar{D}_{11}-\frac{\bar{B}_{11}^2}{\bar{A}_{11}}\right)\frac{\partial^4 w}{\partial x^4}+\left(\frac{\bar{A}_{11}}{L}\int_0^L\left[\frac{1}{2}\left(\frac{\partial w}{\partial x}\right)^2-\frac{\bar{B}_{11}}{\bar{A}_{11}}\frac{\partial^2 w}{\partial x^2}\right]dx-N^T\right)\frac{\partial^2 w}{\partial x^2}+Q_e(x,t)=I_1\frac{\partial^2 w}{\partial t^2}. \tag{15}$$

where Q_e is the external transverse loading function on the beam and the beam inertia I_1 is defined as

$$I_1=\sum_{k=1}^{K}\rho_k\left(z_k-z_{k-1}\right). \tag{16}$$

Introducing the following dimensionless quantities

$$\begin{gathered}\eta=\frac{x}{L},\quad \tilde{w}=\frac{w}{H},\quad \gamma=\frac{H}{L},\quad \tilde{I}_1=\frac{I_1}{I_{10}},\quad \tau=\frac{t}{L}\sqrt{\frac{\bar{A}_{110}}{I_{10}}},\\ \tilde{A}=\frac{\bar{A}_{11}}{\bar{A}_{110}},\quad \tilde{\theta}^T=\frac{N^T}{\bar{A}_{110}},\\ \tilde{B}=\frac{\bar{B}_{11}}{L\bar{A}_{110}},\quad \tilde{D}=\frac{\bar{D}_{11}}{L^2\bar{A}_{110}},\tilde{d}_0=\tilde{D}-\frac{\tilde{B}^2}{\tilde{A}},\\ \tilde{Q}_e(\xi,\tau)=\frac{Q_e(x,t)L^2}{H\bar{A}_{110}},\end{gathered} \tag{17}$$

where A_{110} and I_{10} are taken as the values of A_{11} and I_1 of a homogeneous epoxy matrix beam of matrix material and neglecting the over-tilde sign for w, Eq. (15) can be rewritten in dimensionless form as

$$\left(\frac{\tilde{B}^2}{\tilde{A}}-\tilde{D}\right)\frac{\partial^4 w}{\partial\eta^4}+\left(\int_0^1\left[\frac{\tilde{A}\gamma^2}{2}\left(\frac{\partial w}{\partial\eta}\right)^2-\gamma\tilde{B}\frac{\partial^2 w}{\partial\eta^2}\right]d\eta-\tilde{\theta}^T\right)\times\frac{\partial^2 w}{\partial\eta^2}+\tilde{Q}_e(\eta,\tau)=\tilde{I}_1\frac{\partial^2 w}{\partial\tau^2}. \tag{18}$$

3. Solution methodology

To investigate the nonlinear behavior of GNPs/fiber/polymer multiscale laminated composite beam, calculation of the free natural vibration is carried out first. The dimensionless governing equation for linear free vibration of piezoelectric GFPMC beams can be obtained by eliminating the nonlinear terms in Eq. (18), such that

$$\left(\frac{\tilde{B}^2}{\tilde{A}}-\tilde{D}\right)\frac{\partial^4 w}{\partial\eta^4}-\tilde{\theta}^T\frac{\partial^2 w}{\partial\eta^2}=\tilde{I}_1\frac{\partial^2 w}{\partial\tau^2}. \tag{19}$$

For linear free vibration, the solution of Eq. (18) considering the first mode has the form

$$w(\eta,\tau)=X(\eta)\,g(\tau)=X(\eta)\,e^{i\omega_0\tau}, \tag{20}$$

where $\omega_0=\omega_L L\sqrt{I_{10}/A_{110}}$ is the dimensionless linear natural frequency and ω_L is the linear natural frequency.

Substituting Eq. (20) into Eq. (19) and then solving the resulting differential equation, one obtains

$$X(\eta) = c_1 \sin\left(\hat{\lambda}\eta\right) + c_2 \cos\left(\hat{\lambda}\eta\right) + c_3 \sinh(\hat{\mu}\eta) + c_4 \cosh(\hat{\mu}\eta), \tag{21}$$

where

$$\hat{\mu} = \left(\frac{\widetilde{\theta}^T}{2\left(\widetilde{D} - \widetilde{B}^2/\widetilde{A}\right)} + \left(\left(\frac{\widetilde{\theta}^T}{2\left(\widetilde{D} - \widetilde{B}^2/\widetilde{A}\right)}\right)^2 + \left(\frac{\widetilde{I}_1\omega_0^2}{\widetilde{D} - \widetilde{B}^2/\widetilde{A}}\right)\right)^{\frac{1}{2}}\right)^{\frac{1}{2}} \tag{22a}$$

$$\hat{\lambda} = \left(-\frac{\widetilde{\theta}^T}{2\left(\widetilde{D} - \widetilde{B}^2/\widetilde{A}\right)} + \left(\left(\frac{\widetilde{\theta}^T}{2\left(\widetilde{D} - \widetilde{B}^2/\widetilde{A}\right)}\right)^2 + \left(\frac{\widetilde{I}_1\omega_0^2}{\widetilde{D} - \widetilde{B}^2/\widetilde{A}}\right)\right)^{\frac{1}{2}}\right)^{\frac{1}{2}} \tag{22b}$$

and a_1 to a_4 are unknown constants to be determined from the boundary conditions.

The boundary conditions are given by

$$X(0) = X(1) = X''(0) = X''(1) = 0, \tag{23a}$$

$$X(0) = X'(0) = X(1) = X'(1) = 0, \tag{23b}$$

for hinged–hinged and clamped–clamped beams respectively. Inserting Eq. (20) into the boundary conditions of Eqs. (23), one obtains a homogeneous matrix $H(\omega_0)$ whose determinant should be zero to guarantee non-trivial solutions

$$\det\left[H\left(\omega_0\right)\right] = 0 \tag{24}$$

The characteristic equation for ω_0 can be expressed as:

for hinged–hinged boundary conditions:

$$\sin(\hat{\mu}) = 0 \tag{25}$$

and for clamped–clamped boundary conditions:

$$\sqrt{\frac{\widetilde{I}_1\omega_L^2}{\widetilde{D}_0}} - \frac{\widetilde{\theta}^T}{2\widetilde{D}_0}\sinh\left(\hat{\lambda}\right)\sin(\hat{\mu}) - \sqrt{\frac{\widetilde{I}_1\omega_L^2}{\widetilde{D}_0}}\cosh\left(\hat{\lambda}\right)\cos(\hat{\mu}) = 0 \tag{26}$$

The Newton method was used to find the roots of this equation in terms of natural frequency ω_0; the iterations were stopped when the absolute value of the difference of the natural frequency obtained between two successive iterations was less than 10^{-5}.

The linear mode shapes for a GFPMC beams can be solved from (19) by

for hinged–hinged boundary conditions:

$$X(\eta) = \sin\left(\hat{\lambda}\eta\right), \tag{27}$$

and for clamped–clamped boundary conditions:

$$\begin{aligned} X(\eta) = \sinh(\hat{\mu}\eta) &+ \frac{\hat{\mu}\cos\hat{\lambda} - \hat{\lambda}\sinh\hat{\mu}}{\hat{\lambda}\left(\cosh\hat{\mu} - \cos\hat{\lambda}\right)}\cosh(\hat{\mu}\eta) - \frac{\hat{\mu}}{\hat{\lambda}}\sin\left(\hat{\lambda}\eta\right) \\ &- \frac{\hat{\mu}\cos\hat{\lambda} - \hat{\lambda}\sinh\hat{\mu}}{\hat{\lambda}\left(\cosh\hat{\mu} - \cos\hat{\lambda}\right)}\cos\left(\hat{\lambda}\eta\right), \end{aligned} \tag{28}$$

The nondimensional transverse mechanical load can be expanded as

$$\widetilde{Q}_e(\eta,\tau) = \frac{q_{0m}L^2}{hA_{110}}\cos(\Omega\tau)X(\eta) = \widetilde{q}_{0m}\cos(\Omega\tau)X(\eta) \tag{29}$$

In Eq. (29), Ω is the nondimensional frequency of the external forcing function and coefficient q_{0m} for two types of external loads over the outer surface of GFPMC laminated beam can be expressed as

$$q_{0m} = \frac{16q_0}{m\pi^2}\ (m = 1,3,5,\ldots)\ \text{for loads with uniform distribution} \tag{30a}$$

$$q_{0m} = q_0\ (m = 1)\ \text{for loads with sinusoidal distribution} \tag{30b}$$

where q_0 is the amplitude of the forcing function.

Substituting $w\ (\eta,\tau)$ from Eq. (20) into Eq. (18) and applying Galerkin's procedure yields a second order nonlinear ordinary differential equation for the free vibration of the system

$$\ddot{g} + \delta_a g + \delta_b g^2 + \delta_c g^3 = \delta_q \cos(\Omega\tau), \tag{31}$$

where a dot denotes differentiation with respect to time, and

$$\begin{aligned} \delta_a &= \frac{1}{\Delta}\left(\left(\widetilde{D} - \frac{\widetilde{B}^2}{\widetilde{A}}\right)\int_0^1 X\frac{d^4X}{d\eta^4}d\eta + \widetilde{\theta}^T\int_0^1 X\frac{d^2X}{d\eta^2}d\eta\right), \\ \delta_b &= \frac{\gamma\widetilde{B}}{\Delta}\left(\int_0^1 X\left(\frac{d^2X}{d\eta^2}\right)d\eta\right)\int_0^1\frac{d^2X}{d\eta^2}d\eta, \\ \delta_c &= -\frac{\widetilde{A}\gamma^2}{2\Delta}\left(\int_0^1 X\frac{d^2X}{d\eta^2}d\eta\right)\int_0^1\left(\frac{dX}{d\eta}\right)^2 d\eta, \\ \delta_q &= -\frac{1}{\Delta}\int_0^1\widetilde{q}_{0m}X\,d\xi, \quad \Delta = \widetilde{I}_1\int_0^1 X^2 d\eta. \end{aligned} \tag{32}$$

Note that $\delta_a = \omega_0^2$.

3.1. Nonlinear bending analysis

The nonlinear bending load–deflection relation for the problem in the absence of in-plane loads can be obtained from Eq. (31) by dropping the time-differentiated terms as

$$\delta_a g + \delta_b g^2 + \delta_c g^3 = \delta_q. \tag{33}$$

Static deflection g can be calculated by solving Eq. (33) using the Newton method and the nonlinear bending ratio can be obtained by dividing terms in (33) by linear term $\delta_a g$

$$\frac{q_{NL}}{q_L} = 1 + \frac{\delta_b}{\delta_a}g + \frac{\delta_c}{\delta_a}g^2. \tag{34}$$

3.2. Thermal buckling and post-buckling analysis

The post-buckling load–deflection relation for the problem in the absence of transverse load (i.e., $q_0 = 0$) can be obtained from Eq. (31) by dropping the time-differentiated terms as

$$\hat{\delta}_a + \delta_b g + \delta_c g^2 = -\widetilde{\theta}^T\int_0^1 X\frac{\mathrm{d}^2X}{\mathrm{d}\eta^2}\mathrm{d}\eta \tag{35}$$

where

$$\hat{\delta}_a = \widetilde{D}_0\int_0^1 X\frac{\mathrm{d}^4X}{\mathrm{d}\eta^4}\mathrm{d}\eta \tag{36}$$

3.2.1. Linear critical buckling

By neglecting the contribution of g and g^2 terms in Eq. (35), the critical buckling load can be determined using

$$\hat{\delta}_a + \widetilde{\theta}^T\int_0^1 X\frac{\mathrm{d}^2X}{\mathrm{d}\eta^2}\mathrm{d}\eta = 0. \tag{37}$$

Eq. (37) may be used to determine the critical load as

$$T^{cr} = -\frac{\hat{J}_3A_{110}}{\int_0^1 X\frac{\mathrm{d}^2X}{\mathrm{d}\eta^2}\mathrm{d}\eta\int_{-h/2}^{h/2}E\alpha dz} + T_0. \tag{38a}$$

3.2.2. Post-buckling load–deflection relation

Using Eq. (35), the load–deflection relation can be written as

$$\frac{\Delta T}{\Delta T^{cr}} = \frac{\hat{\delta}_a + \delta_b g + \delta_c g^2}{\hat{\delta}_a}. \tag{39}$$

Knowing the applied temperature rise ΔT in the postbuckling range, Eq. (39) can be solved for g. Thus, the unknown maximum deflection corresponding to the post-buckling load can be determined. For the specified maximum deflection, the post-buckling load can be determined directly from Eq. (39).

Table 1
Typical material properties of nanocomposite beam used in the examples unless otherwise specified.

Source	Symbol	Value	Unit	Description
General geometric parameters and loading conditions				
	h	2.4×10^{-3}	m	Beam thickness
	L	$50\,H$	m	Length of the beam
	q_0	1×10^5	N/m	Applied distributed load
Graphene nanoplatelets				
	$\hbar_{\mathrm{GNP}}$	1.5×10^{-9}	m	Thickness of graphene nanoplatelets
	$\mathfrak{M}_{\mathrm{GNP}}$	1.5×10^{-6}	m	Width of graphene nanoplatelets
	ℓ_{GNP}	2.5×10^{-6}	m	Length of graphene nanoplatelets
	w^{GNP}	1	%	Weight percentage of graphene nanoplatelets
	ρ^{GNP}	1062.5	kg/m^3	Mass density of graphene nanoplatelets
	E_{11}^{GNP}	1×10^{12}	kg/m^2	Young's modulus of graphene nanoplatelets
	$\alpha_{11}^{\mathrm{GNP}}$	5×10^{-6}	1/K	Thermal expansion coefficient
	ν_{12}^{GNP}	0.186	–	Poisson's ratio of graphene nanoplatelets
Epoxy resin polymer matrix				
	ρ^{MER}	1072	kg/m^3	Mass density of epoxy resin matrix
	E^{MER}	3.355×10^9	kg/m^2	Young's modulus of epoxy resin matrix
	α^{MER}	9.756×10^{-5}	1/K	Thermal expansion coefficient of epoxy resin matrix
	ν^{MER}	0.2	–	Poisson's ratio of epoxy resin matrix
E-Glass fibers				
	ρ^{F}	2500	kg/m^3	Mass density of E-Glass fibers
	E_{11}^{F}	69×10^9	kg/m^2	Young's modulus of E-Glass fibers
	α^{F}	5×10^{-6}	1/K	Thermal expansion coefficient of E-Glass fibers
	ν^{F}	0.22	–	Poisson's ratio of E-Glass fibers
	V^{F}	0.5	–	Volume fraction of E-Glass fibers

Table 2
Comparison of the fundamental frequency $\omega_0 = \omega_L L^2 \sqrt{\rho/(4E_{11}H^2)}$ for a four-layer (0°/90°/90°/0°) moderately thin hinged–hinged symmetric cross-ply beam (E_{11} = 144.8 GPa, E_{22} = 9.65 GPa, L/h = 30, υ_{12} = 0.3, ρ = 1389.23 kg/m^3, h = 0.5 m).

Source	FSDT [33]	FSDT1 [34]	FSDT2 [34]	Euler–Bernoulli (Present)
	2.5023	2.4922	2.4952	2.6651
Difference (%)	6.51	6.94	6.81	–

Difference = 100% [(*Present*– Ref.)/Ref.]

3.3. Nonlinear vibration analysis

The initial conditions considered in the current work were:

$$w\left(L/2,0\right) = w_{\max}, \quad \frac{\partial w\left(L/2,0\right)}{\partial t} = 0 \tag{40}$$

Such that the dimensionless initial conditions became

$$w\left(1/2,0\right) = \frac{w_{\max}}{h} = Y_{\max}, \quad \frac{\partial w\left(1/2,0\right)}{\partial \tau} = 0. \tag{41}$$

Eq. (31) contains a quadratic nonlinear term due to the presence of a bending–extension coupling effect in generally laminated beams (i.e. $B_{11} \neq 0$). This term, however, vanishes for beams with a symmetric stacking sequence, including no GNPs reinforcement, because $\delta_b = 0$ in this case. Then, Eq. (31) reduces to a Duffing equation.

Eq. (31) can be solved analytically using the method of multiple scales in general. The approximate solution of Eq. (31) was assumed as a second-order expansion in terms of a small positive parameter ς, which is a measure of the amplitude of the motion.

The expression for dimensionless circular frequency of the system can be obtained as

$$\Omega = \omega_0 \left(1 + \frac{9\delta_a\delta_c - 10\delta_b^2}{24\delta_a^2}\varsigma^2 Y_{\max}^2\right) + O(\varsigma^3), \tag{42}$$

where $Y_{\max}$ is considered as the amplitude described in polar form [3,7,32].

Finally, the time history of the system in steady state motion as a solution for Eq. (32) can be obtained as

$$g = \varsigma Y_{\max}\cos(\omega_0\tau + \psi_0) - \frac{\varsigma^2 Y_{\max}^2 \delta_b}{2\delta_a}\left(1 - \frac{1}{3}\cos\left(2\omega_0\tau + 2\psi_0\right)\right) + O(\varsigma^3) \tag{43}$$

where ψ_0 is a constant.

4. Numerical results and discussion

The nonlinear bending, thermal buckling and post buckling, and large amplitude transverse vibration of GNPs/fiber/polymer laminated multiscale composite beams were investigated under clamped–clamped and simply supported boundary conditions. Typical geometric parameters, material properties and loading conditions are listed in Table 1 unless otherwise specified. The laminate stacking sequence of (0°/90°/90°/0°) was considered for the examples presented in this section.

To validate the present analysis, the fundamental frequency $\omega_0 = \omega_L L^2 \sqrt{\rho/(4E_{11}H^2)}$ for a hinged–hinged four-layer (0°/90°/90°/0°) symmetric cross-ply beam was calculated and shown in Table 2 and compared with the finite element results of Subramanian [33] and Chandrashekhara et al. [34] which are based on the first-order shear deformation beam theory (FSDT). The geometric parameters and material properties were E_{11} = 144.8 GPa, E_{22} = 9.65 GPa, L/h = 30, υ_{12} = 0.3, ρ = 1389.23 kg/m^3, h = 0.5 m. All layers were assumed to have the same thickness. From the results in Table 2, it can be observed that the present results are within 7% of the published results, which constitutes a good agreement.

Comparison of nonlinear frequency ratio for isotropic homogeneous isotropic beams (υ = 0.19, L/h = 20, T = 300 K, h = 100 mm, ρ = 1190 kg/m^3, E = 2.5 GPa) at different vibration amplitudes are listed in Table 3. The present results agree very well with those obtained by Rafiee et al. [35] and Fu et al. [36].

Table 4 shows the effect of GNPs content, and the volume fraction of fibers on the dimensionless nonlinear deflection, critical temperature

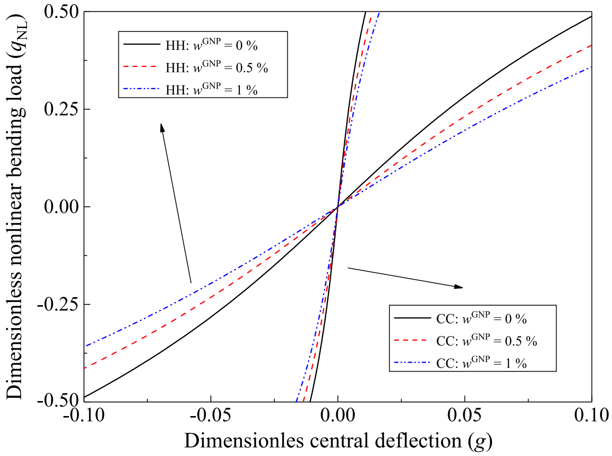

Fig. 4. The dimensionless static central deflection of clamped–clamped and hinged–hinged GFPMC beams for different uniform transverse mechanical loads.

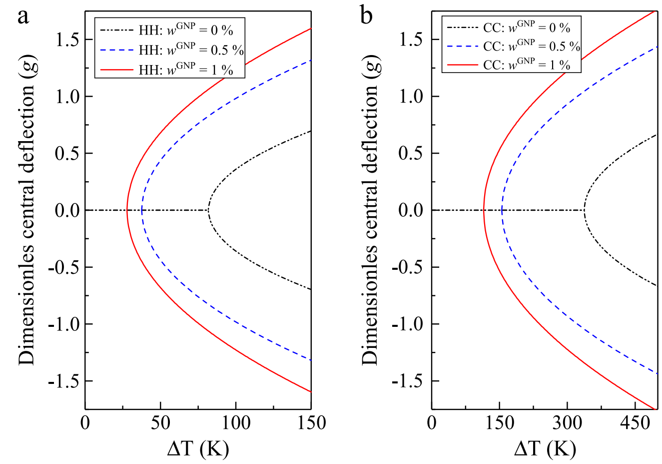

Fig. 5. Effect of GNPs weight percentage on the bifurcation diagram of GFPMC beams for clamped–clamped and hinged–hinged boundary conditions.

Table 3
Comparison of nonlinear frequency ratio for an isotropic homogeneous beam ($L/h = 20$, $h = 100$ mm, $E = 2.5$ GPa, $\rho = 1190$ kg/m^3).

Source	w_{max}/h				
	0.5	1	1.5	2	3
Present	1.00460	1.01833	1.04105	1.07249	1.15999
Ref. [36]	1.0058	1.0231	–	1.0892	1.1831
Ref. [35]	1.00460	1.01833	1.04105	1.07249	1.15999

difference and linear fundamental natural frequency of the GFPMC beams with different boundary conditions. It can be observed that the deflection of laminated composite beam significantly reduces with the addition of a small amount of GNPs (See also Fig. 4). For instance, 11% and 20% improvement can be seen with 0.5 wt% and 1 wt% of GNPs, respectively (with $V^F = 0.4$ and hinged–hinged boundary conditions). The critical buckling temperature difference also significantly reduces with a small addition of graphene content. This feature could be expected because the addition of thermally conductive graphene sheets leads to a more conductive structure and therefore more expansion undergoing thermal load (See Fig. 5). Significant improvements can be also seen for the fundamental natural frequencies. With $V^F = 0.4$ and hinged–hinged boundary conditions, 17% and 32% improvement can be seen by adding 0.5 wt% and 1 wt% of GNPs. Similar to the case of bending deflection, the beam becomes stronger from GNP reinforcement. The reduction in central deflection and buckling temperature and increase in fundamental natural frequency, however, become less significant with higher volume fractions of fibers under the same boundary conditions. This is because higher volume fractions of fibers make the structure stiffer and t the resulting laminated composite beam is less sensitive to reinforcement. For clamped–clamped GFPMC beams, similar trends can be observed. Clamped boundary conditions result in smaller static deflection, higher critical buckling temperature and higher natural frequencies as could be expected.

The influence of graphene content on the nonlinear bending (q_{NL}/q_{LF}), critical temperature ($\Delta T/\Delta T_{cr}$) and fundamental frequency (Ω/ω_0) ratios of the clamped GFPMC beams is presented in Table 5. Our finding is that addition of GNPs does not affect the nonlinear bending, critical temperature and fundamental frequency ratios of the clamped fiber reinforced laminated composite thin beams. This could be expected from the presence of δ_a containing stiffness properties as a dividing term in Eq. (34), (39) and (42).

Fig. 6 displays the curves for nonlinear to linear frequency ratio of GFPMC beams for both clamped–clamped and hinged–hinged boundary conditions. One can observe that small wt.% of GNPs result in higher

Table 4
Effect of GNPs loading, and the volume fraction of fibers on the dimensionless nonlinear deflection, critical temperature difference and linear fundamental natural frequency of the GFPMC beams with different boundary conditions.

End condition	V^F	Nonlinear deflection (q)			Critical temperature difference (ΔT_{cr})			Fundamental natural frequency (ω_0)		
		0%	0.5%	1%	0%	0.5%	1%	0%	0.5%	1%
HH										
	0.4	1.4	1.24 −11%	1.12 −20%	66.64	26.29 −61%	19.62 −71%	0.139	0.163 17%	0.183 32%
	0.5	1.3	1.18 −9%	1.09 −16%	81.9	37.67 −54%	27.91 −66%	0.147	0.164 12%	0.18 22%
	0.6	1.21	1.13 −7%	1.07 −12%	94.87	53.46 −44%	40.65 −57%	0.152	0.165 9%	0.176 16%
CC										
	0.4	0.568	0.457 −20%	0.381 −33%	274.7	108.4 −61%	80.88 −71%	0.316	0.369 17%	0.416 32%
	0.5	0.496	0.421 −15%	0.365 −26%	337.6	155.3 −54%	115 −66%	0.333	0.373 12%	0.409 23%
	0.6	0.439	0.39 −11%	0.35 −20%	391.1	220.4 −44%	167.6 −57%	0.345	0.374 8%	0.4 16%

$$*[X\%]:\ X\% = 100\%\ \frac{\text{Freq.}|_{n\%\ \text{GNPs}} - \text{Freq.}|_{0\%\ \text{GNPs}}}{\text{Freq.}|_{0\%\ \text{GNPs}}}.$$

Table 5
Effects of graphene content on the nonlinear bending (q_{NL}/q_{LF}), critical temperature ($\Delta T/\Delta T_{cr}$) and fundamental frequency (Ω/ω_0) ratios of the clamped GFPMC beams.

w^{GNP}	[g, ΔT_{cr}, ω_0]	Source	Initial condition				
			0.1	0.2	0.3	0.4	0.5
0%	$g = 0.496$	q_{NL}/q_{LF} Eq. (34)	1.011	1.043	1.097	1.172	1.268
	$\Delta T_{cr} = 337.6$	$\Delta T/\Delta T_{cr}$ Eq. (39)	1.011	1.043	1.097	1.172	1.268
	$\omega_0 = 0.365$	Ω/ω_0 Eq. (42)	1.001	1.005	1.012	1.021	1.034
0.5%	$g = 0.421$	q_{NL}/q_{LF} Eq. (34)	1.011	1.043	1.097	1.172	1.268
	$\Delta T_{cr} = 155.3$	$\Delta T/\Delta T_{cr}$ Eq. (39)	1.011	1.043	1.097	1.172	1.268
	$\omega_0 = 0.373$	Ω/ω_0 Eq. (42)	1.002	1.006	1.014	1.024	1.038
1%	$g = 0.365$	q_{NL}/q_{LF} Eq. (34)	1.011	1.043	1.097	1.172	1.268
	$\Delta T_{cr} = 115.0$	$\Delta T/\Delta T_{cr}$ Eq. (39)	1.011	1.043	1.097	1.172	1.268
	$\omega_0 = 0.409$	Ω/ω_0 Eq. (42)	1.002	1.007	1.015	1.026	1.041

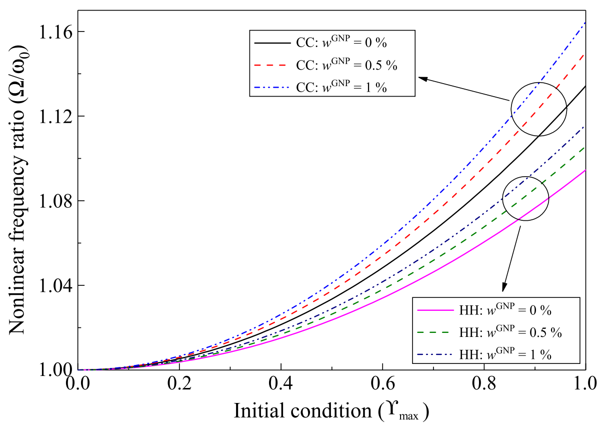

Fig. 6. Nonlinear to linear frequency ratio of GFPMC beams for clamped–clamped and hinged–hinged boundary conditions.

nonlinear to linear frequency ratios. This behavior is called stiffening behavior [28,37,38], and was observed for both types of boundary conditions.

5. Conclusions

Large deflections, thermal post-buckling and nonlinear free oscillation of GNPs/fiber/polymer multiscale composite beams were studied within the framework of the Euler–Bernoulli beam theory, with a von Kármán-type displacement–strain relationship. The GNPs were assumed to be uniformly distributed and randomly oriented through the epoxy resin matrix. An analytical solution approach to the Galerkin procedure was used to obtain a second order nonlinear ordinary equation. The nonlinear bending and post-buckling equations were numerically solved by the Newton method, and the multiple time scales method was used to study the nonlinear free vibration and dynamic response of laminated nanocomposite beam under two set of boundary conditions. A parametric study was carried out. The numerical results showed that the central deflection, and natural frequency significantly improved with a small percentage of GNPs. However, addition of GNPs led to lower critical buckling temperatures. The results also confirmed that GNPs in laminated composite beams produce less improvement when combined with higher volume fractions of fibers.

Acknowledgments

The first author gratefully acknowledges the financial support from Ontario Trillium Scholarship (OTS), Government of Ontario and University of Ottawa, Canada.

References

[1] M.J. Allen, V.C. Tung, R.B. Kaner, Honeycomb carbon : A review of graphene, Chem. Rev. 110 (2010) 132–145.

[2] R. Miranda, A.L.V. De Parga, Graphene: Surfing ripples towards new devices, Nat. Nanotechnol. 4 (2009) 549–550. http://dx.doi.org/10.1038/nnano.2009.250.

[3] M. Rafiee, X.Q. He, S. Mareishi, K.M. Liew, Modeling and stress analysis of smart CNTs/fiber/polymer multiscale composite plates, Int. J. Appl. Mech. 6 (2014) 1450025. http://dx.doi.org/10.1142/S1758825114500252.

[4] P.K. Valavala, G.M. Odegard, Modeling techniques for determination of mechanical properties of polymer nanocomposites, Rev. Adv. Mater. Sci. 9 (2005) 34–44.

[5] E.T. Thostenson, T.-W. Chou, On the elastic properties of carbon nanotube-based composites: modelling and characterization, J. Phys. D. Appl. Phys. 36 (2003) 573–582. http://dx.doi.org/10.1088/0022-3727/36/5/323.

[6] S. Kanagaraj, F.R. Varanda, T.V. Zhil'tsova, M.S.A. Oliveira, J.A.O. Simões, Mechanical properties of high density polyethylene/carbon nanotube composites, Compos. Sci. Technol. 67 (2007) 3071–3077. http://dx.doi.org/10.1016/j.compscitech.2007.04.024.

[7] X.Q. He, M. Rafiee, S. Mareishi, K.M. Liew, Large amplitude vibration of fractionally damped viscoelastic cnts/fiber/polymer multiscale composite beams, Compos. Struct. 131 (2015) 1111–1123. http://dx.doi.org/10.1016/j.compstruct.2015.06.038.

[8] M. Rafiee, F. Nitzsche, M.R. Labrosse, Cross-sectional design and analysis of multiscale carbon nanotubes-reinforced composite beams and blades, Int. J. Appl. Mech. (2018) 1850032. http://dx.doi.org/10.1142/S1758825118500321.

[9] J. Du, H.-M. Cheng, The fabrication, properties, and uses of graphene/polymer composites, Macromol. Chem. Phys. 213 (2012) 1060–1107. http://dx.doi.org/10.1002/macp.

[10] A.S. Wajid, H.S. Tanvir Ahmed, S. Das, F. Irin, A.F. Jankowski, M.J. Green, High-performance pristine graphene/epoxy composites with enhanced mechanical and electrical properties, Macromol. Mater. Eng. 298 (2013) 339–347. http://dx.doi.org/10.1002/mame.201200043.

[11] T.K. Das, S. Prusty, Graphene-based polymer composites and their applications, Polym. Plast. Technol. Eng. 52 (2013) 13022710444400. http://dx.doi.org/10.1080/03602559.2012.751410.

[12] S. Nazarpour, Graphene Technology, 2016.

[13] X. Sun, H. Sun, H. Li, H. Peng, Developing polymer composite materials: Carbon nanotubes or graphene?, Adv. Mater. 25 (2013) 5153–5176. http://dx.doi.org/10.1002/adma.201301926.

[14] N. Saravanan, R. Rajasekar, S. Mahalakshmi, T. Sathishkumar, K. Sasikumar, S. Sahoo, Graphene and modified graphene-based polymer nanocomposites - A review, J. Reinf. Plast. Compos. 33 (2014) 1158–1170. http://dx.doi.org/10.1177/0731684414524847.

[15] D. Verma, P.C. Gope, A. Shandilya, A. Gupta, Mechanical-thermal-electrical and morphological properties of graphene reinforced polymer composites: A review, Trans. Indian Inst. Met. 67 (2014) 803–816. http://dx.doi.org/10.1007/s12666-014-0408-5.

[16] Z.U. Khan, A. Kausar, H. Ullah, A. Badshah, W.U. Khan, A review of graphene oxide, graphene buckypaper, and polymer/graphene composites: Properties and fabrication techniques, J. Plast. Film Sheeting (2015) 1–45. http://dx.doi.org/10.1177/8756087915614612.

[17] Z. Anwar, A. Kausar, I. Rafique, B. Muhammad, Advances in epoxy/graphene nanoplatelet composite with enhanced physical properties: A review, Polym. Plast. Technol. Eng. 2559 (2015) 03602559.2015.1098695. http://dx.doi.org/10.1080/03602559.2015.1098695.

[18] R. Shah, A. Kausar, B. Muhammad, S. Shah, Progression from graphene and graphene oxide to high performance polymer-based nanocomposite: a review, Polym. Plast. Technol. Eng. 54 (2015) 173–183. http://dx.doi.org/10.1080/03602559.2014.955202.

[19] A. Kausar, Z. Anwar, B. Muhammad, Recent developments in epoxy/graphite, epoxy/graphene and epoxy/graphene nanoplatelet composites: A comparative review, Polym. Plast. Technol. Eng. 2559 (2016) 03602559.2016.1163589. http://dx.doi.org/10.1080/03602559.2016.1163589.

[20] N.T. Kamar, M.M. Hossain, A. Khomenko, M. Haq, L.T. Drzal, A. Loos, Interlaminar reinforcement of glass fiber/epoxy composites with graphene nanoplatelets, Composites A 70 (2015) 82–92. http://dx.doi.org/10.1016/j.compositesa.2014.12.010.

[21] T.-H. Hsieh, W.-J. Chen, C.-L. Chiang, M.-Y. Shen, Environmental aging effect on interlaminar properties of graphene nanoplatelets reinforced epoxy/carbon fiber composite laminates, J. Reinf. Plast. Compos. (2016). http://dx.doi.org/10.1177/0731684416637219.

[22] F. Wang, L.T. Drzal, Y. Qin, Z. Huang, Size effect of graphene nanoplatelets on the morphology and mechanical behavior of glass fiber/epoxy composites, J. Mater. Sci. 51 (2016) 3337–3348. http://dx.doi.org/10.1007/s10853-015-9649-x.

[23] M. Bulut, Mechanical characterization of basalt/epoxy composite laminates containing graphene nanopellets, Composites B 122 (2017) 71–78. http://dx.doi.org/10.1016/j.compositesb.2017.04.013.

[24] G.V. Seretis, G. Kouzilos, D.E. Manolakos, C.G. Provatidis, On the graphene nanoplatelets reinforcement of hand lay-up glass fabric/epoxy laminated composites, Composites B 118 (2017) 26–32. http://dx.doi.org/10.1016/j.compositesb.2017.03.015.

[25] M. Rafiee, F. Nitzsche, M. Labrosse, Dynamics, vibration and control of rotating composite beams and blades: A critical review, Thin-Walled Struct. 119 (2017) 795–819. http://dx.doi.org/10.1016/j.tws.2017.06.018.

[26] M. Rafiee, F. Nitzsche, M. Labrosse, Rotating nanocomposite thin-walled beams undergoing large deformation, Compos. Struct. 150 (2016) 191–199. http://dx.doi.org/10.1016/j.compstruct.2016.05.014.

[27] M. Rafiee, X.Q. He, S. Mareishi, K.M. Liew, Nonlinear response of piezoelectric nanocomposite plates: large deflection, post-buckling and large amplitude vibration, Int. J. Appl. Mech. 7 (2015). http://dx.doi.org/10.1142/S175882511550074X.

[28] M. Rafiee, X.F. Liu, X.Q. He, S. Kitipornchai, Geometrically nonlinear free vibration of shear deformable piezoelectric carbon nanotube/fiber/polymer multiscale laminated composite plates, J. Sound Vib. 333 (2014) 3236–3251. http://dx.doi.org/10.1016/j.jsv.2014.02.033.

[29] H.S. Shen, F. Lin, Y. Xiang, Nonlinear bending and thermal postbuckling of functionally graded graphene-reinforced composite laminated beams resting on elastic foundations, Eng. Struct. 140 (2017) 89–97. http://dx.doi.org/10.1016/j.engstruct.2017.02.069.

[30] J. Yang, H. Wu, S. Kitipornchai, Buckling and postbuckling of functionally graded multilayer graphene platelet-reinforced composite beams, Compos. Struct. 161 (2017) 111–118. http://dx.doi.org/10.1016/j.compstruct.2016.11.048.

[31] C. Feng, S. Kitipornchai, J. Yang, Nonlinear free vibration of functionally graded polymer composite beams reinforced with graphene nanoplatelets (GPLs), Eng. Struct. 140 (2017) 110–119. http://dx.doi.org/10.1016/j.engstruct.2017.02.052.

[32] A. Shooshtari, M. Rafiee, Nonlinear forced vibration analysis of clamped functionally graded beams, Acta Mech. 221 (2011) 23–38. http://dx.doi.org/10.1007/s00707-011-0491-1.

[33] P. Subramanian, Dynamic analysis of laminated composite beams using higher order theories and finite elements, Compos. Struct. 73 (2006) 342–353. http://dx.doi.org/10.1016/j.compstruct.2005.02.002.

[34] K. Chandrashekhara, K. Krishnamurthy, S. Roy, Free vibration of composite beams including rotary inertia and shear deformation, Compos. Struct. 14 (1990) 269–279. http://dx.doi.org/10.1016/0263-8223(90)90010-C.

[35] M. Rafiee, J. Yang, S. Kitipornchai, Large amplitude vibration of carbon nanotube reinforced functionally graded composite beams with piezoelectric layers, Compos. Struct. 96 (2013) 716–725.

[36] Y. Fu, J. Wang, Y. Mao, Nonlinear analysis of buckling, free vibration and dynamic stability for the piezoelectric functionally graded beams in thermal environment, Appl. Math. Model. 36 (2012) 4324–4340. http://dx.doi.org/10.1016/j.apm.2011.11.059.

[37] M. Rafiee, M. Mohammadi, B. Sobhani Aragh, H. Yaghoobi, Nonlinear free and forced thermo-electro-aero-elastic vibration and dynamic response of piezoelectric functionally graded laminated composite shells, Part I: Theory and analytical solutions, Compos. Struct. 103 (2013) 179–187. http://dx.doi.org/10.1016/j.compstruct.2012.12.053.

[38] S.M. Hosseini, S. Mareishi, H. Kalhori, M. Rafiee, Large amplitude free and forced oscillations of functionally graded beams, Mech. Adv. Mater. Struct. 21 (2014) 255–262. http://dx.doi.org/10.1080/15376494.2012.680670.

Chapter 6

6. Effect of functionalization of carbon nanotubes on vibration and damping characteristics of epoxy nanocomposites

as published* in Polymer Testing, 69(2018) 385–395

https://doi.org/10.1016/j.polymertesting.2018.05.037

*In accordance with University of Ottawa regulations, the contact email address has been removed from this article.

Foreword

This chapter is the first chapter in this dissertation that focuses on experimental results from nanocomposites. In this chapter, an experimental study was carried out to study the vibrations and damping of p-MWCNTs/epoxy and f-MWCNTs/epoxy two-phase nanocomposites. The frequency response functions, coherence and phase diagrams of nanocomposites can explain the vibration and damping behaviors of epoxy nanocomposites.

Polymer Testing 69 (2018) 385–395

Contents lists available at ScienceDirect

Polymer Testing

journal homepage: www.elsevier.com/locate/polytest

Material Properties

Effect of functionalization of carbon nanotubes on vibration and damping characteristics of epoxy nanocomposites

M. Rafiee[a,*], F. Nitzsche[b], M.R. Labrosse[a]

[a] Department of Mechanical Engineering, University of Ottawa, 161 Louis Pasteur, Ottawa, ON K1N 6N5, Canada
[b] Department of Mechanical and Aerospace Engineering, Carleton University, 1125 Colonel By Drive, Ottawa, ON K1S 5B6, Canada

ARTICLE INFO

Keywords:
Polymer composite
Experimental vibration
Carbon nanotubes
Vibration damping
Functionalize CNTs
Epoxy nanocomposite

ABSTRACT

The vibration and damping characteristics of epoxy composites reinforced by pristine and functionalized multi-walled carbon nanotubes (MWCNTs) were investigated experimentally for potential use as integral passive damping elements in structural composite applications. The MWCNTs were introduced into the acetone solvent and then mixed with epoxy resin through a sonication process and mechanical stirring. The solvent was evaporated from the mixture by means of magnetic hot plate and the hardener was added once it was cooled down to room temperature. The MWCMTs/epoxy mixture was then injected into a mold to form the nanocomposite specimens. Nanocomposite specimens were fabricated for six different MWCNT loadings (0.02, 0.041, 0.061, 0.123, 0.25 and 0.37 wt%). Microstructural analysis, tensile and bending tests were carried out to examine the effect of pristine multi-walled carbon nanotubes (p-MWCNTs) and functionalized multi-walled carbon nanotubes (f-MWCNTs). The frequency response functions (FRFs), coherence and phase diagrams of nanocomposites were measured using a forced vibration technique. A periodic up-chirp signal was generated by a shaker to excite the cantilever nanocomposite specimen at the base. The damped natural frequencies and damping ratios were obtained for different loadings of MWCNTs. The experimental results indicated that the damped natural frequencies of p-MWCNTs/epoxy and f-MWCNTs/epoxy composites increased by adding MWCNTs up to 0.12 wt.%, and decreased at higher MWCNTs content. Addition of p-MWCNTs were improved the damping ratio of nanocomposites. While the damping ratios from f-MWCNTs at loadings of 0.02–0.06 wt.% were higher than those from p-MWCNTs, they did not increase at higher CNTs contents for the first mode of vibration.

1. Introduction

The development of carbon nanotube-reinforced polymers has attracted considerable interest due to the opportunity they afford to modify the physicochemical (such as mechanical, electrical, and thermal) properties of otherwise inert hosting polymers. Carbon nanotubes (CNTs) composites have been studied by researchers and found to improve such properties when mixed with polymer materials [1–4].

The two main challenges in using CNTs in composites are the prevention of CNT clusters that tend to form, and the improvement of the bond between the CNTs and the matrix, which is usually inadequate. Chemical functionalization of CNTs is one of the ways to improve dispersion and strengthen the interfacial bonding strength between CNTs and polymer matrix [5]. Montazeri et al. [6] used untreated CNT and CNT-COOH to reinforce the diglycidyl ether bisphenol A epoxy resin. Compared to the untreated CNT, CNT-COOH reinforced epoxy composites showed higher Young's modulus values. Effects of noncovalently functionalized multiwalled carbon nanotube with hyperbranched polyesters on mechanical properties of epoxy composites were studied by Qi et al. [7]. Zhu et al. [8] reported 30–70% improvement in ultimate strength and modulus of epoxy composites with the addition of only small quantities of single-walled CNT-NH_2. Srikanth et al. [9] explored amino functionalized MWCNT (MWCNT-NH_2) to reinforce carbon fiber/epoxy composites. Their results showed that mechanical properties, such as flexural strength and interlaminar shear strength (ILSS), were improved with the incorporation of MWCNT-NH_2 at a loading of 0.5 wt.%. However, functionalized CNTs do not always improve their matrices. Guadagno et al. [10] reported that the presence of carboxyl-functionalized MWCNT (MWCNT-COOH) did not induce any evident increase in the storage modulus of epoxy nanocomposites. On the contrary, an almost constant or even decreased value with the increasing content of MWCNT-COOH was observed. Cui et al. [11] found that the tensile strength of MWCNT-COOH/epoxy composites tended to degrade quickly with the increase of MWCNT-COOH content.

Investigation of the vibration and damping behavior of composites with or without nanoparticles is an important issue in mechanical and

* Corresponding author.
E-mail addresses:

https://doi.org/10.1016/j.polymertesting.2018.05.037
Received 9 March 2018; Received in revised form 20 May 2018; Accepted 25 May 2018
Available online 30 May 2018
0142-9418/

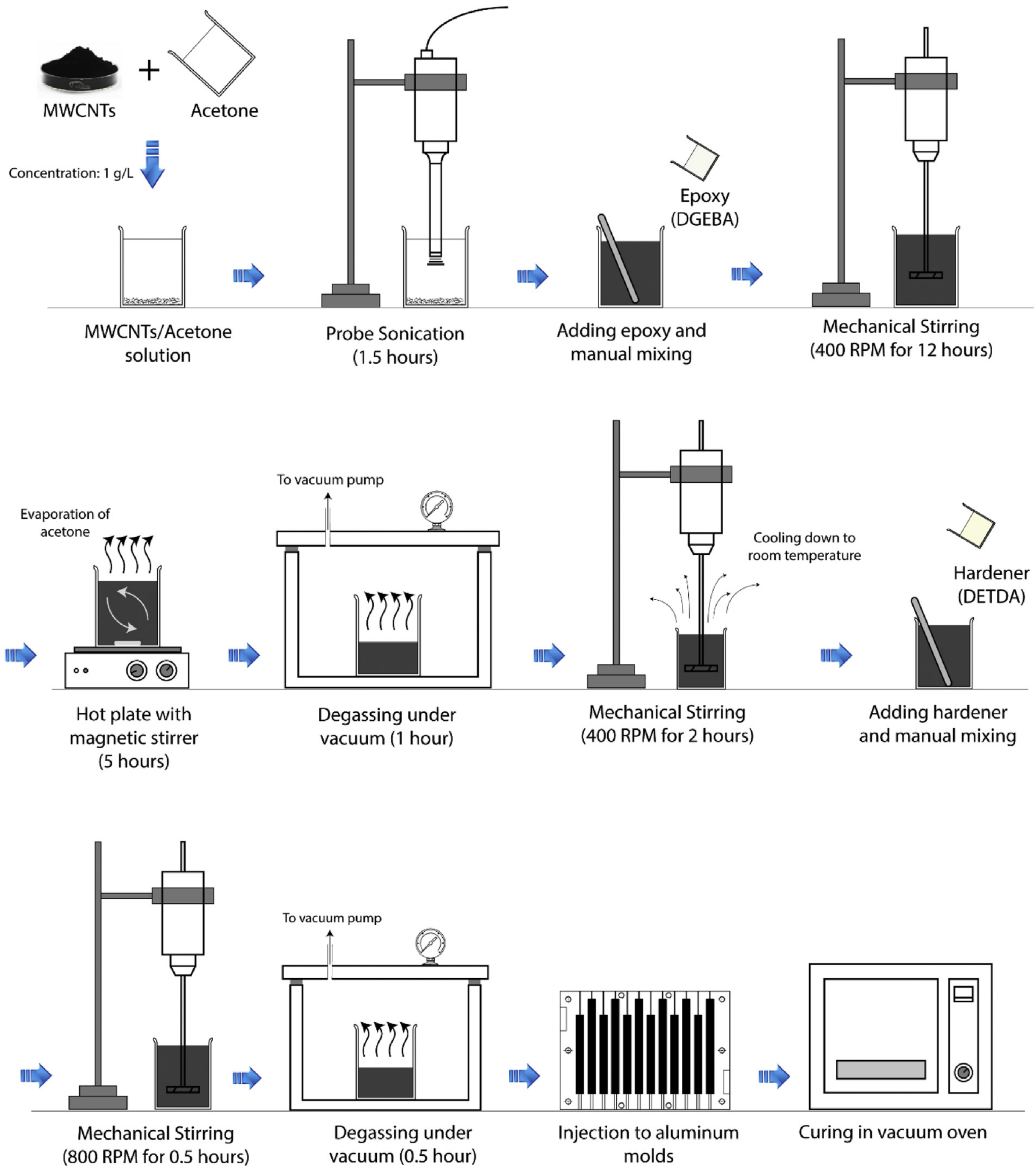

Fig. 1. Fabrication process of MWCNTs/epoxy two-phase composites.

aerospace engineering. Many researchers have studied them both experimentally [12–21] and theoretically [1,15,22–30]. A state-of-the-art review of vibration of composite beams and blades was presented by Rafiee et al. [2]. Studies in the recent years have shown that carbon nanotubes can introduce damping to attenuate the vibrations and noise of two-phase [12–17] and three-phase [16–20] epoxy nanocomposites by dissipating substantial amounts of vibration energy. Rajoria and Jalili [12] studied the stiffness and damping properties of pristine single-walled and multiwalled carbon nanotube-epoxy composites through free and forced vibration. Up to 700% increase in damping ratio was observed by using 5.0% wt.% MWCNTs in epoxy as compared to plain epoxy. Jangam et al. [14] studied the influence of randomly oriented and aligned pristine multi-walled carbon nanotubes on vibration damping of epoxy nanocomposites at three different CNTs loadings (0.1, 0.2, and 0.3 wt%). Their results showed an improvement by up to 37% in structural damping of aligned MWCNTs compared with randomly oriented ones. Theoretical and experimental investigation of vibration characteristics of carbon nanotubes-reinforced polymer composite plate was performed by Mehar et al. [15]. Jamal-Omidi and Shayanmehr [16] experimentally investigated the effects of adding single-walled carbon nanotubes (SWCNTs) on the nonlinear free vibration of neat resin and carbon fiber reinforced polymer composites (CFRPs). Their results indicated that the nonlinear vibration behavior of all models was close to homogenous materials with increasing SWCNTs. The natural frequency and damping ratio of the p-MWCNTs-reinforced epoxy composites were evaluated using free vibration tests by Her and Yeh [13]. Their results showed that the natural frequency of the nanocomposite increased with the addition of MWCNTs, while the

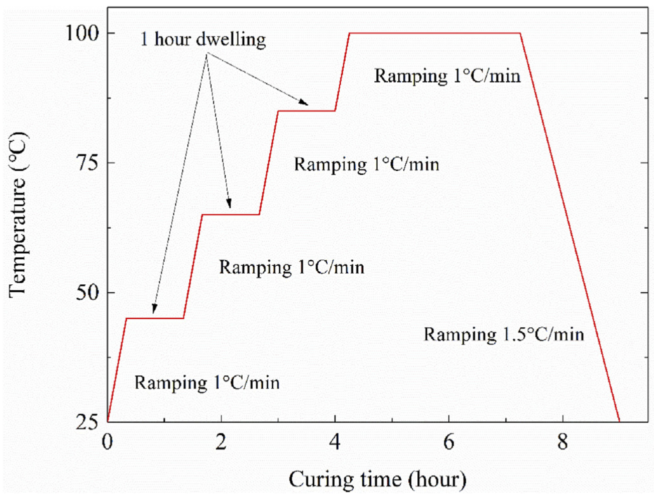

Fig. 2. Cure schedule for epoxy matrix composites.

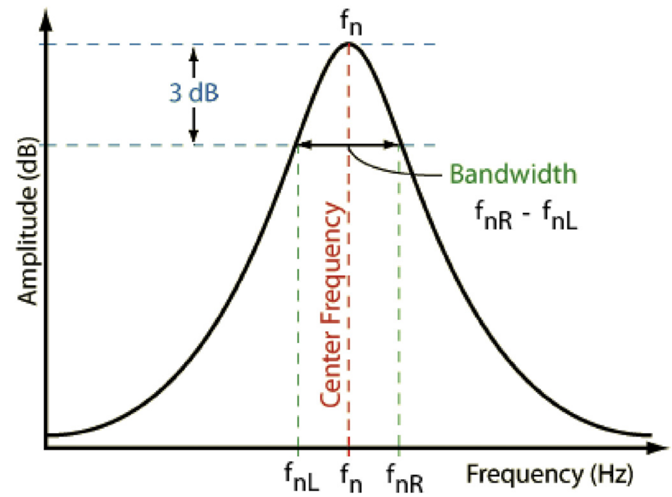

Fig. 4. Half-bandwidth (3 dB bandwidth) method.

Table 1
Typical material properties of nanocomposite beam used in the examples unless otherwise specified.

Source	Symbol	Value	Unit	Description
General geometric parameters and loading conditions				
	h	3.175	mm	Beam thickness
	L	130	mm	Effective length of the beam
	b	12.7	mm	Beam width
Multi-walled walled carbon nanotubes [32]				
	d^{CN}	9.5×10^{-9}	m	Outer diameter of carbon nanotubes
	ℓ^{CN}	1.5×10^{-6}	m	Length of carbon nanotubes
	ρ^{CN}	60	kg/m^3	Bulk density of carbon nanotubes
Epoxy resin polymer matrix (Part A + Part B) [33]				
	ρ^{ER}	1080	kg/m^3	Mass density of epoxy resin matrix
	E^{ER}	19.251×10^9	kg/m^2	Young's modulus of epoxy resin matrix
	α^{ER}	9.756×10^{-5}	1/K	Thermal expansion coefficient of epoxy resin matrix

damping ratio decreased. Vibrations of CNTs/fiber/polymer multiscale composites were also reported on in the literature. The vibration damping characteristics of nanocomposites and carbon fiber reinforced polymer composites (CFRPs) containing multiwall carbon nanotubes (CNTs) were studied by Khan et al. [18]. Their methods included free vibration by means of an imposed initial amplitude at the tip of the beam, as well as forced vibrations by means of a shaker. The free vibration test indicated that the damping ratio of the CFRP-CNTs composites increased with increasing CNTs content. Their results also showed a higher rate of increase in damping ratio than in the epoxy nanocomposites. Johnson et al. [17] presented an experimental study to quantify the structural damping in composites due to the addition of CNTs to thermosetting resin systems with and without fiberglass reinforcement. Their results showed an increase in specific damping capacity with the addition of CNTs. The addition of fiberglass reinforcement to composite samples was shown to reduce the effective damping ratio compared to plain epoxy samples and CNT-filled epoxy samples. Kim et al. [19] investigated the damping characteristics of woven carbon fiber/epoxy composites using high loading of CNTs. The damping ratio was improved by up to 12.3% (at the 1st natural frequency) and 16.1% (at the 2nd natural frequency), in the 7 wt% dispersed CNT specimen. Khashaba [20] investigated the effect of MWCNTs on the damping properties of glass-fiber reinforced epoxy composites. They concluded that the addition of MWCNTs increased the natural frequencies and damping ratio of multiscale composites. Rafiee et al. [30] addressed the cross-sectional design and analysis of fiber-reinforced multiscale composite beams of general cross-sectional shape

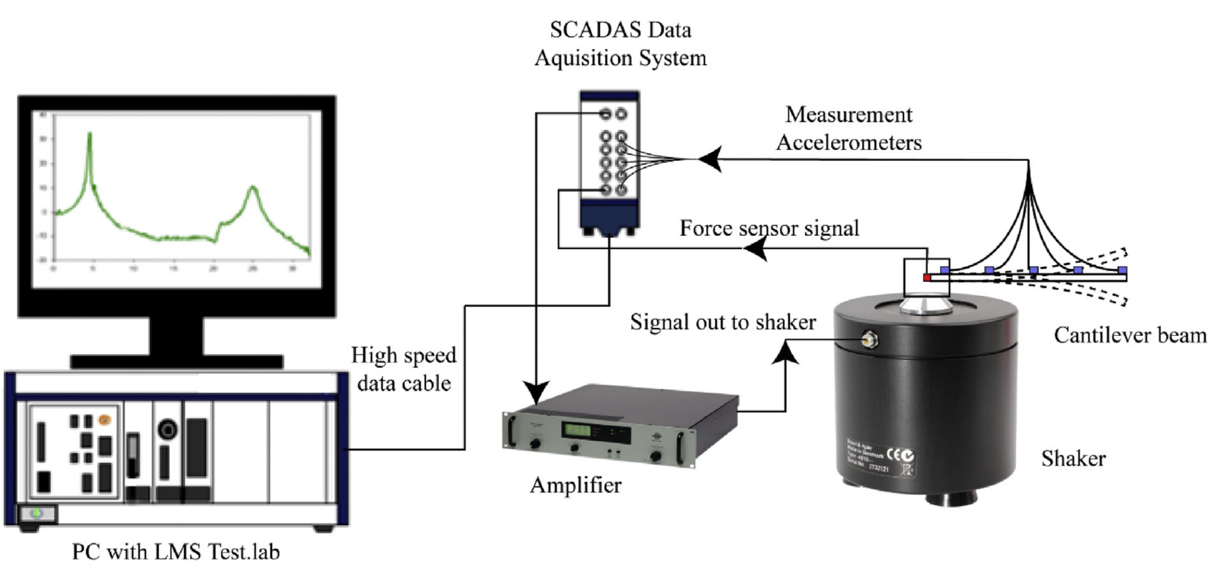

Fig. 3. Schematic diagram of the experimental procedure for vibration testing of MWCNTs-reinforced composites.

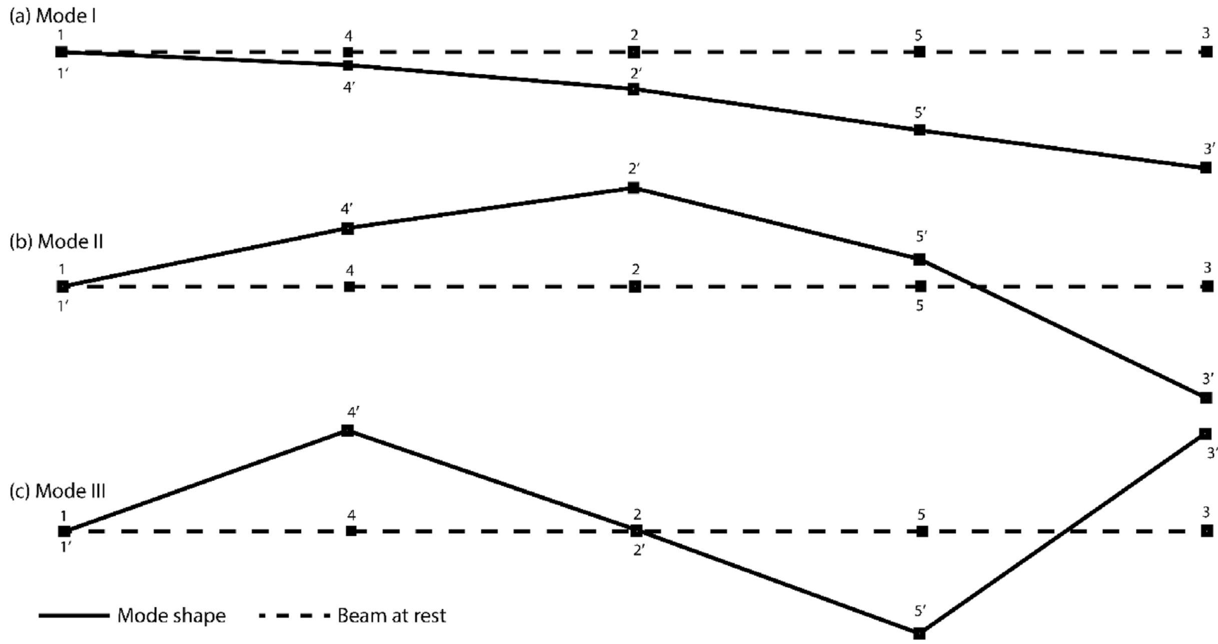

Fig. 5. Three first mode shapes of cantilever composite beams calculated from Polymax module (a) Mode I, (b) Mode II, (c) Mode III (accelerometers locations are shown by solid squares and a number).

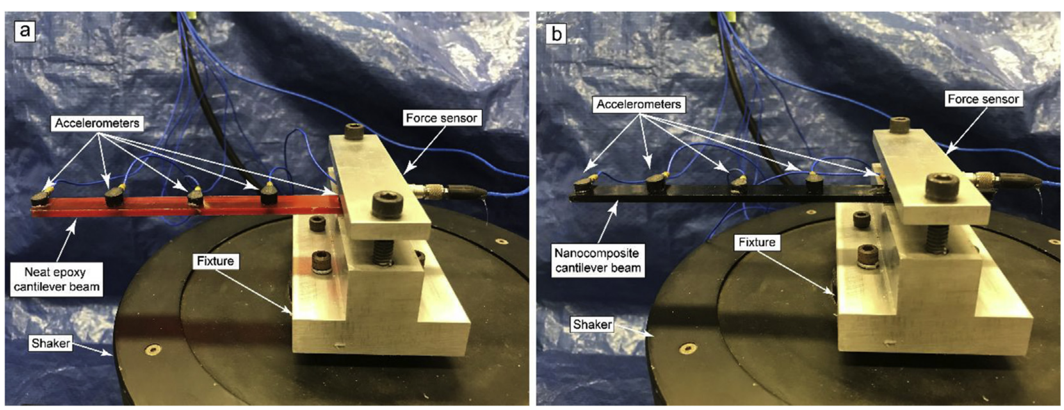

Fig. 6. Experimental set-up with (a) neat epoxy specimen, (b) nanocomposite specimen.

Table 2
Data acquisition details.

Source	Type
Excitation signal	Periodic Chirp (Chirp Sine or Sweep Sine) – up-chirp
Sampling frequency	1024 Hz
Frequency range of interest	10–1000 Hz
Frequency resolution	0.125
FRF estimator	H1

and arbitrary anisotropic material properties and investigated the effect of carbon nanotubes on their stiffness properties. In another study, they developed a mathematical model to predict the effective material properties of graphene nanoplatelets/fiber/polymer multiscale composites. The numerical results showed that the central deflection and natural frequency were significantly improved by a small percentage of graphene nanoplatelets (GNPs).

As evident from the aforementioned literature references, no study has been reported on the vibration and damping characteristics of functionalized MWCNTs-reinforced epoxy composites. The present research aimed to understand the practical aspects related to the vibration and damping behavior of pristine and functionalized MWCNTs/

Table 3
Accelerometers specifications.

Location (See Fig. 5)	Model	Height (mm)	Weight (g)	Sensitivity	Frequency Range (± 5%) (Hz)
1 (Base)	352C22	3.6	0.5	9.6	1.0 to 10000
2 (Middle)	352C22	3.6	0.5	9.73	1.0 to 10000
3 (Tip)	352C22	3.6	0.5	9.26	1.0 to 10000
4	352A24	4.8	0.8	98.1	1.0 to 8000
5	352A24	4.8	0.8	100.7	1.0 to 8000

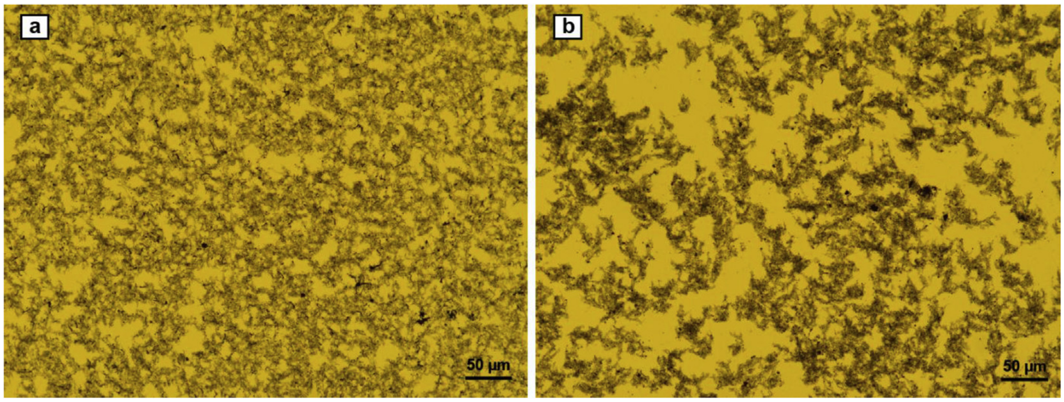

Fig. 7. Optical micrograph of (a) p-MWCNTs/DGEBA and (b) f-MWCNTs/DGEBA at 0.123 wt.%.

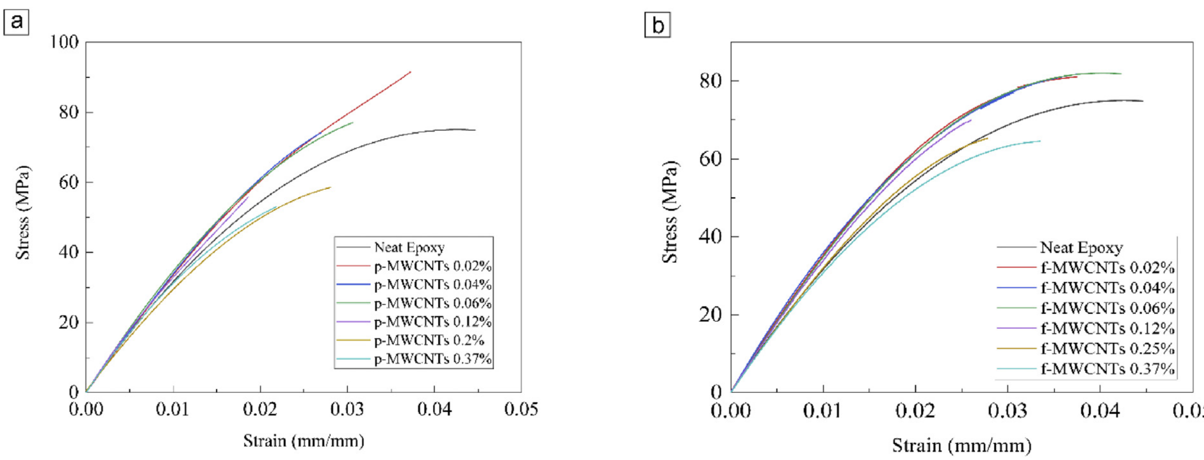

Fig. 8. Tensile stress-strain average curves of epoxy beams reinforced with (a) p-MWCNTs and (b) f-MWCNTs.

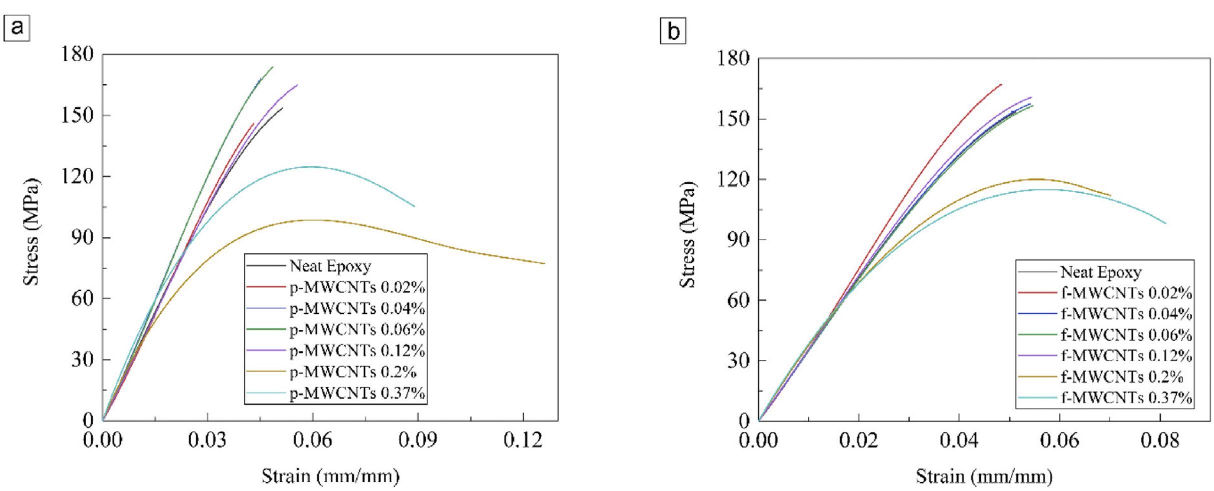

Fig. 9. Flexural stress-strain average curves of epoxy beams reinforced with (a) p-MWCNTs and (b) f-MWCNTs.

epoxy composites for potential use as integral passive damping elements in structural composite applications. In addition, the study was also focused on evaluating the effect of MWCNTs functionalization on the mechanical properties of two-phase epoxy resin composites.

2. Materials, processing and fabrication

2.1. Materials

The pristine multi-wall carbon nanotube (NC7000) and amine functionalized multi-wall carbon nanotube (NC7000-NH_2) were obtained from Nanocyl S.A., Belgium. They featured an average diameter and length of 9.5 nm and 1.5 µm, respectively. MWCNTs were produced via the Catalytic Chemical Vapor Deposition (CCVD) process with carbon purity of 90%. The low viscosity diglycidyl ether of bisphenol-A (DGEBA) epoxy resin PT-2712 Part A and the diethyltoluenediamine (DETDA) curing agent PT-2712 Part B1 produced by PTM&W Industries, Inc., USA were used. Epoxy resin Part A and B mixing weight ratio was 100/22 as per manufacturer recommendation.

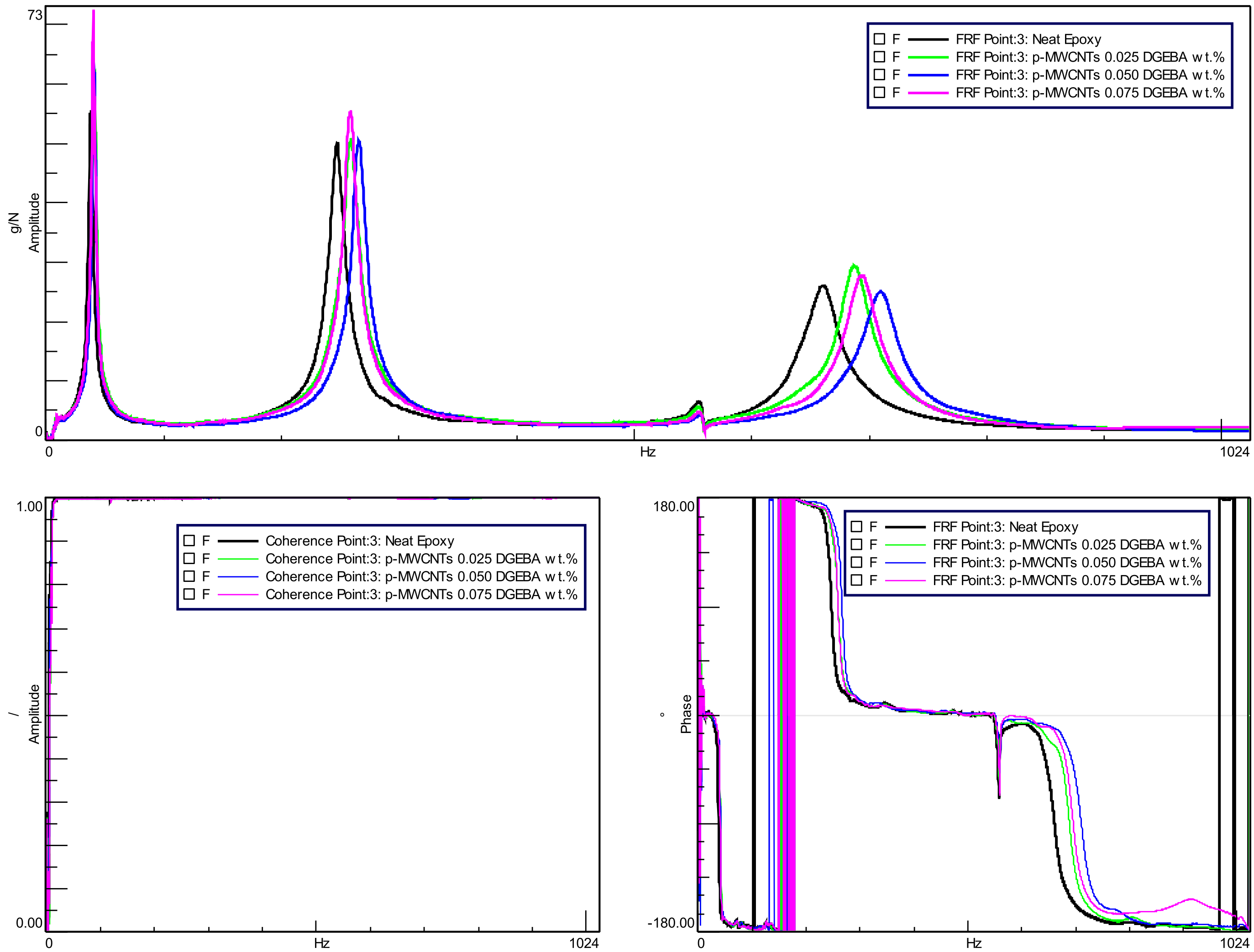

Fig. 10. FRFs, coherence and phase diagrams for neat epoxy and p-MWCNTs (0.025, 0.050 and 0.075 DGEBA wt.%) reinforced composites.

2.2. Processing and fabrication of MWCNTs/polymer nanocomposites

The two-phase polymer matrix composites reinforced by pristine multi-wall carbon nanotube (p-MWCNTs) or functionalized multi-wall carbon nanotube (f-MWCNTs) were prepared with nanotube loadings of 0.025, 0.050, 0.075, 0.15, 0.3 and 0.45 of DGEBA wt%. The equivalent nanotube loadings with respect to total weight (DGEBA + DETDA) were 0.020, 0.041, 0.061, 0.123, 0.246 and 0.369 wt%, respectively. Fig. 1 shows a schematic of the method for the preparation of the MWCNTs/epoxy nanocomposites. The MWCNTs were dispersed at a ratio of 1 g of MWCNTs per each liter of acetone. This mixture was sonicated using an ultrasonic probe (Q700 Sonicator, Qsonica LLC, USA) for half an hour. To avoid any adverse high temperature effects, sonication was performed by 20-sec ON pulses followed by 10-sec OFF cycles. The mixture was then stirred by "high shear" laboratory shear mixer at 400 rpm for 12 h. During mixing, dispersion of CNTs takes place in the resin. After this step, the mixture was simultaneously heated and stirred by a Teflon-coated magnetic bar on a magnetic stir plate for 4 h at 70 °C. The objective was to remove the acetone by evaporation. To fully complete the acetone removal, the mixture was placed in a vacuum chamber for half an hour. After this step, the slurry of epoxy resin DGEBA and MWCNTs were allowed to cool to room temperature before the curing agent was added, to avoid premature curing during mixing. Low viscosity curing agent DETDA was added with a curing agent to resin ratio of 22:100. The mixture was shear-mixed at 800 rpm for 30 min using a mechanical stirrer with stainless steel axial impeller. The mixture was degassed in a vacuum chamber at ambient temperature for about 30 min, and poured into aluminum molds. The samples were cured at room temperature for 15 h followed by a post cure of 1 °C/min ramp rate, held every 20 °C for an hour, then continuing until a final hold of 3 h at 100 °C to remove the possible thermal history (See Fig. 2).

3. Characterization

3.1. Tensile and bending

The tensile and three-point bending tests were carried out using an Instron 4482 machine at a crosshead speed of 1 mm/min according to ASTM D638 and ASTM D70, respectively. Tensile specimens were of the type I of ASTM D638 with the overall dimension $165 \times 19 \times 3.175\ mm^3$. Advanced video extensometer was used to measure the strain of the specimen. Three-point flexural specimen were $165 \times 12.7 \times 3.175\ mm^3$. Blue hill 2 software was used to run the test, acquire and process the data to obtain the tensile and bending properties.

3.2. Vibration

The shaker vibration test was used to measure the natural frequencies and damping factors of nanocomposites specimens in the form of cantilever beams. The clamped-free beam was excited by a vibration

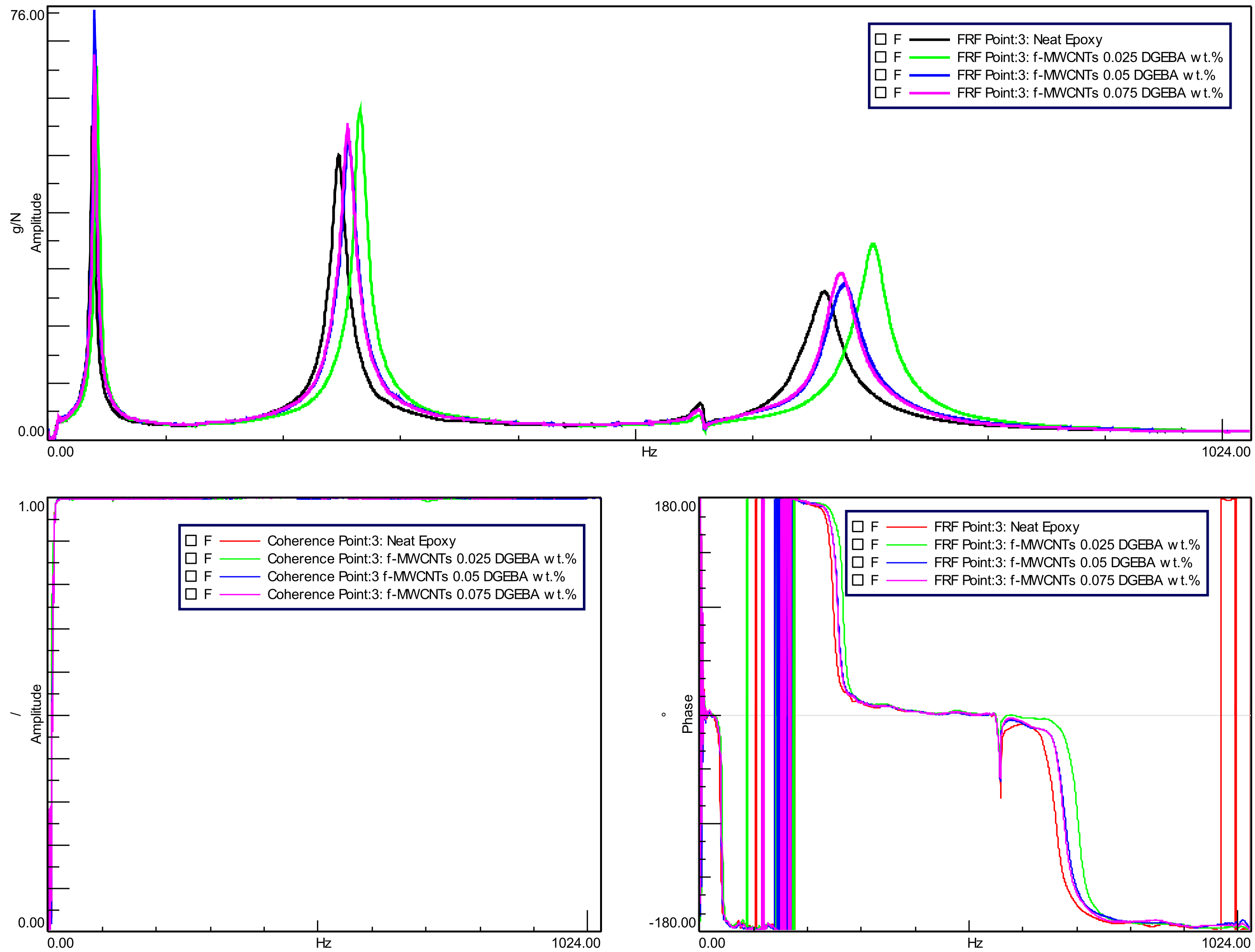

Fig. 11. FRFs, coherence and phase diagrams for neat epoxy and f-MWCNTs (0.025, 0.050 and 0.075 DGEBA wt.%) reinforced composites.

shaker (Brüel & Kjær Sound & Vibration Measurement A/S, Denmark) at the clamped end, and the response of the beam was tracked by means of accelerometers and the computed frequency response functions (FRFs) gave information about the natural frequencies of the composite beam.

Rectangular specimens of 12.7 mm (0.5 in) wide, 3.175 mm thick (1/8 in) and 152.4 mm long (6 in) were prepared for vibration tests according to ASTM E756. The free beam length was defined as the distance between the clamp and the specimen tip and was measured as 130 mm (See Table 1). Fig. 3 shows the schematic of instrumentation used for vibration test. Acceleration was measured at a total of five points by means of miniature lightweight accelerometers (See Table 3) and a piezoelectric crystal force transducer (Quartz ICP® Force Ring, PCB® Model 201B03, measurement range of 2.224 kN) was used to measure the excitation force exerted by the electrodynamic shaker (See Fig. 6). A power amplifier was required to drive the shaker. Periodic chirp excitation signals were used with a frequency bandwidth of 0–1024 Hz to guarantee high quality measurements. The tests were performed using the LMS Test.Lab by Siemens®, which is an integrated solution for experimental vibrational analysis including tools for data acquisition (LMS SCADAS III with eight measurement channels and two output channels), test execution and data processing (LMS Testing Solution Software). The LMS SCADAS III was used to acquire the signals from the force sensor and the piezoelectric accelerometers and to control the amplifier connected to the shaker, by means of a digital-analog converter output. Spectral Testing module of LMS Testing Solution Software was used for the shaker test. The Modal Analysis module was then used to analyze the power spectral density (PSD) of the excitation signal, the FRFs and the coherence functions, and to calculate FRF sum functions (i.e. the sum of the five FRFs). Finally, the PolyMAX frequency domain identification method [31], which is based on a least squares fit, was used to identify the natural frequencies, damping ratios and vibration modes of MWCNTs/epoxy nanocomposites. All measurements were acquired in the frequency range 10–1024 Hz, with a resolution of 0.125 Hz. Each measurement was averaged over 20 acquisitions. A list of data acquisition details is given in Table 2.

There are many methods for measuring the damping of a vibration system such as the logarithmic decrement (for damping measurement in time domain) method and the bandwidth method (for damping measurement in frequency domain). For the present study, the half-power bandwidth method (also known as 3 dB bandwidth method and cut off frequency method) was used in LMS Test.Lab for measurement of damping factor (Q factor), damping ratio (ζ), and loss factor (η) (See Fig. 4):

$$\eta_n = \frac{1}{Q_n} = 2\varsigma_n = \frac{\Delta f_{3dB}}{f_n}, \tag{1}$$

where $\Delta f_{3\mathrm{dB}}$ is the difference between frequencies corresponding to 3 dB points around the damped natural frequencies and n is the mode number.

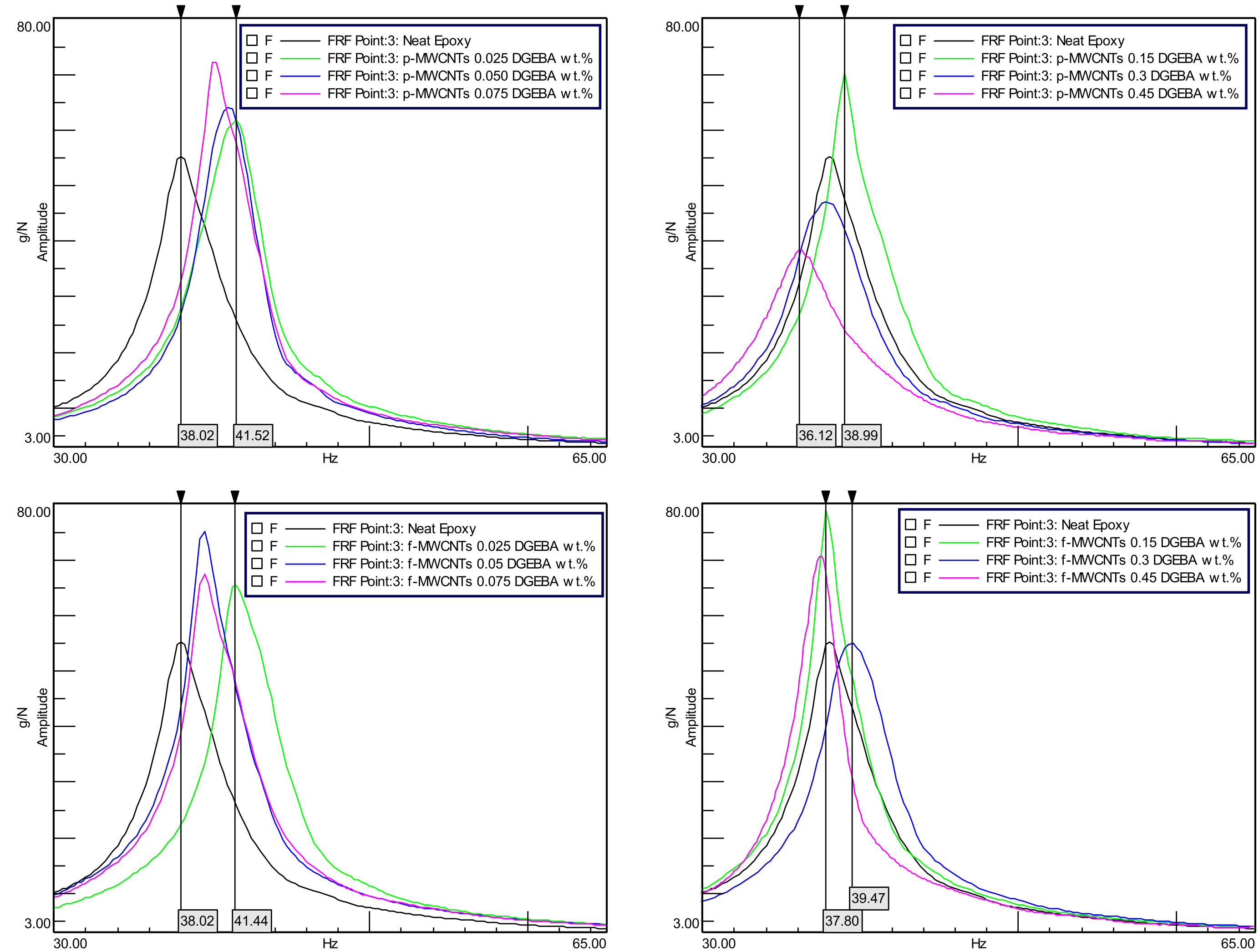

Fig. 12. Magnification of FRFs, coherence and phase diagrams around fundamental resonance peak of MWCNTs/epoxy.

4. Results and discussion

A ZEISS (AX10 model) optical microscopy was used to observe the distribution of pristine and functionalized MWCNTs in epoxy resin at room temperature. Fig. 7 shows the optical micrographs of p-MWCNTs and f-MWCNTs dispersed in epoxy. Since the uniform dispersion state of CNTs in epoxy resin is unstable at different times and temperatures, the optical images were taken at a specific time and temperature (120 min and room temperature in this case) after finishing the process of mixing MWCNTs/acetone with DGEBA. The MWCNTs dispersion was obtained by mixing both individual MWCNTs and micro MWCNTs aggregates connected by MWCNTs in epoxy resin, as seen in Fig. 7.

4.1. Tensile and flexural properties

The effects of pristine and functionalized carbon nanotubes on tensile and bending properties of MWCNTs/epoxy composite are shown in Figs. 8 and 9. The curves were averaged from five specimens. It can be observed that the incorporation of p-MWCNTs and f-MWCNTs in the polymer matrix had significant effects on the tensile strength up to 0.06 wt.%. For instance, 0.02 wt.% of p-MWCNTs and f-MWCNTs improved the strength of nanocomposite by 22.2% and 6.3%, respectively. At higher loading of MWCNTs, the material exhibited brittle behavior and both the elongation and strength became lower than those of neat epoxy.

Bending test results also showed the effects of pristine and functionalized MWCNTs on the strength and elongation of nanocomposite specimens (Fig. 9). The maximum bending strength of p-MWCNTs and f-MWCNTs were observed at 0.06 and 0.02 wt.%, respectively. A significant increase in ultimate strain can be seen in p-MWCNTs (145.8% at 0.25 wt%) while the maximum increase in f-MWCNTs was 58.0% at the loading of 0.37 wt.%.

4.2. Vibration and damping results

Damped natural frequencies, frequency-response functions (FRFs), phase diagram, coherence, and damping ratios about the first three vibration modes were obtained and shown in Fig. 10 through 15. We can see from Table 4, Figs. 12 and 13 that the damped natural frequencies of p-MWCNTs/epoxy and f-MWCNTs/epoxy composites increased by adding CNTs up to 0.12 wt.% and decreased with higher MWCNTs content. The maximum improvements happened at 0.02 wt%, and reached 9.4% in f-MWCNTs/epoxy composites compared to 7.2% in p-MWCNTs/epoxy. It was also observed that the improvement in fundamental natural frequency was more pronounced than that for higher natural frequencies. For instance, addition of 0.02% of f-MWCNTs improved the fundamental, second and third damped natural frequencies by 9.4%, 7.5% and 6.3%, respectively.

The effects of pristine and functionalized carbon nanotubes on the damping ratios of epoxy-based composite beams were investigated and depicted in Figs. 14 and 15, Fig. 15, respectively. As one can observe from Fig. 14, the damping ratios dropped by 18% till loading of 0.06 wt.

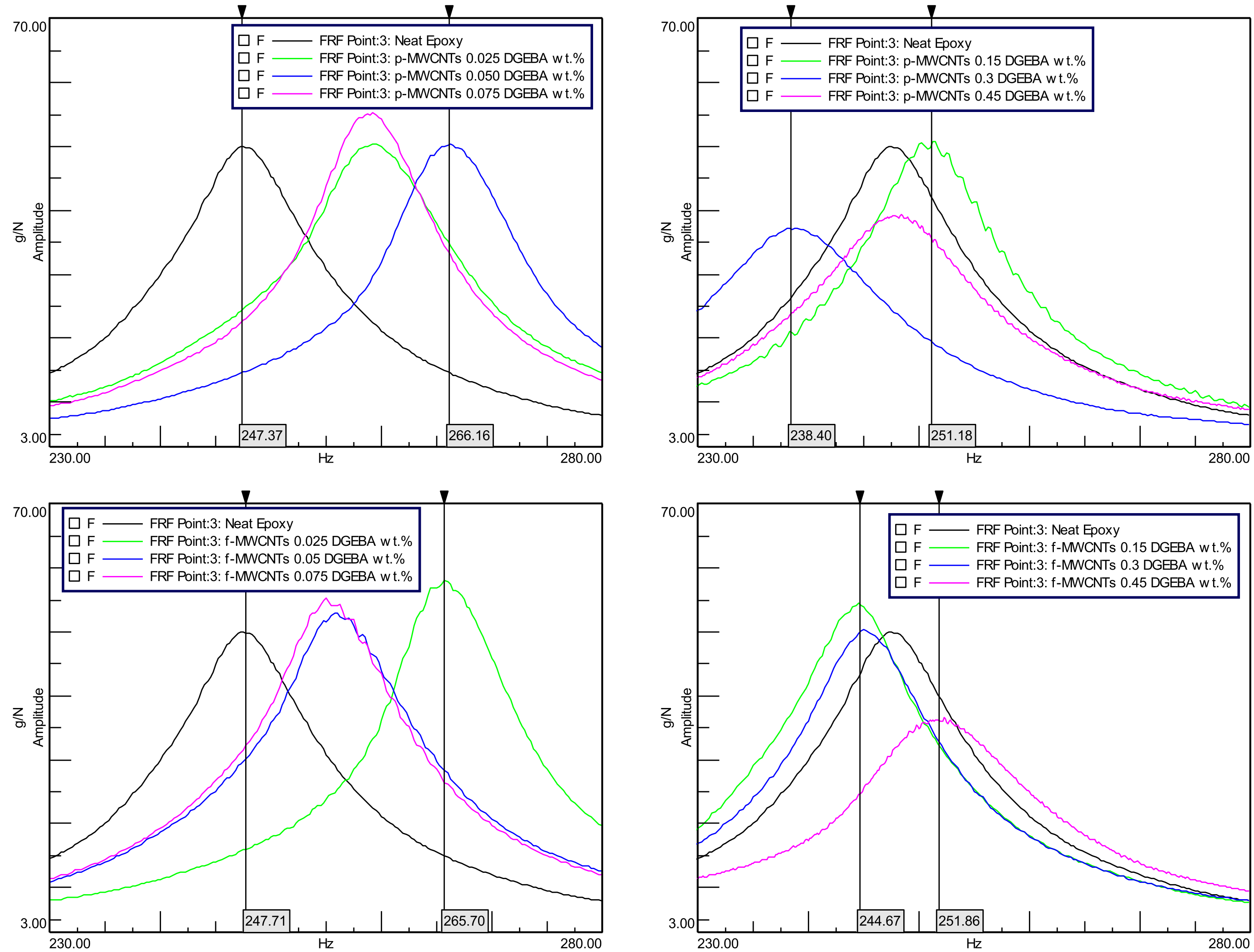

Fig. 13. Magnification of FRFs, coherence and phase diagrams around second resonance peak of MWCNTs/epoxy.

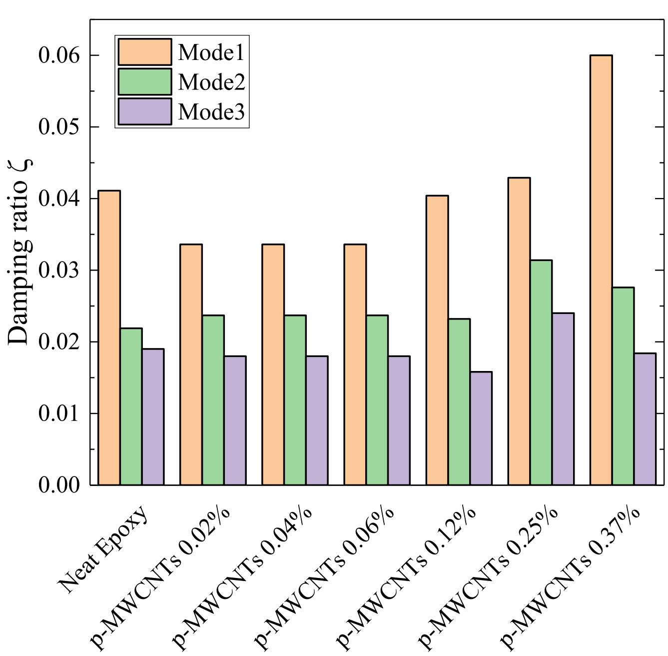

Fig. 14. Damping ratio of p-MWCNTs-reinforced composites at different loadings.

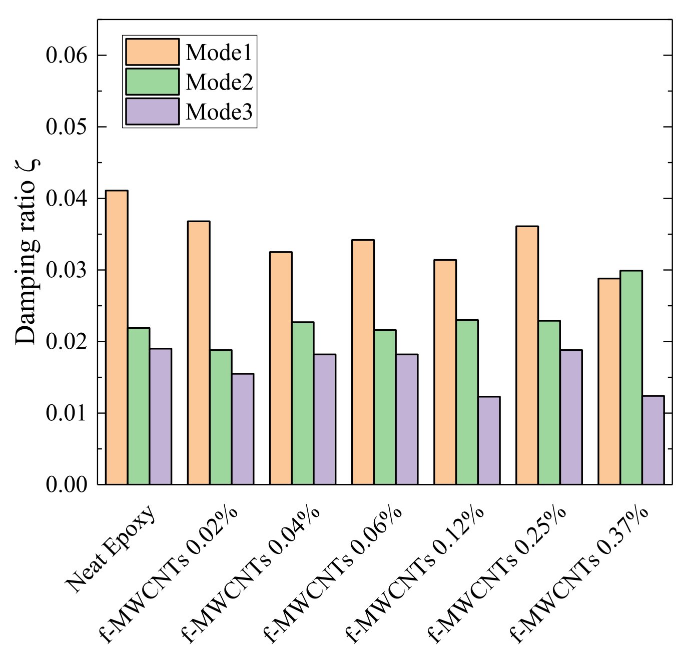

Fig. 15. Damping ratio of f-MWCNTs-reinforced composites at different loadings.

Table 4
Comparison of linear damped frequencies of pristine and functionalized MWCNTs/epoxy composites.

MWCNTs type	Damped natural frequency	MWCNTs wt.%						
		0 (Neat Epoxy)	0.02% (0.025 DGEBA wt.%)	0.04% (0.05 DGEBA wt.%)	0.06% (0.075 DGEBA wt.%)	0.12% (0.15 DGEBA wt.%)	0.25% (0.3 DGEBA wt.%)	0.37% (0.45 DGEBA wt.%)3
p-MWCNTs	f_{d1}	38.34	41.09 7.2%[a]	41.09 7.2%	41.09 7.2%	39.133 2.1%	37.798 −1.4%	36.323 −5.3%
	f_{d2}	247.504	259.459 4.8%	259.459 4.8%	259.459 4.8%	250.974 1.4%	239.104 −3.4%	247.836 0.1%
	f_{d3}	661.378	687.777 4.0%	687.777 4.0%	687.777 4.0%	669.42 1.2%	641.225 −3.0%	659.76 −0.2%
f-MWCNTs	f_{d1}	38.34	41.945 9.4%	39.824 3.9%	40.028 4.4%	38.086 −0.7%	39.601 3.3%	37.464 −2.3%
	f_{d2}	247.504	266.099 7.5%	256.355 3.6%	255.538 3.2%	244.302 −1.3%	245.216 −0.9%	251.815 1.7%
	f_{d3}	661.378	702.979 6.3%	678.869 2.6%	675.292 2.1%	654.476 −1.0%	647.509 −2.1%	667.917 1.0%

[a] $X\% = 100\% \frac{Freq.|_{n\%\ \ MWCNTs} - Freq.|_{Neat\ epoxy}}{Freq.|_{Neat\ epoxy}}$.

% and then improved by adding the p-MWCNTs in the composites for the first vibration modes. For instance, a 46% improvement in damping ratio in p-MWCNTs/epoxy composite can be seen at a loading of 0.37 wt.%. In f-MWCNTs/epoxy composites, a relatively monotonous decrease in damping ratio can be observed. While the damping ratios from f-MWCNTs at loadings of 0.02–0.06 wt.% were higher than those from p-MWCNTs, they did not increase at higher CNTs contents for the first mode of vibration.

For the second mode of vibration, both pristine and functionalized multiwalled CNTs improved the damping characteristics of nanocomposite beams. For instance, an over 40% improvement was recorded in damping ratio of p-MWCNTs/epoxy composites at 0.25 wt.% loading. A maximum improvement by 36.5% in damping ratio of f-MWCNTs/epoxy composites was observed at 0.37 wt.% loading. Damping ratio results of third mode of vibration showed no significant improvements.

5. Conclusion

The experimental vibration and damping of p-MWCNTs/epoxy and f-MWCNTs/epoxy nanocomposites were studied. Nanocomposite specimens were fabricated for six different MWCNT loadings (0.02, 0.041, 0.061, 0.123, 0.25 and 0.37 wt%). Microstructural analysis, as well as tensile and bending tests were carried out to examine the effects of p-MWCNTs and f-MWCNTs. The frequency response functions, coherence and phase diagrams of nanocomposites were measured using periodic up-chirp forced vibration technique. The experimental results indicated that the damped natural frequencies in p-MWCNTs/epoxy and f-MWCNTs/epoxy composites increased with MWCNTs loading up to 0.12 wt.% and decreased at higher MWCNTs content. Another finding was that the improvement in fundamental natural frequency was more pronounced than at higher natural frequencies. The forced vibration test confirmed the beneficial effect of p-MWCNTs on the damping ratio of nanocomposites for the first and second vibration modes. However, a decrease in damping ratio was observed in f-MWCNTs/epoxy composites. For instance, a 46% improvement in damping ratio for the fundamental vibration mode was observed at a loading of 0.37 wt.% in p-MWCNTs/epoxy composite. While the damping ratios from f-MWCNTs at loadings of 0.02–0.06 wt.% were higher than those from p-MWCNTs, they did not increase at higher CNTs contents for the first mode of vibration.

Acknowledgements

The first author gratefully acknowledges the financial support from Ontario Trillium Scholarship (OTS), Government of Ontario and University of Ottawa, Canada.

References

[1] M. Rafiee, X.Q. He, S. Mareishi, K.M. Liew, Modeling and stress analysis of smart CNTs/fiber/polymer multiscale composite plates, Int. J. Appl. Mech 6 (2014) 1450025, , http://dx.doi.org/10.1142/S1758825114500252.
[2] M. Rafiee, F. Nitzsche, M. Labrosse, Dynamics, vibration and control of rotating composite beams and blades: a critical review, Thin-walled Struct. 119 (2017) 795–819, http://dx.doi.org/10.1016/j.tws.2017.06.018.
[3] I. Rafique, A. Kausar, B. Muhammad, Epoxy resin composite reinforced with carbon fiber and inorganic filler: overview on preparation and properties, Polym. Plast. Technol. Eng. 55 (2016), http://dx.doi.org/10.1080/03602559.2016.1163597 03602559.2016.1163597.
[4] G. Mittal, V. Dhand, K.Y. Rhee, S.-J. Park, W.R. Lee, A review on carbon nanotubes and graphene as fillers in reinforced polymer nanocomposites, J. Ind. Eng. Chem. 21 (2015) 11–25, http://dx.doi.org/10.1016/j.jiec.2014.03.022.
[5] R. Blake, Y.K. Gun'ko, J. Coleman, M. Cadek, A. Fonseca, J.B. Nagy, W.J. Blau, A generic organometallic approach toward ultra-strong carbon nanotube polymer composites, J. Am. Chem. Soc. 126 (2004) 10226–10227, http://dx.doi.org/10.1021/ja0474805.
[6] M. Li, Y. Gu, Y. Liu, Y. Li, Z. Zhang, Interfacial improvement of carbon fiber/epoxy composites using a simple process for depositing commercially functionalized carbon nanotubes on the fibers, Carbon N. Y. 52 (2013) 109–121, http://dx.doi.org/10.1016/j.carbon.2012.09.011.
[7] Z. Qi, Y. Tan, H. Wang, T. Xu, L. Wang, C. Xiao, Effects of noncovalently functionalized multiwalled carbon nanotube with hyperbranched polyesters on mechanical properties of epoxy composites, Polym. Test. 64 (2017) 38–47, http://dx.doi.org/10.1016/j.polymertesting.2017.09.031.
[8] M. Sánchez, M. Campo, A. Jiménez-Suárez, A. Ureña, Effect of the carbon nanotube functionalization on flexural properties of multiscale carbon fiber/epoxy composites manufactured by VARIM, Compos. B Eng. 45 (2013) 1613–1619, http://dx.doi.org/10.1016/j.compositesb.2012.09.063.
[9] A. Godara, L. Mezzo, F. Luizi, A. Warrier, S.V. Lomov, A.W. van Vuure, L. Gorbatikh, P. Moldenaers, I. Verpoest, Influence of carbon nanotube reinforcement on the processing and the mechanical behaviour of carbon fiber/epoxy composites, Carbon N. Y. 47 (2009) 2914–2923, http://dx.doi.org/10.1016/j.carbon.2009.06.039.
[10] X. Jia, G. Li, B. Liu, Y. Luo, G. Yang, X. Yang, Multiscale reinforcement and interfacial strengthening on epoxy-based composites by silica nanoparticle-multiwalled carbon nanotube complex, Composer Part a Appl. Sci. Manuf 48 (2013) 101–109, http://dx.doi.org/10.1016/j.compositesa.2013.01.001.
[11] K. Lau, Effectiveness of using carbon nanotubes as nano-reinforcements for advanced composite structures, Carbon N. Y. 40 (2002) 1605–1606, http://dx.doi.org/10.1016/S0008-6223(02)00157-4.
[12] H. Rajoria, N. Jalili, Passive vibration damping enhancement using carbon nanotube-epoxy reinforced composites, Compos. Sci. Technol. 65 (2005) 2079–2093, http://dx.doi.org/10.1016/j.compscitech.2005.05.015.
[13] S.C. Her, S.W. Yeh, Fabrication and characterization of the composites reinforced with multi-walled carbon nanotubes, J. Nanosci. Nanotechnol. 12 (2012)

8110–8115, http://dx.doi.org/10.1166/jnn.2012.4518.
[14] S. Jangam, S. Raja, S. Uma Maheswar Gowd, Influence of multiwall carbon nanotube alignment on vibration damping of nanocomposites, J. Reinforc. Plast. Compos. 35 (2016) 617–627, http://dx.doi.org/10.1177/0731684415626285.
[15] K. Mehar, S.K. Panda, T.R. Mahapatra, Theoretical and experimental investigation of vibration characteristic of carbon nanotube reinforced polymer composite structure, Int. J. Mech. Sci. 133 (2017) 319–329, http://dx.doi.org/10.1016/j.ijmecsci.2017.08.057.
[16] M. Jamal-Omidi, M. ShayanMehr, An experimental study on the nonlinear free vibration response of epoxy and carbon fiber-reinforced composite containing single-walled carbon nanotubes, J. Vib. Contr. (2017), http://dx.doi.org/10.1177/1077546317729628 107754631772962.
[17] R.J. Johnson, J. Tang, R. Pitchumani, Characterization of damping in carbon-nanotube filled fiberglass reinforced thermosetting-matrix composites, J. Mater. Sci. 46 (2011) 4545–4554, http://dx.doi.org/10.1007/s10853-011-5349-3.
[18] S.U. Khan, C.Y. Li, N.A. Siddiqui, J.K. Kim, Vibration damping characteristics of carbon fiber-reinforced composites containing multi-walled carbon nanotubes, Compos. Sci. Technol. 71 (2011) 1486–1494, http://dx.doi.org/10.1016/j.compscitech.2011.03.022.
[19] H.C. Kim, E.H. Kim, I. Lee, J.H. Byun, B.S. Kim, S.M. Ahn, Fabrication of carbon nanotubes dispersed woven carbon fiber/epoxy composites and their damping characteristics, J. Compos. Mater. 47 (2012) 1045–1054, http://dx.doi.org/10.1177/0021998312445513.
[20] U.A. Khashaba, Toughness, flexural, damping and interfacial properties of hybridized GFRE composites with MWCNTs, Composer Part a Appl. Sci. Manuf 68 (2015) 164–176, http://dx.doi.org/10.1016/j.compositesa.2014.10.008.
[21] J. Vanwalleghem, I. De Baere, S. Huysman, L. Lapeire, K. Verbeken, A. Nila, S. Vanlanduit, M. Loccufier, W. Van Paepegem, Effective use of transient vibration damping results for non-destructive measurements of fibre-matrix adhesion of fibre-reinforced flax and carbon composites, Polym. Test. 55 (2016) 269–277, http://dx.doi.org/10.1016/j.polymertesting.2016.09.009.
[22] M. Rafiee, F. Nitzsche, M.R. Labrosse, Modeling and mechanical analysis of multiscale fiber-reinforced graphene composites : nonlinear bending, thermal post-buckling and large amplitude vibration, Int. J. Non Lin. Mech. 103 (2018) 104–111, http://dx.doi.org/10.1016/j.ijnonlinmec.2018.05.004.
[23] M. Rafiee, J. Yang, S. Kitipornchai, Thermal bifurcation buckling of piezoelectric carbon nanotube reinforced composite beams, Comput. Math. Appl. 66 (2013) 1147–1160, http://dx.doi.org/10.1016/j.camwa.2013.04.031.
[24] M. Rafiee, J. Yang, S. Kitipornchai, Large amplitude vibration of carbon nanotube reinforced functionally graded composite beams with piezoelectric layers, Compos. Struct. 96 (2013) 716–725.
[25] M. Rafiee, X.Q. He, K.M. Liew, Nonlinear analysis of piezoelectric nanocomposite energy harvesting plates, Smart Mater. Structure 23 (2014) 065001, http://dx.doi.org/10.1088/0964-1726/23/6/065001.
[26] M. Rafiee, X.Q. He, K.M. Liew, Non-linear dynamic stability of piezoelectric functionally graded carbon nanotube-reinforced composite plates with initial geometric imperfection, Int. J. Non Lin. Mech. 59 (2014) 37–51, http://dx.doi.org/10.1016/j.ijnonlinmec.2013.10.011.
[27] M. Rafiee, X.F. Liu, X.Q. He, S. Kitipornchai, Geometrically nonlinear free vibration of shear deformable piezoelectric carbon nanotube/fiber/polymer multiscale laminated composite plates, J. Sound Vib. 333 (2014) 3236–3251, http://dx.doi.org/10.1016/j.jsv.2014.02.033.
[28] X.Q. He, M. Rafiee, S. Mareishi, Nonlinear dynamics of piezoelectric nanocomposite energy harvesters under parametric resonance, Nonlinear Dynam. 79 (2014) 1863–1880, http://dx.doi.org/10.1007/s11071-014-1780-8.
[29] M. Rafiee, F. Nitzsche, M. Labrosse, Rotating nanocomposite thin-walled beams undergoing large deformation, Compos. Struct. 150 (2016) 191–199, http://dx.doi.org/10.1016/j.compstruct.2016.05.014.
[30] M. Rafiee, F. Nitzsche, M.R. Labrosse, Cross-sectional design and analysis of multiscale carbon nanotubes-reinforced composite beams and blades, Int. J. Appl. Mech. 1850032 (2018), http://dx.doi.org/10.1142/S1758825118500321.
[31] B. Peeters, H. Van der Auweraer, P. Guillaume, J. Leuridan, The PolyMAX frequency-domain method: a new standard for modal parameter estimation? Shock Vib. 11 (2004) 395–409, http://dx.doi.org/10.1155/2004/523692.
[32] Safety Data Sheet: Multiwalled Carbon nanotubes NC7000, Nano. (n.d.). http://www.nanocyl.com/wp-content/uploads/2016/02/DM-Qual-05-MSDS-NC7000-V11.pdf. (Accessed 15 January 2018).
[33] PT2712 Low Viscosity System for tough parts & Structures, PTM&W Ind. Inc. (n.d.). https://www.ptm-w.com/technical-library/product-bulletins/Epoxy-N-Fusion Bulletins/PT2712 Bulletin.pdf. (Accessed 15 January 2018).

Chapter 7

7. Simultaneous reinforcement of matrix and fibers for enhancement of mechanical properties of graphene-modified laminated composites

This chapter is based on an article that is under review for possible publication in the journal *Polymer Composites*.

Foreword

This chapter covers a novel fabrication method that combines a nanoparticle spraying process with nanoparticle/epoxy mixture to incorporate nanoparticles for enhancement of mechanical properties of laminated multiscale epoxy composites. Several graphene-based nanomaterials including graphene oxide, reduced graphene oxide, graphene nanoplatelets, and multi-walled carbon nanotubes are employed to modify the epoxy matrix and the surface of glass fibers. The morphological, rheological, and mechanical properties of the glass fiber-reinforced multiscale composites are investigated.

Simultaneous reinforcement of matrix and fibers for enhancement of mechanical properties of graphene-modified laminated composites

M. Rafiee [a], F. Nitzsche[b], J. Laliberte[b], J. Thibault[c], M. R. Labrosse[a]

[a] *Department of Mechanical Engineering, University of Ottawa, 161 Louis Pasteur, Ottawa, ON K1N 6N5, Canada*

[b] *Department of Mechanical and Aerospace Engineering, Carleton University, 1125 Colonel By Drive, Ottawa, ON K1S 5B6, Canada*

[c] *Department of Chemical Engineering, University of Ottawa, 161 Louis Pasteur, Ottawa, ON K1N 6N5, Canada*

Abstract

Fiber and matrix-dominant properties of fiber-reinforced polymer composites are important in many structural applications. Pre-mixing the polymer matrix with nanoparticles could enhance the through-thickness or matrix-dominant properties. Surface treatment of fiber reinforcements with nanoparticles, on the other hand, could improve the in-plane or fiber-dominated properties of laminated composites, as well as interfacial adhesion. In this paper, a novel low cost manufacturing method, combining surface treatment of fibers with matrix modification techniques, was devised to incorporate nanoparticles for the simultaneous reinforcement of matrix and fibers without increasing the viscosity of the epoxy matrix. Several graphene-based nanomaterials, including graphene oxide (GO) and its thermally reduced version (rGO), graphene nanoplatelets (GNPs), and multi-walled carbon nanotubes (MWCNTs) were employed to modify the epoxy matrix and the surface of glass fibers. Unmodified and modified epoxy and fibers were used for fabricating multiscale glass fiber-reinforced composites following the vacuum-assisted resin transfer molding (VARTM) process. The composites obtained combined improvements in both the fiber and matrix-dominant properties, resulting in superior composites. We investigated the morphological,

rheological and mechanical properties of the glass fiber-reinforced multiscale composites. The results from testing for tensile properties and interlaminar shear strength (ILSS) of the glass fiber reinforced composites indicates that the introduction of graphene nanoplatelets, graphene oxide, reduced-graphene oxide, and multi-walled carbon nanotubes enhanced mechanical properties. In particular, addition of 0.1, 1 and 0.01 wt.% of graphene nanoplatelets, graphene oxide, and reduced-graphene oxide leads to 6.8, 14.6 and 8.2% improvement in ultimate load capacity of the glass fiber reinforced composite, respectively. Compared with the control neat epoxy/fiberglass composite, the average ILSS value of multiscale nanocomposites increases up to 15.4, 8.9, 13.3 and 10.7% with 0.15, 0.2,1.0 and 0.042 wt.% of MWCNTs, GNP, GO and rGO, respectively. The fracture surfaces of the fiber-reinforced composites were examined by scanning electron microscopy (SEM) and we used the micrographs to explain the tensile and ILSS results.

Keywords: polymer composite; graphene nanoplatelets, graphene oxide, multiscale nanocomposite, matrix and fiber treatment.

7.1 Introduction

There is a need for developing new manufacturing methods to fabricate polymer resins enhanced with carbon nanomaterials for applications where weight, stiffness and strength are critical, and to assess the nanoparticle reinforcement achieved compared to conventional laminates such as glass fiber and carbon fiber reinforced polymer composites. Multiscale nanocomposites are a novel class of multifunctional composite materials that have received special attention because of their improved properties at very low loading levels compared with conventional filler composites [1,4–6]. While conventional polymer composite materials reinforced by continuous fibers are strong in in-plane direction, they are usually weak against matrix-dominated failures. Graphene nanomaterials such as single- and multi-walled carbon nanotubes (SWCNTs and MWCNTs), graphene nanoplatelets (GNPs), graphene oxide (GO) and reduced-graphene oxide (rGO) are light nano-sized small materials with excellent thermo-electro-mechanical properties. When conventional fiber-reinforced laminates are modified with graphene nanomaterials, new materials with improved mechanical, thermal and electrical properties may be developed [1,4–8]. Carbon nanotubes are an allotrope of sp2 hybridized carbon with one or several tubes in concentric cylinders. GNPs are composed of several layers of graphene and are considered as smart reinforcing fillers [4,9]. GNPs' properties can be influenced by their manufacturing methods.

GNPs were also observed as a probable substitute to carbon nanotube in terms of cost and better targeted properties [10]. Graphene oxide is a compound of carbon, oxygen, and hydrogen in variable ratios. It can be synthesized by exfoliating layered graphite oxide (graphite with strong oxidizers) [11,12]. GO does not require functionalization as it consists of graphene sheets with hydroxyl, carboxyl, and epoxide groups. Reduced-graphene oxide (rGO) can be obtained as a powder form by reducing GO using several methods such as microwave, laser, electrochemical, or hydrazine vapor treatment.

Typical manufacturing methods to fabricate laminates composite parts are vacuum-assisted resin transfer molding (VARTM) [6,56], autoclave molding [6], compression molding (including hot pressing) and hand lay-up [57]. A review of some of the techniques for manufacturing of multiscale composite and challenges can be found in the work of McCrary-Dennis and Micah [6]. Due to minimal pressures, ambient temperature and low-cost tooling involved, VARTM is the method of choice for large, complex parts like boat hulls or large transportation parts like bus bodies. Fiber reinforcements are placed in a one-sided mold, like fiberglass, metal or even wood, and the layup is sealed using vacuum bagging materials to create a vacuum-tight seal. Resin is infused into the fiber reinforcements (preform) at strategically-placed ports and is drawn by the vacuum pump throughout the layup.

Pre-mixing the polymer matrix with nanoparticles could enhance the through-thickness or matrix-dominant properties [8,52]. In pre-mixed polymer infusion, nanoparticles are initially dispersed in the resin to form a nanoparticle-resin mixture that is then infused into the preform to manufacture the final composite part. The limitations of this approach arise from agglomeration, self-filtration and viscosity issues. For instance, at CNT loadings higher than 0.075% wt.% of epoxy, high viscosity of the mixture does not allow the resin to be infused throughout the fabrics and leads to self-filtration. Filtration effects can be minimized by using low loading fractions (generally <0.1 wt.% of epoxy matrix) and short CNTs (generally <1 μm); however, these approaches, in turn, reduce the potential for significant mechanical reinforcement.

Surface treatment of fiber reinforcements with nanoparticles, on the other hand, could improve the in-plane, fiber-dominant properties of laminated composites as well as interfacial adhesion. Some examples of surface treatment are chemical grafting [58], electrochemical method [59,60], plasma treatment [61], and sizing method [62,63]. Surface treatment allows for higher loadings of nanoparticles and alleviates the problem of agglomeration commonly observed when nanoparticles are freely dispersed in a matrix. However, matrix-dominant properties such as structural damping could not be improved with this approach.

A review of the literature reveals that multiscale fiber reinforced composites are manufactured by either modifying the resin matrix or the fiber reinforcement. While the simultaneous enhancement of fiber and matrix could benefit the material properties of laminated composites, to the best of authors' knowledge, no study has considered the manufacture and assessment of the mechanical properties of hierarchical multiscale laminated composites produced following such an approach.

In this paper, we investigate the processing, fabrication and characterization of graphene nanomaterials-modified fiberglass/epoxy composites. A novel method combing spraying and nanoparticle-resin mixture techniques was devised to incorporate different nanoparticles for simultaneous reinforcement of matrix and fibers without increasing the viscosity of the epoxy matrix. Several panels were manufactured using the VARTM method incorporating carbon nanomaterials. The mechanical, and rheological and morphological characteristics of the resulting multiscale hierarchical composites were studied experimentally.

7.2 Materials, processing and fabrication

7.2.1 Materials

The pristine and amino-functionalized graphene nanoplatelets (p-GNPs and f-GNPs) were obtained from Cheap Tubes Inc., U.S.A. They were made by exfoliating graphite down to 5-15 atomic layers and featured an average thickness and diameter of 1.5 nm and 5 µm, respectively. Their bulk density was 0.21 g/cm^3. The single layer graphene oxide (GO) with bulk density of 1 g/cm^3 was received in the form of powder from Abalonyx, Norway. Reduced graphene oxide (rGO) produced by thermal reduction of graphene oxide was also obtained from Abalonyx, Norway. The rGO had a carbon content of about 86 % atomic or about 82 wt.% and its bulk density was 0.01 g/cm^3. The pristine multi-wall carbon nanotubes (NC7000-MWCNTs) were obtained from Nanocyl S.A., Belgium. They featured an average diameter and length of 9.5 nm and 1.5 µm, respectively. The unidirectional E-glass fabrics with an average fiber diameter of 20 µm was provided by NMG, China. The low viscosity diglycidyl ether of bisphenol-A (DGEBA) epoxy resin PT-2712 Part A and the diethyltoluenediamine (DETDA) curing agent PT-2712 Part B1 were produced by PTM&W Industries, Inc., USA. Epoxy resin Part A and B mixing weight ratio was 100:22 as per manufacturer recommendation. The typical material properties for the materials used in this study are listed in Table 1.

Table 7-1. Typical material properties for the materials used in this study.

Source	Symbol	Value	Unit	Description
Graphene nanoplatelets				
	h	1.5×10^{-9}	m	Average thickness of graphene nanoplatelets
	d	5×10^{-6}	m	Average diameter of graphene nanoplatelets
	w^{GNP}	1	%	Weight percentage of graphene nanoplatelets
	ρ^{GNP}	1062.5	kg/m^3	Mass density of graphene nanoplatelets
	E_{11}^{GNP}	1×10^{12}	kg/m^2	Young's modulus of graphene nanoplatelets
Epoxy resin polymer matrix (Part A+ Part B) [54]				
	ρ^{ER}	1080	kg/m^3	Mass density of epoxy resin matrix
	E^{ER}	19.251×10^{9}	kg/m^2	Young's modulus of epoxy resin matrix
	α^{ER}	9.756×10^{-5}	1/K	Thermal expansion coefficient of epoxy resin matrix

7.2.2 Processing and fabrication of multiscale nanocomposites

7.2.2.1 Two-phase epoxy/nanoparticle composites

The two-phase polymer matrix composites modified with MWCNTs, GNPs, GO and rGO were prepared with different loadings of nanoparticles as indicated in Table 2. The nanoparticle loadings were calculated with respect to epoxy (DGEBA), epoxy and hardener (DGEBA+DETDA), and total fiber reinforced composite. Fig. 1 shows a schematic of the method for the preparation of the multiscale nanocomposites. As mentioned in the Introduction section, when manufacturing nanocomposite laminates by VARTM, a filtration effect was observed for CNTs loading higher than 0.075 wt.% of DGEBA. Therefore, part of the nanoparticle/acetone mixture was used for sizing of fabrics while the rest of the mixture was kept for preparation of the infusion epoxy as indicated in Fig. 2. Table 3 lists the different loadings of carbon nanomaterials that were sprayed on fabrics as well as the percentage that was used for infusion of the epoxy.

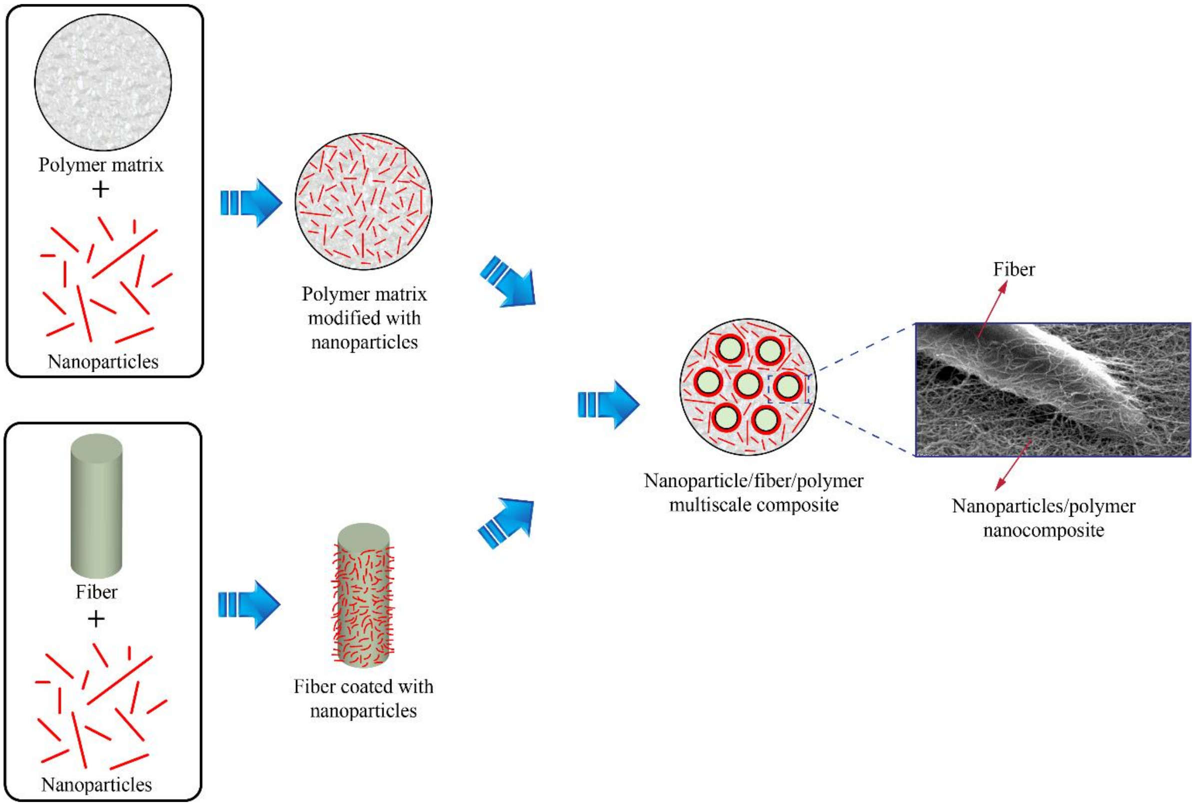

Fig. 7-1. New route for fabricating multiscale nanocomposite.

Table 7-2. Loadings of nanoparticle used for modification of fiberglass/epoxy composites.

	wt% of DGEBA	vol.% of DGEBA	wt% of matrix (DGEBA+ DETDA)	vol.% of matrix (DGEBA+ DETDA)	wt% of total (DGEBA+ DETDA+ fibers)	vol.% of total (DGEBA+ DETDA+fibers)
MWCNT	0.075	1.38	0.06	1.1	0.02	0.55
	0.15	2.75	0.12	2.2	0.04	1.1
	0.3	5.5	0.25	4.4	0.07	2.2
GNP	0.1	0.55	0.08	0.44	0.02	0.22
	0.2	1.1	0.16	0.88	0.05	0.44
	0.4	2.2	0.33	1.76	0.1	0.88
	1	5.5	0.82	4.4	0.25	2.2
GO	1	1.1	0.82	0.88	0.25	0.44
	2	2.2	1.64	1.76	0.5	0.88
rGO	0.01	1.1	0.008	0.88	0.002	0.44
	0.03	3.3	0.025	2.64	0.007	1.32
	0.042	4.6	0.034	3.7	0.010	1.85

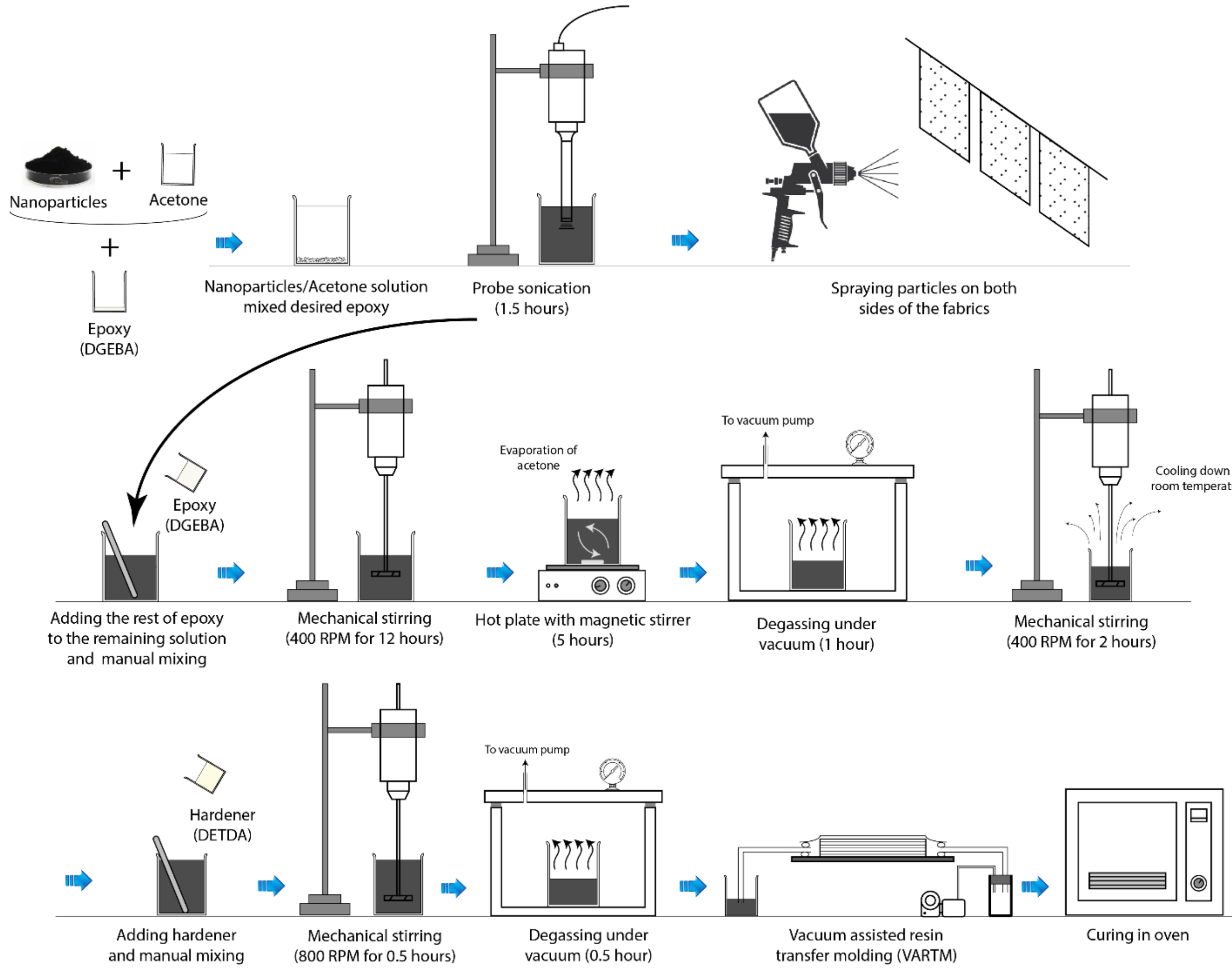

Fig. 7-2. Fabrication process of multiscale fiber glass/epoxy composites modified with graphene-based nanoparticles.

The nanoparticles were dispersed at a concentration of one gram of nanoparticles per liter of acetone. For the sizing of fabrics, the nanoparticle/acetone mixture was mixed with the desired amount of epoxy (See Table 3) and then was sonicated using an ultrasonic probe (Q700 Sonicator, Qsonica LLC, USA) for half an hour. To avoid any adverse high temperature effects, sonication was performed by 20-sec ON pulses followed by 10-sec OFF cycles. The desired amount of mixture was used for the sizing of fibers via a spraying process. The ratio of epoxy per square meter of fabrics (both fabric sides) was 14. A laboratory mixer stirred the remainder of the mixture at 400 rpm for 12 hours to ensure good dispersion of nanoparticles in the epoxy resin. After this step, the mixture was placed on a magnetic hot plate stirrer, using a Teflon-coated magnetic bar, to mix the solution for 4 hours at 70°C. The objective was to remove the acetone by evaporation. To ensure the complete removal of acetone, the mixture was placed in a vacuum chamber for 30 minutes. The slurry of epoxy resin DGEBA and GNPs was allowed to cool to room temperature before the curing agent was added, to avoid premature curing during mixing. Low viscosity curing agent DETDA was added to give a curing agent to resin ratio of 22:100. The mixture was mixed at 800 rpm for 30 minutes using a mechanical stirrer with stainless steel axial impeller. The mixture was degassed in a vacuum chamber at ambient temperature for about 30 minutes. The mixture was used as an infusion epoxy for manufacturing of laminates, which is explained in the next section.

Table 7-3. Weight and volume percentile of nanoparticle used for spray process and infusion of fiber-glass/epoxy composites.

	wt.% of DGEBA	vol.% of DGEBA	Sprayed vol. %	Infusion vol.%
MWCNT	0.075	1.38	0.69	0.69
	0.15	2.75	1.37	1.38
	0.3	5.5	4.12	1.38
GNP	0.1	0.55	0.275	0.275
	0.2	1.1	0.55	0.55
	0.4	2.2	1.1	1.1
	1	5.5	4.4	1.1
GO	1	1.1	0.55	0.55
	2	2.2	1.1	1.1
rGO	0.01	1.1	0.55	0.55
	0.03	3.3	2.2	1.1
	0.042	4.6	3.5	1.1

7.2.2.2 Three-phase laminated composites

We fabricated multiscale fiber reinforced laminated composites with the nanoparticle-filled epoxy resin through a VARTM process. The reinforcement was three layers of unidirectional glass fabrics in cross ply form [0°,90°,0°] where 0° was the main direction of testing.

After the infusion of the nanoparticle/epoxy dispersions, the laminates were cured at room temperature for 15 hours. A post curing step was then performed where the temperature of the laminates was ramped at a rate of 1°C/min, held constant every 20°C for an hour, then continuing until a final hold of three hours at 100°C to remove the possible thermal history. The vacuum bagging system combined with the two-stage degassing process can achieve a low void content for thermoset composites. The composite coupons were 1.9 ± 0.1 mm in thickness, and cut by water jet for testing.

The fiber volume fraction, V_f, for each laminate configuration, was calculated in accordance with ASTM D 3171 as

$$V_f = \frac{A_w \times N}{\rho_f \times h} \tag{1}$$

where A_w is the fabric areal weight, N is the number of plies, ρ_f is the fiber density and h is the laminate thickness. The approximate calculated values of E-glass fibers volume and weight fractions were 50% and 70%, respectively.

7.3 Characterization

7.3.1 Morphology

The morphology of nanoparticles, as well as two-phase and three-phase composites were observed through A ZEISS (AX10 model) optical microscopy. Since the dispersion of CNTs in epoxy resin is unstable at different times and temperatures, the optical images were taken at a specific time and temperature (120 minutes and room temperature in this case) after finishing the process of mixing MWCNTs/acetone with DGEBA. The dispersion of the carbon nanoparticles was also investigated by TECNAI Spirit transmission electron microscopy (TEM) operated at 120 kV. The analysis of fracture surfaces was done using Zeiss EVO10 SEM scanning electron microscope (SEM) at 5kV accelerating voltage.

7.3.2 Rheology

Several tests were also performed to investigate the rheological behavior of the epoxy resin (DGEBA) containing different loading of nanoparticles. Experiments were carried out on a rotational rheometer (MCR 301) from Anton Paar Inc. Steady shear tests were performed to measure the viscosity over the range of shear rates between 0.1 to 100 s^{-1}. All rheological measurements were carried out at room temperature.

7.3.3 Mechanical properties

7.3.3.1 Tensile test

The tensile tests were carried out using an Instron 4482 mechanical testing machine with a calibrated 100 kN load cell at a crosshead speed of 1 mm/min according to ASTM D3039. The overall dimension of the tensile specimens were 150 x 25 x 3 mm^3. An Advanced Video Extensometer was used to measure the strain of the specimens. Blue Hill 2 software was used to run the tests, acquire and process the data to obtain the tensile properties. Five specimens of each type of material were tested.

7.3.3.2 Short beam shear test

Interlaminar shear strength (ILSS) was determined by short beam shear (SBS) test according to ASTM D2344. SBS tests were carried out on an Instron 4482 test machine at room temperature with a cross-head speed of 1 mm/min. The specimens were prepared with outer dimensions of 3 mm × 6 mm × 24 mm and a span of 18 mm. Five specimens of each material type were tested. Interlaminar shear strength was calculated by $0.75P_m/(bh)$ where P_m is the maximum load observed during the test in Newtons, and b and h are the measured specimen width and thickness in millimeters, respectively.

7.4 Results and discussion

7.4.1 Morphology of nanoparticles, epoxy and fibers

7.4.1.1 TEM micrographs

Fig. 3 (a–h) present TEM micrographs of materials fabricated in this investigation: (a-b) MWCNTs, (c-d) GNPs, (e-f) Go, and (g-h) rGO. Occasional localizations of carbon nanotubes and graphene aggregates can be observed in the TEM images, which suggest the existence of van der Waals forces and interactions between GNPs, GO and rGO sheets.

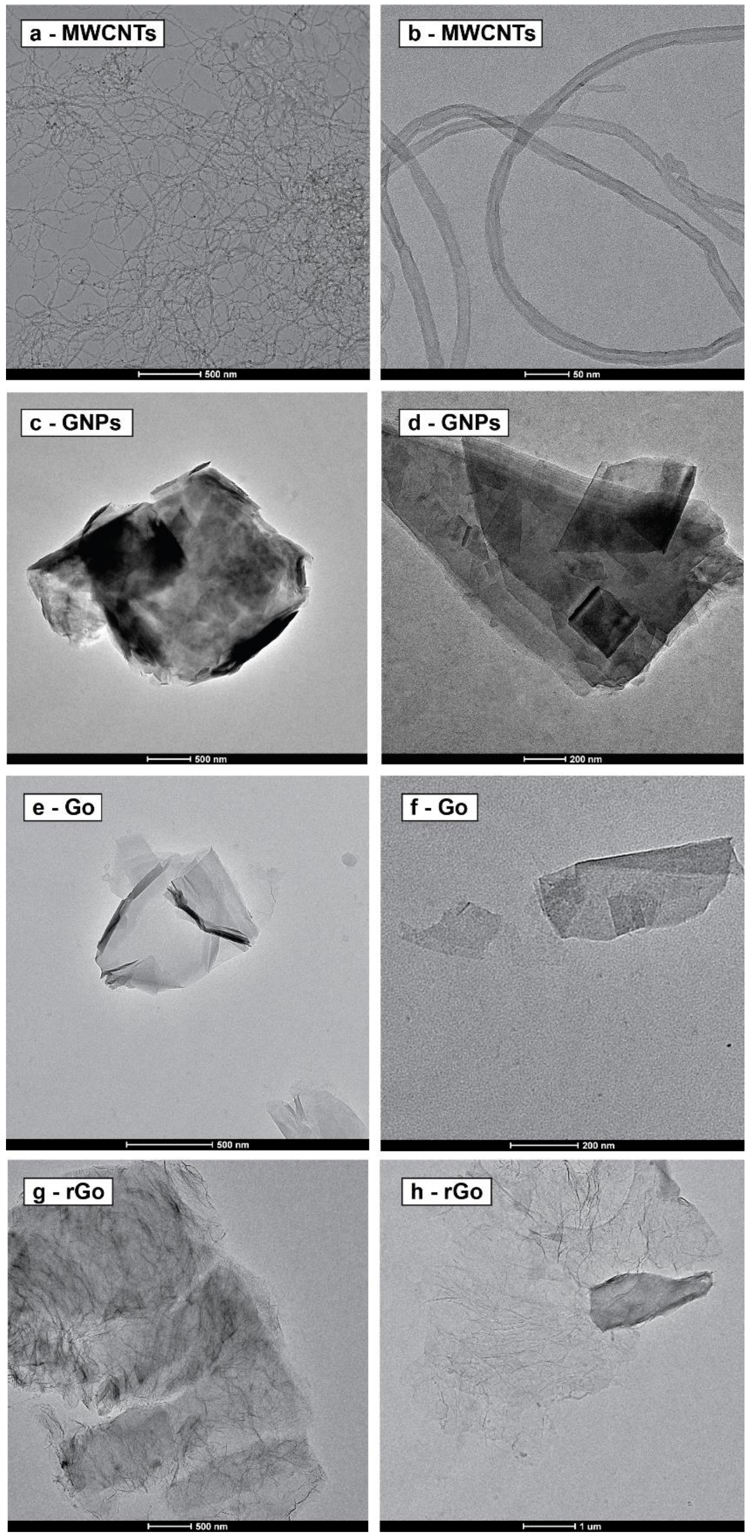

Fig. 7-3. TEM images of nanoparticles: (a-b) MWCNTs, (c-d) GNPs, (e-f) GO, and (g-h) rGO.

7.4.1.2 Optical micrographs

Fig. 4 shows the optical micrographs of GNPs and MWCNTs dispersed in epoxy matrix. Optical micrographs were obtained at different magnification levels for the nanoparticle/epoxy suspensions. Micrographs for the GNP/epoxy suspensions (Fig. 4 a-b) show relatively homogenous distributed aggregates due to favorable GNP interactions with the epoxy matrix [64]. At high magnification, the presence of large size GNP aggregates can be observed, primarily due to van der Waals forces and strong π–π interactions between the GNP sheets [65]. By contrast, the MWCNTs/epoxy suspensions (Fig. 4 c-d) show more loosely packed isolated aggregates of carbon nanotubes, resulting in a relatively inhomogeneous suspension. Such aggregates form due to CNT unfavorable interactions with the epoxy matrix [66] and van der Waals attraction forces between the CNTs.

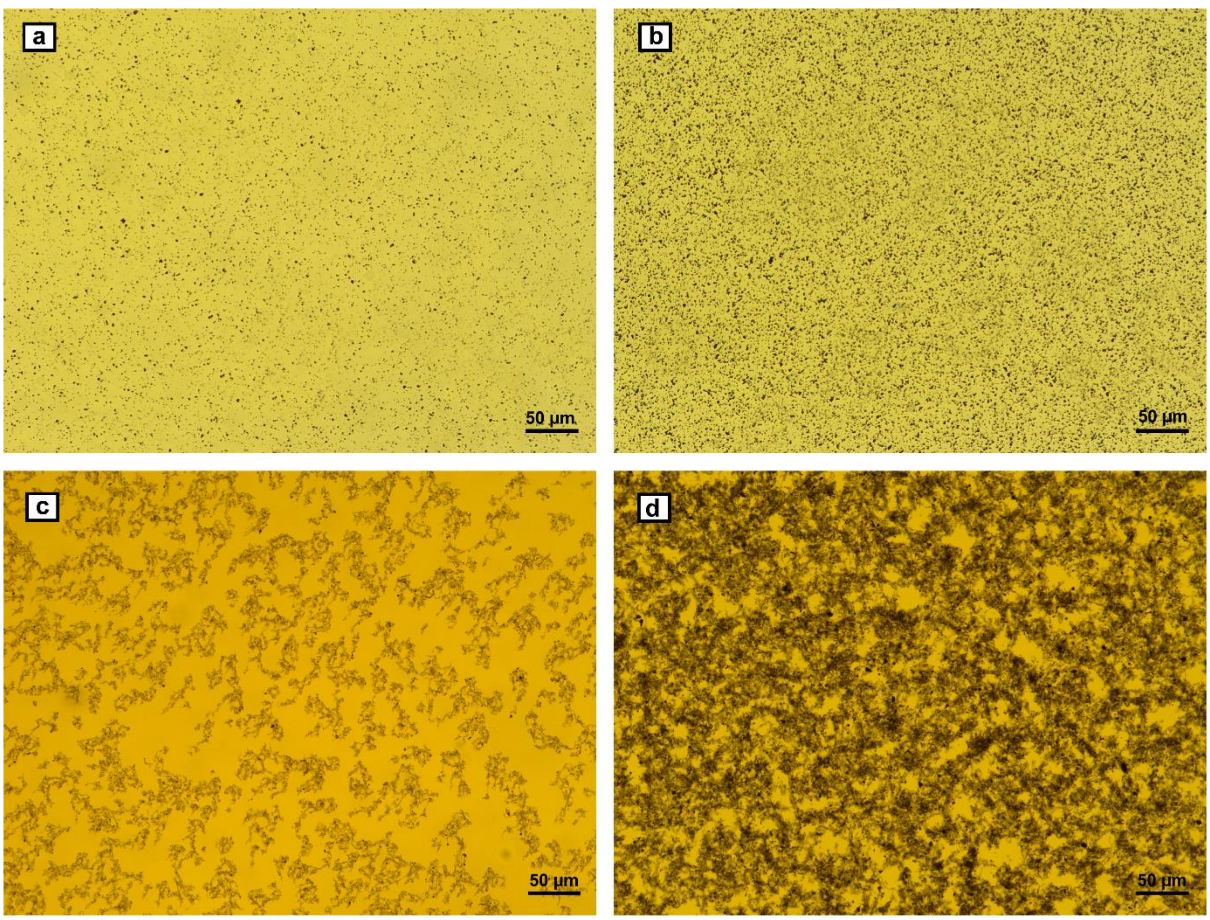

Fig. 7-4. Optical micrograph of (a) GNPs 0.2%, (b) GNPs 1.2%, (c) MWCNTs 0.075%, and (d) MWCNTs 0.3% in DGEBA.

7.4.1.3 SEM micrographs

The surface morphology of glass fibers coated with nanoparticles at different magnifications was observed by SEM. Fig. 5 shows the SEM micrographs of rGO-coated glass fibers at different magnifications. As can be seen from these images, the coverage of nanoparticles coating is uniform on the outer layer yarns.

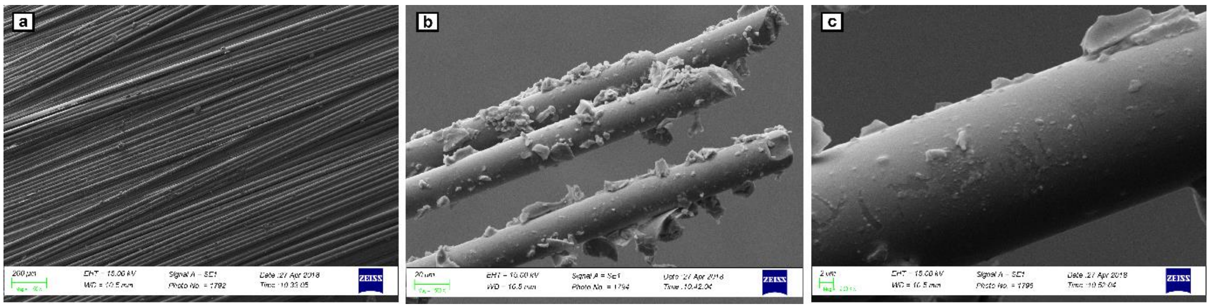

Fig. 7-5. SEM micrographs of fiber surfaces coated with nanoparticles (rGO) at different magnifications: (a) 50, (b) 500 and (c) 2000X.

7.4.2 Viscosity

Steady shear viscosity of nanoparticles/epoxy dispersion was investigated to determine the impact of nanoparticle loading. Fig. 7-6 shows the variations in the steady shear viscosity with shear rate for neat epoxy and nanoparticle/epoxy dispersions. The steady shear viscosity profile for both MWCNTs and GNPs demonstrated a shear-thinning (shear viscosity decreases sharply with increasing the shear rate) behavior, which is an important non-Newtonian fluid phenomenon. This phenomenon is more obvious for functionalized nanoparticles than pristine ones. Besides, MWCNTs exhibited stronger non-Newtonian behavior than the other nanoparticles considered. The viscosity versus shear rate curve for the p-MWCNTs/epoxy and f-MWCNTs dispersions (Fig. 7-6 a-b) with content beyond 0.075 wt.% suggest that they would be problematic to use as nanocomposite matrix for VARTM manufacturing process. Indeed, at MWCNT loadings higher than 0.075 wt.% of epoxy, high viscosity of the mixture does not allow the resin to be infused throughout the fabrics and leads to self-filtration. The results from GNPs viscosity confirmed that at least to loadings up to 1.2 wt% of DGEBA, pristine and functionalized GNPs can be used for infusion-based manufacturing methods such as VARTM. Similar to GNPs, GO and rGO are expected to have lower viscosities for the same vol. % of nanoparticles.

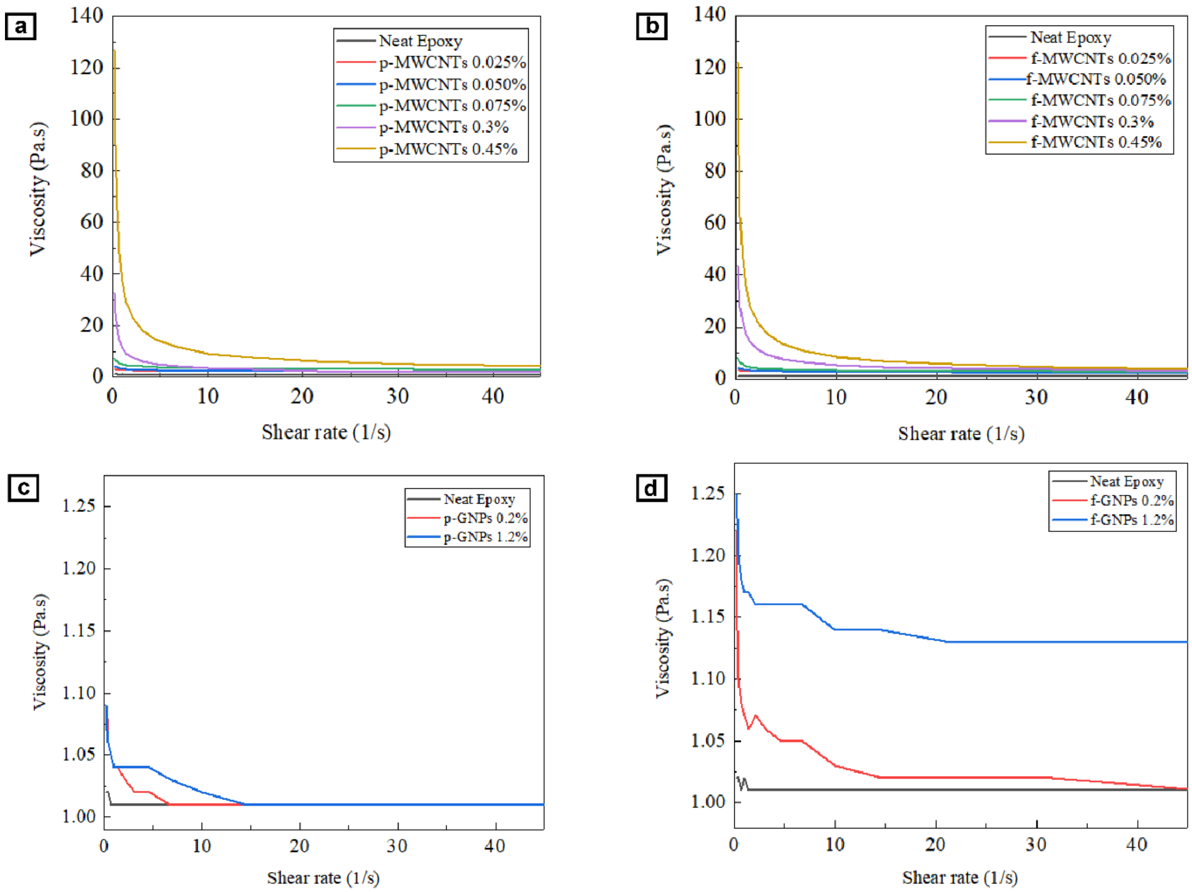

Fig. 7-6. Steady shear viscosity of nanoparticle/epoxy dispersion as a function of shear rate.

For pure epoxy resin, which is a Newtonian fluid, the viscosity value was almost equal to 1 Pa.s and the observed shear-thinning behavior from the nanoparticle/epoxy mixture was caused by the break-down of the percolated structure. The viscosity increased as the concentration of nanoparticles increased. The space between nanoparticles decreased, reducing the mobility and increasing the dispersion's resistance to flow. Fig. 6 a-d reveals that the increase was more pronounced at lower shear rates than that at higher shear rates. The noticeable shear thinning effect was also nanoparticle loading-dependent. The gap in viscosities between different nanoparticle concentrations narrowed dramatically as shear rate increased.

7.4.3 *Tensile characteristics*

7.4.3.1 *Morphology*

The morphology of fiber pullout on the fracture surface of fiberglass/epoxy composites was observed after the tensile tests to investigate the quality of interfacial bonding. In Fig. 7 a, a glass fiber was pulled out from the neat epoxy matrix and very little epoxy resin matrix remained on the surface of the fiber. The edge of holes left by the fiber pullout was round and the sidewall was smooth, indicating that stresses did not uniformly transfer between carbon fibers and the resin matrix under tensile load. By contrast, in Fig. 7 b, it can be observed that there were no gaps between the graphene-coated glass fibers and the epoxy matrix containing nanoparticle reinforcements, suggesting a strong interfacial bound between fibers and matrix. The more cohesive structure could help to increase the absorption of rupture energy and achieve an effective load transfer between fiber and polymer matrix. The edges of holes were irregular and the sidewalls were rough, indicating the destruction of the resin matrix around the fibers due to the improved interfacial cohesion after adding the nanoparticle reinforcements.

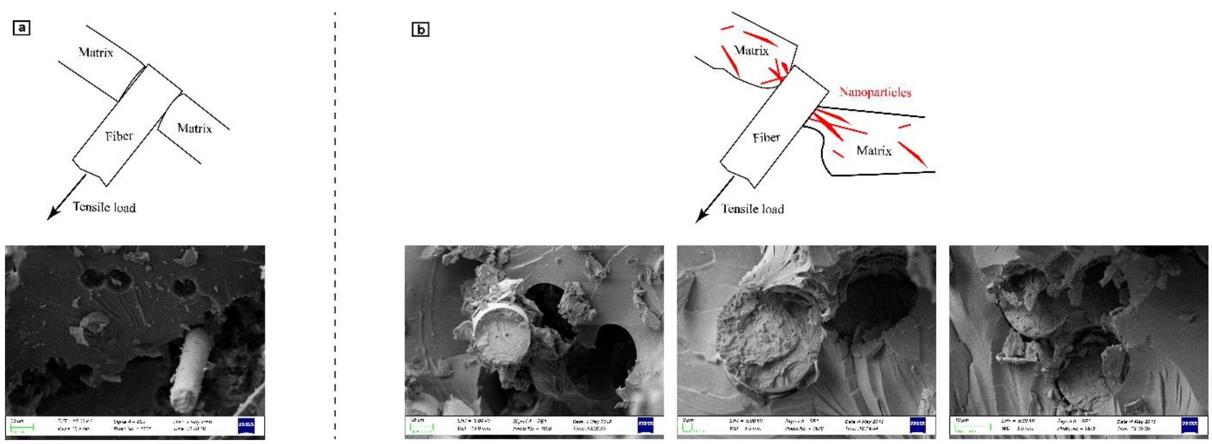

Fig. 7-7. SEM images of the failure surface with the hole left by the fiber pullout in composite specimens after tensile test: (a) fractured conventional glass fiber/ neat epoxy composite; (b) fractured nanoparticle-sized glass fiber in nanocomposite epoxy composite; The top insets show simplified models for the anchoring effect of nanoparticle reinforcements at the interface under tensile load.

7.4.3.2 Tensile properties

Figs. 8 through 11 show the tensile test results of graphene-coated glass fiber composites with different epoxy matrices. The ultimate tensile load capacity and elongation of nanocomposite beams reinforced with graphene nanoplatelets, graphene oxide, and reduced-graphene oxide are shown in Fig. 8 and Fig. 9, respectively. It can be seen that the combination of glass fiber/neat epoxy exhibited a tensile load capacity of 8.63±0.9 kN, while the nanocomposite specimens modified with graphene nanoparticles exhibited higher load capacities, indicating improved ultimate tensile load capacities of nanocomposite specimens. For instance, nanocomposite beams reinforced with 0.1 wt.% of graphene nanoplatelets underwent 9.22±0.48 kN before failure, which indicates an enhancement of 6.8%. Likewise, specimens with 1 wt. % of GO and 0.01 wt.% of rGO exhibited 14.6% and 8.2% improvements in ultimate load capacity, respectively.

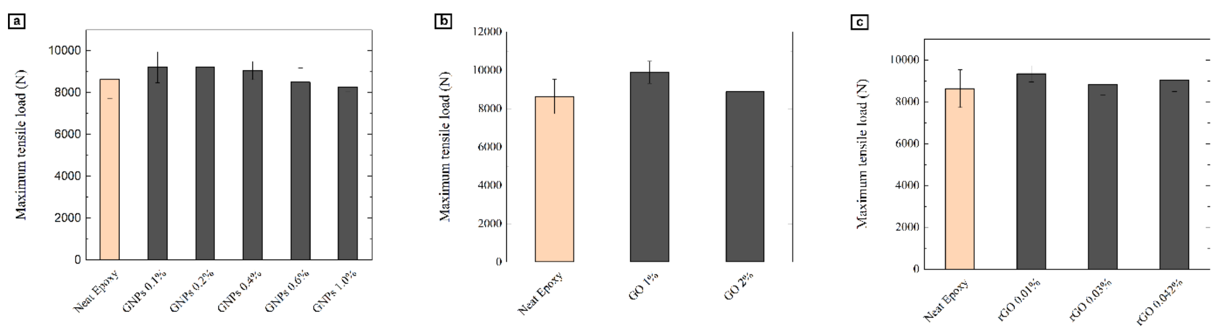

Fig. 7-8. Ultimate tensile load capacity of nanocomposite beams reinforced with (a) graphene nanoplatelets (GNP), (b) graphene oxide (GO), and (c) reduced-graphene oxide (rGO)

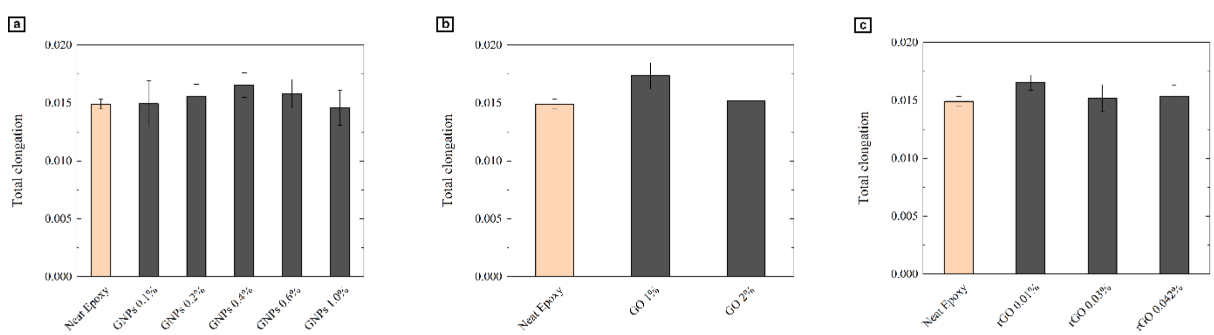

Fig. 7-9. Total elongation (ultimate total strain) of nanocomposite beams reinforced (a) graphene nanoplatelets (GNP), (b) graphene oxide (GO), and (c) reduced-graphene oxide (rGO)

Fig. 9 shows an increase in elongation at break (ultimate strain) of nanocomposite specimens at lower nanoparticle loadings. The enhancement in the tensile load capacity may be due to strong bonding between the epoxy matrix and graphene nanoparticles, which leads to good dispersion of nanoparticles in the nanocomposites. These well-dispersed nanoparticles may serve as physical cross-linking points, and thus increase the tensile properties. A good interfacial bonding between the nanoparticles and the epoxy is quite vital for a material to withstand stresses. Under tensile load, the matrix distributes stresses to the nanoparticles which carry most of the applied load. When the concentration (loading) of nanoparticles is higher than the optimum amount, the nanoparticles cannot disperse well in the epoxy matrix and agglomerate into big clusters because of the surface energy of nanoparticles, causing a decrease in load capacity and elongation. It is an indicator of the material flexibility, which shows that the inclusion of nanoparticles makes the epoxy stronger but more brittle.

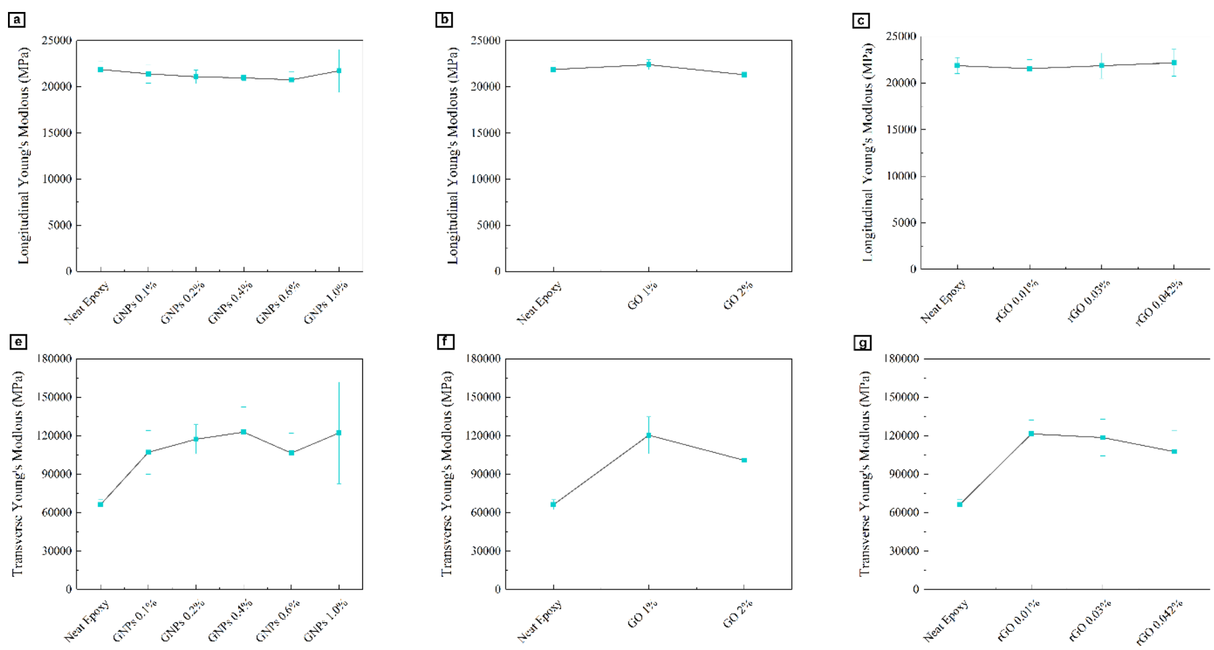

Fig. 7-10. Longitudinal (a-c) and transverse (e-g) tensile moduli of nanocomposite beams reinforced with (a,e) pristine graphene nanoplatelets (GNPs), (b,f) graphene oxide (GO) and (c,g) reduced graphene oxide (rGO).

Tensile and tensile chord moduli of elasticity and Poisson's ratio of nanocomposite coupons for different nanoparticle content are presented in Figs. 10-11 and Table 4. The longitudinal modulus (Young's modulus) remained almost unchanged for the loadings of nanoparticles studied in this investigation. The longitudinal modulus of the composite laminates in the direction of the unidirectional carbon fibers is a fiber-dominated property. There is a large difference between the matrix properties and fiber properties, and thus, a slight improvement in matrix property had no visible effect on the overall laminate longitudinal modulus. It is worth mentioning that a significant volume fraction of glass fibers (68% of total fibers) were aligned in the longitudinal direction.

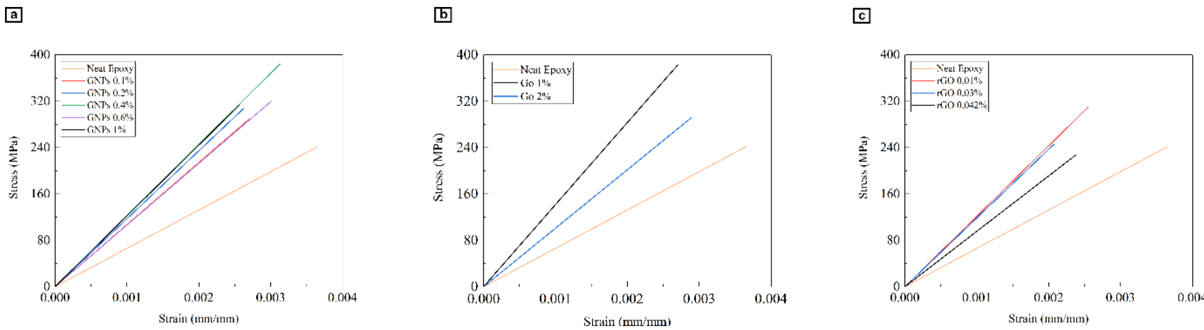

Fig. 7-11. Transverse stress-strain curves of nanocomposite beams reinforced with (a) graphene nanoplatelets (GNP), (b) graphene oxide (GO), and (c) reduced-graphene oxide (rGO)

On the other hand, the tensile chord modulus of elasticity showed significant improvement. The higher weight fraction of nanoparticles exhibited the greatest improvement. The best results were obtained when 1 wt.% GNPs, 1 wt.% GO and 0.01 wt.% rGO were present throughout the composites. The improvement in tensile chord modulus of elasticity was about 85.7%, 82.0% and 83.6% for specimens associated with the three weight fractions, respectively. The numerical values of tensile and tensile chord moduli of elasticity and Poisson's ratio are shown in Table 4.

Table 7-4. Effective tensile material properties of nanocomposite specimens for different nanoparticle content (Tensile and tensile chord moduli of elasticity and Poisson's ratio)

Material	Effective material properties		
	Tensile modulus of elasticity (E_{11eff}) ×10^9	Tensile chord modulus of elasticity (E^{Chord}) ×10^9	Poisson ratio (υ_{eff})
Neat epoxy/fiber	21.86±0.86	66.14±3.89	0.33±0.00
GNPs0.1%/epoxy/fiber	21.39±1.00 [-2.1%]*	107.08±17.01 [61.9%]	0.20 [-39.5%]
GNPs0.2%/epoxy/fiber	21.06±0.73 [-3.6%]	117.22±11.40 [77.2%]	0.18 [-45.7%]
GNPs0.4%/epoxy/fiber	20.96±0.27 [-4.1%]	122.79±19.53 [85.7%]	0.17 [-48.5%]
GNPs0.6%/epoxy/fiber	20.73±0.89 [-5.1%]	106.41±15.47 [60.9%]	0.19 [-41.5%]
GNPs1.0%/epoxy/fiber	21.72±2.31 [-0.6%]	122.16±39.60 [84.7%]	0.17 [-47.5%]
GO 1%/epoxy/fiber	22.38±0.54 [2.4%]	120.35±14.41 [82.0%]	0.16±0.01 [-51.3%]
GO 2%/epoxy/fiber	21.29±0.29 [-2.6%]	100.84±5.17 [52.5%]	0.21±0.01 [-35.1%]
rGO 0.01%/epoxy/fiber	21.55±0.96 [-1.4%]	121.41±10.64 [83.6%]	0.18±0.01 [-45.8%]
rGO 0.03%/epoxy/fiber	21.85±1.36 [0.0%]	118.55±14.27 [79.2%]	0.19±0.00 [-43.0%]
rGO 0.042%/epoxy/fiber	22.17±1.44 [1.4%]	107.58±16.53 [62.6%]	0.23±0.01 [-29.1%]

$$*[X\%]= [100\% \; \frac{\text{Properties}\big|_{n\%\ \text{nanoparticle}} - \text{Properties}\big|_{\text{Neat epoxy}}}{\text{Properties}\big|_{\text{Neat epoxy}}}].$$

7.4.4 Interfacial characteristics

7.4.4.1 ILSS characterization

The SEM images of the interphase regions in the nanocomposites following ILSS tests are shown in Fig. 12. It can be observed that the failure surfaces of the glass fiber composites showed different micro-morphology patterns. In Fig. 12 (a), the composites involving neat epoxy matrix were destroyed from the fiber surface during the ILSS testing due to a weak interfacial bonding, and the smooth fiber surface was exposed after material fracture. However, in Fig. 12 (b-e), with the addition of nanoparticle reinforcements, the glass fibers were well covered in the matrix after interlaminar fracture and the surface was rough.

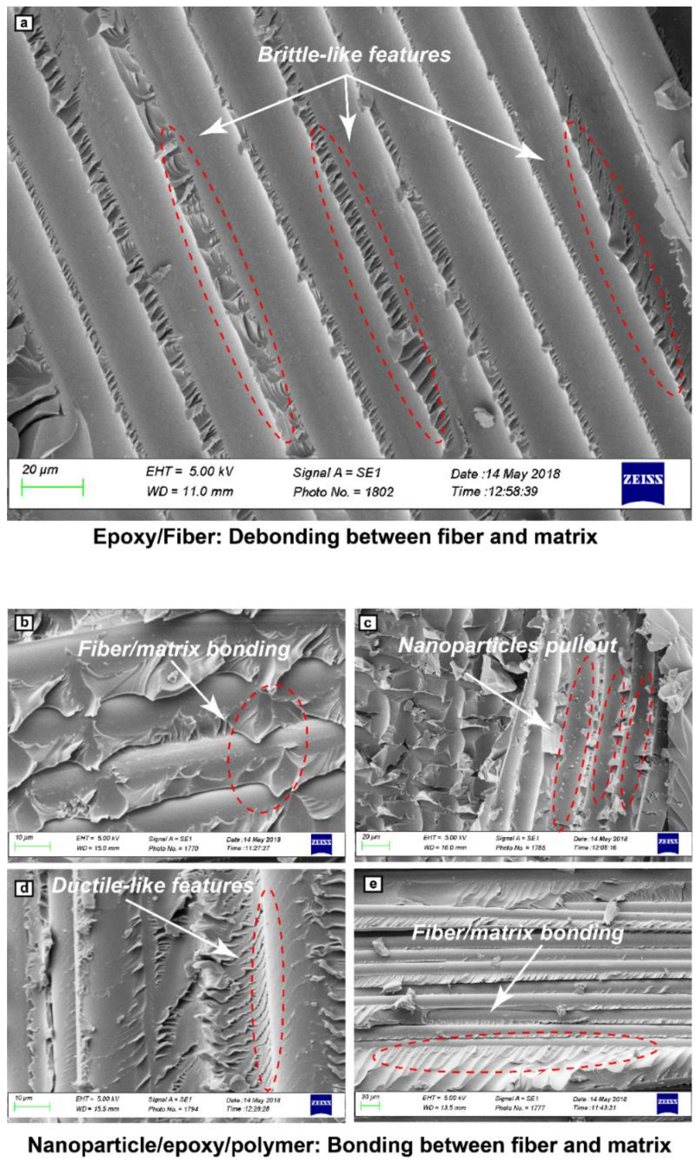

Fig. 7-12. SEM images of the interphase region in composite specimens after ILSS test: (a) glassfiber/neat epoxy composite; (b) MWCNTs-modified glassfiber/epoxy composite; (c) GNPs-modified glassfiber/epoxy composite; (d) Go-modified glassfiber/epoxy composite; and (d) rGO-modified glassfiber/epoxy composite

The influence of incorporated graphene nanomaterials on the load-deflection and interlaminar shear strength (ILSS) from Short Beam Shear (SBS) tests of glass fiber composite laminates are depicted in Figs. 13 and 14. The load-deflection curves confirm the improvements in the interlaminar shear strength of glass fiber nanocomposite laminates.

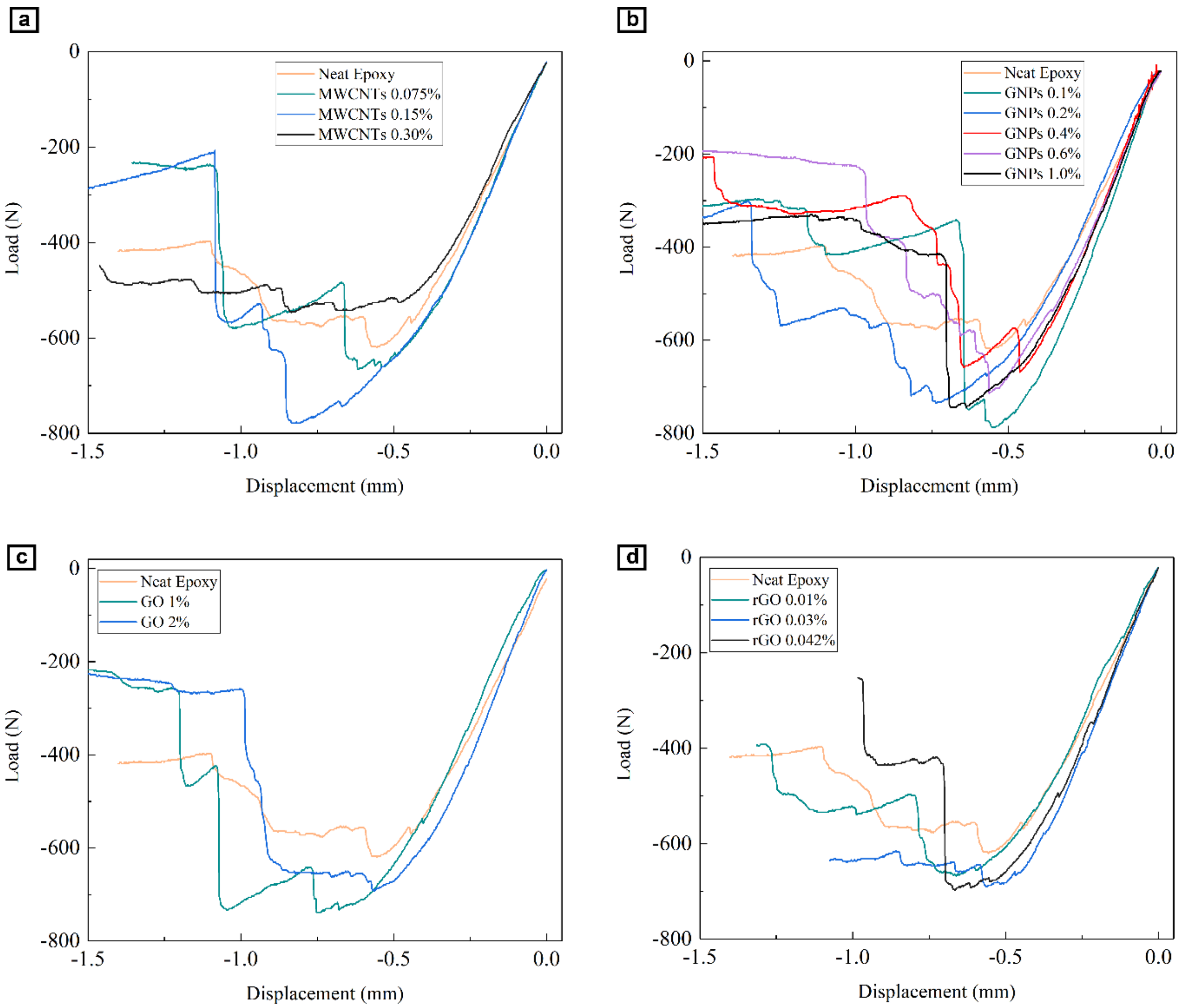

Fig. 7-13. Load-deflection curves for measurement of interlaminar shear strength (ILSS) from Short Beam Shear (SBS) test of glass fiber composite laminates modified with: (a) pristine MWCNTs, (b) graphene nanoplatelets (GNPs), (c) graphene oxide (GO), and (d) reduced-graphene oxide (rGO)

Compared with the control material, the average ILSS value of neat epoxy/fiberglass composite was 51.6 MPa and increased up to 15.4, 8.9, 13.3 and 10.7% with the 0.15, 0.2,1.0 and

0.042 wt.% of MWCNTs, GNP, GO and rGO, respectively. However, the ILSS slightly decreased with a further increase in the GO and GNP contents.

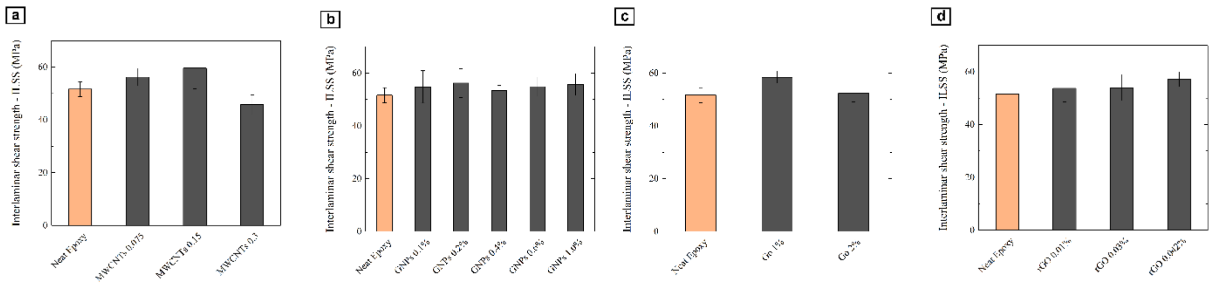

Fig. 7-14. Interlaminar shear strength (ILSS) from Short Beam Shear (SBS) test of glass fiber composite laminates modified with: (a) multi-walled carbon nanotubes (MWCNTs), (b) graphene nanoplatelets (GNP), (c) graphene oxide (GO), and (c) reduced-graphene oxide (rGO)

7.5 Conclusion

A novel fabrication method that combines the spraying process with nanoparticle-resin mixture techniques was used to incorporate nanoparticles for simultaneous reinforcement of matrix and fibers without increasing the viscosity of the epoxy matrix. Several graphene-based nanomaterials including graphene oxide, reduced graphene oxide, graphene nanoplatelets, and multi-walled carbon nanotubes were employed to modify the epoxy matrix and the surface of glass fibers. The morphological, rheological and mechanical properties of the glass fiber-reinforced multiscale composites were investigated. The shear viscosity was Newtonian for dilute suspensions, as shown by pure epoxy, and became non-Newtonian for semi-dilute suspensions, as shown by MWCNT/epoxy. The viscosity results confirmed that viscosity is a serious issue for MWCNTs/epoxy suspension as filtration of nanoparticles in VARTM process occurs with nanotube loadings higher than 0.075 wt. % of DGEBA. However, the viscosity of graphene suspension for infusion into glass fabrics did not seem to be an issue. As a result, loadings for MWCNTs in the epoxy matrix can reach up to 0.075 wt. %, and for GNP, GO and rGO, can be decided according to the intended applications. The tensile properties and interlaminar shear strength (ILSS) of the glass fiber reinforced composites was studied and the results indicated that the introduction of graphene nanoplatelets, graphene oxide, reduced-graphene oxide, and multi-walled carbon nanotubes enhanced the mechanical properties. In particular, the addition of 0.1, 1 and 0.01 wt. % of graphene nanoplatelets, graphene oxide, and reduced-graphene oxide led to 6.8, 14.6 and 8.2% improvements in ultimate load capacity of the glass fiber reinforced composite, respectively. Compared with the neat epoxy/fiberglass composite control results, the average ILSS value of multiscale nanocomposites increased by up to 15.4, 8.9, 13.3 and 10.7% with the 0.15, 0.2,1.0 and 0.042 wt.% of MWCNTs, GNP, GO and rGO, respectively. Micrographic examinations showed that the tensile loading capacity and interlaminar shear properties enhancements were most likely attributable to the improvements in resin toughness and the adhesion between glass fibers and epoxy resin being enhanced by the introduction of carbon nanoparticles.

Acknowledgements

The authors acknowledge Drs. Marianne Fenech and Mohammed Yandouzi (Department of Mechanical Engineering, University of Ottawa) for their technical supports on optical and SEM imaging. We are pleased to thank Dr. Xudong Cao (Department of Chemical and Biological Engineering, University of Ottawa) and Aaron Miller (Composites Canada, Mississauga, ON, Canada) for their great support and help during the design of experiments. Technical support from Dr. Christopher Lan and Dr. Mohammadali Baghbanzadeh (both from Department of Chemical and Biological Engineering, University of Ottawa) for probe sonication and dispersion of nanoparticles was much appreciated. The authors also acknowledge the supply of nanoparticles: MWCNTs by Nanocyl S.A. (Belgium), Cheap Tubes Inc. (U.S.A.), GO and rGO by Abalonyx (Norway). In addition, the first author gratefully acknowledges the financial support from the Ontario Trillium Scholarship (OTS), Government of Ontario and the University of Ottawa, Canada.

References

[1] M. Rafiee, F. Nitzsche, M.R. Labrosse, Modeling and mechanical analysis of multiscale fiber-reinforced graphene composites : Nonlinear bending , thermal post-buckling and large amplitude vibration, Int. J. Non. Linear. Mech. 103 (2018) 104–111. doi:10.1016/j.ijnonlinmec.2018.05.004.

[2] M. Rafiee, X.Q. He, S. Mareishi, K.M. Liew, Modeling and stress analysis of smart CNTs/fiber/polymer multiscale composite plates, Int. J. Appl. Mech. 6 (2014) 1450025. doi:10.1142/S1758825114500252.

[3] G.V. Seretis, G. Kouzilos, D.E. Manolakos, C.G. Provatidis, On the graphene nanoplatelets reinforcement of hand lay-up glass fabric/epoxy laminated composites, Compos. Part B Eng. 118 (2017) 26–32. doi:10.1016/j.compositesb.2017.03.015.

[4] M.C.L. McCrary-Dennis, O.I. Okoli, A review of multiscale composite manufacturing and challenges, J. Reinf. Plast. Compos. 31 (2012) 1687–1711. doi:10.1177/0731684412456612.

[5] D. Verma, P.C. Gope, A. Shandilya, A. Gupta, Mechanical-Thermal-Electrical and Morphological Properties of Graphene Reinforced Polymer Composites: A Review, Trans. Indian Inst. Met. 67 (2014) 803–816. doi:10.1007/s12666-014-0408-5.

[6] M. Rafiee, F. Nitzsche, M.R. Labrosse, Effect of functionalization of carbon nanotubes on vibration and damping characteristics of epoxy nanocomposites, Polym. Test. 69 (2018) 385–395.

[7] I. Mutlay, L.B. Tudoran, Percolation behavior of electrically conductive graphene nanoplatelets/polymer nanocomposites: Theory and experiment, Fullerenes Nanotub. Carbon Nanostructures. 22 (2014) 413–433. doi:10.1080/1536383X.2012.684186.

[8] F. Wang, L.T. Drzal, Y. Qin, Z. Huang, Mechanical properties and thermal conductivity of graphene nanoplatelet/epoxy composites, J. Mater. Sci. 50 (2014) 1082–1093. doi:10.1007/s10853-014-8665-6.

[9] F. Perrozzi, S. Prezioso, L. Ottaviano, Graphene oxide: from fundamentals to applications,

J. Phys. Condens. Matter. 27 (2015) 013002. doi:10.1088/0953-8984/27/1/013002.

[10] R.M. Larsen, E.A. Jensen, Epoxy-graphite oxide nanocomposites: Mechanical properties, J. Appl. Polym. Sci. 133 (2016) 4–11. doi:10.1002/app.43591.

[11] S. Advani, K.-T. Hsiao, Manufacturing techniques for polymer matrix composites (PMCs), 2012.

[12] C.H. Park, W.I. Lee, Compression molding in polymer matrix composites, Woodhead Publishing Limited, 2012. doi:10.1016/B978-0-85709-067-6.50003-1.

[13] M. Rafiee, F. Nitzsche, M.R. Labrosse, Cross-Sectional Design and Analysis of Multiscale Carbon Nanotubes-Reinforced Composite Beams and Blades, Int. J. Appl. Mech. (2018) 1850032. doi:https://doi.org/10.1142/S1758825118500321.

[14] F. Zhao, Y. Huang, Grafting of polyhedral oligomeric silsesquioxanes on a carbon fiber surface: novel coupling agents for fiber/polymer matrix composites, J. Mater. Chem. 21 (2011) 3695. doi:10.1039/c0jm03128c.

[15] H. Cao, Y. Huang, Z. Zhang, J. Sun, Uniform modification of carbon fibers surface in 3-D fabrics using intermittent electrochemical treatment, Compos. Sci. Technol. 65 (2005) 1655–1662. doi:10.1016/j.compscitech.2005.02.018.

[16] R. Samsur, V.K. Rangari, S. Jeelani, L. Zhang, Z.Y. Cheng, Fabrication of carbon nanotubes grown woven carbon fiber/epoxy composites and their electrical and mechanical properties, J. Appl. Phys. 113 (2013). doi:10.1063/1.4808105.

[17] K.K.C. Ho, A.F. Lee, A. Bismarck, Fluorination of carbon fibres in atmospheric plasma, Carbon N. Y. 45 (2007) 775–784. doi:10.1016/j.carbon.2006.11.015.

[18] Z. Dai, F. Shi, B. Zhang, M. Li, Z. Zhang, Effect of sizing on carbon fiber surface properties and fibers/epoxy interfacial adhesion, Appl. Surf. Sci. 257 (2011) 6980–6985. doi:10.1016/j.apsusc.2011.03.047.

[19] W. Qin, F. Vautard, L.T. Drzal, J. Yu, Mechanical and electrical properties of carbon fiber composites with incorporation of graphene nanoplatelets at the fiber-matrix interphase, Compos. Part B Eng. 69 (2015) 335–341. doi:10.1016/j.compositesb.2014.10.014.

[20] PT2712 Low Viscosity System for Tough Parts & Structures, PTM&W Ind. Inc. (n.d.).

https://www.ptm-w.com/technical-library/product-bulletins/Epoxy-N-Fusion Bulletins/PT2712 Bulletin.pdf (accessed January 15, 2018).

[21] H.C. Schniepp, J.L. Li, M.J. McAllister, H. Sai, M. Herrera-Alonson, D.H. Adamson, R.K. Prud'homme, R. Car, D.A. Seville, I.A. Aksay, Functionalized single graphene sheets derived from splitting graphite oxide, J. Phys. Chem. B. 110 (2006) 8535–8539. doi:10.1021/jp060936f.

[22] M.Y. Yen, M.C. Hsiao, S.H. Liao, P.I. Liu, H.M. Tsai, C.C.M. Ma, N.W. Pu, M. Der Ger, Preparation of graphene/multi-walled carbon nanotube hybrid and its use as photoanodes of dye-sensitized solar cells, Carbon N. Y. 49 (2011) 3597–3606. doi:10.1016/j.carbon.2011.04.062.

[23] S.C. Schulz, W. Bauhofer, Shear influenced network dynamics and electrical conductivity recovery in carbon nanotube/epoxy suspensions, Polymer (Guildf). 51 (2010) 5500–5505. doi:10.1016/j.polymer.2010.09.027.

Chapter 8

8. Thermal properties of doubly reinforced fiberglass/epoxy composites with graphene nanoplatelets, graphene oxide and reduced-graphene oxide

This chapter is based on an article that is under review for possible publication in the journal of *Composites Part B: Engineering*.

Foreword

This chapter is the extension of the previous chapter and is mostly focused to investigate the thermal properties of multiscale laminates. Thermal conductivity is one of the key thermal characteristics of polymer composites. Glass fibers and most polymer matrix materials have low thermal or electrical conductivity on their own, limiting their applications in many fields. Carbon nanomaterial fillers which show very high thermal conductivity have been considered as promising candidates to enhance the thermal conductivity of polymers. The thermal properties of the epoxy/nanoparticle composites were studied through DSC, TGA and thermal conductivity measurements.

Thermal properties of doubly reinforced fiberglass/epoxy composites with graphene nanoplatelets, graphene oxide and reduced-graphene oxide

M. Rafiee [a], F. Nitzsche[b], J. Laliberte[b], S. Hind[c], F. Robitaille[a], M. R. Labrosse[a],

[a] *Department of Mechanical Engineering, University of Ottawa, 161 Louis Pasteur, Ottawa, ON K1N 6N5, Canada*

[b] *Department of Mechanical and Aerospace Engineering, Carleton University, 1125 Colonel By Drive, Ottawa, ON K1S 5B6, Canada*

[c] *National Research Council Canada, Aerospace Research Center, 1200 Montreal Road, Ottawa, ON K1A 0R6, Canada*

Abstract

A novel manufacturing method that combines a spraying process with nanoparticle/epoxy mixture technique was used to incorporate carbon nanoparticles for enhancement of thermal properties of multiscale laminates. Several graphene-based nanomaterials including graphene oxide (GO), reduced graphene oxide (rGO), graphene nanoplatelets (GNPs) and multi-walled carbon nanotubes (MWCNTs) were employed to modify the epoxy matrix and the surface of glass fibers. The morphological, rheological and thermal properties of the resulting glass fiber-reinforced multiscale composites were investigated. The thermal properties of the epoxy/nanoparticle composites were studied through differential scanning calorimetry (DSC), thermo-gravimetric analysis (TGA) and thermal conductivity measurements. The thermal characterization results indicated that the introduction of GNPs, GO, rGO, and MWCNTs enhanced thermal conductivity. Compared with the neat epoxy/fiberglass composite control results, improvement in thermal conductivity of fiberglass/epoxy modified with MWCNTs 0.3%, GNPs 1%, GO 2% and rGO 0.042% were 8.8, 12.6, 8.2 and 4.1%, respectively. It was concluded that for the same volume fraction of nanoparticles, the thermal conductivity improvement in graphene nanoplatelets-modified composites is more pronounced compared with other nanoparticles. A better dispersion of nanoparticles and a better interfacial interaction between

nanoparticles and epoxy are essential in enhancing the thermal conductivity of nanocomposite materials.

Keywords: polymer composite; graphene, thermal properties, thermal conductivity, multiscale composite laminates.

8.1 Introduction

Glass fiber-reinforced polymer (GFRP) composites have been widely used in a variety of engineering applications such as aircraft, marine, chemical processing, civil infrastructure, wind turbine blades, and electronics. Thermal conductivity is one of the key thermal characteristics of polymer composites. Glass fibers and most polymer matrix materials have low thermal or electrical conductivity on their own, limiting their applications in many fields. Recently, carbon nanomaterial fillers which show very high thermal conductivity have been considered as promising candidates to enhance the thermal conductivity of polymers. The superior thermal conductivity of these carbon allotropes arises from their strong covalent sp2 bonds of carbon atoms that favor phonon transport through the lattice plane [67]. Among the large number of carbon nanomaterials, graphene and its derivatives have attracted intensive interest in many fields due to their exceptional physical and chemical properties. Graphene materials such as graphene nanoplatelets (GNPs), graphene oxide (GO) and reduced-graphene oxide (rGO) are available as very light nano-sized particles with excellent thermo-electro-mechanical properties. GNPs are composed of several layers of graphene and are considered as smart reinforcing fillers [9]. GNP properties can be influenced by their manufacturing methods. GNPs were also identified as a probable substitute to carbon nanotubes in terms of superior target properties and lower cost [10]. Graphene oxides are compounds of carbon, oxygen and hydrogen in variable ratios. They can be synthesized by exfoliating layered graphite oxide (graphite with strong oxidizers). GO does not require functionalization as it consists of graphene sheets with hydroxyl, carboxyl, and epoxide groups. Reduced-graphene oxide can be obtained by reducing GO using several methods such as microwave, laser, electrochemically, and hydrazine vapor treatment [68]. GNPs [10,69–81], GO [82–88] and rGO [84,88–94] have been shown to improve the thermal conductivity of two-phase epoxy resins [17,18]. Wang et al. [10] studied the thermal conductivity of GNP/epoxy nanocomposites. A marked improvement in thermal conductivity was measured with the incorporation of larger GNPs size reaching 115% at 5 wt% loading. GNPs were also used in the work of Zhu et al. [81] for enhancing the thermal conductivity of GNP/epoxy resin composites. In another study, the influence of GNPs and carbon black on the thermal properties of epoxy nanocomposites was studied by Krieg et al. [73]. Gao et al. [85] reported a simple and efficient method to prepare three-dimensional graphene oxide (3DGO) networks by freeze drying, and investigated the effect of 3DGO networks on the thermal properties of epoxy composites. The thermal conductivity value of epoxy composite in their work, with 1.3 wt% 3DGO was increased by 148% in comparison with that of the neat epoxy. A thermally conductive epoxy polymer composite comprising copper nanowires and reduced graphene oxide as hybrid fillers was prepared and tested by Li et al. [95]. The authors showed that the combination of those fillers not only improves interfacial interaction between fillers and the resin matrix, but it also improve the thermal conductivity of composites. Thermal conductivity of multiscale laminates modified with MWCNTs were also reported in the literature [96,97]. For instance, Li et al. [96] manufactured multiscale GFRP modified with functionalized MWCNTs. MWCNTs were deposited on insulating woven glass fibers through an Electrophoretic deposition (EPD) method. The authors showed that the thermal conductivity of MWCNTs composites were significantly improved compared with that of pure GFRP.

Glass transition temperature is another thermal characteristics of polymer composites. Differential scanning calorimetry (DSC) is a thermoanalytical technique that can be employed to study the glass transition temperature of epoxy composites. The DSC of two-phase epoxy composites modified with GNPs [79,84,98], GO [99–101] and rGO [99,102,103] composites were reported in the literature. For instance, Monteserín et al. [99] studied the effects of graphene oxide and chemically reduced graphene oxide on the curing kinetics of epoxy amine composites using DSC. Experimental and modeling results demonstrated that the presence of the GO slightly improved the glass transition temperature of epoxy/GO cured nanocomposites. This improvement was also reported by some other researchers [98,104–106].

Thermal stability or the ability of polymers to retain their useful properties at elevated temperatures is of great importance as well. The measurement of thermal stability can be performed with thermo-gravimetric analysis (TGA) which is a characterization technique where a mass of a material is monitored as a function of temperature and time as a specimen is subjected to a set temperature program under controlled atmosphere. Researchers studied the weight loss of epoxy nanocomposites modified with GNPs [107,108], GO [99,109] and rGO [89,99,110] aiming at elevating thermal stability. For instance, TGA analysis in the work of Liu et al. [109] indicated that the introduction of GO up to 1.5 wt% did not have obvious effects on the thermal stability of epoxy/GO nanocomposites. The thermal stability of the rGO/epoxy composites appeared to decrease with increasing rGO content in the work of Olowojoba et al. [89].

Studies of the thermal properties of graphene-based epoxy nanocomposites, such as through-the-thickness thermal conductivity, mainly focused on either two-phase epoxy/nanoparticle or three-phase MWCNTs/GFRP composites. While the thermal properties of laminated multiscale GFRP nanocomposites modified with conductive graphene nanoparticles are important in many applications such as electronics, to the best of authors' knowledge, no study was devoted to investigating them.

In this paper, the thermal properties of graphene nanomaterials-modified fiberglass/epoxy composites was investigated. A novel manufacturing method based on Vacuum Assisted Resin Transfer Molding (VARTM) was devised to incorporate different carbon nanoparticles (MWCNTs, GNPs, GO and rGO) for simultaneous modification of matrix and fibers without increasing the viscosity of the epoxy matrix. The thermal characteristics of the resulting multiscale hierarchical composites were studied experimentally.

8.2 Materials, processing and fabrication

8.2.1 Materials

Single layer GO (product number 1.8) with approximate bulk density of 1 g/cm^3 was received in the form of powder from Abalonyx, Norway. Reduced graphene oxide (product number 2.1) produced by thermal reduction of graphene oxide was also obtained from Abalonyx, Norway. The rGO had a carbon content of about 86% atomic or about 82 wt% and its bulk density was approximately 0.01 g/cm^3. The pristine and amino-functionalized graphene nanoplatelets (p-GNPs and f-GNPs) were obtained from Cheap Tubes Inc., U.S.A with product number of 050111 and 050114, respectively. They were made by exfoliating graphite down to 5-15 atomic layers and featured average thickness and diameter of 1.5 nm and 5 µm, respectively, as per the manufacturer datasheet. The bulk density was 0.21 g/cm^{3}for both materials. Unidirectional E-glass fabric with average fiber diameter of 20 µm and surface density of 0.78 kg/m^2 was supplied by NMG, China. Low viscosity diglycidyl ether of bisphenol-A (DGEBA) infusion epoxy resin PT-2712 Part A and the diethyltoluenediamine (DETDA) curing agent PT-2712 Part B1 were produced by PTM&W

Industries, Inc., USA. The viscosity of mixed Part A and Part B1 at room temperature was 1 Pa.s and the pot life at room temperature was approximately two hours, as per the manufacturer datasheet. Epoxy resin Part A and B mixing weight ratio was 100:22 as per the manufacturer recommendation.

8.2.2 Experimental

8.2.2.1 Two-phase epoxy/nanoparticle composites

Table 8-1 shows the different loadings of nanoparticles used for preparing two-phase epoxy matrix composites modified with MWCNTs, GNPs, GO and rGO. Nanoparticle loadings were calculated relative to epoxy (DGEBA), epoxy and hardener (DGEBA+DETDA), and total fiber reinforced composite. Fig. 8-1 shows a general schematic of the method for the preparation of the multiscale nanocomposites whilst a detailed description is provided in Fig. 8-2. As mentioned in the Introduction, when manufacturing nanocomposite laminates by VARTM, a filtration effect was observed in this study for MWCNTs loading higher than 0.075 wt% of DGEBA. Therefore, part of the nanoparticle was used for sizing fabrics while the rest of the mixture was kept for preparation of the infusion epoxy as indicated in Fig. 8-2. Table 8-2 lists the different loadings of carbon nanomaterials that were sprayed on fabrics as well as the percentage that was used for infusion of the epoxy.

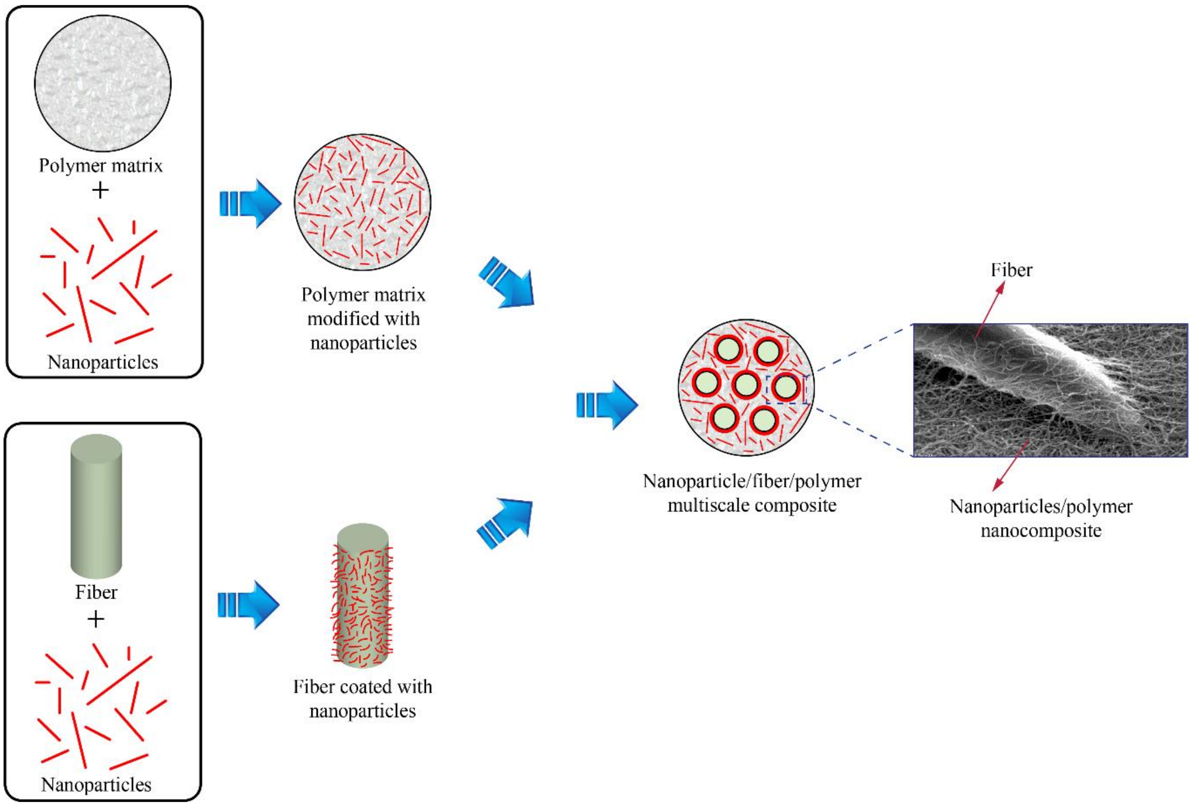

Fig. 8-1. New route for fabricating multiscale nanocomposite.

Table 8-1. Loadings of nanoparticle used for modification of fiberglass/epoxy composites.

	wt% of DGEBA	vol.% of DGEBA	wt% of matrix (DGEBA+ DETDA)	vol.% of matrix (DGEBA+ DETDA)	wt% of total (DGEBA+ DETDA+ fibers)	vol.% of total (DGEBA+ DETDA+fibers)
MWCNT	0.075	1.38	0.06	1.1	0.02	0.55
	0.15	2.75	0.12	2.2	0.04	1.1
	0.3	5.5	0.25	4.4	0.07	2.2
GNP	0.1	0.55	0.08	0.44	0.02	0.22
	0.2	1.1	0.16	0.88	0.05	0.44
	0.4	2.2	0.33	1.76	0.1	0.88
	1	5.5	0.82	4.4	0.25	2.2
GO	1	1.1	0.82	0.88	0.25	0.44
	2	2.2	1.64	1.76	0.5	0.88
rGO	0.01	1.1	0.008	0.88	0.002	0.44
	0.03	3.3	0.025	2.64	0.007	1.32
	0.042	4.6	0.034	3.7	0.010	1.85

Acetone was used to disperse nanotubes because of its low boiling point, low toxicity, good dispersion of carbon nanoparticles [8] and less destructive effect on mechanical performance of the composites during the pre-curing process of the composites [111]. A dosage of one gram of nanoparticles per liter of acetone was used for dispersion of the nanoparticles in the acetone solvent. For the sizing of fabrics, the nanoparticle/acetone mixture was mixed with the desired amount of epoxy (Table 8-2) and was then sonicated using an ultrasonic probe (Q700 Sonicator, Qsonica LLC, USA) for 90 minutes including on and off pulse cycles. To avoid any adverse high temperature effects, sonication was performed by 20-sec ON pulses followed by 10-sec OFF cycles. The desired amount of mixture (as per Table 8-2) was used for sizing fibers via a spray gun inside a fume hood. The fabrics were kept in fume hood for 24 hours to ensure the evaporation of solvent on the fabrics. The ratio of epoxy per square meter of fabrics (both sides) was 14 grams. A laboratory mixer was used for stirring the remainder of the mixture at 400 rpm for 12 hours to ensure good dispersion of nanoparticles in the epoxy resin. After this step, the mixture was placed on a magnetic hot plate stirrer, using a Teflon-coated magnetic bar, to stir the solution for 4 hours at 70°C. The objective was to remove the acetone by evaporation. Complete removal of acetone was ensured by placing the mixture in a vacuum chamber for 30 minutes. The slurry of epoxy resin DGEBA and GNPs was allowed to cool to room temperature before the curing agent was added, to avoid premature curing during mixing. The low viscosity curing agent DETDA was added with a curing agent to resin ratio of 22:100. The mixture was mixed at 800 rpm for 30 minutes using a mechanical stirrer with stainless steel axial impeller. The mixture was degassed in a vacuum chamber at ambient temperature for about 30 minutes. The mixture was then used as an infusion epoxy for the manufacturing of laminates, as explained in the next section.

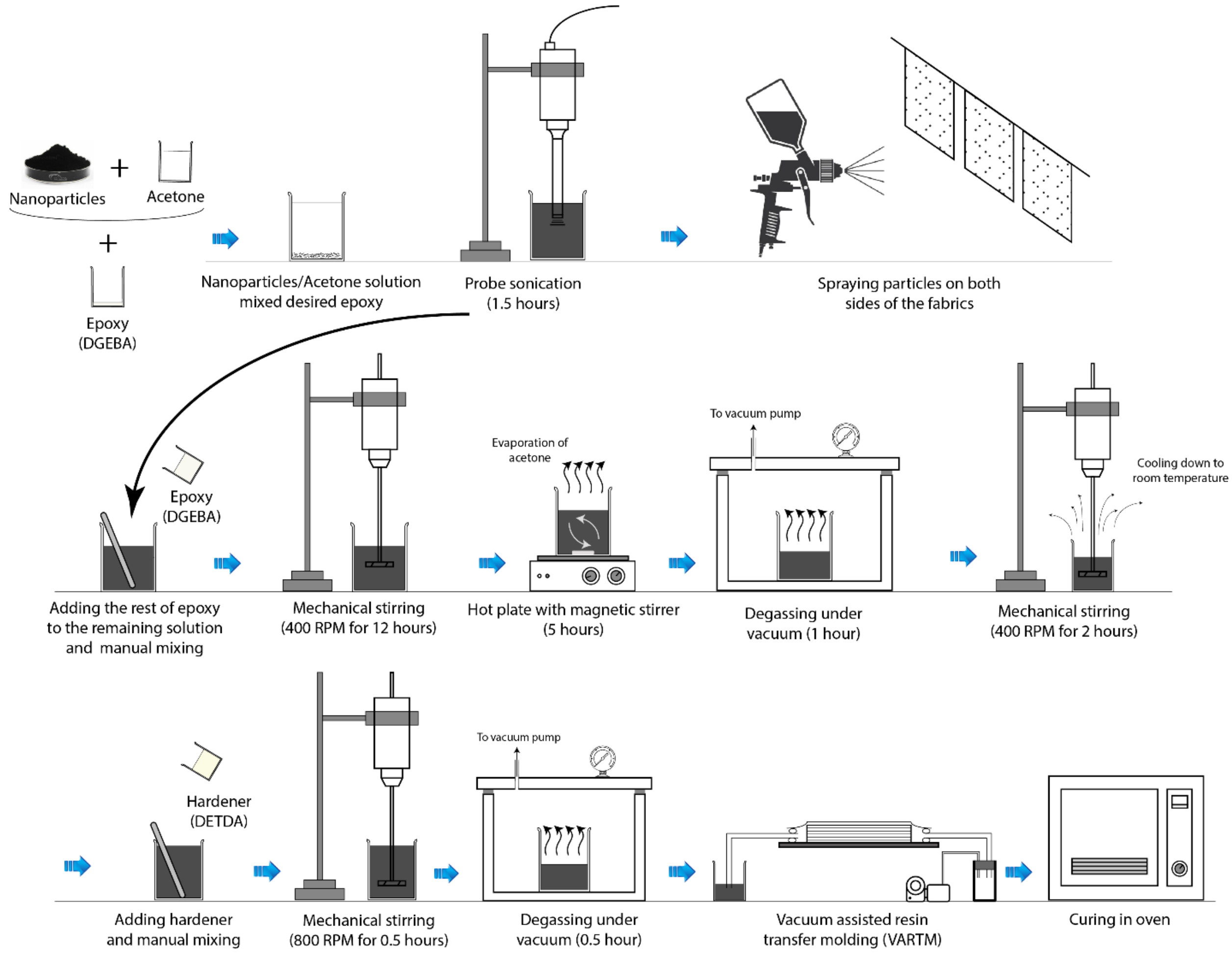

Fig. 8-2. Fabrication process of multiscale fiber glass/epoxy composites modified with graphene-based nanoparticles.

8.2.2.2 Three-phase laminated composites

The VARTM process was used to fabricate the multiscale fiber reinforced laminated composites with the nanoparticle-filled epoxy resin. The reinforcement was made of three layers of unidirectional glass fabrics in cross-ply form [0°, 90°, 0°] where 0° was the main direction of testing.

After the infusion of the nanoparticle/epoxy dispersions, laminates were cured at room temperature for 15 hours, followed by a post cure at 1°C/min ramp rate, held every 20°C for an hour, then continuing until a final hold of three hours at 100°C. The vacuum bagging system combined with the two-stage degassing process can achieve extremely low void content for thermoset composites. Composite coupons with thickness of 1.9 ± 0.1 mm were cut by water jet for testing. The approximate fiber volume and weight fraction were calculated for each laminate configuration in accordance with ASTM D 3171 standard as 50% and 70%, respectively.

Table 8-2. Weight and volume percentile of nanoparticle used for spray process and infusion of fiber-glass/epoxy composites.

	wt% of DGEBA	vol.% of DGEBA	Sprayed vol. %	Infusion vol.%
MWCNT	0.075	1.38	0.69	0.69
	0.15	2.75	1.37	1.38
	0.3	5.5	4.12	1.38
GNP	0.1	0.55	0.275	0.275
	0.2	1.1	0.55	0.55
	0.4	2.2	1.1	1.1
	1	5.5	4.4	1.1
GO	1	1.1	0.55	0.55
	2	2.2	1.1	1.1
rGO	0.01	1.1	0.55	0.55
	0.03	3.3	2.2	1.1
	0.042	4.6	3.5	1.1

8.3 Characterization

8.3.1 Morphology

The morphology of nanoparticles, two-phase and three-phase composites were observed through a ZEISS (AX10) optical microscope. Since the dispersion of CNTs in epoxy is unstable at different times and temperatures, the optical images were taken at room temperature and 120 minutes after finishing of mixing nanoparticles/acetone with DGEBA. The dispersion of carbon nanoparticles was also investigated using a TECNAI Spirit transmission electron microscope (TEM) operated at 120 kV. The analysis of fracture surfaces was done using Zeiss EVO10 SEM scanning electron microscope (SEM) at 5 kV accelerating voltage.

8.3.2 Rheology

Several tests were also performed to investigate the rheological behavior of the epoxy resin (DGEBA) containing different loading of nanoparticles. Experiments were carried out on a rotational rheometer MCR 301 from Anton Paar Inc. Steady shear tests were performed to measure the viscosity over the range of shear rates between 0.1 to 100 s^{-1}. All rheological measurements were carried out at room temperature.

8.3.3 Thermal properties

8.3.3.1 Differential scanning calorimetry

A Q2000 differential scanning calorimeter from TA instruments was used to measure the glass transition temperatures (T_g) of cured epoxy/nanoparticle composites. The measurements were conducted in a dry atmosphere, under nitrogen constant flow of 50 ml/min at temperature ranging from 50 to 250ºC and a heating rate of 15ºC/min. Samples ranging from 7 to 10 mg were weighted in aluminum pans. The glass transition temperatures were defined as the midpoint of the heat capacity change.

8.3.3.2 Thermogravimetric analysis

Thermogravimetric analyses were carried out using a TGA Q50 from TA instruments, from ambient temperature to 550ºC, at a heating rate of 30ºC/min. and under a constant nitrogen flow of 50 ml/min. Crucibles used in this analysis were made of alumina with a 90 mL volume.

8.3.3.3 Thermal conductivity

A THASYS through-the-thickness thermal conductivity measurement device from Hukseflux Thermal Sensors was used for experimental data collection. THASYS is equipped with a thin heater apparatus (THA01) and a measurement and control unit (MCU) and requires two flat samples measuring approximately 70 × 110 mm. Samples were immersed in glycerol to reduce contact heat transfer resistance. Through-the-thickness thermal conductivity, λ, was determined by measuring the heat flux, Φ, derived from heater power, the differential temperature, ΔT, through the samples and the effective sample thickness, H_{eff}:

$$\lambda = \frac{\Phi H_{eff}}{\Delta T}, \quad H_{eff} = \frac{1}{\dfrac{1}{H_{sample1}} + \dfrac{1}{H_{sample2}}} \tag{2}$$

where $H_{samp1e1}$ and $H_{samp1e2}$ are the thicknesses of samples 1 and 2 respectively. The instrument can accommodate samples ranging from 1 to 6 mm in thickness.

8.4 Results and discussion

8.4.1 Morphology of nanoparticles, epoxy and fibers

8.4.1.1 TEM micrographs

Fig. 3(a–h) present TEM micrographs of materials fabricated in this work: (a-b) MWCNTs, (c-d) GNPs, (e-f) Go, and (g-h) rGO. Occasional localizations of carbon nanotubes and graphene aggregates can be observed in the TEM images, suggesting the existence of van der Waals forces and interactions between GNPs, GO and rGO sheets.

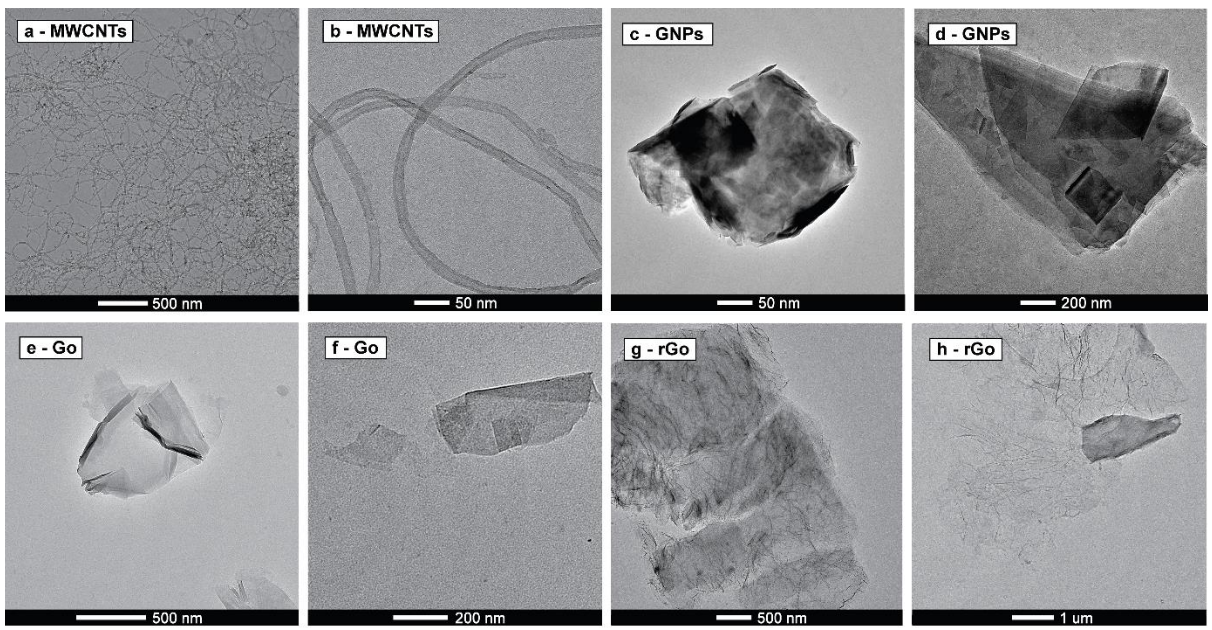

Fig. 8-3. TEM images of nanoparticles: (a-b) MWCNTs, (c-d) GNPs, (e-f) GO, and (g-h) rGO.

8.4.1.2 Optical micrographs

Optical micrographs of GNPs and MWCNTs dispersed in epoxy matrix appear in Fig. 8-4. Optical micrographs were obtained at different magnification levels for the nanoparticle/epoxy suspensions. Micrographs for the GNP/epoxy suspensions (Fig. 8-4a-b) show relatively homogenous distributions aggregates due to favorable GNP interactions with the epoxy matrix [64]. At higher magnification, the presence of large size GNP aggregates can be observed, primarily due to van der Waals forces and strong π–π interactions between the GNP sheets [65]. By contrast, the MWCNTs/epoxy suspensions (Fig. 8-4c-d) show more loosely packed and isolated aggregates of carbon nanotubes, resulting in a relatively inhomogeneous suspension. Such aggregates form due to CNT unfavorable interactions with the epoxy matrix [66] and van der Waals attraction forces between the CNTs.

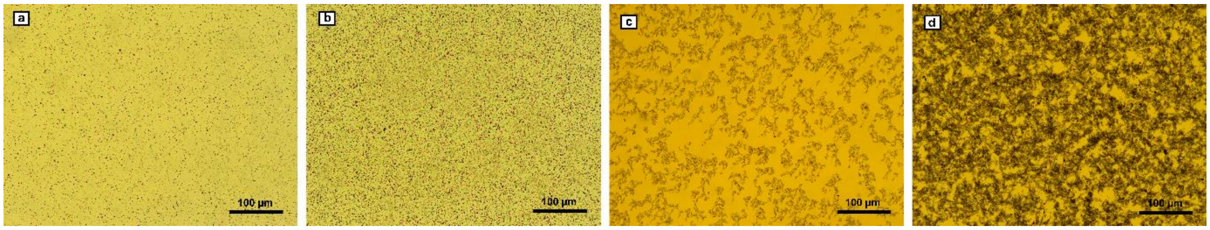

Fig. 8-4. Optical micrograph of (a) GNPs 0.2%, (b) GNPs 1.2%, (c) MWCNTs 0.075%, and (d) MWCNTs 0.3% in DGEBA.

8.4.1.3 SEM micrographs

The surface morphology of glass fibers coated with nanoparticles at different magnifications was observed using SEM. Fig. 8-5 shows the SEM micrographs of rGO-coated glass fibers at different magnifications. As seen from these images, the coverage of nanoparticles coating on the outer layer yarns is uniform.

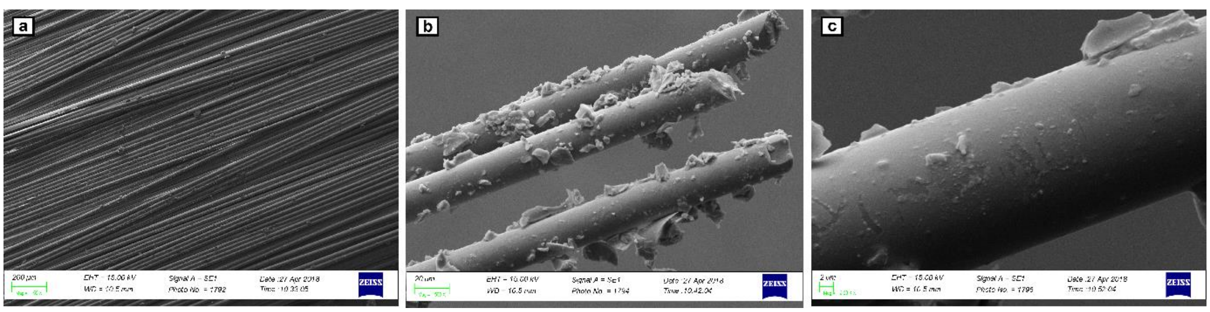

Fig. 8-5. SEM micrographs of fiber surfaces coated with nanoparticles (rGO) at different magnifications: (a) 50, (b) 500 and (c) 2000X.

8.4.2 Rheology

The steady shear viscosity of nanoparticles/epoxy dispersions and the effect of nanoparticle loading was studied. Fig. 8-6 shows relations between steady shear viscosity and shear rate for neat epoxy and nanoparticle/epoxy dispersions. Steady shear viscosity profiles for MWCNTs and GNPs demonstrate a shear-thinning behavior where shear viscosity decreases sharply with increasing the shear rate. This phenomenon is more obvious for functionalized nanoparticles compared with pristine ones. Besides, MWCNTs lead to stronger non-Newtonian behavior than the other nanoparticles considered in this work. Viscosity versus shear rate curve for the p-

MWCNTs/epoxy and f-MWCNTs dispersions (Fig. 8-6a-b) with content beyond 0.075 wt% suggest that they would be problematic to use as nanocomposite matrix for VARTM manufacturing. Indeed, at MWCNT loadings higher than 0.075 wt% of epoxy, high viscosity of the mixture does not allow it to be infused through fabrics, and leads to filtration. Results from GNPs viscosity confirmed that at least up to loadings of 1.2 wt% of DGEBA, pristine and functionalized GNPs can be used for infusion-based manufacturing methods such as VARTM. Similar to GNPs, GO and rGO was observed to have lower viscosities for the same vol.% of nanoparticles in the experiments.

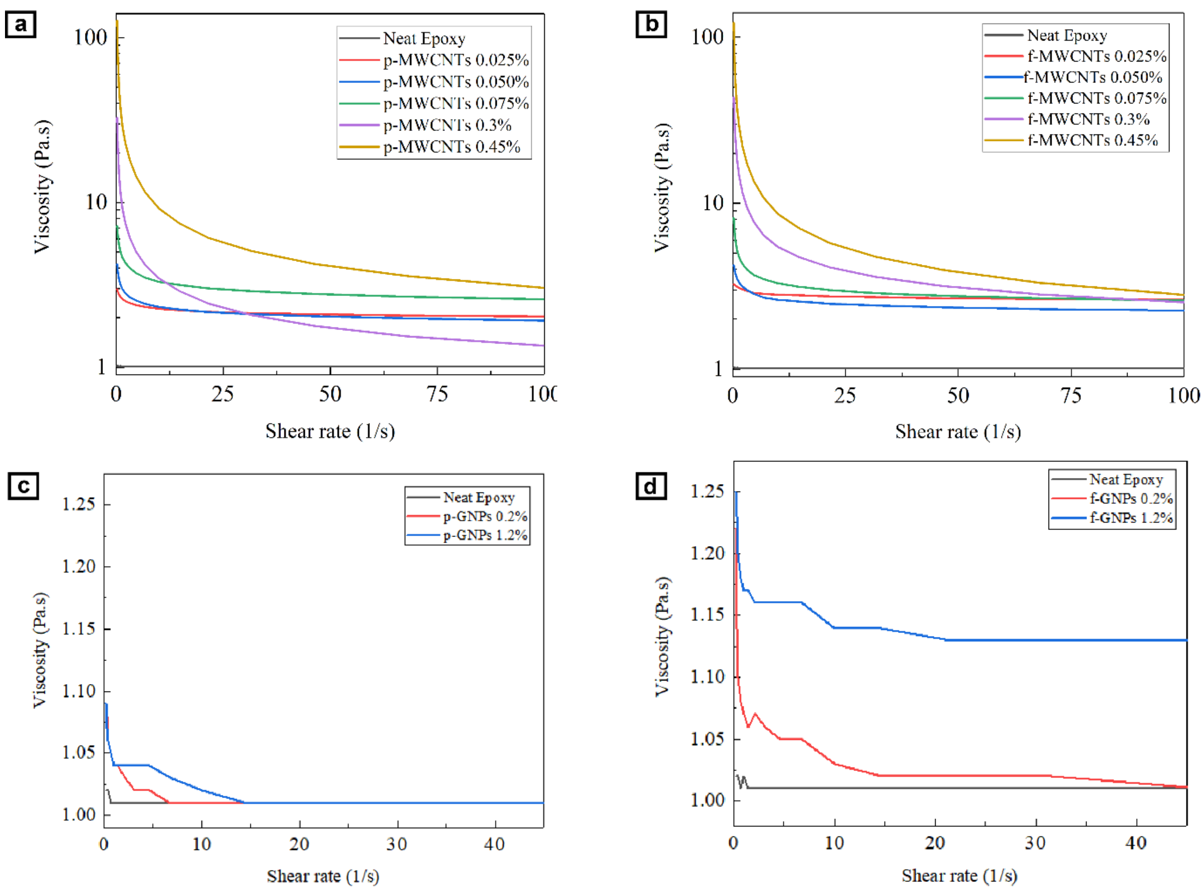

Fig. 8-6. Steady shear viscosity of nanoparticle/epoxy dispersion as a function of shear rate.

For pure epoxy resin, which behaves as a Newtonian fluid, the viscosity was equal to 1.0 Pa.s and the shear-thinning behavior observed from the nanoparticle/epoxy mixture was caused by the break-down of the worm-like percolated structure of MWCNTs clusters by shear. Viscosity increased as the concentration of nanoparticles increased. The space between nanoparticles decreased, reducing the mobility and increasing the dispersion's resistance to flow. Fig. 8-6a-d reveals that the increase was more pronounced at lower shear rates than at higher shear rates. The noticeable shear thinning effect was also nanoparticle loading-dependent. Gaps in viscosities between different nanoparticle concentrations narrowed dramatically as shear rate increased.

8.4.3 Thermal properties

8.4.3.1 Glass transition temperature

DSC curves for cured neat epoxy (DGEBA+DETDA) and its nanocomposites modified with MWCNTs and GNPs are shown in Fig. 8-7a-b. Compared with the cured neat epoxy, the nanocomposite sample reinforced with MWCNTs or GNPs shows a lower T_g, indicating that the epoxy matrix in the nanocomposites has less cross-linking degree than the neat DGEBA+DETDA. However, the reduction in T_g is small.

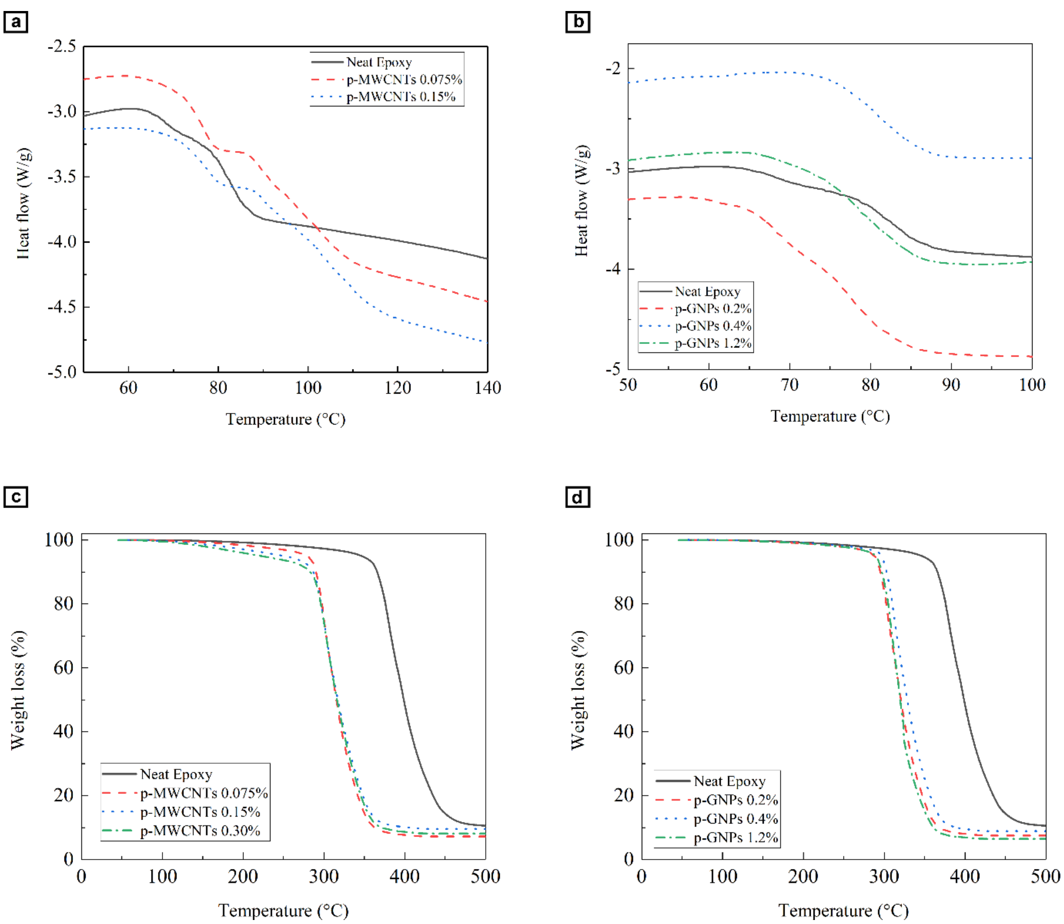

Fig. 8-7. DSC (a and b) and TGA (c and d) curves of cured epoxy/nanoparticle composites.

8.4.3.2 Thermal stability

Fig. 8-7c-d depicts weight loss curves for cured neat epoxy (DGEBA+DETDA), and its nanocomposites modified with MWCNTs and GNPs, respectively. TGA results for thermal degradation indicate a structural modification of the epoxy system. The MWCNTs and GNPs influence the thermal degradation profile, particularly the temperature at which the degradation rate is maximum, which is lower for cured nanocomposite epoxy than for cured neat epoxy. This is likely due to reduced crosslinking in the presence of nanoparticles.

8.4.3.3 Thermal conductivity

Results obtained from thermal conductivity measurements of two-phase and three-phase composites appear in Fig. 8-8 and Fig. 8-9, respectively. Clearly, thermal conductivities increases with an increase in the weight percentage of nanofillers. However, the improvement in thermal conductivities does not vary linearly with nanoparticle loading. For the same volume fraction, GNPs result in the highest increase in thermal conductivity while GO results in the lowest relative increase when compared with other nanoparticles investigated in this study. This is probably due to the presence of large quantities of oxygen groups in the GO. The presence of oxygen groups can act as scattering points for the phonons through the graphene layers that weaken the interfacial connection between nanoparticles and epoxy.

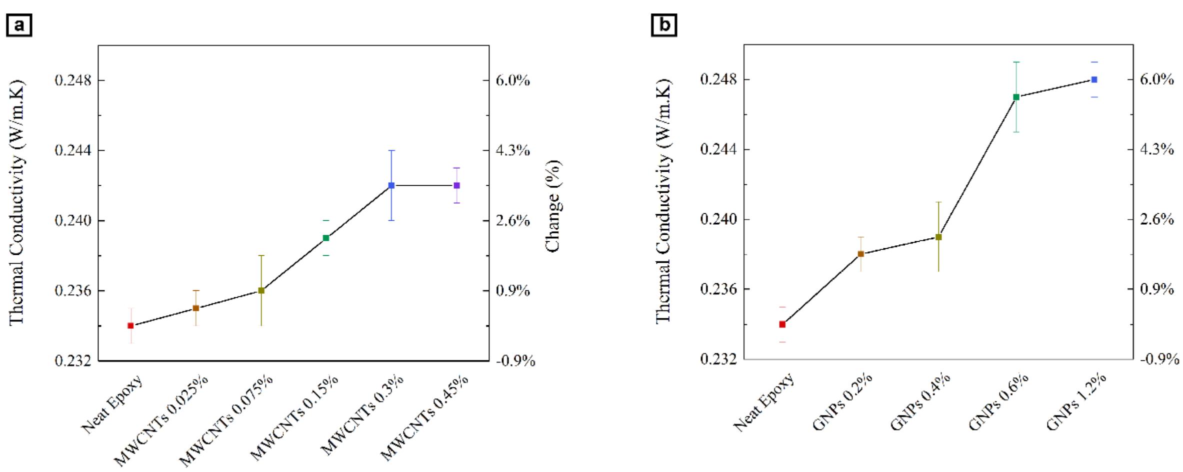

Fig. 8-8. Thermal conductivity of epoxy modified with different loading of MWCNTs and GNPs with respect to DGEBA.

MWCNTs are generally very good thermal conductors along the tube, but good insulators lateral to the tube axis. This property makes MWCNTs less effective compared to GNPs for enhancement of thermal conductivity of their composites. Another reason for less improvement of thermal conductivity in MWCNTs/epoxy may be due to poor dispersion of the MWCNTs in the epoxy compared with other nanoparticles.

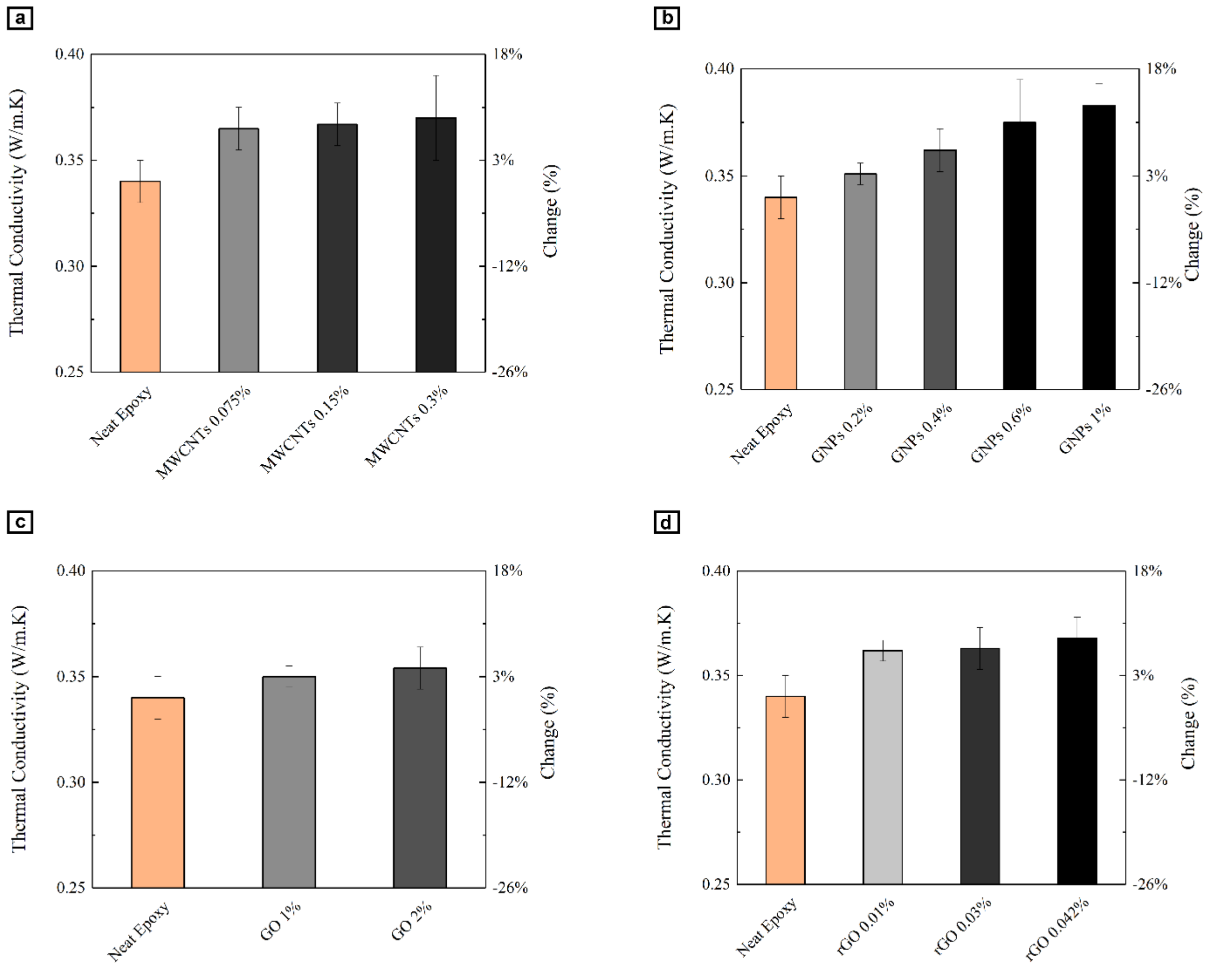

Fig. 8-9. Thermal conductivity of glass fiber composites modified with different loading of carbon nanoparticles.

The thermal conductivity of two-phase epoxy/nanoparticle composites (Fig. 8-8) were improved up to 3.4 and 6.0% for MWCNTs and GNPs, respectively. We speculate that the higher loading of MWCNTs and GNPs in resin led to agglomeration and bad dispersion. Thermal conductivity improvement in carbon nanotubes is relatively less pronounced in compared with GNPs. This could be due to weaker conductivity of nanotubes through their cross-section. Maximum thermal conductivity improvement in GFRP modified with MWCNTs 0.3%, GNPs 1%, GO 2% and rGO 0.042% are 8.8, 12.6, 8.2 and 4.1%, respectively (Fig. 8-9). It seems that larger size, better exfoliation degree, and better dispersion of nanoparticles and better interfacial connection between nanoparticles and epoxy are important factors in enhancing the thermal conductivity of nanocomposite samples.

8.5 Conclusion

Simultaneous reinforcement of matrix and fibers was carried out via a novel method that combines a nanoparticle spraying process with nanoparticle/epoxy mixture to incorporate nanoparticles for enhancement of thermo-mechanical properties of laminated multiscale epoxy composites. Several graphene-based nanomaterials including graphene oxide, reduced graphene oxide, graphene nanoplatelets, and multi-walled carbon nanotubes were employed to modify the epoxy matrix and the surface of glass fibers. The morphological, rheological, and thermal properties of the glass fiber-reinforced multiscale composites were investigated. Increased epoxy viscosity, due to the addition of MWCNTs, is not suitable for VARTM or other types of relatively low pressure infusion processing. On the other hand, the viscosity of epoxy / GNPs did not increase dramatically by addition of nanoparticles up to 1 wt% of GNPs in DGEBA. Based on the experiments performed in this study, MWCNTs loading in the epoxy matrix can reach up to 0.075 wt% to avoid filtration by fabrics, and for GNP, GO and rGO, loadings can be tailored according to the intended applications.

Thermal properties of epoxy/nanoparticle composites were also studied. The results indicated that the introduction of GNPs, GO, rGO, and MWCNTs enhance thermal conductivity. The thermal conductivity of two-phase epoxy/nanoparticle composites was increased by up to 6.0% for 1.2 wt% of GNPs in DGEBA. Compared with the neat GRFP control results, thermal conductivity improvement in fiberglass/epoxy modified with MWCNTs 0.3%, GNPs 1%, GO 2% and rGO 0.042% were 8.8, 12.6, 8.2 and 4.1 %, respectively. It was concluded that for the same volume fraction, GNPs exhibit more improvement to thermal conductivity compared with other nanoparticles studied. Controlling dispersion of nanoparticles and interfacial interaction between nanoparticles and epoxy are critical factors essential to optimally enhancing the thermal conductivity of nanocomposite materials.

Acknowledgements

The authors acknowledge the supply of nanoparticles: MWCNTs by Nanocyl S.A. (Belgium), GNPs by Cheap Tubes Inc. (U.S.A.), GO and rGO by Abalonyx (Norway). In addition, the first author gratefully acknowledges the financial support from the Ontario Trillium Scholarship, Government of Ontario and the University of Ottawa, Canada.

References

[1] Balandin AA. Thermal properties of graphene and nanostructured carbon materials. Nat Mater 2011;10:569. doi:10.1038/nmat3064.

[2] Mutlay I, Tudoran LB. Percolation behavior of electrically conductive graphene nanoplatelets/polymer nanocomposites: Theory and experiment. Fullerenes Nanotub Carbon Nanostructures 2014;22:413–33. doi:10.1080/1536383X.2012.684186.

[3] Wang F, Drzal LT, Qin Y, Huang Z. Mechanical properties and thermal conductivity of graphene nanoplatelet/epoxy composites. J Mater Sci 2014;50:1082–93. doi:10.1007/s10853-014-8665-6.

[4] Sadasivuni KK, Ponnamma D, Kim J, Thomas S. Graphene-based polymer nanocomposites in electronics. Graphene-Based Polym Nanocomposites Electron 2015:1–382. doi:10.1007/978-3-319-13875-6.

[5] Chatterjee S, Wang JW, Kuo WS, Tai NH, Salzmann C, Li WL, et al. Mechanical reinforcement and thermal conductivity in expanded graphene nanoplatelets reinforced epoxy composites. Chem Phys Lett 2012;531:6–10. doi:10.1016/j.cplett.2012.02.006.

[6] Guo W, Chen G. Fabrication of graphene/epoxy resin composites with much enhanced thermal conductivity via ball milling technique. J Appl Polym Sci 2014;131. doi:10.1002/app.40565.

[7] Wang Y, Yu J, Dai W, Song Y, Wang D, Zeng L, et al. Enhanced thermal and electrical properties of epoxy composites reinforced with graphene nanoplatelets. Polym Compos 2015;36:556–65. doi:10.1002/pc.22972.

[8] Moriche R, Prolongo SG, Sánchez M, Jiménez-Suárez A, Chamizo FJ, Ureña A. Thermal conductivity and lap shear strength of GNP/epoxy nanocomposites adhesives. Int J Adhes Adhes 2016;68:407–10. doi:10.1016/j.ijadhadh.2015.12.012.

[9] Wang F, Drzal LT, Qin Y, Huang Z. Effects of functionalized graphene nanoplatelets on the morphology and properties of epoxy resins. High Perform Polym 2016;28:525–36. doi:10.1177/0954008315588983.

[10] Messina E, Leone N, Foti A, Di Marco G, Riccucci C, Di Carlo G, et al. Double-Wall

Nanotubes and Graphene Nanoplatelets for Hybrid Conductive Adhesives with Enhanced Thermal and Electrical Conductivity. ACS Appl Mater Interfaces 2016;8:23244–59. doi:10.1021/acsami.6b06145.

[11] Prolongo MG, Salom C, Arribas C, Sanchez-Cabezudo M, Masegosa RM, Prolongo SG. Influence of graphene nanoplatelets on curing and mechanical properties of graphene/epoxy nanocomposites. J Therm Anal Calorim 2016;125:629–36. doi:10.1007/s10973-015-5162-3.

[12] Ghaleb ZA, Mariatti M, Ariff ZM. Graphene nanoparticle dispersion in epoxy thin film composites for electronic applications: effect on tensile, electrical and thermal properties. J Mater Sci Mater Electron 2017;28:808–17. doi:10.1007/s10854-016-5594-y.

[13] Zhu D, Qi Y, Yu W, Chen L, Wang M, Xie H. Enhanced Thermal Conductivity for Graphene Nanoplatelets/Epoxy Resin Composites. J Therm Sci Eng Appl 2017;10:011011. doi:10.1115/1.4036796.

[14] Atif R, Shyha I, Inam F. Modeling and experimentation of multi-layered nanostructured graphene-epoxy nanocomposites for enhanced thermal and mechanical properties. J Compos Mater 2017;51:209–20. doi:10.1177/0021998316640060.

[15] Lu H, Zhang J, Luo J, Gong W, Li C, Li Q, et al. Enhanced thermal conductivity of free-standing 3D hierarchical carbon nanotube-graphene hybrid paper. Compos Part A Appl Sci Manuf 2017;102:1–8. doi:10.1016/j.compositesa.2017.07.021.

[16] Yao H, Hawkins SA, Sue HJ. Preparation of epoxy nanocomposites containing well-dispersed graphene nanosheets. Compos Sci Technol 2017;146:161–8. doi:10.1016/j.compscitech.2017.04.026.

[17] Krieg AS, King JA, Jaszczak DC, Miskoglu I, Mills OP, Odegard GM. Tensile and conductivity properties of epoxy composites containing carbon black and graphene nanoplatelets. J Compos Mater 2018;0:1–10. doi:10.1177/0021998318771460.

[18] Song SH, Park KH, Kim BH, Choi YW, Jun GH, Lee DJ, et al. Enhanced thermal conductivity of epoxy-graphene composites by using non-oxidized graphene flakes with non-covalent functionalization. Adv Mater 2013;25:732–7. doi:10.1002/adma.201202736.

[19] Zhang B, Asmatulu R, Soltani SA, Le LN, Kumar SSA. Mechanical and thermal properties

of hierarchical composites enhanced by pristine graphene and graphene oxide nanoinclusions. J Appl Polym Sci 2014;131. doi:10.1002/app.40826.

[20] Zeng C, Lu S, Xiao X, Gao J, Pan L, He Z, et al. Enhanced thermal and mechanical properties of epoxy composites by mixing noncovalently functionalized graphene sheets. Polym Bull 2015;72:453–72. doi:10.1007/s00289-014-1280-5.

[21] Gao J, Yu J, Wu X, Rao B, Song L, He Z, et al. Enhanced thermal properties for epoxy composites with a three-dimensional graphene oxide filler. Fibers Polym 2015;16:2617–26. doi:10.1007/s12221-015-5637-7.

[22] Suresh Kumar SM, Subramanian K. Enhancement in Mechanical, Thermal, and Dielectric Properties of Functionalized Graphene Oxide Reinforced Epoxy Composites. Adv Polym Technol 2016;37:1–10. doi:10.1002/adv.21702.

[23] Yuan W, Xiao Q, Li L, Xu T. Thermal conductivity of epoxy adhesive enhanced by hybrid graphene oxide/AlN particles 2016;106:1067–74. doi:10.1016/j.applthermaleng.2016.06.089.

[24] Aradhana R, Mohanty S, Nayak SK. Comparison of mechanical, electrical and thermal properties in graphene oxide and reduced graphene oxide filled epoxy nanocomposite adhesives. Polym (United Kingdom) 2018;141:109–23. doi:10.1016/j.polymer.2018.03.005.

[25] Olowojoba GB, Eslava S, Gutierrez ES, Kinloch AJ, Mattevi C, Rocha VG, et al. In situ thermally reduced graphene oxide/epoxy composites: thermal and mechanical properties. Appl Nanosci 2016;6:1015–22. doi:10.1007/s13204-016-0518-y.

[26] Sun Y, Tang B, Huang W, Wang S, Wang Z, Wang X, et al. Preparation of graphene modified epoxy resin with high thermal conductivity by optimizing the morphology of filler. Appl Therm Eng 2016;103:892–900. doi:10.1016/j.applthermaleng.2016.05.005.

[27] Li M, Tang C, Zhang L, Shang B, Zheng S, Qi S. A thermally conductive epoxy polymer composites with hybrid fillers of copper nanowires and reduced graphene oxide. J Mater Sci Mater Electron 2017;28:15694–700. doi:10.1007/s10854-017-7459-4.

[28] Sun Y, Chen L, Lin J, Cui P, Li M, Du X. Thermal conductivity of epoxy composites filled by thermally reduced graphite oxide with different reduction degree. J Compos Mater

2017;51:1743–52. doi:10.1177/0021998317696137.

[29] Sánchez-Hidalgo R, Yuste-Sanchez V, Verdejo R, Blanco C, Lopez-Manchado MA, Menéndez R. Main structural features of graphene materials controlling the transport properties of epoxy resin-based composites. Eur Polym J 2018;101:56–65. doi:10.1016/j.eurpolymj.2018.02.018.

[30] Kulkarni HB, Tambe P, M. Joshi G. Influence of covalent and non-covalent modification of graphene on the mechanical, thermal and electrical properties of epoxy/graphene nanocomposites: a review. Compos Interfaces 2018;25:381–414. doi:10.1080/09276440.2017.1361711.

[31] Li M, Tang C, Zhang L, Shang B, Zheng S, Qi S. A thermally conductive epoxy polymer composites with hybrid fillers of copper nanowires and reduced graphene oxide. J Mater Sci Mater Electron 2017;0:0. doi:10.1007/s10854-017-7459-4.

[32] Li J, Wu Z, Huang C, Li L. Multiscale carbon nanotube-woven glass fiber reinforced cyanate ester/epoxy composites for enhanced mechanical and thermal properties. Compos Sci Technol 2014;104:81–8. doi:10.1016/j.compscitech.2014.09.007.

[33] Yang Y. Thermal conductivity of carbon fibre fabrics and multi-scale composites with heat transfer simulations for RFI manufacturing. 2013.

[34] Park S, Kim DS. Preparation and physical properties of an epoxy nanocomposite with amine-functionalized graphenes. Polym Eng Sci 2014;54:985–91. doi:10.1002/pen.23368.

[35] Monteserín C, Blanco M, Aranzabe E, Aranzabe A, Vilas JL. Effects of graphene oxide and chemically reduced graphene oxide on the curing kinetics of epoxy amine composites. J Appl Polym Sci 2017;134:12–6. doi:10.1002/app.44803.

[36] Qi B, Yuan Z, Lu S, Liu K, Li S, Yang L, et al. Mechanical and thermal properties of epoxy composites containing graphene oxide and liquid crystalline epoxy. Fibers Polym 2014;15:326–33. doi:10.1007/s12221-014-0326-5.

[37] Katti P, Kundan K V., Kumar S, Bose S. Improved mechanical properties through engineering the interface by poly (ether ether ketone) grafted graphene oxide in epoxy based nanocomposites. Polym (United Kingdom) 2017;122:184–93. doi:10.1016/j.polymer.2017.06.059.

[38] Vazquez-Moreno JM, Yuste-Sanchez V, Sanchez-Hidalgo R, Verdejo R, Lopez-Manchado MA, Fernandez-Garcia L, et al. Customizing thermally-reduced graphene oxides for electrically conductive or mechanical reinforced epoxy nanocomposites. Eur Polym J 2017;93:1–7. doi:10.1016/j.eurpolymj.2017.05.026.

[39] Lei L, Xia Z, Zhang L, Zhang Y, Zhong L. Preparation and properties of amino-functional reduced graphene oxide/waterborne polyurethane hybrid emulsions. Prog Org Coatings 2016;97:19–27. doi:10.1016/j.porgcoat.2016.03.011.

[40] Bello RH, Coelho LA, Becker D. Role of chemical funcionalization of carbon nanoparticles in epoxy matrices. J Compos Mater 2017:002199831770908. doi:10.1177/0021998317709082.

[41] Du X, Zhou H, Sun W, Liu HY, Zhou G, Zhou H, et al. Graphene/epoxy interleaves for delamination toughening and monitoring of crack damage in carbon fibre/epoxy composite laminates. Compos Sci Technol 2017;140:123–33. doi:10.1016/j.compscitech.2016.12.028.

[42] Wang F, Drzal LT, Qin Y, Huang Z. Effects of functionalized graphene nanoplatelets on the morphology and properties of epoxy resins. High Perform Polym 2016;28:525–36. doi:10.1177/0954008315588983.

[43] Teng CC, Ma CCM, Lu CH, Yang SY, Lee SH, Hsiao MC, et al. Thermal conductivity and structure of non-covalent functionalized graphene/epoxy composites. Carbon N Y 2011;49:5107–16. doi:10.1016/j.carbon.2011.06.095.

[44] Kausar A, Anwar Z, Khan LA, Muhammad B. Functional graphene nanoplatelet reinforced epoxy resin and polystyrene-based block copolymer nanocomposite. Fullerenes, Nanotub Carbon Nanostructures 2017;25:47–57. doi:10.1080/1536383X.2016.1251418.

[45] Liu Q, Zhou X, Fan X, Zhu C, Yao X, Liu Z. Mechanical and Thermal Properties of Epoxy Resin Nanocomposites Reinforced with Graphene Oxide. Polym Plast Technol Eng 2012;51:251–6. doi:10.1080/03602559.2011.625381.

[46] Tschoppe K, Beckert F, Beckert M, Mulhaupt R. Thermally reduced graphite oxide and mechanochemically functionalized graphene as functional fillers for epoxy nanocomposites. Macromol Mater Eng 2015;300:140–52. doi:10.1002/mame.201400245.

[47] Rafiee M, Nitzsche F, Labrosse MR. Effect of functionalization of carbon nanotubes on

vibration and damping characteristics of epoxy nanocomposites. Polym Test 2018;69:385–95.

[48] Lau K tak, Gu C, Hui D. A critical review on nanotube and nanotube/nanoclay related polymer composite materials. Compos Part B Eng 2006;37:425–36. doi:10.1016/j.compositesb.2006.02.020.

[49] Schniepp HC, Li JL, McAllister MJ, Sai H, Herrera-Alonson M, Adamson DH, et al. Functionalized single graphene sheets derived from splitting graphite oxide. J Phys Chem B 2006;110:8535–9. doi:10.1021/jp060936f.

[50] Yen MY, Hsiao MC, Liao SH, Liu PI, Tsai HM, Ma CCM, et al. Preparation of graphene/multi-walled carbon nanotube hybrid and its use as photoanodes of dye-sensitized solar cells. Carbon N Y 2011;49:3597–606. doi:10.1016/j.carbon.2011.04.062.

[51] Schulz SC, Bauhofer W. Shear influenced network dynamics and electrical conductivity recovery in carbon nanotube/epoxy suspensions. Polymer (Guildf) 2010;51:5500–5. doi:10.1016/j.polymer.2010.09.027.

Chapter 9

9. General discussion and conclusions

9.1 Summary of results

Before discussing the general implications of the work contained in this dissertation or discussing how the results fit together with one another and the big picture, this section briefly summarizes the previous chapters.

Chapter 2 reviewed the previous studies on the subject of advanced composite materials and beam-type structures. The review addressed analytical, semi-analytical and numerical studies dealing with dynamic problems involving adaptive/smart/intelligent materials (e.g. piezoelectric materials, electrorheological fluids, shape memory alloys, etc.), damping and vibration control, advanced composite materials (e.g. functionally graded materials and nanocomposites), complicating effects and loadings (e.g. added mass, tapered beams, initial curve and twist, etc.), and experimental methods. Chapter 3 introduced a computational model to study the nonlinear steady state static response and free vibrations of thin-walled carbon nanotubes/fiber/polymer laminated multiscale composite beams and blades. Chapter 4 addressed the cross-sectional design and analysis of fiber-reinforced multiscale composite beams of general cross-sectional shape and arbitrary anisotropic material properties and investigated the effect of carbon nanotubes on their stiffness properties. In Chapter 5, a mathematical model was developed to predict the effective material properties of graphene nanoplatelets/fiber/polymer multiscale composites. The large deflection, post-buckling and free nonlinear vibrations of graphene nanoplatelets-reinforced multiscale composite beams were studied through a theoretical study. The vibration and damping characteristics of epoxy composites reinforced by pristine and functionalized multi-walled carbon nanotubes were investigated experimentally in Chapter 6 for potential use as integral passive damping elements in structural composite applications. In Chapter 7, a novel low cost manufacturing method, combining surface treatment of fibers with matrix modification techniques, was introduced to incorporate nanoparticles for the simultaneous reinforcement of matrix and fibers. Finally, Chapter 8 looked at the thermal conductivities of the epoxy/fiberglass/nanoparticle composites. The DSC, TGA and thermal conductivity measurements were also performed for two-phase epoxy/nanoparticle mixtures.

9.2 General discussion

This section serves the purpose of uniting many of the ideas presented in this dissertation (and summarized above). The following discussion builds upon the conclusions from each chapter, brings them together and discusses some other results from this dissertation that are not necessarily the focus of any of the preceding chapters, such as the experimental methods that were developed over the course of this research. Furthermore, several broad conclusions are drawn from all of the above results.

9.2.1 Mathematical modeling

In this dissertation, structural models have been specifically developed to investigate the effects of both CNTs and GNPs on the mechanical behavior of nanocomposite structures. Nonlinear steady state response and linear free vibrations of rotating and non-rotating beams and blades made of CNTs-reinforced multiscale laminates were studied. Being analytical, the proposed models allow for convenient parametric analyses and are less computationally expensive than finite element models. However, they do not resort to one-dimensional governing equations, and therefore, they are expected to be more accurate than theories assuming a priori knowledge of the cross-sectional deformation. SWCNT reinforcement was found to produced more pronounced effect on the natural frequencies of the beam compared to MWCNT reinforcement. This may be attributed to the defect-free structure of SWCNTs. The results also confirmed that low aspect ratio CNTs in laminated composite beams bring about less significant improvement in nonlinear steady state response and natural frequencies of the composite beams. Another finding was that the rise in fundamental natural frequency of beams due to addition of carbon nanotubes is more significant in nonrotating conditions than rotating ones. The results and tools presented in this study may assist in the design of a new generation of rotating blades made of nanocomposite materials.

Mathematically, this dissertation also detailed the incorporation of graphene nanoparticles on the effective material properties and nonlinear mechanical analysis of the multiscale laminates. Large deflections, thermal post-buckling and nonlinear free oscillation of GNPs/fiber/polymer multiscale composite beams were studied within the framework of the Euler–Bernoulli beam theory, with a von Kármán-type displacement–strain relationship. The nonlinear bending and post-buckling equations were numerically solved by the Newton method, and the multiple timescales method was used to study the nonlinear free vibrations and dynamic response of laminated nanocomposite beam under two sets of boundary conditions. The numerical results showed that the central deflection, and natural frequency significantly improved with a small percentage of GNPs. However, addition of GNPs led to lower critical buckling temperatures. The results also confirmed that GNPs in laminated composite beams produce less improvement when combined with higher volume fractions of fibers.

Another mathematical investigation introduced was the formulation of a finite-element-based, cross-sectional analysis for CNTs-reinforced multiscale composite beams from geometrically nonlinear, 3D elasticity. The 3D strain field was formulated in terms of 1D generalized strains and a 3D warping displacement. The developed formulation was numerically implemented in tVABS to compute the cross-section stiffness matrices and mass properties. The results indicated that the inclusion of a small weight percentage of carbon nanotubes in the polymer matrix was sufficient to induce a significant improvement in stiffness properties. In some cases, CNTs may also be used to weaken specific structural couplings. SWCNTs were shown to have more significant effects than MWCNTs on the stiffness properties. This may be due to the defect structure of MWCNTs. Overall, CNTs can be used to tailor the design of beams and blades for specific stiffness properties.

9.2.2 Experimental investigation

Simultaneous reinforcement of matrix and fibers was carried out via a novel method that combined a nanoparticle spraying process with nanoparticle/epoxy mixture to incorporate nanoparticles for the enhancement of thermo-mechanical properties of laminated multiscale epoxy composites. Several graphene-based nanomaterials including graphene oxide, reduced graphene oxide, graphene nanoplatelets, and multi-walled carbon nanotubes were employed to modify the epoxy matrix and the surface of glass fibers. The morphological, rheological, thermal and mechanical properties of the glass fiber-reinforced multiscale composites were investigated. Increased epoxy viscosity, due to the addition of MWCNTs, is not suitable for the VARTM process or other types of relatively low pressure infusion processes On the other hand, the viscosity of epoxy / GNPs did not increase dramatically by addition of nanoparticles up to 1 wt% of GNPs in DGEBA. Based on the experiments performed in this study, MWCNTs loading in the epoxy matrix can reach up to 0.075 wt% to avoid filtration by fabrics, and for GNP, GO and rGO, loadings, can be tailored according to the intended applications.

Thermal properties of epoxy/nanoparticle composites were also studied. The results indicated that the introduction of GNPs, GO, rGO, and MWCNTs enhanced thermal conductivity. The thermal conductivity of two-phase epoxy/nanoparticle composites was increased by up to

6.0% for 1.2 wt% of GNPs in DGEBA. Compared with the neat GRFP control results, thermal conductivity improvement in fiberglass/epoxy modified with MWCNTs 0.3%, GNPs 1%, GO 2% and rGO 0.042% were 8.8, 12.6, 8.2 and 4.1 %, respectively. It was concluded that, for the same volume fraction, GNPs exhibit more improvement to thermal conductivity than the other nanoparticles studied. Controlling dispersion of nanoparticles and interfacial interaction between nanoparticles and epoxy is critical to optimally enhancing the thermal conductivity of nanocomposite materials.

The tensile properties and interlaminar shear strength (ILSS) of the glass fiber reinforced composites were investigated and the results indicated that the introduction of graphene nanoplatelets, graphene oxide, reduced-graphene oxide, and multi-walled carbon nanotubes enhanced the mechanical properties. In particular, the addition of 0.1, 1 and 0.01 wt. % of graphene nanoplatelets, graphene oxide, and reduced-graphene oxide led to 6.8, 14.6 and 8.2% improvements in ultimate load capacity of the glass fiber reinforced composite, respectively. Compared with the neat epoxy/fiberglass composite control results, the average ILSS value of multiscale nanocomposites increased by up to 15.4, 8.9, 13.3 and 10.7% with the 0.15, 0.2,1.0 and 0.042 wt.% of MWCNTs, GNP, GO and rGO, respectively. Micrographic examinations showed that the tensile loading capacity and interlaminar shear properties enhancements were most likely attributable to the improvements in resin toughness and the adhesion between glass fibers and epoxy resin being enhanced by the introduction of carbon nanoparticles.

The experimental vibration and damping behaviors of p-MWCNTs/epoxy and f-MWCNTs/epoxy nanocomposites were also studied. Nanocomposite specimens were fabricated for six different MWCNT loadings (0.02, 0.041, 0.061, 0.123, 0.25 and 0.37 wt%). The frequency response functions, coherence and phase diagrams of nanocomposites were measured using periodic up-chirp forced vibration technique. The experimental results indicated that the damped natural frequencies in p-MWCNTs/epoxy and f- MWCNTs/epoxy composites increased with MWCNTs loading up to 0.12 wt.% and decreased at higher MWCNTs content. Another finding was that the improvement in fundamental natural frequency was more pronounced than at higher natural frequencies. The forced vibration test confirmed the beneficial effect of p-MWCNTs on the damping ratio of nanocomposites for the first and second vibration modes. However, a decrease in damping ratio was observed in f-MWCNTs/epoxy composites. For instance, a 46% improvement in damping ratio for the fundamental vibration mode was observed at a loading of

0.37 wt.% in p-MWCNTs/epoxy composite. While the damping ratios from f-MWCNTs at loadings of 0.02–0.06 wt.% were higher than those from p-MWCNTs, they did not increase at higher CNTs contents for the first mode of vibration.

9.3 Conclusions

To summarize, the main conclusions from this dissertation are:

1. The state of the art in rotating composite beams and blades was investigated and a presentation of the remaining challenges and future research needs was provided.
2. The nonlinear steady state static response and free vibrations of CNTs/fiber/polymer laminated multiscale composite beams was studied and it was found that the SWCNTs reinforcement produces more pronounced effect in comparison with MWCNTs on the nonlinear steady state static response and natural frequencies of the composite beams. Another finding was that the rise in fundamental natural frequency of beams due to addition of carbon nanotubes is more significant in nonrotating conditions than in rotating ones.
3. The effective material properties of multiscale graphene-modified composite laminates were developed analytically and insightful information about the effect of the GNPs on the large deflection, buckling and post-buckling and nonlinear free vibration of multiscale composite laminates was obtained. The results confirmed that GNPs in laminated composite beams produce less improvement when combined with higher volume fractions of fibers.
4. A finite-element-based, cross-sectional analysis for CNTs-reinforced multiscale composite beams was formulated from geometrically nonlinear, 3D elasticity. The results indicated that the inclusion of a small weight percentage of carbon nanotubes in the polymer matrix was sufficient to induce a significant improvement in stiffness properties. In some cases, however, CNTs may be used to weaken specific structural couplings. SWCNTs were shown to have more significant effects than MWCNTs on the stiffness properties. This may be due to lower specific surface area and defect structure of MWCNTs. Overall, CNTs can be used to tailor the design of beams and blades for specific stiffness properties.
5. The morphology of carbon nanomaterials-modified composites provide insightful information. TEM results gave information about the particle size and shape. Optical micrographs demonstrated the dispersion state and agglomeration of nanoparticles dispersed in the epoxy matrix. At higher loadings of nanoparticles, the presence of large size nanoparticle aggregates

was observed, primarily due to van der Waals forces between the nanoparticles. The surface morphology of glass fibers coated with nanoparticles was observed by SEM and a relatively uniform coating was observed. The fracture surfaces of the fiber-reinforced composites were examined by SEM and the micrographs was used to explain the tensile and ILSS results.

6. Steady shear viscosity profiles for MWCNTs and GNPs demonstrate a shear-thinning behavior where shear viscosity decreases sharply with increasing the shear rate. This phenomenon was more obvious for functionalized nanoparticles than pristine ones. Besides, MWCNTs led to stronger non-Newtonian behavior than the other nanoparticles considered in this dissertation. This increased viscosity, due to the addition of MWCNTs, is not suitable for VARTM or other types of relatively low pressure infusion processes. On the other hand, the viscosity of epoxy/GNPs did not increase dramatically by addition of nanoparticles up to 1 wt% of GNPs in DGEBA. Based on the experiments performed in this study, MWCNTs loading in the epoxy matrix can reach up to 0.075 wt% to avoid filtration by fabrics, and for GNPs, loadings can be tailored according to the intended applications.
7. The tensile properties and interlaminar shear strength (ILSS) of the glass fiber reinforced composites was studied and the results indicated that the introduction of graphene nanoplatelets, graphene oxide, reduced-graphene oxide, and multi-walled carbon nanotubes enhanced the mechanical properties. Micrographic examinations showed that the tensile loading capacity and interlaminar shear properties enhancements were most likely attributable to the improvements in resin toughness and the adhesion between glass fibers and epoxy resin being enhanced by the introduction of carbon nanoparticles. The composites involving neat epoxy matrix were destroyed from the fiber surface during the ILSS testing due to a weak interfacial bonding, and the smooth fiber surface was exposed after material fracture. However, with the addition of nanoparticle reinforcements, the glass fibers were well covered in the matrix after interlaminar fracture and the surface was rough. This indicated better bonding between fibers and matrix compared with neat GFRP composite.
8. The experimental vibration results indicated that the damped natural frequencies in p-MWCNTs/epoxy and f- MWCNTs/epoxy composites increased with MWCNTs loading up to 0.12 wt.% and decreased at higher MWCNTs content. Another finding was that the improvement in fundamental natural frequency was more pronounced than at higher natural frequencies. The forced vibration test confirmed the beneficial effect of p-MWCNTs on the

damping ratio of nanocomposites for the first and second vibration modes. However, a decrease in damping ratio was observed in f-MWCNTs/epoxy composites.

9. Thermal conductivity of two-phase and three-phase composites increased with an increase in the weight percentage of nanofillers. However, the improvement in thermal conductivities did not vary linearly with nanoparticle loading. For the same volume fraction of nanoparticles, GNPs resulted in the highest increase in thermal conductivity while GO resulted in the lowest relative increase when compared with other nanoparticles investigated in this study. This was probably due to the presence of large quantities of oxygen groups in GO. The presence of oxygen groups can act as scattering points for the phonons through the graphene layers that weaken the interfacial connection between nanoparticles and epoxy. MWCNTs are generally very good thermal conductors along the tube, and good insulators perpendicularly to the tube axis. This property makes MWCNTs less effective compared to GNPs for enhancement of thermal conductivity of their composites. Another reason for less improvement of thermal conductivity in MWCNTs/epoxy may be due to poor dispersion of the MWCNTs in the epoxy compared with other nanoparticles.

The structural problems mathematically studied hereininclude the nonlinear static deflections of non-rotating and rotating cantilever beams and blades; the free vibrations of non-rotating and rotating cantilever beams and blades; the nonlinear static, large-amplitude free vibrations and post-buckling analyses of simply-supported and clamped beams. In the context of structural mechanics, these are important analyses to describe the behavior of composite beams and to provide guidance on how to optimize such structures.

The experimental processing techniques, and concepts proposed in this dissertation will assist others in the development of multiscale nanocomposite materials and will aid them by providing directions fortheir research to produce composites tailored to their specific intended applications. The results and conclusions of this dissertation represent a step toward an optimized processing and fabrication, and toward a future where carbon nanomaterials-reinforced multiscale composites are fully understood, with many exciting potential applications turning into reality.

9.4 Recommendations for future work

Based on the observations from the current research, the following recommendations are suggested for future work:

- Mathematical models have been developed to determine the effective material properties of GFRP composites reinforced with GNPs and CNTs. It would be worth investigating mathematical models that can also handle the incorporation of GO and rGO toward the prediction of the effective material properties.
- Halpin-Tsai model is unable to account for agglomeration and local debonding of nanoparticles. Therefore, a rigorous mathematical model that can account for both agglomeration and local debonding is needed.
- The mathematical models developed in this dissertation are based on the assumption of uniformly distributed nanoparticles within the epoxy matrix. Because some level of agglomeration exists in the epoxy/nanoparticle mixture, mathematical/computational models to take this agglomeration into account are required for better understanding and prediction of nanocomposites.
- All mathematical models available in the literature are based on pristine nanoparticles. Our literature review reveals that the influence of functionalization on the effective material properties has not been investigated numerically. Therefore, mathematical models that can take into account the effect of nanoparticle functionalization are needed.
- The present study focused on low content graphene-modified nanocomposite laminates. However, it would be interesting to explore the trend of the results at higher wt% of nanoparticles for both epoxy and fiber reinforced epoxy composites.
- This dissertation focused on MWCNTs, GNPs, GO and rGO. Carbon nanothread is a new allotrope of carbon discovered in 2015. It would be worth investigating the effect of this new allotrope on the thermo-mechanical properties of nanocomposite materials.